Physiology-based Mathematical Models for the Intensive Care Unit: Application to Mechanical Ventilation

Antonio Albanese

Submitted in partial fulfillment of the
requirements for the degree of
Doctor of Philosophy
in the Graduate School of Arts and Sciences

COLUMBIA UNIVERSITY

2014

ABSTRACT

Physiology-based Mathematical Models for the Intensive Care Unit: Application to Mechanical Ventilation

Antonio Albanese

This work takes us a step closer to realizing personalized medicine, complementing empirical and heuristic way in which clinicians typically work. This thesis presents mechanistic models of physiology. These models, given continuous signals from a patient, can be fine-tuned via parameter estimation methods so that the model's outputs match the patient's. We thus obtain a virtual patient mimicking the patient at hand. Therapeutic scenarios can then be applied and optimal diagnosis and therapy can thus be attained. As such, personalized medicine can then be achieved without resorting to costly genetics.

In particular we have developed a novel comprehensive mathematical model of the cardiopulmonary system that includes cardiovascular circulation, respiratory mechanics, tissue and alveolar gas exchange, as well as short-term neural control. Validity of the model was proven by the excellent agreement with real patient data, under normo-physiological as well as hypercapnic and hypoxic conditions, taken from literature.

As a concrete example, a submodel of the lung mechanics was fine-tuned using real patient data and personalized respiratory parameters (resistance, R_{rs}, and compliance, C_{rs}) were estimated continually. This allows us to compute the patient's effort (Work of Breathing), continuously and more importantly noninvasively.

Finally, the use of Bayesian estimation techniques, which allow incorporation of population studies and prior information about model's parameters, was proposed in the contest of patient-specific physiological models. A Bayesian Maximum a Posteriori

Probability (MAP) estimator was implemented and applied to a case-study of respiratory mechanics. Its superiority against the classical Least Squares method was proven in data-poor conditions using both simulated and real animal data.

This thesis can serve as a platform for a plethora of applications for cardiopulmonary personalized medicine.

Table of Contents

List of Figures

List of Tables

Acknowledgments

It is time for the acknowledgments and yet it is hard for me to realize that a very important chapter of my professional career and life is about to end. If I picture myself a couple of years ago, I would have never thought I could be able to write these pages. This PhD has been a long and exciting journey and many people have contributed to this success. I can only hope these words will make justice to those who have supported me throughout these years.

I'll begin with my thesis supervisor and now colleague at Philips Research North America, **Dr. Nicolas W. Chbat**. Nick is a fantastic advisor and without his help and mentoring this work would have not been possible. I met Nick a while ago, while still studying for my Master Degree, and ever since I have always found him an extremely useful source of inspiration. His vision and passion for a quantitative approach to physiology and medicine has driven my work and set my career goals throughout these years. Without him, I would still be thinking that biomedical research is something confined to the walls of few academic labs, detached from real world applications and industry. He has taught me that physiology and medicine are fields that deserve to be studied and analyzed with the same engineering rigour that is typically applied to traditional mechanical systems. With his work, he has also taught me that if you truly believe in your research and you constantly fight for it, then eventually people will recognize the importance of your work. This is an important lesson that I will carry for my entire career and for this I am extremely grateful to him. Throughout these years he has always been available for me, for academic, research and personal advises, despite his very busy schedule even during nights and weekends. I believe that such level of dedication and attention is reserved to very few lucky PhD students. Nick, thanks for all you have done for me throughout these years!

My academic advisor at Columbia University, **Professor Andrew Laine**, has been very helpful in guiding me throughout coursework and student's life at Columbia, especially in the first period of my studies when the US education system was a big challenge for me. He has facilitated the development of this work in every possible way, providing me space and resources in the Heffner Biomedical Imaging Lab at Columbia and making my time there as pleasant as possible.

This work has been carried out in the **Cardiopulmonary Group**, led by Dr. Chbat at Philips Research North America, and it would have not been accomplished without the help and support of all the members of the team. All of them have contributed to my research and for this I will always be grateful to them. Particularly, **Dr. Dong Wang** and **Francesco Vicario** have tremendously contributed to the development of the estimation methods that are described in Chapter 3 of this thesis. **Dr. Limei Cheng** has contributed to the cardiopulmonary model development and validation, described in Chapter 2. **Nikolaos Karamolegkos** has been tremendously valuable in any software/hardware interface related issue, always ready to help, and he has been a very important player in the project. **Roberto Buizza** has been the main contributor to the GUI development for the cardiopulmonary model. I would also like to mention the contribution of **Valentin Siderskiy**, whose dedication and work in the lab has laid down the basis for real-time applications of the modelling and estimation methods described in this thesis. Finally, the interactions with **Dr. Srini Vairavan**, **Dr. Reza Sharifi**, **Dr. Syed Haider, Dr. Miriam Makhlouf** and **Caitlyn Chiofolo** have been very beneficial for my research and my professional development. On a personal note, many people of the group have contributed in making my periods of research at Philips as enjoyable as possible. A special thank goes to the “Mediterranean group”: Roberto, Francesco, Nikos and Miriam, I feel lucky to have you as colleagues and friends, and to be able to share with you work and life events.

I would also like to thank **Dr. Adam Seiver**, of Philips Healthcare Therapeutic Care business unit, for very helpful discussions, ideas and support throughout this work.

Now comes the list of silent contributors. A big merit goes to my wife **Anna** for believing in me, for pushing me to pursue my PhD studies, for being patient throughout these years and for accepting the challenge of relocating to US and leave everything just to satisfy my professional ambitions. Anna, you have proven to be the perfect life partner and without your help I would have never been able to accomplish this. Thanks for your constant love and support, especially in this last period of studies when you took all the family responsibilities to allow me to focus on my thesis and complete my PhD journey in the best possible way. Our little son, **Pietro**, who was born during this period of studies, has filled our lives and with his smiles and laughs has helped me finding the energy needed to complete my PhD. Finally, I would like to thank my parents, **Enzo** and **Maria**, for their unconditional love and support during my entire life. You have thought me the most fundamental principles of life and how these are important not only from a personal life perspective but also in your every-day profession and work.

I thank **Philips Research North America** for providing a 4 year Van der Pol Fellowship that has supported my studies and for providing an environment rich of intellectual and material resources that have facilitated the development of this work. I feel privileged for being able to perform my research in such environment.

Dedication

To my son and wife: without your love and care I could not have reached this point. I dedicate this dissertation to you.

Chapter 1: Introduction

1.1 Motivation

Medicine is by and large an empirical field. Clinicians make diagnostic and therapeutic decisions based on their experience. *Evidence-based medicine* is the current trend. It consists in integrating individual clinical expertise with the best available external clinical evidence from systematic research. Recently, strong effort has been put to help clinicians in their decision making process via intelligent computerized systems (Clinical Decision Support Systems, CDSS). The majority of these systems have focused on simply translating clinicians' current way of thinking into a set of rules (rule-based systems). Others have tried to address the problem by exploiting the information contained in the data that are collected from patients and looking for patterns or correlations (data mining/machine learning-based systems). However, both approaches do not describe a complete picture to improve current standard of care. A complementary alternative is to bring a mechanistic understanding of the physiology via physiology-based mathematical models into the picture. Model-based approaches can be used to:

1. Understand the cause-effect relationships of diseases and test new physiological hypothesis.
2. Perform generic "what-if" scenarios and predict the effects of new therapies and interventions on a generic patient (or class of patients).
3. Perform personalized ”what-if" scenarios on a specific patient to quantitatively predict his/her response to different therapies or interventions. This leads to providing optimal and personalized therapy (*personalized medicine*). To accomplish this, the parameters of the physiological model will need to be fine-tuned to the specific patient (*patient-specific model*) via parameter estimation techniques.

4. Probe the physiological system under exam and provide noninvasive estimates of physiological variables and/or parameters that are otherwise hidden to the clinicians due to the invasiveness, cost and patient discomfort that come with their measurements. This information can be crucial for the assessment of patients' health status.
5. Detect and predict specific diseases.

Figure 1.1 shows a diagram of current standard of diagnostic and therapeutic medicine and how different sources of knowledge can be used to build CDSS to improve current standard of care. As highlighted in red, mechanistic physiology-based mathematical models can lead to *personalized medicine* as opposed to *population-based medicine*. Two main advantages of physiology-based models: they have the potential for optimizing diagnosis and therapy for the individual patient, and they are more readily acceptable in the medical community. The above comes with the understanding that a hybrid combination of two or all of the approaches shown in Figure 1.1 may be needed for specific applications.

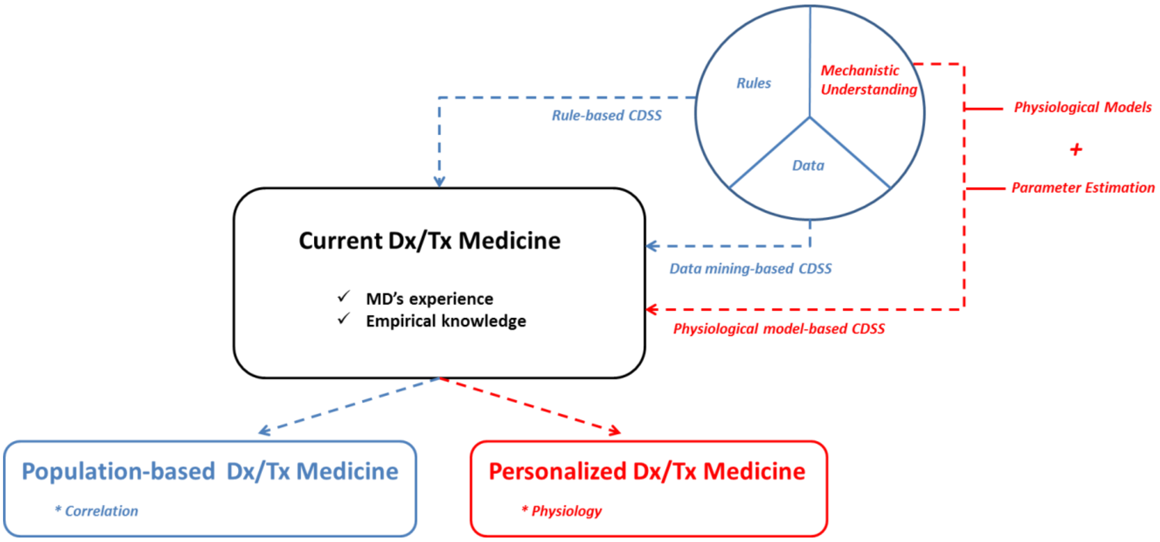

Figure 1.1 – Schematic of the current standard of diagnostic (Dx) and therapeutic (Tx) medicine and source of information for CDSS.

This thesis is a small step toward reaching personalized medicine. We accomplish this goal via advancing physiological modeling and parameter estimation. This work has been carried out in the Cardiopulmonary Group led by Dr. Chbat at Philips Research North America. The specific therapeutic application we choose is mechanical ventilation (MV).

MV is a commonly-used life-saving procedure. It is required when a patient is not able to achieve adequate ventilation (and thereby gas exchange). This may occur under many circumstances, for example in connection with surgery after anesthetics suppress the activity of the respiratory muscles, or in acute respiratory failure caused by chronic obstructive pulmonary disease (COPD), acute lung injury (ALI) or acute respiratory distress syndrome (ARDS). It is estimated that MV is required by nearly 1.5 million patients in the United States every year [1] and this number is set to increase. Most patients under MV would die without one. Hence, MV is the most viable therapy available today for patients suffering of respiratory failure.

However, since MV is not optimized for the specific patient, it can cause injury (8-10 % of the cases, with a 2013 figure placing this range to 10-24%). A main issue with a ventilator is that it exposes patients’ lungs to potentially destructive fluid/mechanical energy. As a result, if MV is not optimized, ventilator-induced lung injury (VILI) can occur, exacerbating existing conditions, prolonging length of stay in the ICU and increasing the risk of infection, pneumonia and fatality due to multiple organ failure. Apart from patient safety and clinical outcomes related concerns, there are also economic aspects associated with MV. The average cost of a day in the ICU is somewhere between \$3,518 [2] and \$31,574 [3], depending on the specific therapy used. Hence, an extra day under MV not only increases the risk of the patient developing ventilator-related complications but also increases healthcare cost.

Although mechanical ventilation has been used in the ICU for many years, the management of the mechanically ventilated patient is still largely based on empirical knowledge. Particularly, selecting the best ventilation mode and adjusting the ventilator settings as the conditions or the status of the patient change has remained a challenging task even for the most experienced clinicians. This is due to the fact that the effects of ventilator setting on the patient status are hardly predictable. The ventilator settings to be adjusted can be many and each may have counteracting effects on the patient health. In fact, the degree of interaction between the cardiovascular and the respiratory system is so high that often times beneficial effects of ventilator resetting on one system are offset by detrimental effects on the other system. For these reasons and given the limited time available for making clinical decisions, ventilator settings adjustments are mostly driven by intuition or empirical knowledge, rather than by quantitative mechanistic arguments. Furthermore, a trial-error strategy is typically used when making ventilator settings adjustments. Clearly, this strategy is suboptimal and may cause harm to the patient, as the effects of ventilator settings can only be evaluated after these have been actually applied to the patient.

Standardized ventilator management protocols and guidelines do exist. However, these are rigid generalized approaches, not tailored to the specific patient’s pathophysiology. As a result, a high number of patients are still ventilated with sub-optimal ventilator settings. A recent study [4] has shown that during 4 hours of conventional mechanical ventilation according to clinical guidelines, only 12% of the times the patients were receiving appropriate mechanical ventilation therapy.

In the ICU only arterial blood pressure (ABP), heart rate (HR), oxygen saturation (SpO2), end-tidal CO_2 ($EtCO_2$) and very few other variables are monitored. Many other meaningful clinical variables/parameters remain hidden, to the clinicians, as their monitoring would require invasive procedures or interference with the normal operation of the ventilator. As a result, since clinicians rely on available measurements to make diagnosis and therapeutic decisions, their judgment and decisions are based only on a “partial” view of the patient status. For instance, in spontaneous modes of MV (where patient can actively breathe), quantitative assessment of patient respiratory efforts (Work of Breathing) is crucial in order to avoid respiratory muscles atrophy or fatigue, and ultimately lead to liberation (or weaning). However, this information (respiratory efforts assessment) can only be obtained via invasive procedures, such as pleural pressure or esophageal pressure manometry, and hence it is rarely offered at the bedside. Further, assessment of respiratory system’s mechanics during MV is typically accomplished by measuring two parameters, termed resistance (R_{rs}) and compliance (C_{rs}). These two describe the resistive and elastic properties of the respiratory system comprising airways, lung parenchyma and chest wall assuming a simplistic model of the lung mechanics. Knowledge of these parameters allows to optimize ventilation strategy or to even decide whether a therapeutic drug treatment is appropriate or not for that particular patient. The most accepted technique to measure R_{rs} and C_{rs} is the end-inspiratory hold maneuver, which requires a fully relaxed patient. Even though this maneuver is not invasive per se, it, however, interferes with the normal operation of the ventilator and cannot be applied during spontaneous modalities of MV when the patient is actively breathing. In these cases, monitoring of intrapleural pressure is required in order to offset the effects of patient inspiratory activity, which comes with the drawback already mentioned above. As a result, continuous monitoring of respiratory mechanics is not always done at the bedside.

Physiology-based mathematical models (or physiological models) can help improve this standard of MV therapy and can offer a valid tool to address some of the above limitations.

1. First, they can be used to quantitatively predict the patient response to ventilator settings adjustments. Hence, by using patient-specific physiological models of the

cardiopulmonary system, the effects of a particular choice of ventilator settings could be evaluated in virtual mode, without actually being applied to the patient.

2. Second, these models can be used to obtain continuous noninvasive estimates of those physiological variables and/or parameters (WOB, R_{rs}, C_{rs}, etc.) that are crucial to the assessment of the health status but are not monitored at the bedside. The additional information provided by these parameters and variables can be used, along with the already available measurements from the patient, to form a ”complete” view of his/her health status. This, in turn, provides better guidance for ventilator adjustments.

3. Third, since physiological models are a mathematical representation of the physical system under exam, they can be used with advanced mathematical optimization or control theory techniques, so to automatically select (closed-loop modality) ventilation strategy and settings that would maximize/minimize an objective function or maintain certain physiological variables within specific ranges. The closed-loop modality would also address the current shortage of respiratory care practitioners at the bedside.

This thesis develops methods to promote the use of physiology-based mathematical models of the cardiovascular and respiratory systems in order to improve current standard of care in mechanical ventilation. In order to be useful in the clinical setting, a mathematical model not only has to be accurate enough to capture the physiological mechanisms of the real biological system (in our case the cardiopulmary system), but it also needs to become “patient-specific” or “personalized”. Two fundamental ingredients are, hence, necessary in order to accomplish our goal: *1)* an accurate mathematical model of the cardiopulmonary system; *2)* efficient parameter estimation methods to fine tune the model to the particular patient under study, thus making it “patient specific”. For this reason, the aim of this thesis will be on both fronts of modeling and parameter estimation.

Our conjecture is that by taking full advantage of physiological models, mechanical ventilation therapy will no longer be an ”art” dictated by assumptions based on empirical knowledge, but rather a ”science” dictated by mechanistic understanding of the system under exam and of the underlying physiological processes. The use of physiological model-based clinical decision support (CDS) tools, or even closed-loop modalities, will eventually lead to a drastic change in MV therapy: from shift-by-shift ventilator adjustments to breath-by-breath personalized ventilation therapy - a major change in respiratory medicine.

1.2 Thesis Organization

The structure of this thesis is as follows:

Chapter 1 provides the introduction and motivation, and describes the scope, the organization of the thesis and its novel contributions.

Chapter 2 provides a review of existing physiological models of the cardiopulmonary system, emphasizing their limitation. It then describes the development and validation of a novel comprehensive model that overcomes some of these limitations.

Chapter 3 provides a description of current techniques for respiratory mechanics and work of breathing assessment, emphasizing their limitations. It then describes the development and validation of a novel model-based approach for simultaneous estimation of respiratory mechanics and work of breathing in spontaneously breathing mechanically ventilated patients.

Chapter 4 provides a comparison between classic and Bayesian parameter estimation techniques. It then describes the implementation of a Bayesian Maximum a Posteriori (MAP) estimator and its application to a case-study of respiratory mechanics.

Chapter 5 concludes the dissertation and details future research directions arising from this work.

1.3 Novel Contributions of the Thesis

The novel contributions of the thesis are:

1. **Development and validation of a novel comprehensive model of the cardiopulmonary system:** several key improvements differentiate this model from previous wok [5, 6]:
    a. Inclusion of tidal breathing lung mechanics;
    b. Inclusion of respiratory muscle pressure generator;
    c. Inclusion of lung gas exchange model;
    d. Inclusion of tissue gas exchange and venous blood transport models;
    e. Development and inclusion of a novel respiratory control model;
    f. Validation during hypercapnic, hypoxic and isocapnic hypoxic conditions.

    This work has so far resulted in the following publications:

    Albanese A, Cheng L, Ursino M, Chbat NW. A comprehensive mathematical model of the human cardiopulmonary system: Model development, *Am J Physiol Heart Circ Physiol* (submitted)

    Cheng L, Albanese A, Chbat NW. A comprehensive mathematical model of the human cardiopulmonary system: Sensitivity analysis and validation, *Am J Physiol Heart Circ Physiol* (to be submitted April 2014)

    Albanese A, Chbat NW, Ursino M. Transient respiratory response to hypercapnia: analysis via a cardiopulmonary simulation model, in Proceedings of *33rd Annual International Conference of the IEEE EMBS, Boston, USA, 2011*

    Albanese A, Cheng L, Chbat NW. Cardiopulmonary simulator and medical devices using cardiopulmonary simulator, *Philips Invention Disclosure,* January 2014

2. **Development and validation of a novel technique for the assessment of respiratory mechanics and patient's efforts in spontaneously breathing mechanically ventilated patients:** several key features differentiate this technique from existing methods [7, 8, 9] :
    a. Suitable for both active and passive patients;
    b. Noninvasive;
    c. Model-based and hence physiologically interpretable;
    d. Not interfering with normal ventilator operation;
    e. Inclusion of physiologically based constrained;
    f. The use of optimization techniques.

    This work resulted in the following publications:

    Albanese A, Karamolegkos N, Haider SW, Seiver A, Chbat NW. Real-time noninvasive estimation of intrapleural pressure in mechanically ventilated patients: a feasibility study. in Proceedings of *35th Annual International Conference of the IEEE EMBS, Osaka, Japan, 2013*

    Albanese A, Karamolegkos N, Haider SW, Seiver A, Chbat NW. Real-time Non-invasive Pleural Pressure and Work of Breathing Estimation, *Philips Technical Report*, February 2013

    Chbat NW, Albanese A, Karamolegkos N, Haider SW, Seiver A. Real-time Non-invasive Estimation of Work of Breathing, *Patent Pending*, February 2013

    Albanese A, Vicario F, Wang D, Karamolegkos N, Chbat NW. Simultaneous Estimation of Respiratory Mechanics and Patient's Effort via Constrained Optimization Method, *Philips Invention Disclosure*, January 2014

    Wang D, Vicario F, Albanese A, Karamolegkos N, Chbat NW. Non-invasive method for monitoring patient respiratory status via successive parameter estimation, *Philips Invention Disclosure*, January 2014

3. **Implementation of a Bayesian MAP estimator for respiratory mechanics:** the concept of MAP Bayesian estimation is known; however, to the best of our knowledge it has never been applied to respiratory mechanics studies.

   A conference and a journal papers are envisioned.

Chapter 2: Cardiopulmonary Modeling

2.1 Introduction

As mentioned in *Chapter 1–Introduction*, a prerequisite to the development of model-based intelligent systems that optimize mechanical ventilation is the development of a comprehensive and accurate mathematical model of the cardiovascular and respiratory systems.

Mathematical representation of the mechanistic function of the cardiovascular and respiratory systems is a challenging task. These two systems in humans interact via several mechanisms, continuously, in a complex and non-linear manner. Oxygen (O_2) and carbon dioxide (CO_2) are exchanged between pulmonary capillary blood and alveolar air, and the efficacy of such exchange depends on the success of their coupling. Furthermore, the amount of blood pumped by the heart and the degree of vessel vasoconstriction affect the blood gas transport delay, which is a key determinant of O_2 and CO_2 blood contents. These, in turn, modulate the depth and frequency of respiratory efforts via the action of specific receptors (*chemoreceptors*), which become active when O_2 and CO_2 are out of their normal ranges. The resulting increased tidal volume is sensed by receptors in the lungs that detects stretch of the pulmonary tissues (*lung stretch receptors*). When activated, these receptors induce peripheral vasoconstriction and bradycardia via modulation of the *sympathetic* and *parasympathetic* (*vagal*) activities of the autonomic nervous system (ANS). Mechanical interactions also exist due to the fact that the chest contains the respiratory system and a significant portion of the cardiovascular system. These are particularly important during mechanical ventilation, when elevated intra-thoracic pressure could compromise ventricular filling and stroke volume, thus reducing arterial blood pressure (ABP). ABP, in turn, modulates the activity of specific cardiovascular receptors (*baroreceptors*) that induce neural activity changes in both the *sympathetic* and *parasympathetic* branches of the ANS, ultimately affecting heart rate, cardiac contractility and vasomotor tone. Mechanisms outside ANS control also exist. Local *autoregulation* and central nervous system (CNS) *ischemic response* are such examples. These become active in extreme conditions, such as severe hypoxia, to preserve perfusion and oxygen supply to vital organs (e.g brain and coronary arteries).

From the above description, it appears evident that the development of an accurate and comprehensive mathematical model that accounts for such complex interactions is a challenging task. Several physiological models of the cardiopulmonary system have been proposed in the literature, but the majority are primarily either cardiovascular or pulmonary and as such do not address their coupling. In this chapter, some of these existing cardiopulmonary models are first reviewed, emphasizing their limitations and hence the need for a novel integrative cardiopulmonary model. Then, the developed model will be described, focusing on the new aspects with respect to previous models. Finally, model validation under normal and pathological conditions will be shown via comparison with experimental data from humans or animals.

2.2 History and Review of Cardiopulmonary Models

Pioneering work in cardiorespiratory modeling was started by Grodins and his colleagues in the 1950s. To the best of our knowledge, Grodins was the first one to suggest the use of control theory to describe the respiratory system and its regulation mechanisms. In the seminal 1954 paper [10], Grodins and colleagues described the respiratory system as a closed-loop feedback system (see Figure 2.1) where the controlled system (*plant*) was represented by a combined lung-blood-tissue compartment, the controlled variable was the tissue CO_2 concentration, the controlling quantity was the pulmonary ventilation, the disturbing quantity was the concentration of CO_2 in the inspired air ($FiCO_2$) and the controlling system (*controller* + *actuator*) was represented by the combination of the medullary respiratory centers (including the *chemorecptors*), the motor nerves to the respiratory muscles and the ventilatory pump itself. The equations describing the lung-blood-tissue compartment were derived based on first principles (conservation of mass), whereas the equations describing the controlling system were derived based on empirical observations. The resulting model was then described by a set of coupled non-linear differential equations, whose solutions (obtained with the aid of an analog computer) yielded predictions for the relationship between ventilation and arterial P_{CO2} that were in agreement with the observed physiological responses.

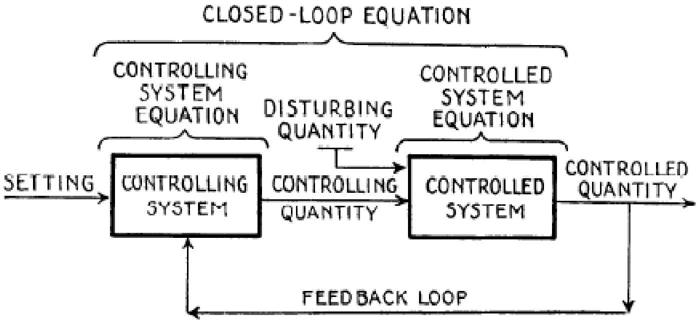

Figure 2.1- Block diagram of the feedback control system described in Grodins *et al.* [10]

The model was subsequently expanded in 1967 [11] to include a more detailed description of the plant and the effects of O_2 and hydrogen ions (H^+) on ventilation. The subsequent model is shown in Figure 2.2. The controlled system was then represented by three compartments (lung, brain and tissue) connected by the circulating blood. An additional cerebrospinal fluid (CSF) compartment was also included in the model, as well as acid-base buffering, gas transport delays and the effects of local autoregulation and chemoreceptors on cardiac output. The model has formed the basis of much further work [12, 13, 14] and it is considered a landmark achievement in the field. However, several limitations can be observed: *1)* The description of the plant is extremely simplified, with only three compartments representing the whole system; *2)* The events of the respiratory cycle are ignored and the lung is modelled as a compartment of constant volume, uniform content, and no deadspace, ventilated by a continuous unidirectional flow; *3)* Description of the cardiovascular system is completely neglected, hence the cardiac output is regarded as a nonpulsatile quantity, which can vary only based on the O_2 and CO_2 blood contents via the action of chemoreceptors and local autoregulation mechanisms.

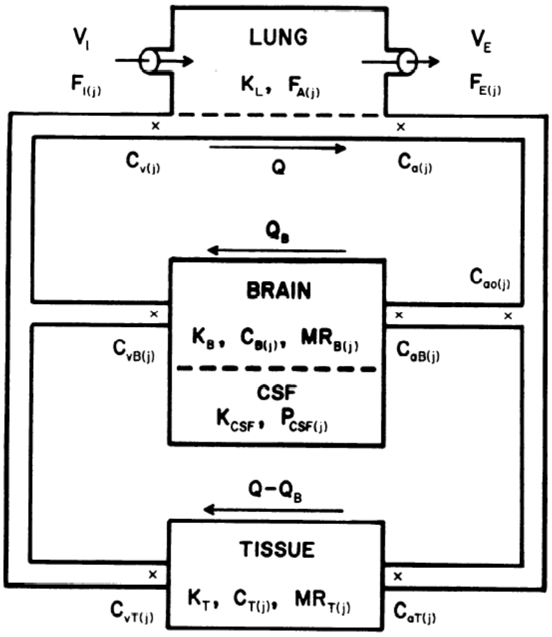

Figure 2.2 - Block diagram of the controlled system used in Grodins *et al.* [11]. V, flow rate; F, air gas fraction; K, volume; Q, blood flow; C, blood gas concentration; MR, metabolic rate; P, partial pressure. Subscripts: I, inspiratory ; E, expiratory; j, O_2 or CO_2; A, alveoli; T, tissue; B, brain; CSF, cerebrospinal fluid; a, arteries; v, veins; ao, aorta; aB, brain arteries; aT, tissue arteries; vT, tissue veins; vB, brain veins.

Another seminal paper in the field was presented by Guyton and his co-workers in 1972 [15]. It describes the first large-scale integrated cardiovascular model that allowed for the dynamic simulation of circulation, arterial pressure control mechanisms and body fluids regulation. The description of the model in the original article was not given in terms of mathematical equations, but in the form of a single graphical chart showing computing blocks interconnected via wires (see Figure 2.3). The model is constructed around a central circulatory dynamics module in interaction with 17 peripheral modules corresponding to various physiological functions. The cardiovascular module distinguishes between left heart, systemic arteries, systemic veins, right heart and pulmonary circulation (see Figure 2.4).

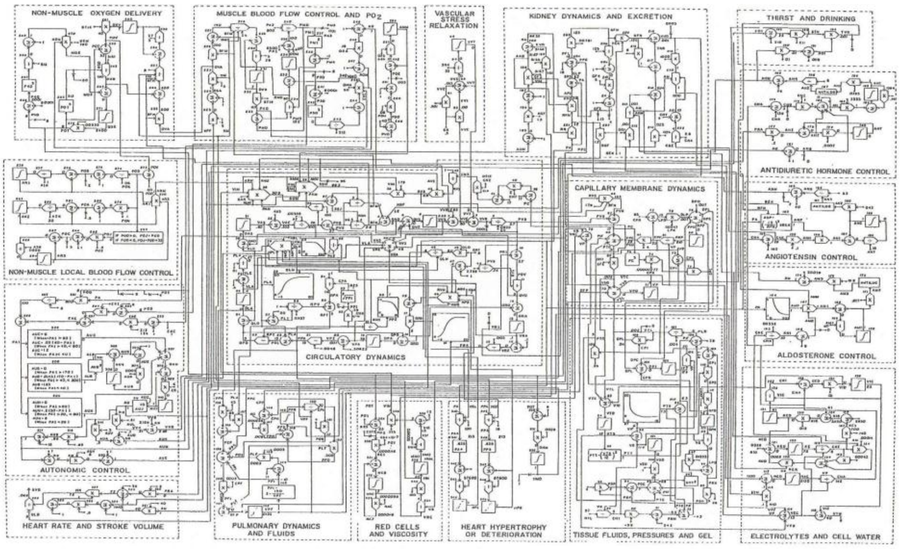

Figure 2.3- Block diagram of the original Guyton’s 1972 model [15]

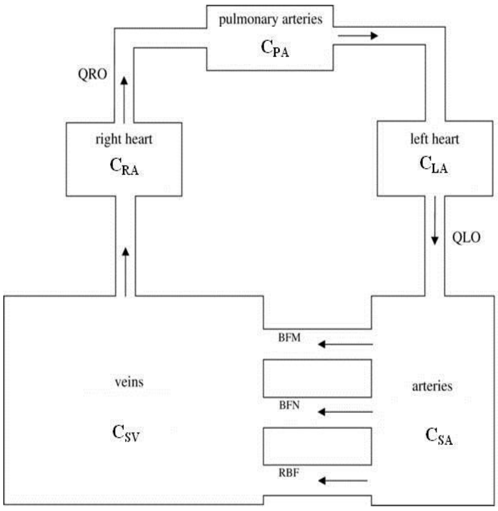

Figure 2.4 - Block diagram of the cardiovascular module in Guyton’s 1972 model [15]. QLO, cardiac output from left heart; QRO, cardiac output from right heart; C, compliance ; SA, systemic arteries; SV, systemic veins; RA, right atrium; PA, pulmonary artery; LA, left heart; BFM, muscle blood flow; BFN, non-muscle blood flow; RBF, renal blood flow. Figure adapted from [16].

The model includes autonomic regulation via the *baroreceptors* and *chemoreceptors*, local *autoregulation* of blood flow, kidney dynamics, fluid shifts among circulation, interstitium and cells, and the cardiovascular and renal effects of angiotensin, aldosterone and antidiuretic hormone. As described by Thomas *et al*. [16], from a global standpoint the model is governed by conservation relationships concerning sodium, potassium, oxygen, protein, water and blood volumes in the circulatory loop. Each conservation relation is expressed by a set of ordinary differential equations, which are combined with empirical curve fits of experimental data. Despite the complexity and the high number of different physiological mechanisms included, fundamental limitations of the model are: *1)* Pulsatility of the heart is not considered, hence all the variables computed by the model represent average values over the heart cycle; *2)* The model of autonomic regulation is not very accurate and because of the absence of cardiovascular pulsatility, the model is inadequate to reproduce short-term cardiovascular adjustments; *3)* The description of gas exchange in the lungs, lung mechanics and respiratory control is completely absent; *4)* O_2 dynamics are included in the model, but due to the absence of a respiratory module their description does not obey to physiological laws; for instance, O_2 saturation is computed as a linear function of pulmonary fluid volume, which seems a strong assumption; *5)* The dynamics of CO_2, which is known to play an important role in cardiovascular regulation, are neglected; *6)* Finally, the model mostly relies on empirical relationships based on common physiological knowledge rather than first-principles physiological laws. Nevertheless, Guyton's model has been extensively considered in the last decades and is currently used as a base for a number of research studies in the field of physiology [16, 17].

Hence, we can conclude that Grodins and Guyton can be considered the "fathers" of the field of cardiouplumonary modeling. However, due to the physiological knowledge and limited computational power of the time, the interactions between the cardiovascular and respiratory systems were not completely described in their early models. In the past few decades, thanks to the advancement in computational technology, scientific activity in this field has notably increased, and modeling complexity presented in the literature has grown to more accurately describe physiological mechanisms and their dynamics. However, the majority of these models, still remains primarily either cardiovascular or pulmonary and thus do not permit a comprehensive exploration of cardiopulmonary response to different acute conditions. Very few models have tried to address the strong dynamic interactions between the cardiovascular and respiratory systems albeit with some limitations. In the following sections, a brief review of some of these more recent models is provided.

Coleman *et al.* The model originally developed by Coleman, disciple of Guyton, in 1979 [18] and subsequently described by Coleman and Randall in 1983 under the name HUMAN [19] is probably considered today the most comprehensive and largest model of physiological functions. HUMAN is an extension of the 1972 Guyton's model [15] and represents a truly integrative simulator of the almost entire human physiology. It includes the circulatory system, the respiratory system, the kidneys and body fluid volume control, the autonomic nervous system, blood constituents, acid-base balance, thermo-regulation and some hormones. A schematic block diagram representing most of these physiological modules is shown in Figure 2.5. In HUMAN, some of the above mentioned limitations that characterized his predecessor [15] have been overcome. Particularly, ventilation, gas exchange, and O_2 and CO_2 dynamics based on conservation of mass principles have beeen included. However, some other linitations have not been addressed: *1)* The cardiovascular model is still nonpulsatile, hence only average pressures and flows can be computed; *2)* The respiratory mechanics is not modeled and air flow into and out of the lungs is described using a simple sinusoidal input function whose amplitude and frequency are controlled by a chemorceptor model.

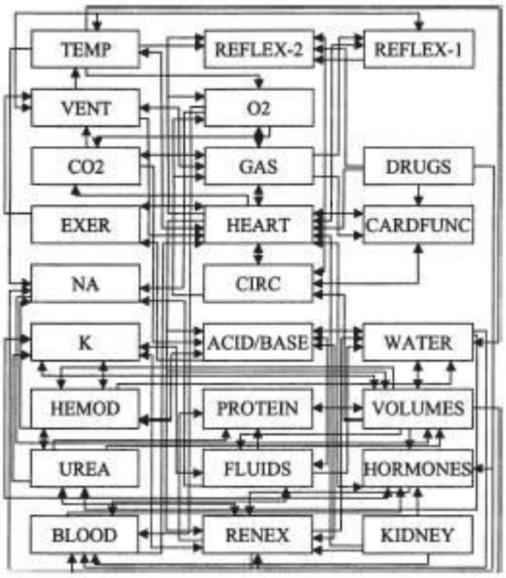

Figure 2.5 - Block diagram of HUMAN model showing the main physiological function modules [18]. Modules' names are as follows: HEART, calculation of blood flows and cardiac output; CARDFUNC, strength of left and right heart; CIRC, general circulation; REFLEX-1, sympathetic nerves ; REFLEX-2, parasympathetic nerves; TEMP, thermoregulation; EXER, control of exercise; DRUGS, pharmacology; O2,oxygen balance; CO2, carbon dioxide balance; VENT, control of ventilation; GAS, gas exchange; HORMONES, basic renal hormones; KIDNEY, kidney function and status; RENEX, kidney excretion; HEMOD, hemodialysis; FLUIDS, fluid infusion and loss; WATER, water balance; NA, sodium balance; ACID/BASE, acid-base balance; UREA, urea balance; K, potassium balance; PROTEIN, blood protein balance; VOLUMES, blood distribution; BLOOD, blood volume and red cell volume.

Nevertheless, HUMAN has been recognized and used worldwide as an important educational tool and, over the years, has been constantly modified to reflect current physiological knowledge and to keep up with technological advancement. In 2007, Abram *et al.* [20] described the benefits of using an integrative model of human physiology for medical education. The model was called Quantitative Circulatory Physiology (QCP) and represents an extension of HUMAN. QCP, which is freely available online [21], was written and compiled in C++ and this limited somehow the ability of the users to change or add equations. For this reason a further version of the model, called HumMod, in which all the model details are described in Extensible Markup Language (XML) files, was recently developed by Hester and his collegues [22] and distributed as open source [23].

Batzel, Kappel and Tmischl: Cardiopulmonary dynamics and regulation has been the object of several models proposed by researchers at the Institute for Mathematics and

Scientific Computing of the University of Graz. In 1998, a global model of the cardiovascular and respiratory system was proposed by Timischl [24] as the result of her PhD research. The model is divided into a respiratory component and a cardiovascular component, whose schematic diagrams are shown in Figure 2.6. The respiratory component consists of lung and lumped body tissue, connected by the circulating blood. The cardiovascular component consists of the series arrangement of systemic and pulmonary circulation and includes the left and right ventricles. Each circulation is lumped into 2 compartments, a single elastic artery and a single elastic vein, connected by a single resistance vessel, accounting for both arterioles and capillaries.

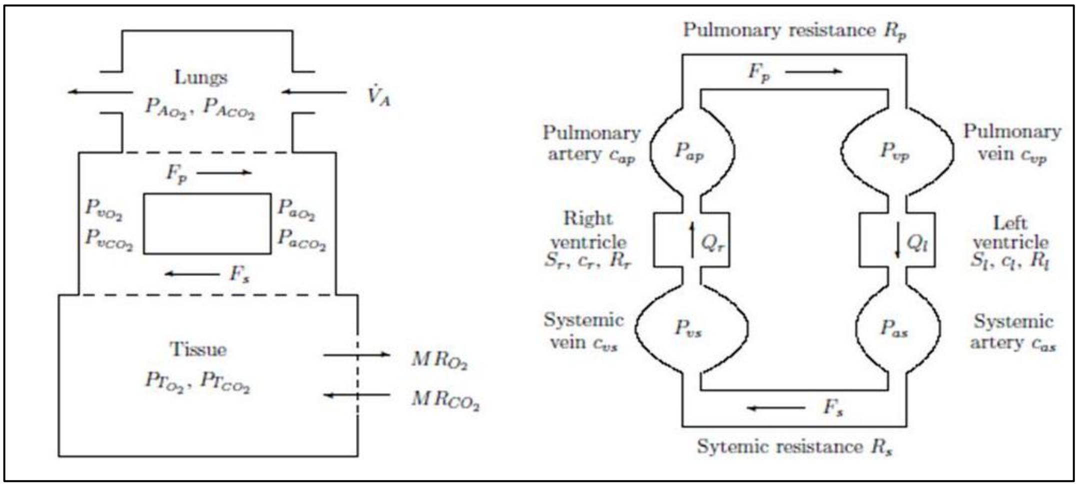

Figure 2.6 - (Left Panel) The respiratory part of the model reported in [24]. Fs and Fp, systemic and peripheral blood flow respectively; $\dot{V}_A$, alveolar ventilation; PiO2 and PiCO2, oxygen and carbon dioxide concentration in the i-compartment respectively, i = a,v,T, arteries, veins and tissues; MR_{O2} and MR_{CO2}, oxygen and carbon dioxide metabolic rate respectively. (Right panel) The cardiovascular part of the model as reported in [24]. Ql and Qr, left and right cardiac output respectively; Pas and Pvs, systemic arterial and venous pressure respectively; Pap and Pvp, pulmonary arterial and venous pressure respectively; cl and cr, left and right ventricle compliance respectively; Rl and Rr, left and right ventricle resitance respectively; Sl and Sr, left and right ventricle contractility respectively; cas and cav, systemic artery and vein compliance respectively; cps and cpv, pulmonary artery and vein compliance respectively; Rs and Rv, systemic and pulmonary resistance respectively.

Gas exchange equations are imposed in the lungs and tissues based on conservation of mass, in order to compute gas partial pressures in blood (PaO_2, $PaCO_2$, PvO_2 and $PvCO_2$). These equations represent the linkage between the cardiovascular and respiratory systems and assume O_2 and CO_2 tissue metabolic rates to be functions of workload intensity. The model is used to simulate cardiorespiratory response to exercise. The non-linear system of differential equations describing the model is solved at steady-state in resting conditions and for different increasing workload levels. Different steady-state solutions correspond to different sets of the parameters, which are dependent on the workload intensity. Transition from rest to exercise is regulated by an optimal two-inputs/two-outputs controller that drives the system from the steady-state characterizing the resting physiological condition to the steady-state characterizing the exercise condition. Inputs to the controller are systemic arterial pressure, P_{as}, and carbon dioxide arterial blood partial pressure, $PaCO_2$. Outputs of the controller are the changes in heart rate, H, and alveolar ventilation, $\dot{V}_A$. The transition between states is optimal in the sense that the controller minimizes a cost functional in order to stabilize P_{as} and $PaCO_2$ such that deviations from their final steady-state values are as small as possible. Hence, the optimal controller accounts for the cardiovascular control mechanism mediated by the *baroreceptors*, and for the respiratory control mechanism mediated by the *chemoreceptors*. The steady-state solution in terms of the main cardiorespiratory variables showed a good level of agreement with both physiological and measured data. However, despite the introduction of the original concept of optimal control, the model presents some strong limitations: *1)* The cardiovascular model is nonpulsatile, hence the model cannot provide continuous intra-beat values for any of its output variables; *2)* The lung is considered as a single compartment ventilated by a continuous unidirectional stream of gas; the events of the respiratory cycle are ignored and no description of the lung mechanics is included; *3)* The description of the cardiorespiratory control mechanisms is simplistic: the baroreceptors are assumed to affect cardiovascular function only via changes in heart rate; systemic peripheral resistance is assumed to be function of the exercise intensity and independent from baroreflex stimulation; chemoreceptors are assumed to be acting upon the respiratory system via the optimal controller based on $PaCO_2$ values only; the effects of chemoreflex stimulation on the cardiovascular system are completely neglected. The original model presented in [24] was subsequently adapted in several studies. In 2000, Timischl *et al*. [25] extended the optimal controller to account for PaO_2 effects on ventilation and applied the model to simulate transition from resting awake state to non-REM sleep. In 2005, Batzel *et al*. [26] further revised the model in order to include the effects of transport delays between tissues and lungs and vice versa. In 2004, Fink *et al*. [27] modified the cardiovascular component of the model to distinguish between upper and lower compartments and simulate cardiorespiratory response to orthostatic stress during head up tilt (HUT) experiments. Finally, in 2007, Kappel *et al*. [28] further extended the model to simulate orthostatic stress induced by lower body negative pressure (LBNP). However, despite few improvements in the description of the control mechanisms, the limitations due to the absence of cardiovascular pulsatility and tidal breathing lung mechanics still remained not addressed.

Ursino and Magosso: Several models of the cardiorespiratory system [5, 6, 13, 14] have been developed by Ursino and Magosso, from the Department of Electronic Computer Science and Systems of the University of Bologna. To the best of our knowledge, these models provide the most complete quantitative description of the main physiological mechanisms involved in short-term cardiopulmonary regulation. Particularly, the model in [5] aims at describing the cardiovascular system and the adjustments involved in the response to hypoxia. The model is an extension of a previous baroreflex model [29] developed by the same authors, and it includes pulsatile left and right hearts, systemic and pulmonary circulations, and some of the most important short term cardiovascular regulatory mechanisms. The circulatory portion of the model (shown in Figure 2.7) is quite detailed, including a total of 14 different compartments. An interesting feature of this model is that in order to account for the differences in the sensitivity of the reflex mechanisms among specific vascular districts, the peripheral and venous systemic circulations are divided into 5 different compartments arranged in parallel: brain, skeletal muscle, coronary, splanchnic and extrasplanchnic circulation. The cardiovascular control model (see Figure 2.7) is quite detailed as well, including arterial *baroreceptors*, *peripheral chemoreceptors* and *lung stretch receptors*, along with *sympathetic* and *vagal* neural pathways. The effects of the reflex mechanisms on the cardiovascular function are mediated by changes in systemic peripheral resistance, venous capacity, heart rate and left ventricular contractility. The effects of peripheral chemoreceptors on ventilation are also included in the model, even though no attempt to model the mechanics of the lung is made. In other terms, the tidal volume, which is the input to the lung stretch receptors, is computed in the model as function of the peripheral chemoreceptor activity without any description of the mechanical events that characterize the respiratory cycle. Moreover, the model includes the local vasodilatory effect of O_2 (*autoregulation*) on the brain, skeletal muscle and coronary circulation, and the cardiovascular effects of CNS hypoxia (*CNS ischemic response*). The model was further extended by the same authors in 2001 [6] to include the effects of CO_2 on the cardiovascular system and on minute ventilation. These additions allowed the model to simulate the response to a variety of cardiovascular and respiratory challenges (hypoxia, hypercapnia, isocapnic hypoxia, hemorrhage, etc.), and model predictions were shown to be in good agreement with experimental data. However, due to the absence of the mechanical description of the lungs, strong limitations can be found in these models: *1)* Cardiorespiratory interactions via gas exchange are not included; *2)* PaO_2 and $PaCO_2$ cannot be directly computed and hence remain external source inputs to the model, which therefore cannot be considered fully closed-loop cardiopulmonary models.

If the focus of the above models [5, 6] was on cardiovascular regulation with only minor details on respiratory control, the opposite is true for the models in [13, 14] developed by the same authors. These are extensions of Grodins' 1967 model [11], with additional ventilatory control mechanisms, and as such suffer of the same limitations.

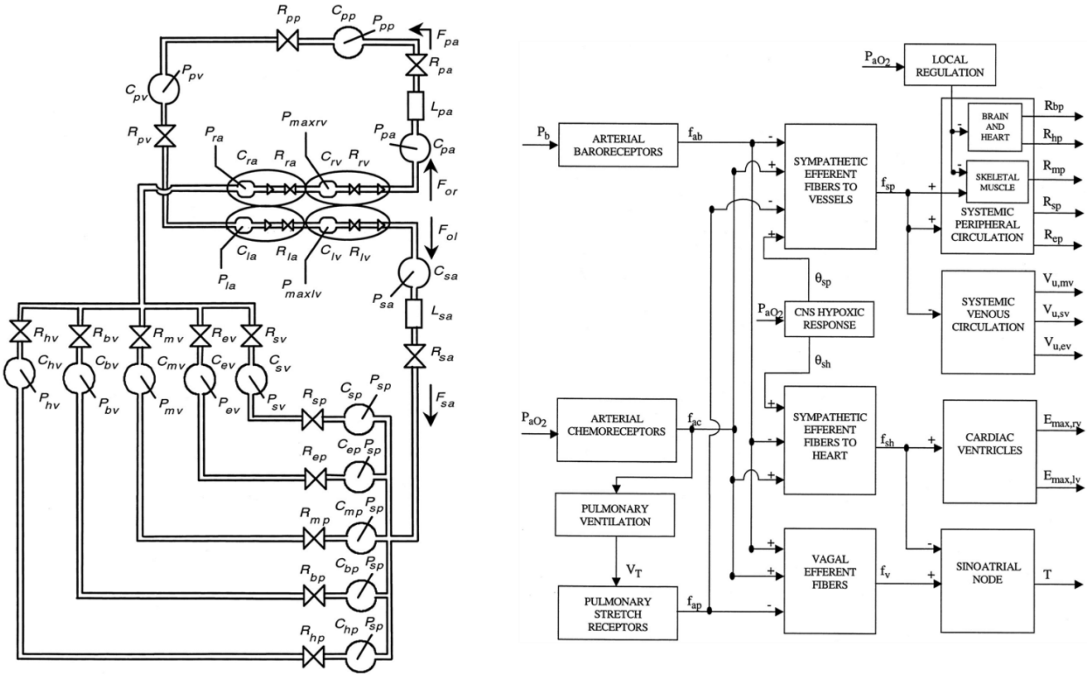

Figure 2.7 - (Left panel) Hydraulic analog of the cardiovascular system as reported in [5]. P, pressures; R, hydraulic resistances; C, compliances; L, inertances; F, flows; sa, systemic arteries; sp and sv, splanchnic peripheral and splanchnic venous circulation; ep and ev, extrasplanchnic peripheral and extrasplanchnic venous circulation; mp and mv, peripheral and venous circulation in the skeletal muscle vascular bed; bp and bv, peripheral and venous circulation in the brain vascular bed; hp and hv, peripheral and venous circulation in the heart (coronary vascular bed); la, left atrium; lv, left ventricle; pa, pulmonary arteries; pp and pv, pulmonary peripheral and pulmonary venous circulation; ra, right atrium; rv, right ventricle. (Right Panel) Block diagram describing relationships among afferent information, efferent neural activities, and effector responses as reported in [5]. Pb, baroreceptor pressure; PaO_2, arterial PO_2; Vt, tidal volume; fab, fac, and fap, afferent activities from arterial baroreceptors, peripheral chemoreceptors, and lung stretch receptors, respectively; θsh and θsp, offset terms for the cardiac and peripheral sympathetic neurons describing the effect of the central nervous system (CNS) hypoxic response; fsp and fsh, activity in efferent sympathetic fibers directed to the vessels and heart, respectively; fv, activity in the vagal efferent fibers; Rbp, Rhp, Rmp, Rsp, and Rep, peripheral resistance in the brain, heart, skeletal muscle, splanchnic, and remaining extrasplanchnic systemic vascular beds; Vu,mv, Vu,sv, and Vu,ev, unstressed volume in the skeletal muscle, splanchnic, and remaining extrasplanchnic venous circulation; Emax,rv and Emax,lv, end-systolic elastance of the right and left ventricle, respectively; T, heart period.

Lu *et al.*: Another very active group in the field of cardiopulmonary modeling is the Dynamical System Group at Rice University, led by John W. Clark. This group has developed several mathematical models [30, 31, 32] that, to our opinion, are the most exhaustive in terms of gas exchange and cardiorespiratory mechanical interactions.

Particularly, the model proposed by Lu and his coworkers in 2001 [30] is an integrated cardiopulmonary model aimed at simulating the Valsalva maneuver, an important clinical test to assess baroreflex function. The model combines and extends previous models of blood circulation [33], airway mechanics [34] and gas exchange [35] by the same group. The cardiovascular portion of the model is quite detailed and consists of a lumped parameter description of the four heart chambers, the systemic circulation and the pulmonary circulation. The electrical analog of the cardiovascular model is shown in Figure 2.8. The model of the heart is pulsatile and it includes the interacting ventricular free walls and septum, the atria and the pericardium. The systemic circulation includes proximal and distal aorta, proximal and distal arterioles, capillary and venous compartments, and vena cava. Coronary and cerebral circulations are also described as purely resistance vessels, departing from the aortic root and connecting to the vena cava. The pulmonary circulation is similarly described and it also includes a purely resistive compartment mimicking the presence of the pulmonary shunts. The cardiovascular control model (see Figure 2.8) includes arterial *baroreflex* and *sympathetic* and *vagal* neural pathways. These affect cardiovascular function via modifications of heart rate, myocardial contractility and vasomotor tone. The respiratory component of the model is quite detailed as well and partition the airways into upper, middle and small airways (see Figure 2.9). The upper airways are described as a rigid compartment with a nonlinear flow dependent resistance. The middle airways are assumed collapsible and are described by means of a nonlinear volume dependent resistance and a nonlinear P-V relationship. The small airways, representing the alveoli and the lung tissue, are described as a viscoelastic structure composed of a nonlinear compliance in series with the parallel arrangement of a linear spring and a linear resistance. The alveolar region and the collapsible airways are subjected to intrapleural pressure, which is the resultant of the pressure developed by respiratory muscles and the chest wall elastic recoil. The gas exchange portion of the model describes the changes in O_2, CO_2 and N_2 concentrations within three compartments: (1) the constant-volume dead space, represented by the rigid upper airways; (2) the variable-volume mid airways; (3) the variable-volume alveolar compartment. For each species considered, conservation of mass laws are imposed at both inspiration and expiration. In writing the conservation law for the alveolar compartment, the diffusion of O_2, CO_2 and N_2 across the alveolar-capillary membrane is considered.

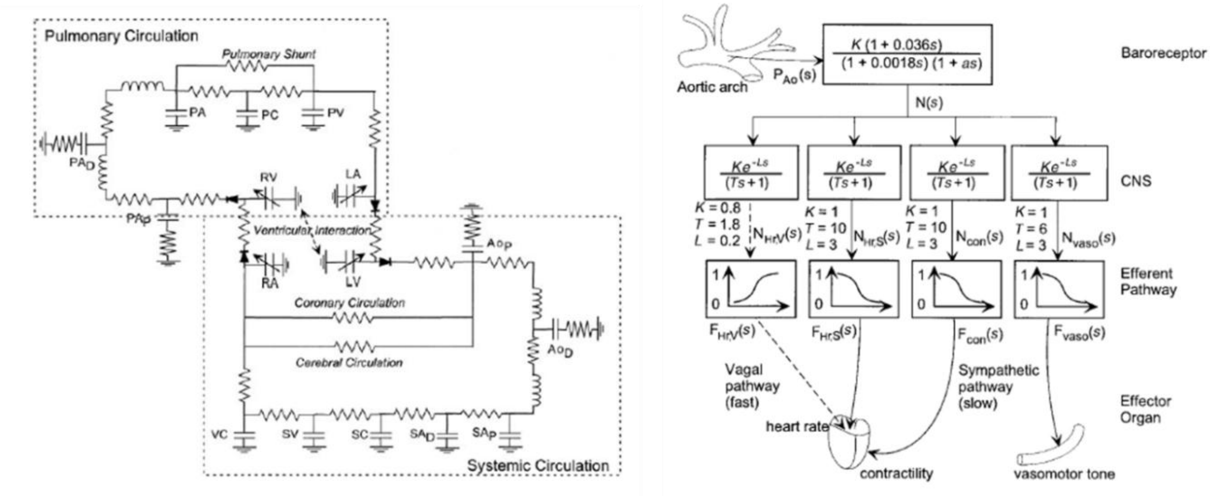

Figure 2.8 - (Left panel) Hydraulic analog of the cardiovascular system according to the model in [30]. (Right Panel) Block diagram describing the baroreflex mechanism as reported in [30]. See reference for explanation of symbols.

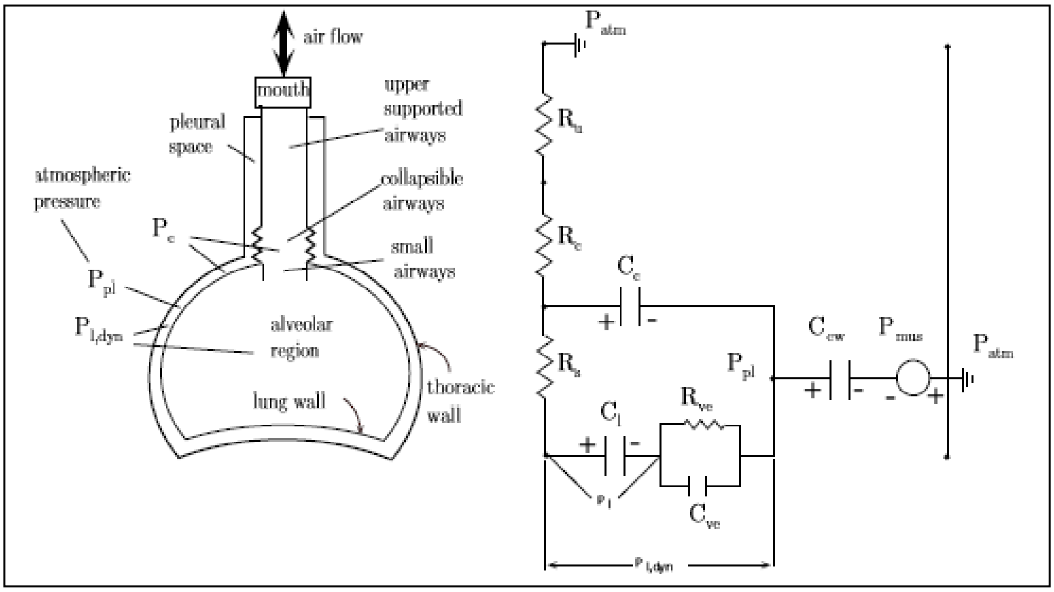

Figure 2.9 - (Left panel) Physical model of the respiratory system as reported in [30]. (Right Panel) Pneumatic analog of the model as reported in [30]. P_{atm}, atmospheric pressure; P_{pl}, intrapleural pressure; $P_{l,dyn}$, lung tissue dynamic elastic recoil pressure; P_c, collapsible airways pressure; P_{mus}, respiratory muscle driving pressure; R_u, upper airways resistance; R_c, collapsible airways resiatnce; R_s, small airways resistance; R_{ve}, lung tissue resistance; C_c, collapsible airways compliance; C_l, static lung tissue compliance; C_{ve}, dynamic lung tissue compliance; C_{cw}, chest wall compliance.

The model produces results in agreement with physiological data for a normal resting subject in supine position and during Forced Vital Capacity (FVC) and Valsalva maneuvers. In comparison to previously described models, Lu’s model includes both a pulsatile cardiac model and a tidal breathing lung mechanics with a good level of details in terms of cardiopulmonary interactions. However, the model still presents some limitations: *1)* The description of the cardiovascular control mechanisms is simplistic, with only cardiovascular *baroreflex* control included; *2)* The respiratory control mechanisms are ignored; *3)* Gas exchange is described only at the alveolar-capillary membrane, neglecting gas exchanges in tissues and other organs, and assuming that gaseous partial pressures in pulmonary arterial blood (at the inlet of the alveolar-capillary membrane) are constant; *4)* Due to the absence of respiratory control mechanisms, the respiratory component of the model needs to be driven by an external respiratory muscle pressure (or intrapleural pressure) source. In 2003, the model was significantly extended by the same group of authors in order to overcome some of these limitations [31]. The main new aspects of the model include the description of a lumped peripheral tissue gas exchanger, which is linked to the lung gas exchanger via a circulatory loop that incorporates transport delays. Moreover, *peripheral chemoreceptors* acting on both the cardiovascular and respiratory systems have also been included, hence the driving respiratory muscle pressure can be internally computed by the model. Finally, the model also describes the *lung stretch receptors* and their effects on cardiovascular control. Despite these substantial improvements, however, one fundamental point is still critical from our point of view and makes this model unsuitable for studying acute conditions such as those related to perturbations of CO_2 arterial blood contents. The model, in fact, does not include description of the *central chemoreceptors*, which under hypercapnic conditions play an important role in respiratory system regulation. This limit was then eventually overcome in a further extension of the model [52] by the same authors. Particularly, the *central chemoreflex* control of respiration was added along with a detailed mathematical description of cerebral circulation, cerebrospinal fluid dynamics, brain gas exchange and cerebral blood flow regulation. All these modifications, however, were more cerebrovascular oriented, such that the model became unnecessarily complex from a cardiopulmonary standpoint. Furthermore, in terms of cardiovascular control mechanisms, the model did not reach the same level of details as Ursino and Magosso's model [6].

Cheng *et al.*: The department of Biomedical Engineering at the University of Southern California, as part of a program dedicated to the advancement of biomedical system modeling and simulation techniques (Biomedical Simulations Resource), has developed an integrated cardiopulmonary model that takes the form of a software package, called PNEUMA, and that is freely available online in its Matlab-SIMULINK implementation [36]. The model was first introduced in 2002 [37] and it has been transformed over the years [38] until reaching its final current stage described by Cheng *et al*. in [39]. The model is divided into a pulsatile cardiovascular component, a tidal breathing respiratory component that includes lung gas exchange, and a central neural control component, all interacting each other. A schematic block diagram of the model highlighting the three different components is shown in Figure 2.10.

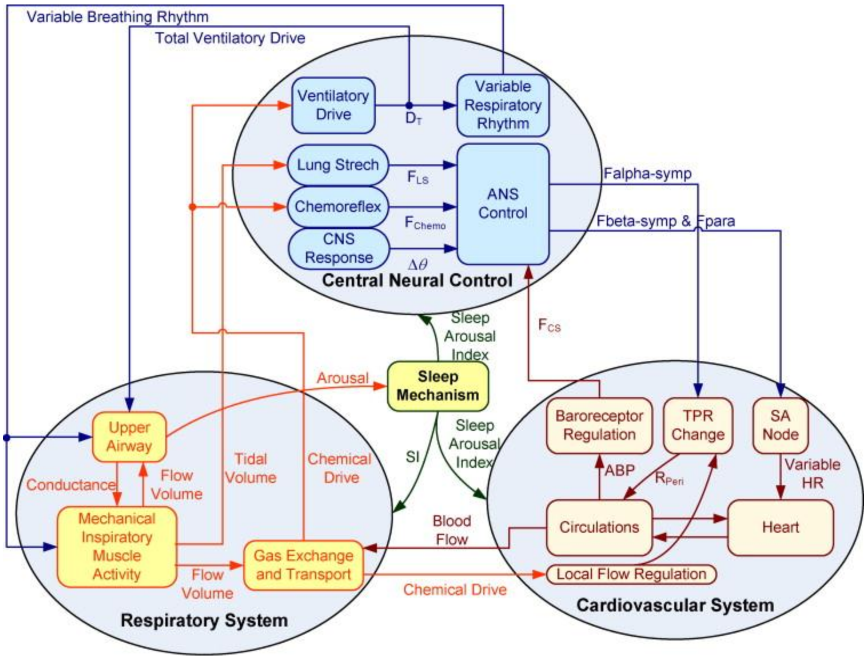

Figure 2.10 - Block diagram of the cardio-respiratory model by Cheng *et al*. [39] .

The model was applied to simulate transitions from sleep to awake state in normal and disease conditions, hence a sleep mechanism module was also included (see Figure 2.10). Both cardiovascular and central neural control components are largely based on Ursino and Magosso’s model [6], with modifications that account for the effects of intrathoracic pressure on the cardiovascular system and of sleep state on neural *sympathetic* and *vagal* activities. The gas exchange and transport component is based on a model previously developed by Khoo [40], which includes gas transport through the dead space, O_2 and CO_2 exchange in the alveoli, and O_2 and CO_2 transport in blood. The dead space is modeled using 5 serially rigid interconnected perfectly-mixed compartments where no gas exchange takes place. Mass balance equations for O_2 and CO_2 are imposed during both inspiration and expiration allowing for computation of breath by breath variations of O_2 and CO_2 partial pressures in these 5 compartments. The alveoli are modeled as a single compartment whose volume changes in synchrony with the breathing cycle. Mass balance equations for both species are applied at the alveoli taking into account the amount of gas that is exchanged at the alveoli-capillary membrane. Differential equations describing mass balance for O_2 and CO_2 are also applied at the tissue level in order to relate gas concentrations in the venous blood to arterial blood gas concentrations. The metabolic rate of the body tissues is assumed to be dependent on the wakefulness state. The respiratory mechanics model distinguishes between upper airways, lung tissues and chest wall dynamics. It is driven by a neuromuscular input that is a function of chemoreceptors activation, sleep/awake state and a basal drive. The ventilation control model computes the contributions from peripheral and central chemoreceptors to the neuromuscular drive, and it is based on previous work by Khoo [40]. An interesting feature of the model is that the sleep/awake state affects the upper airway conductance in a such a way that during sleep the upper airway can collapse if a critical transmural pressure value is reached. This allows the model to simulate obstructive sleep apnea (OSA). Furthermore, the model is shown to be able to simulate several other interesting pathophysiological conditions such as hypoxia, Cheyne-Stokes respiration and CPAP therapy effects on OSA patients. Hence, we can conclude that the model presents several positive characteristics: high versatility; pulsatile cardiovascular model and tidal breathing lung mechanics; detailed cardiovascular control mechanisms deriving from Ursino and Magosso’s model [6]. However, despite these advantages, some limitations can be found: *1)* Even though a physiological model of respiratory mechanics is included, airflow in and out of the lungs is computed using an empirical curvilinear equation [41] that relates lung volume to the neuromuscular input; this choice seems to be arguable. *2)* Gas exchange occurring outside of the lungs (tissue metabolism) is modeled as taking place in a single tissue compartment and correspondence with the 5 systemic compartments of the cardiovascular component [6] is violated; *3)* The inclusion of the interactions between sleep mechanisms and cardiorespiratory system appears to be unnecessary for our purposes.

A summary of the above reviewed models in terms of their main features and limitations is provided in Table 2-1 below. It is worth noticing that many other cardiouplmnary models exist in the literature and have been applied to mechanical ventilation studies [42, 43, 44]. However, none of these models include cardiorespiratory control mechanisms and hence their scope remain limited and they have not been considered in our review. Furthermore, other models may exist but inevitably remain unknown to the author.

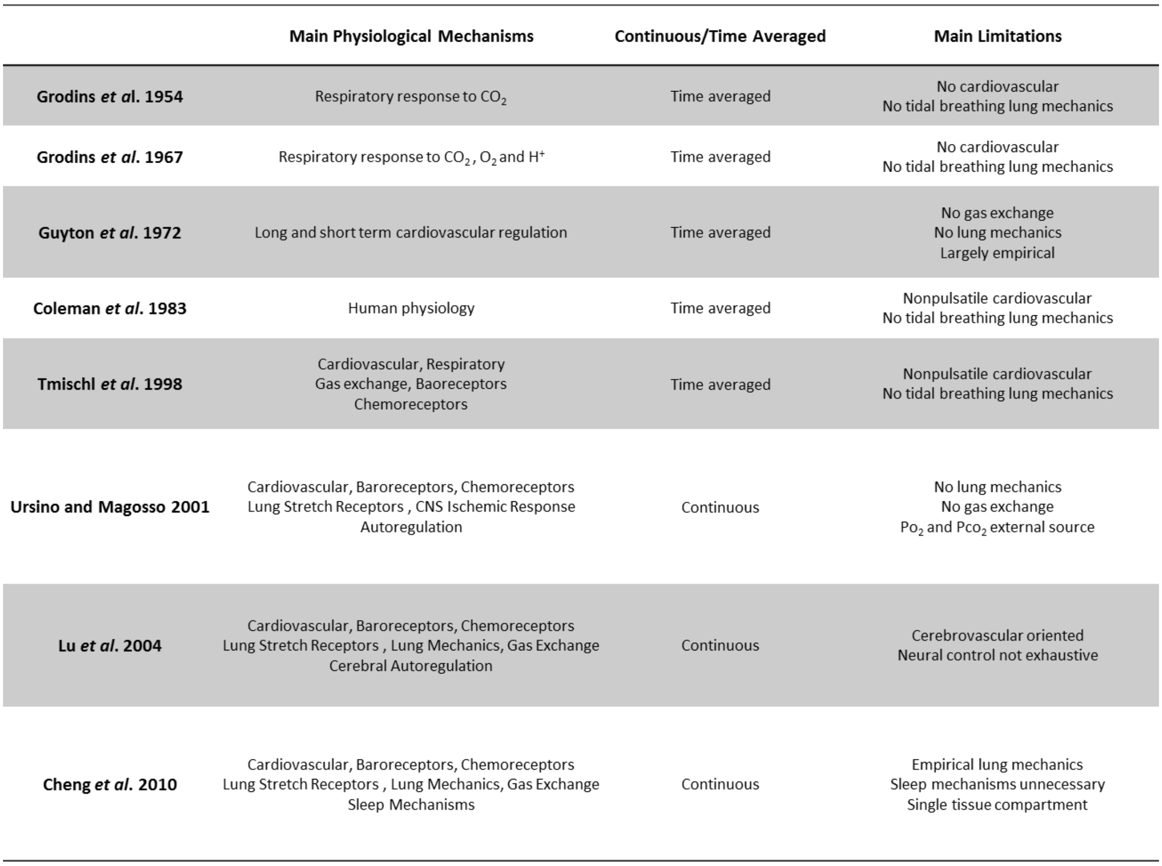

	Main Physiological Mechanisms	**Continuous/Time Averaged**	**Main Limitations**
Grodins *et al*. 1954	Respiratory response to CO_2	Time averaged	No cardiovascular No tidal breathing lung mechanics
Grodins *et al*. 1967	Respiratory response to CO_2 , O_2 and H^+	Time averaged	No cardiovascular No tidal breathing lung mechanics
Guyton *et al*. 1972	Long and short term cardiovascular regulation	Time averaged	No gas exchange No lung mechanics Largely empirical
Coleman *et al*. 1983	Human physiology	Time averaged	Nonpulsatile cardiovascular No tidal breathing lung mechanics
Tmischl *et al*. 1998	Cardiovascular, Respiratory Gas exchange, Baoreceptors Chemoreceptors	Time averaged	Nonpulsatile cardiovascular No tidal breathing lung mechanics
Ursino and Magosso 2001	Cardiovascular, Baroreceptors, Chemoreceptors Lung Stretch Receptors , CNS Ischemic Response Autoregulation	Continuous	No lung mechanics No gas exchange Po_2 and Pco_2 external source
Lu *et al*. 2004	Cardiovascular, Baroreceptors, Chemoreceptors Lung Stretch Receptors , Lung Mechanics, Gas Exchange Cerebral Autoregulation	Continuous	Cerebrovascular oriented Neural control not exhaustive
Cheng *et al*. 2010	Cardiovascular, Baroreceptors, Chemoreceptors Lung Stretch Receptors , Lung Mechanics, Gas Exchange Sleep Mechanisms	Continuous	Empirical lung mechanics Sleep mechanisms unnecessary Single tissue compartment

Table 2-1- Summary of existing cardiopulmonary models

As outcome of this review, the need for an integrative model of the cardiopulmonary system that can overcome the limitations of these existing models becomes evident. This new model should possess the following chracateristics: pulsatile cardiovascular and tidal breathing lung mechanics components; detailed control mechanisms; detailed cardiorespiratory interactions. This is the motivation behind the development of the model that is presented in the following sections.

2.3 Model Development

The present cardiopulmonary model (*CP Model*) includes cardiovascular circulation, respiratory mechanics and gas exchange, along with their main short-term control mechanisms. The model incorporates essential features from existing models and represents a substantial extension of the models by Ursino and Magosso [5, 6], which where chosen as our starting point given their exaustive description of the neural control mechanisms (see Table 2-1). As described in the previous section, their models required arterial Po_2 and Pco_2 as external input source, and completely ignored lung mechanics and gas exchange. Here, separate sub-models of respiratory mechanics, gas exchange in lungs and tissues, gas transport in blood, and respiratory control mechanisms have been added to attain a comprehensive cardiopulmonary model that is able to run in closed-loop mode requiring inspiratory air gas content (FiO_2 and $FiCO_2$) and total blood volume as the only inputs.

A schematic block diagram of the model is shown in Figure 2.11, where the interconnections among the different subsystems are highlighted. The *Cardiovascular System* and the *Respiratory System* interact via the *Gas Exchange and Transport* module. This module describes the gas exchange processes that take place in the lungs and in the systemic tissues, along with the gas transport throughout the circulatory system. Both the cardiovascular and the respiratory systems are subject to their own specific control mechanisms, identified in the block diagram as the *Cardiovascular Control System* and the *Respiratory Control System* modules, respectively. Particularly, the cardiovascular function is regulated by the *Autonomic Nervous System* (ANS) that integrates the afferent information provided by the *Baroreceptors, Peripheral Chemoreceptors* and *Lung Stretch Receptors*. Local *Autoregulation* mechanisms are also included along with a central nervous system (CNS) mediated response to acute ischemic conditions (*CNS Ischemic Response*). The respiratory function is assumed to be governed by the superposition of control mechanisms mediated by both the *Peripheral Chemoreceptors* and the *Central Chemoreceptors*, which modulates the activity of the *Respiratory Muscles* acting on the *Lung Mechanics* module. This, in turn, can also be driven by the action of an external *Mechanical Ventilator*. In the following sections, a qualitative description of these different components is provided. Following a control-system theory approach, the cardiovascular and the respiratory system are first described by the uncontrolled system (plant), in the absence of regulatory actions. Description of their feedback control mechanisms is subsequently provided. A complete set of equations describing the model is presented in the *Appendix* section.

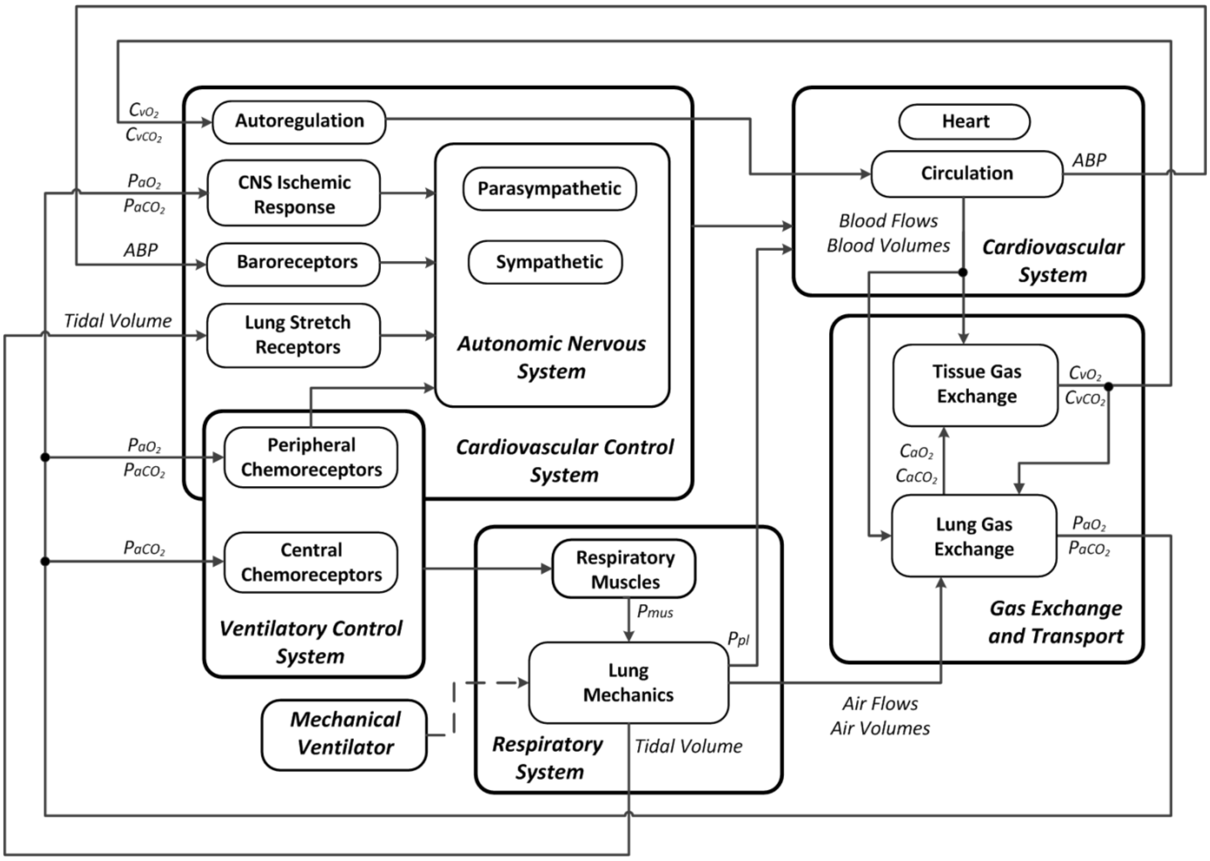

Figure 2.11 - Block diagram of the CP model. C_{vO2} and C_{vCO2}, O_2 and CO_2 gas concentrations in the venous blood, respectively; P_{aO2} and P_{aCO2}, O_2 and CO_2 arterial blood partial pressures, respectively; ABP, arterial blood pressure; P_{pl}, pleural pressure; P_{mus}, respiratory muscle pressure.

2.3.1 The Uncontrolled Cardiovascular System Model

The cardiovascular component of our *CP Model* is largely based on the work of Ursino and Magosso [5, 6], however, some modifications have been introduced to allow a more detailed description of the heart-lung interactions and integration with the lung mechanics and the gas exchange modules. As shown in the schematic diagram in Figure 2.12, the model includes a pulsating heart, a pulmonary circulation and a systemic circulation. The heart model includes both left and right hearts along with their corresponding chambers (atrium and ventricles) and valves (mitral, aortic, tricuspid and pulmonary valve). The systemic circulation is subdivided into five distinct districts arranged in parallel and describing circulation into the coronary, brain, skeletal muscle, splanchnic (comprising the liver, the spleen, and the gastro-intestinal organs) and the remaining extrasplanchnic (kidney, skin, bones, etc.) vascular beds. This distinction is necessary since, as it will be described later, autonomic and local cardiovascular regulatory mechanisms exert different actions on each compartment. The hemodynamic in both systemic and pulmonary circulations distinguish between large arteries, peripheral vessels (which combine arterioles and capillaries) and veins. The modifications with respect to the original model formulation presented in [5, 6] are the following: *1)* A pulmonary shunt compartment has been added in parallel to the pulmonary peripheral circulation, between the pulmonary artery and the pulmonary veins (anatomical shunting) to account for the normal physiological amount of blood that does not pass through the pulmonary capillaries and does not participate in gas exchange. We are aware that this is a high simplification as the anatomical shunts are mostly due to the bronchial circulation and the thebesian veins, which are both not located between the pulmonary arteries and the pulmonary veins. However, our representation is not intended to have anatomical correspondence and is only used to include a circulatory branch that bypasses pulmonary gas exchange. *2)* An additional compartment, representing the thoracic veins, which return blood to the right atrium, has been included in the systemic circulation. *3)* The effects of respiration on venous return and cardiac output (respiratory pump) have been modeled by considering intrapleural pressure (P_{pl}) as the reference extravascular pressure for those compartments that are located inside the thoracic cavity (heart, lungs and thoracic veins); all remaining compartments are assumed to be subject to extravascular atmospheric pressure (P_{atm}). *4)* As a consequence of respiration, transmural pressure in the systemic veins can become negative at their point of entrance in the thoracic cavity; to account for this phenomenon, venous valves have been included by inserting an ideal diode both upstream and downstream of each systemic venous compartment, thus preventing retrograde blood flow [45]. With these modifications, the model includes a total of 20 compartments that are listed in details in Figure 2.12.

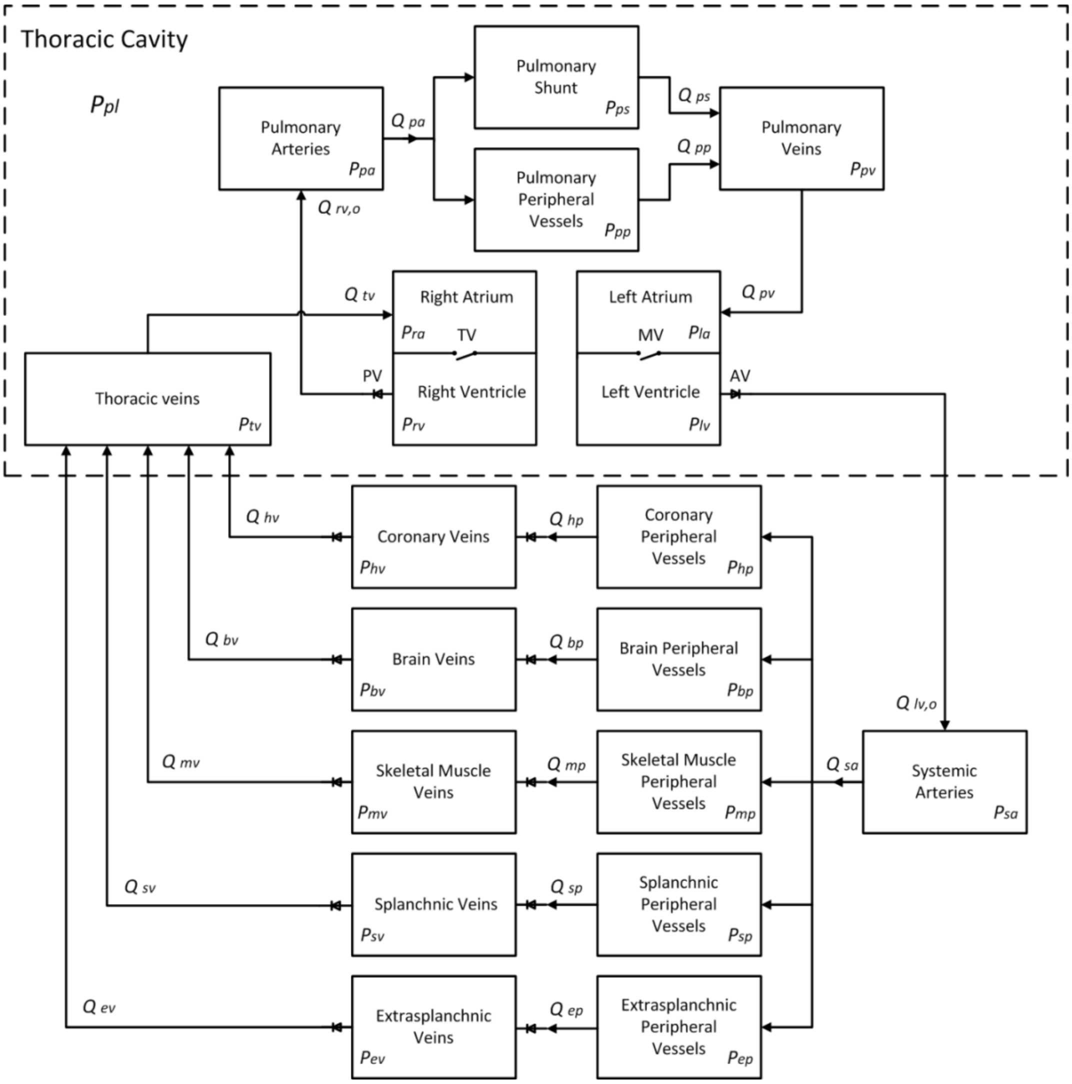

Figure 2.12 - Schematic diagram of the cardiovascular system. P, pressure; Q , blood flow; MV, mitral valve; AV, aortic valve; TV, tricuspid valve; PV, pulmonary valve. Subscripts: la, left atrium; lv, left ventricle; lv, o, left ventricle output; sa, systemic arteries; sp, splanchnic peripheral compartment; sv, splanchnic veins; ep, extrasplanchnic peripheral compartment; ev, extrasplanchnic veins; mp, skeletal muscle peripheral compartment; mv, skeletal muscle veins; bp, brain peripheral compartment; bv, brain veins; hp, coronary peripheral compartment; hv, coronary veins; tv, thoracic veins; ra, right atrium; rv, right ventricle; rv, o, right ventricle output; pa, pulmonary artery; pp, pulmonary peripheral circulation; sh, pulmonary shunt; pv, pulmonary veins; pl, pleural space.

1) The Circulation Model: Each vascular compartment shown in Figure 2.12 is described trough traditional windkessel models, i.e. as the arrangement of a hydraulic resistance (R_j), which accounts for pressure energy losses, and a hydraulic compliance (C_j), which determines the blood volume stored in each compartment at a given pressure. For those compartments where inertial forces in blood are relevant, i.e. large pulmonary and systemic arteries, inertance (L_j) is also included as a third parameter of the corresponding windkessel-type model. The general 3-element windkessel single-compartment model structure is illustrated in Figure 2.13.

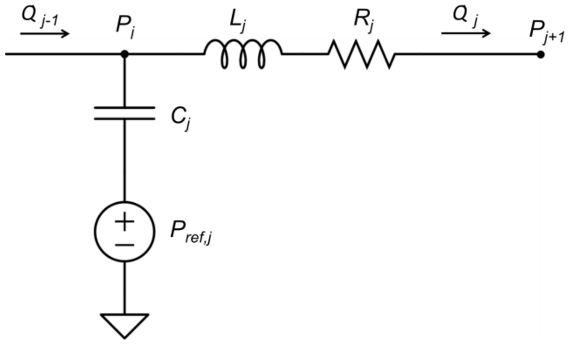

Figure 2.13 - Single-compartment windkessel-type model. P, intravascular pressure; Q, outgoing blood flow rate; R, resistance; C, compliance; L, inertance; $j, j+1, j-1$, compartment index; P_{ref}, extravascular pressure reference (atmospheric pressure or intrapleural pressure, depending on the value of j).

Equations relating pressures (P) and flows (Q) in the vascular system are obtained by enforcing conservation of mass principles for each vascular compartment of Figure 2.12. Hence, in the general case of a 3-element vascular compartment such as the one of Figure 2.13, the following two ordinary differential equations (ODEs) hold:

$$\frac{dV_j}{dt} = Q_{j-1} - Q_j \tag{2-1}$$

$$L_j \cdot \frac{dQ_j}{dt} = P_j - P_{j+1} - R_j \cdot Q_j \tag{2-2}$$

where V_j, Q_j and P_j represents volume, outgoing flow and pressure of the j-th compartment, respectively (see Figure 2.13 legend for further definitions of subscripts). The two equations above need to be combined with the corresponding pressure-volume (PV) relationship of the j-th compartment, in order to solve for the pressures P_j. The typical PV relationship of a blood vessel (artery or vein) is shown in Figure 2.14 below.

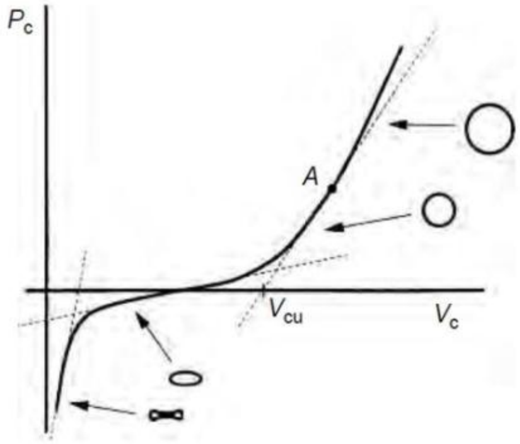

Figure 2.14 - Typical PV relationship of a blood vessel . Pc, transmural pressure; V_c, volume; V_{cu}, unstressed volume. Reproduced with permission from [46]

It is quite linear near the unstressed volume (volume at zero transmural pressure), concaves upward, gradually increases in slope at higher volumes, and concaves downward as the volume decreases and the vessel collapses. Arteries and capillaries are typically subject to high transmural pressure values and the operating point along the PV curve is such that a linear approximation is valid [47, 48]. Hence, in the model, the PV relationships of the systemic arterial and peripheral compartments have been assumed linear over the entire pressure range examined. This is also the common choice in the majority of the lumped-parameter models of the circulatory system that have been presented in the literature [49, 50]. Analogously, the entire pulmonary circulation (including arteries, peripheral and venous compartments) is also assumed to be characterized by linear PV relationships. The assumption of linear PV relationship allows for constant and pressure independent compliances C_j. Hence the volume of each of these compartments is computed as the sum of the unstressed volume component ($V_{u,j}$) and the excess volume component ($V_{e,j}$), which is associated with the increase in the transmural pressure:

$$V_j = \underbrace{C_j \cdot P_{tm,j}}_{V_{e,j}} + V_{u,j} \tag{2-3}$$

where $P_{tm,j}$ is the transmural pressure of the j-th compartment. On the contrary, the hypothesis of linear PV relationship does not always hold for the venous circulation. Particularly, while in most of the venous circulation the pressure inside the vessels is greater than the external pressure and the operating point on the PV curve is such that the linear approximation still holds, in the vena cava, and in the thoracic veins in general, the transmural pressure is typically small and can become negative under the influence of a positive intrathoracic pressure. In these cases, the nonlinear nature of the PV relationship becomes important [46] (see Figure 2.14). For this reason, the same linear PV relationship above (Eq. 2-3) has been used for the systemic venous compartments (splanchnic, extrasplanchnic, skeletal muscle, brain and coronaries), whereas the thoracic veins have been modelled via a non-linear collapsible PV relationship. This has been derived by combining features of slightly different PV curves proposed in the literature for the vena cava compartment [39, 30, 51]:

$$P_{tm,tv} = \begin{cases} D_1 + K_1 \cdot \left(V_{tv} - V_{u,tv}\right) - \Psi & V_{tv} \geq V_{u,tv} \\ D_2 + K_2 \cdot e^{\frac{V_{tv}}{V_{tv,min}}} - \Psi & V_{tv} < V_{u,tv} \end{cases} \tag{2-4}$$

$$\text{with } \Psi = K_{xp}/(e^{\frac{V_{tv}}{K_{xv}}} - 1)$$

where $P_{tm,tv}$ and V_{tv} are the transmural pressure and the volume of the thoracic veins compartment, respectively. Note that Ψ is a curvilinear function that is negligible at volumes above K_{xv} and dominates the PV relationship in the region of collapse, when the volume of the vessel is very small [51]. Hence, according to Eq. 2-4, the PV curve of the thoracic veins compartment is characterized by 3 different regions: in the first region, for volumes above the unstressed value $V_{u,tv}$, the effect of Ψ is negligible and the curve is essentially linear with K_1

and D_1 representing its slope and offset, respectively; in the second region, for volumes below $V_{u,tv}$ but above K_{xv}, the effect of Ψ is still negligible and the curve is exponentially concave downward with $V_{tv,min}$ representing the minimum volume of the compartment and K_2 and D_2 being curve-shaping parameters; in the third region, for volumes below K_{xv}, the curve is dominated by Ψ and is tangent to the pressure axis (that is, it goes toward $-\infty$ as V_{tv} tends to zero). The PV curve corresponding to Eq. 2-4, generated using the parameters in Table 3 (see *Parameter Assignment* section), is shown in Figure 2.15 from which the resemblance with the typical PV curve of Figure 2.14 can be observed.

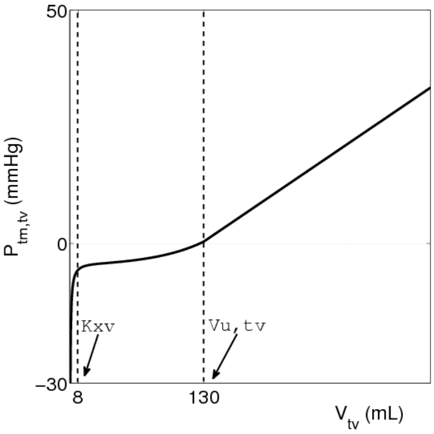

Figure 2.15 - PV relationship of the thoracic veins compartment according to Eq. 4. $P_{tm,tv}$, transmural pressure; V_{tv}, volume; $V_{u,tv}$, unstressed volume; K_{xv}, volume below which Ψ becomes dominant.

To account for the fact that when the vessel collapses the blood flow toward that compartment is extremely reduced, the resistance of the thoracic veins compartment has been varies as a function of the volume according to [30]:

$$R_{tv} = K_R \cdot \left(\frac{V_{tv,max}}{V_{tv}}\right)^2 + R_{tv,0} \tag{2-5}$$

where K_R is a scaling factor, $V_{tv,max}$ is the maximum volume and $R_{tv,0}$ is an offset parameter. All the remaining resistances of the vascular system have been assumed constant, with the exception of those of the systemic peripheral compartments that are assumed to vary under the action of feedback regulatory mechanisms (see *Cardiovascular Control Model* section).

The effects of gravity on the cardiovascular system have been neglected. Hence, the model is suitable for simulating subjects in the supine position only, when no hydrostatic pressure gradient across different compartments is present. Furthermore, since the five systemic peripheral vessels are assumed in parallel and no gravitational effects are considered, the pressures P_{jp} inside each compartment are assumed to be equal. Analogous reasoning applies to the pulmonary shunt and the pulmonary peripheral compartments (see Figure 2.12). Finally, note that in solving the model equations for the pressure variables, atmospheric pressure has been assumed to be zero and hence the resulting values of P_j represent above-atmospheric and not absolute pressure values.

2) The Heart Model: The model of the pulsating heart remains unchanged compared to that one used in [5, 6], where an accurate description can be found. The only modification that has been introduced is the inclusion of the intrapleural pressure as the external reference pressure acting outside the heart chambers. Briefly, the models of the left and right heart are essentially equivalent with different parameter values. The electrical analog of the heart shown in Figure 2.16 pertains to the left heart. Each atrium is described as a passive chamber, characterized by a linear *PV* relationship with constant values of compliance and unstressed volume. Hence, the contractility of the atrium is neglected. Blood passes from the atria to the ventricles through the atrioventricular valves (mitral valve, MV, and tricuspid valve, TV), modelled as ideal unidirectional diodes and connected in series with the corresponding constant atrium resistances. The equations relating pressures and flows in the atria are obtained by combining mass balance equations, similar to Eq. 2.3, with the corresponding linear *PV* relationship. The activity of the ventricles is modelled by means of a variable-elastance model, which accounts for the isometric pressure-volume function, and a time-varying resistance, which reflects the viscous forces in the ventricle. The elastance varies during the cardiac cycle as a consequence of the contractile activity of the ventricle. At diastole, the ventricle fills through an exponential pressure-volume function, while at end systole the pressure-volume function is linear and its slope (called the end-systolic elastance) is denoted by E_{max}. Shifting from the end-diastolic to the end-systolic relationship is governed by a pulsating activation function $\phi(t)$ with period *HP* equals to the heart period. The duration of systole is assumed to decrease linearly with the heart period, which in turn is modulated by the control action of the ANS (see *Cardiovascular Control Model* section). Finally, blood flow leaving the ventricles depends on the opening of the aortic or pulmonary valve and on the difference between the isometric ventricle pressure and the downstream pressure (systemic arterial pressure or pulmonary artery pressure, depending on whether right or left ventricle is considered). Detailed equations describing the heart model can be found in [5] and are also reported in the *Appendix* section.

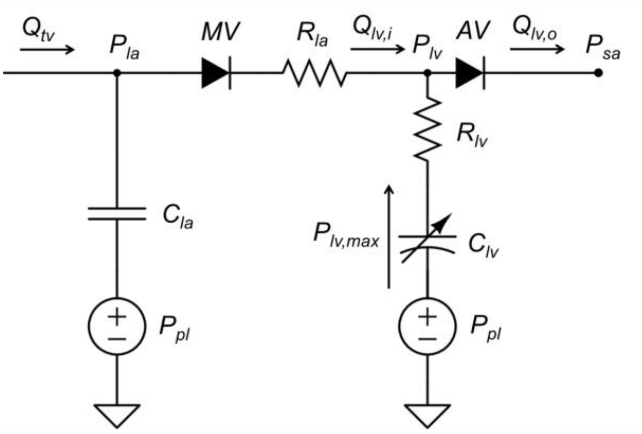

Figure 2.16 - Electrical analog of the left heart. MV and AV represent the mitral and the aortic valve, respectively. P_{la}, P_{lv} and P_{sa} are instantaneous pressure in the left atrium, left ventricle and systemic arteries, respectively; $P_{lv,max}$ is the left ventricle pressure in isometric conditions; Q_{pv} is the blood flow at the exit of the pulmonary veins, equals to the blood flow entering the left atrium; $Q_{lv,i}$ and $Q_{lv,o}$ are blood flow entering the left ventricle and blood flow leaving the left ventricle, respectively; C_{la} and C_{lv} are compliance of the left atrium and left ventricle, respectively; R_{la} and R_{lv} are resistance of the left atrium and left ventricle, respectively (note the transversal arrows in C_{lv} to indicate the time-varying nature of this parameter); P_{pl} is the intrapleural pressure, acting as reference external pressure on the heart.

2.3.2 The Respiratory System Model

As shown in Figure 2.11, the model of the respiratory system includes description of the lung mechanics and of the respiratory muscles. The lung mechanics portion is based on previous work by Rideout and Fukui [52, 53] and has been modified to include chest wall and intrapleural pressure dynamics. shows the equivalent pneumatic circuit representing the lung mechanics model. It consists of the series arrangements of four segments, namely the larynx, the trachea, the bronchea and the alveoli. Each segment has been represented by a linear resistance and a linear compliance, which describe the dissipative and the elastic forces that act on the respiratory system during normal breathing. Inertial forces have not been considered because they have negligible effects within the physiological breathing frequencies [54]. The model can be driven by either an external pressure P_{vent} representing the pressure provided by the ventilator, as in the case of mechanically ventilated patients, or by an internal generator P_{mus} representing the pressure generated by the respiratory muscles, as in the case of spontaneously breathing patients. Note that P_{mus} is a fictitious variable that does not correspond to a physical quantity. In a spontaneously breathing subject, in fact, P_{mus} represents the equivalent pressure that has to be applied outside the thorax if the respiratory muscles were paralyzed in order to maintain normal respiratory flow, volume and pressure waveforms [55]. The chest wall has been modeled as a passive compliant element whose pressure-volume characteristic has been assumed linear and hence described by a constant compliance term, C_{cw}. This is a good approximation in the volume range of quite breathing (2.5 to 3 L), according to the typical assumption of sigmoidal PV relationship [34]. Chest wall viscous resistance to flow has been neglected, as this has typically a small contribution to the overall respiratory system resistance in both health and disease states [56, 57]. The respiratory muscle generator is connected to the chest wall compliance, which acts on the pleural space whose internal pressure P_{pl} is transferred to those segments lying within the chest cavity, i.e. trachea, bronchea and alveoli.

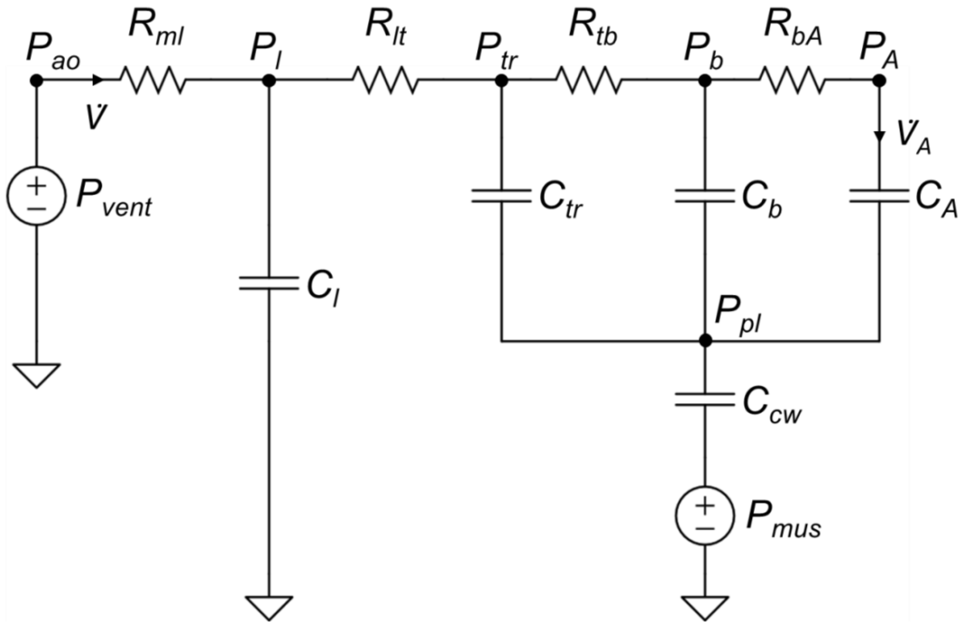

Figure 2.17 - Lung mechanics model. P, pressure; R, resistance; C, compliance; $\dot{V}$, total air flow; $\dot{V}_A$, alveolar air flow. Subscripts: ao, airway opening; l, larynx; tr, trachea; b, bronchea; A, alveoli; pl, pleural space; cw, chest wall

In the present study, since the model was used to simulate spontaneous breathing conditions, the action of the external pressure generator P_{vent} is nullified and the airway pressure P_{ao} is always assumed to be equal to atmospheric pressure. However, the external pressure generator could be restored in order to simulate artificial ventilation conditions, or even superimposed to the action of the internal pressure generator to account for simultaneously natural and artificial breathing.

The respiratory muscle pressure (internal pressure generator), P_{mus}, has been modelled based on the average profile proposed by Mecklemberg [58], obtained from experimental flow and pressure data collected from a group of 12 adult healthy subjects breathing spontaneously from atmosphere. The experimental muscle pressure curve has been reproduced as a piece-wise continuous function consisting of an inspiratory parabolic profile and an exponential expiratory profile. Particularly, under the assumption of complete passive exhalation with no recruitment of the expiratory muscles (reasonable for minute ventilation values up to 40 L/min [59]), P_{mus} is assumed to decrease from 0 to its minimum end-inspiratory value during the inhalation phase and to gradually return to 0 during exhalation, according to:

$$P_{mus}(t) = \begin{cases} \dfrac{-P_{mus,\min}}{T_I \cdot T_E} \cdot t^2 + \dfrac{P_{mus,\min} \cdot T}{T_I \cdot T_E} \cdot t & t \in [0, T_I] \\ \dfrac{P_{mus,\min}}{1 - e^{-\frac{T_E}{\tau}}} \cdot \left(e^{-\frac{(t-T_I)}{\tau}} - e^{-\frac{T_E}{\tau}}\right) & t \in [T_I, T] \end{cases} \tag{2-6}$$

where T_I and T_E represent the duration of the inspiratory and expiratory phase, respectively, T is the inspiratory period, $P_{mus,\min}$ is the minimum end-inspiratory pressure value representing the amplitude of the inspiratory efforts and τ is the time constant of the exponential expiratory profile. The inspiratory and the expiratory times are defined with respect to the P_{mus} waveform, rather than with respect to flow rate, and they are considered fixed fractions of the respiratory period T:

$$\begin{aligned} T_I + T_E &= T = 60/RR \\ T_I &= T_E \cdot IE_{ratio} \end{aligned} \tag{2-7}$$

where RR is the respiratory rate (expressed in breaths/min) and IE_{ratio} is the inspiratory-expiratory time ratio. The muscle pressure waveform is repeated with the respiratory period. The expiratory P_{mus} time constant, τ, is assumed to be directly proportional to the espiratory time T_E and the inspiration-expiration time ratio, IE_{ratio}, is assumed to be fixed during the simulations. Hence, the P_{mus} profile is fully parameterized via the two quantities RR and $P_{mus,\min}$, whose values are assumed to vary from breath to breath and are computed at the beginning of each respiratory cycle as output of the chemoreceptors module (see *Respiratory Control Model* section).

Outputs of the lung mechanics model are the instantaneous pressures and volumes of each compartment, along with the instantaneous air flow into and out of them. The equations for pressures and flows are obtained by solving the electrical circuit shown in Figure 2.17 based on conservation of mass principles, similarly to what we have described above for the circulatory system. Volumes are then computed taking into account the unstressed components (see Eq. 2-3). To allow interaction between the lung mechanics and the gas exchange model (see Figure 2.11), the dead space is also considered and its instantaneous volume is computed as the sum of the volumes of the three compartments that do not participate in gas exchange, i.e. larynx, trachea and bronchea. Hence, differently from the majority of the models available in literature [39, 60], dead space is not assumed to be rigid but its volume is constantly changing throughout the respiratory cycle. As a consequence of the elastic dead space assumption, part of the total air flow entering the lung, denoted as $\dot{V}$, is spent to inflate the dead space and does not contribute to the effective flow that reaches the alveoli, denoted as $\dot{V}_A$. Furthermore, since the difference between the volumes of O_2 and CO_2 that are exchanged between alveoli and pulmonary capillary over a respiratory cycle is typically very small, the net air flow that is transferred from the alveoli to the pulmonary blood is neglected and the inhaled tidal volume over a respiratory cycle is assumed exactly equal to the corresponding exhaled tidal volume.

2.3.3 The Gas Exchange and Transport Model

The model of gas exchange and transport describes the oxygen (O_2) and carbon dioxide (CO_2) exchange between pulmonary capillaries and lungs and between systemic capillaries and tissues, along with O_2 and CO_2 transport by blood throughout the circulatory system. As shown in the block diagram in Figure 2.18, the model is made of three components, namely the *Lung Gas Exchange*, the *Tissue Gas Exchange* and the *Venous Pool Gas Transport*. Venous blood is assumed to have certain gas concentrations, $C_{v,gas}$, where gas indicates either O_2 or CO_2. Once venous blood enters the pulmonary capillaries, it gets in contact with the alveolar space, rich in O_2 and poor in CO_2. O_2 enters the blood from the alveolar compartment along its pressure gradient, and similarly, CO_2 diffuses into the alveolar compartment from blood. The resulting O_2-rich blood, characterized by certain gas concentrations $C_{a,gas}$, is then transported to the peripheral tissues, where O_2 is delivered and utilized by the tissue compartments and the CO_2 generated by cell metabolism is removed. Deoxygenated blood at the outlet of the tissue gas exchanger passes through the venous circulation and then returns to the lung thus completing the loop for gas exchange. Circulatory transport delays, τ_{LT} and τ_{VL}, are included in the model to account for the time it takes to blood to transport gases from the lungs to the systemic tissues and from the thoracic veins back to the pulmonary capillaries. Gas transport throughout the venous pool is instead explicitly modeled since blood flow in the venous section is typically slow and hence this section accounts for the most of the circulatory blood transport delay. Only O_2 and CO_2 gas species are considered in the model, with nitrogen (N_2) and other air gas components being neglected. In the following, a detailed description of the three submodels is provided.

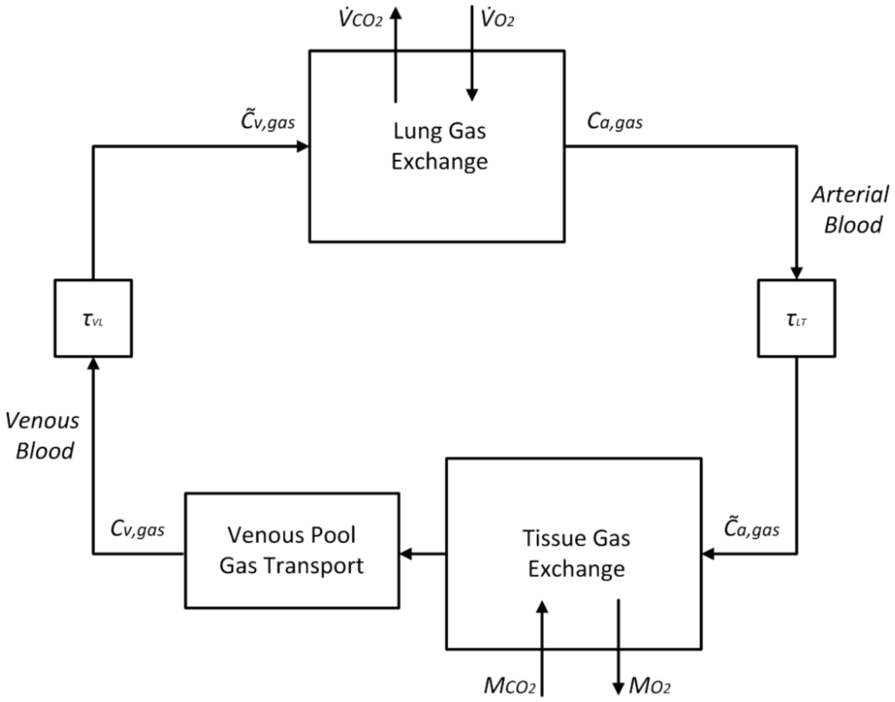

Figure 2.18 - Schematic diagram of the gas exchange and transport model highlighting the alveolar and tissue components, the venous pool gas transport block and the blood transport delays. $C_{a,gas}$, arterial blood gas concentrations; $C_{v,gas}$, mixed venous blood gas concentrations; τ_{LT}, transport delay from lungs to systemic tissues; τ_{VL}, transport delay from thoracic veins to lungs; $\tilde{C}_{a,gas}$, gas concentrations in the blood that enters the tissue gas exchanger; $\tilde{C}_{v,gas}$, gas concentrations in the blood that enters the lung gas exchanger; $\dot{V}_{O2}$ and $\dot{V}_{CO2}$, O_2 and CO_2 gas flow between alveoli and pulmonary capillaries, respectively; M_{O2} and M_{CO2}, metabolic O_2 consumption and CO_2 production rates in the systemic tissues, respectively. The subscript gas indicates either O_2 or CO_2.

1) The Lung Gas Exchange: The lung gas exchange model includes anatomical dead space, alveoli, pulmonary capillaries (also belonging to to the pulmonary peripheral compartment of the cardiovascular system model) and right to left pulmonary shunts. A schematic block diagram is shown in Figure 2.19.

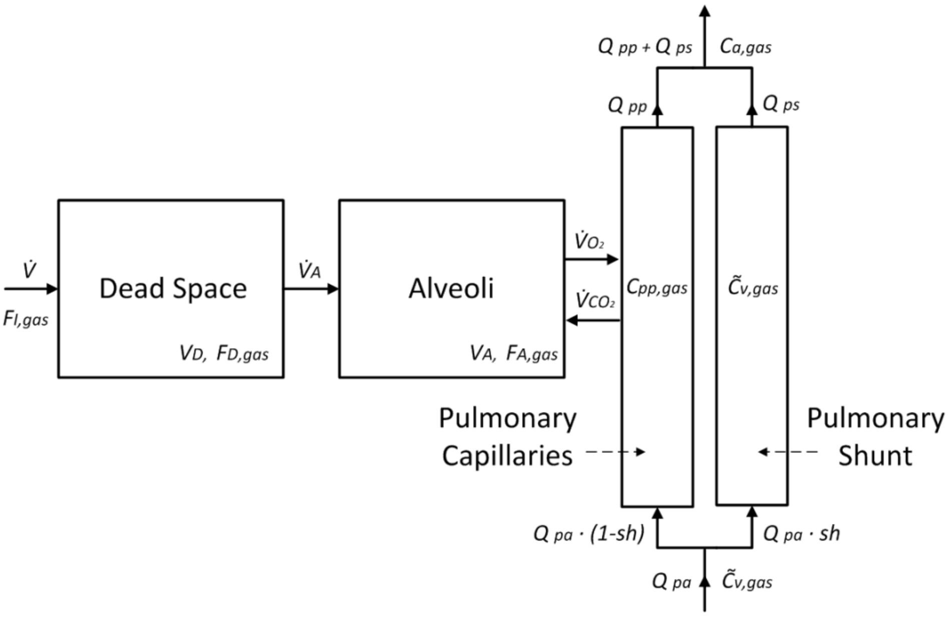

Figure 2.19 - Lung gas exchange model. $\dot{V}$, total air flow; $\dot{V}_A$, alveolar air flow; V_D, dead space volume; V_A, alveolar volume; $F_{I,gas}$, gas fractions in the inspired air; $F_{D,gas}$, gas fractions in the dead space; $F_{A,gas}$, gas fractions in the alveoli; $\dot{V}_{O2}$ and $\dot{V}_{CO2}$, O_2 and CO_2 gas flow between alveoli and pulmonary capillaries, respectively; $\tilde{C}_{v,gas}$, gas concentrations in the blood that enters the pulmonary capillaries; $C_{pp,gas}$, gas concentrations in the pulmonary capillaries; $C_{a,gas}$, gas concentrations in the arterial blood; Q_{pa}, blood flow from the pulmonary arteries; sh, shunt percentage; Q_{pp}, blood flow at the exit of the pulmonary capillaries; Q_{ps}, blood flow at the exit of the pulmonary shunt compartment.

It receives total airflow ($\dot{V}$), alveolar air flow ($\dot{V}_A$), dead space (V_d) and alveolar volume (V_A) as inputs from the lung mechanics model, and pulmonary peripheral volume (V_{pp}) and blood flows through the pulmonary beds as inputs from the cardiovascular model. Furthermore, the model is obviously interconnected to the tissue gas exchange model, as shown in Figure 2.18, as it requires the delayed venous gas concentrations $\tilde{C}_{v,gas}$ as input as well. External inputs to the model are the gas fractions in the inspired air, $F_{I,gas}$. Outputs of the model are the concentrations of gas in the pulmonary capillaries ($C_{pp,gas}$), which are then converted into arterial blood gas concentrations ($C_{a,gas}$). Gas concentrations are computed by applying conservation of mass for each gas species to each of the three compartments in Figure 2.19 (dead space, alveoli and pulmonary capillaries) and assuming that every compartment is homogenous and perfectly-mixed. Gases are assumed to be ideal and gas fractions in the lungs are related to their corresponding partial pressures via the ideal gas law. Blood gas concentrations are related to their corresponding partial pressures via empirical dissociation curves, which are easily invertible and that have been validated and used in previous cardiopulmonary models. Finally, equilibrium between pulmonary capillaries and alveoli in terms of gas partial pressures is assumed to happen instantaneously. The resulting set of equations governing the lung gas exchange model is reported below, while detailed mathematical derivation is reported in the *Appendix* section.

$$V_D \cdot \frac{dF_{D,gas}}{dt} = u(\dot{V}) \cdot \dot{V} \cdot \left(F_{I,gas} - F_{D,gas}\right) \\ +u(-\dot{V}) \cdot \dot{V}_A \cdot (F_{D,gas} - F_{A,gas}) \tag{2-8}$$

$$V_A \cdot \frac{dF_{A,gas}}{dt} = u(\dot{V}) \cdot \dot{V}_A \cdot (F_{D,gas} - F_{A,gas}) \\ -K \cdot \left(Q_{pa} \cdot (1 - sh) \cdot (C_{pp,gas} - \tilde{C}_{v,gas}) + V_{pp} \cdot \frac{dC_{pp,gas}}{dt}\right) \tag{2-9}$$

$$C_{pp,gas} = f_{gas}(P_{pp,O_2}, P_{pp,CO_2}) \tag{2-10}$$

$$P_{pp,gas} = P_{A,gas} \tag{2-11}$$

$$P_{A,gas} = F_{A,gas} \cdot (P_{atm} - P_{ws}) \tag{2-12}$$

where the subscript gas indicates either O_2 or CO_2, u is the Heaviside step function, sh represents the percentage of pulmonary shunt (assumed to be equal to 1.7%, see $ParameterAssignment$ section), f_{gas} is the dissociation curve that relates blood gas concentration to partial pressure, P_{ws} is the water vapor pressure and K is a proportionality constant that allows to convert volumes from BTPS (body temperature pressure saturated) to STPD (standard temperature pressure dry) conditions. Note that the Eqs. 2-8 – 2-12 above are very general, in the sense that they apply to both the inhalation and the exhalation phases, thanks to the use of the step function u, and that they can be specialized for either O_2 or CO_2. The dissociation function f_{gas} deserves few comments. As shown in Eq. 2-10, f_{gas} is a function of both O_2 and CO_2 partial pressures. This means that when specializing this equation for each gas species, the resulting dissociation functions, f_{O_2} and f_{CO_2}, will be interdependent. This interdependency, basically, accounts for the Bohr and Haldane effects, which are both captured in the mathematical description of the O_2 and CO_2 dissociation curves (see *Appendix* section for more details).

The system of equations above, once solved, provide as output the blood gas concentrations (or partial pressures) in the pulmonary capillaries. From these, blood concentrations in the arterial blood are finally computed by averaging between blood coming from the pulmonary capillaries and blood coming from the pulmonary shunts:

$$C_{a,gas} = \frac{Q_{pp} \cdot C_{pp,gas} + Q_{ps} \cdot \tilde{C}_{v,gas}}{Q_{pp} + Q_{ps}} \qquad (2\text{-}13)$$

From the arterial blood gas concentrations, C_{a,O_2} and C_{a,CO_2}, the corresponding partial pressures can be computed by applying the inverse of the dissociation functions f_{O_2} and f_{CO_2}. Finally, arterial O_2 saturation can also be computed from knowledge of $P_{a,O2}$ as:

$$S_{a,O_2}\% = \frac{C_{a,O_2} - P_{a,O_2} \cdot 0.003/100}{Hgb \cdot 1.34} \cdot 100 \qquad (2\text{-}14)$$

where Hgb is the hemoglobin concentration (expressed in g per ml of blood), 1.34 is the oxygen capacity (expressed in ml of O_2 per g of Hgb) and the term 0.003/100 represents the solubility of O_2 in blood (expressed in ml of O_2 per ml of blood per $mmHg$).

2) <u>*The Tissue Gas Exchange and Venous Pool Gas Transport*</u>: The tissue gas exchange model accounts for the O_2 consumption and CO_2 production of tissues and organs at the level of the systemic capillaries, whereas the venous pool gas transport model describe O_2 and CO_2

transport through the systemic and thoracic veins. A schematic diagram of the combined model is shown in Figure 2.20.

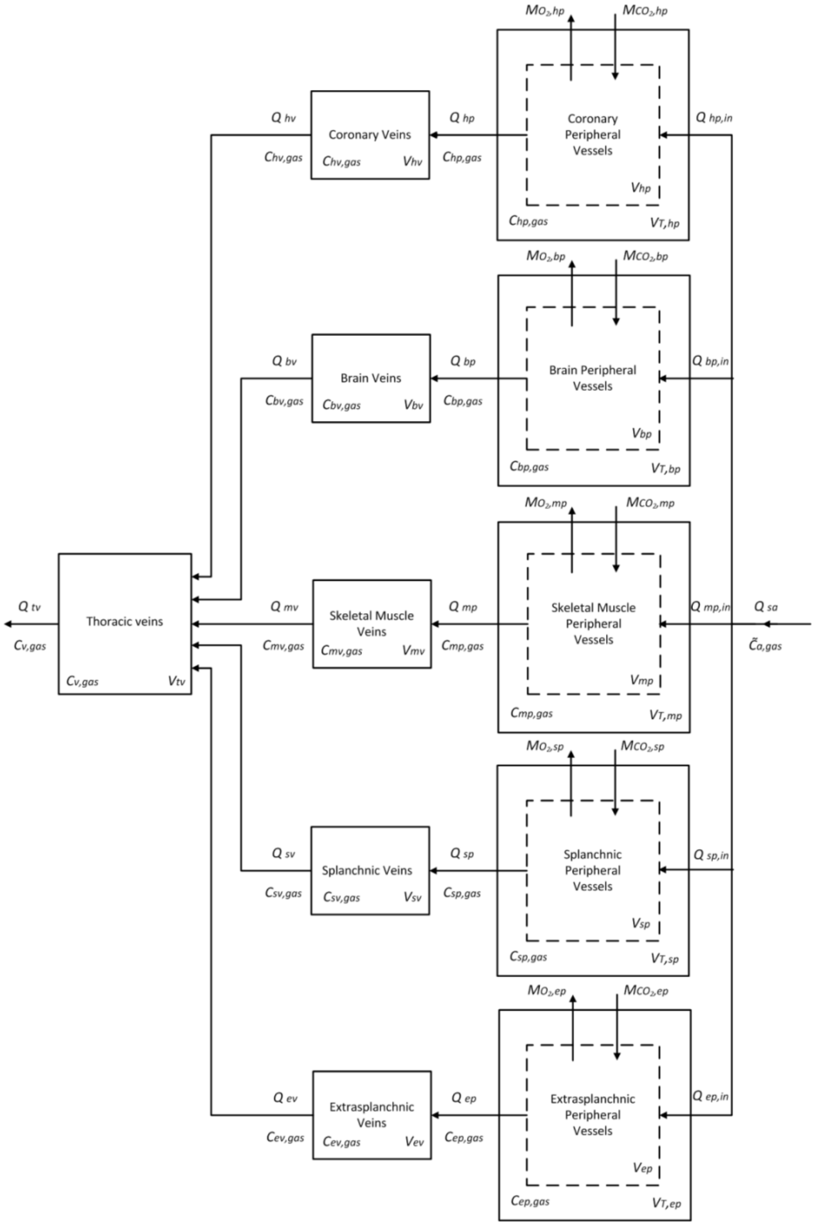

Figure 2.20 - Tissue gas exchange and venous pool gas transport model. $\tilde{C}_{a,gas}$, gas concentration at the entrance of the systemic peripheral compartments; $C_{jp,gas}$, gas concentration in the $j-th$ combined blood-tissue compartment; $C_{jv,gas}$, gas concentrations in the $j-th$ systemic venous compartment; $C_{v,gas}$, gas concentrations in the mixed venous blood; Q_{sa}, blood flow at the exit of the systemic arteries; Q_{jp}, blood flow at the exit of the $j-th$ systemic peripheral compartment; Q_{jv}, blood flow at the exit of the $j-th$ systemic venous compartment; Q_{tv}, blood flow at the exit of the thoracic veins; V_{jp}, blood volume contained in the $j-th$ systemic peripheral compartment; $V_{T,jp}$, blood volume contained in the $j-th$ tissue compartment; V_{jv}, blood volume contained in the $j-th$ systemic venous compartment; V_{tv}, blood volume contained in the thoracic veins; $M_{O2,jp}$ and $M_{CO2,jp}$, O_2 consumption and CO_2 production rates in the $j-th$ blood-tissue compartment, respectively.

The model receives as input the delayed arterial gas concentrations from the lung gas exchange module, $\tilde{C}_{a,gas}$, and provides as output the gas concentrations in the mixed venous blood, $C_{v,gas}$, computed at the exit of the thoracic veins compartment. Furthermore, the model is interconnected with the cardiovascular module, since it requires blood flows and volumes in the different systemic vascular beds as input as well. As shown in Fig. 10, tissue gas exchange is assumed to happen at the level of the five systemic peripheral compartments (coronary, brain, skeletal muscle, splanchnic and extrasplanchnic compartments). Each compartment supplies blood to an organ/tissue (or group of organs/tissues) that is modeled as a simple container, characterized by a constant volume $V_{T,jp}$. Blood and tissues are assumed to form a combined homogenous blood-tissue compartment, characterized by gas concentrations $C_{jp,gas}$ and total volume given by the sum of the tissue volume $V_{T,jp}$ and the blood volume V_{jp} of the corresponding systemic peripheral compartment by which is supplied. Oxygen consumption and carbon dioxide production are assumed to happen within these combined blood-tissue compartments at constant rates, $M_{O_2,jp}$ and $M_{CO_2,jp}$, respectively. Venous blood concentrations are computed based on conservation of mass principles, following a similar approach to the one described above for the lung gas exchange model. Particularly, conservation of mass is first enforced at each of the five combined blood-tissue compartments, assuming that $M_{O_2,j}$ and $M_{CO_2,j}$ are known constants and that each compartment is perfectly-mixed. The solution of the resulting set of differential equations provides the blood gas concentrations at the exit of the systemic peripheral compartments, $C_{jp,gas}$. From these, the blood gas concentrations in the mixed venous blood are finally obtained by applying conservation of mass to the remaining systemic vascular beds (systemic veins and thoracic veins compartments), assuming that the no net gas flow is either generated or consumed in these compartments (no $M_{O_2,j}$ and $M_{CO_2,j}$ are considered in the corresponding mass balance equations). The resulting set of equations governing the tissue gas exchange model is reported below, while detailed mathematical derivation is reported in the *Appendix* section.

$$(V_{T,jp}+V_{jp})\cdot\frac{dC_{jp,gas}}{dt}=Q_{jp,in}\cdot(\tilde{C}_{a,gas}-C_{jp,gas})\ \pm M_{gas,jp} \tag{2-15}$$

$$V_{jv}\frac{dC_{jv,gas}}{dt}=Q_{jp}\cdot(C_{jp,gas}-C_{jv,gas}) \tag{2-16}$$

$$V_{tv}\frac{dC_{v,gas}}{dt}=\sum_{j}Q_{jv}\cdot(C_{jv,gas}-C_{v,gas}) \tag{2-17}$$

$$\text{with } j=h,b,m,s,e$$

where the subscript gas indicates either O_2 or CO_2 and $Q_{jp,in}$ is the blood flow entering the *j-th* peripheral compartment (see Figure 2.20 legend for further definition of subscripts).

2.3.4 The Cardiovascular Control Model

The cardiovascular control model includes the main short-term regulation mechanisms (time duration < 1-2 min) that act on the cardiovascular function in response to acute hemodynamic and blood gas composition perturbations. Responses in the middle period (5-10 min) cannot be simulated due to the existence of slower compensation phenomena (such as hormonal regulation, renal blood volume regulation and fluid shift across capillaries) not included in the present model. The model is taken from previous work by Ursino and Magosso [5, 6], where detailed explanation and mathematical equations can be found. A high level schematic block diagram showing the input-output interconnections between the different components of the model is shown in Figure 2.21 below.

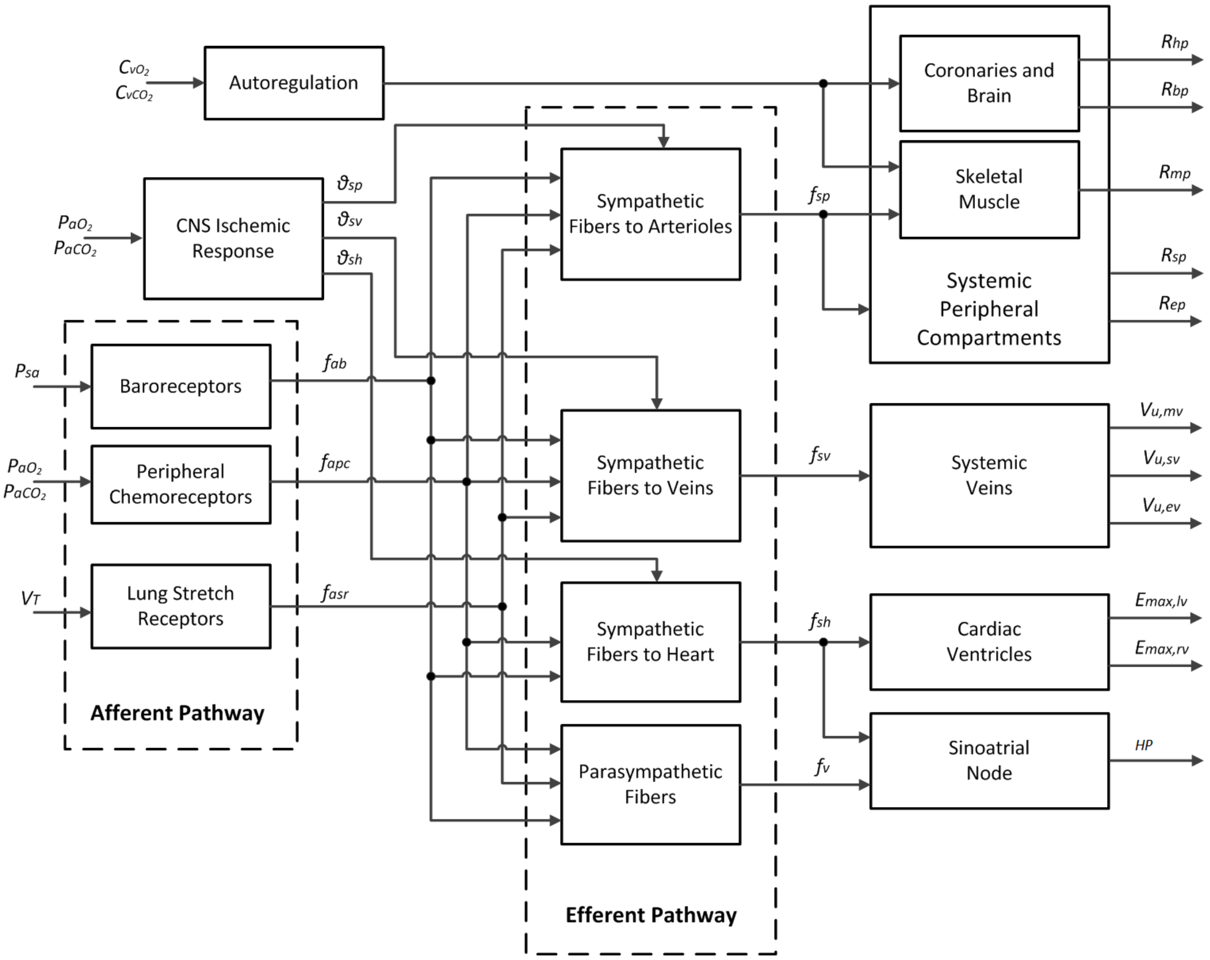

Figure 2.21 - Cardiovascular control model. C_{VO2}, venous O_2 concentration; C_{VCO2}, venous CO_2 concentration; P_{aO2}, arterial O_2 partial pressure; P_{aCO2}, arterial CO_2 partial pressure; P_{sa}, systemic arterial pressure; V_T, tidal volume; f_{ab}, f_{apc} and f_{asr}, afferent firing frequency of barorecptors, peripheral chemoreceptors and lung stretch receptors, respectively; θ_{sp}, θ_{sv} and θ_{sh}, offset terms representing the effect of the CNS ischemic response on the sympathetic fibers directed to peripheral circulation, veins and heart, respectively; f_{sp}, f_{sv} and f_{sh}, activity in the efferent sympathetic fibers directed to the peripheral circulation, the veins and the heart, respectively; f_v, activity in the vagal efferent fibers; R_{hp}, R_{bp}, R_{mp}, R_{sp} and R_{ep}, systemic peripheral resistance in coronary, brain, skeletal muscle, splanchnic and extrasplanchnic vascular beds, respectively; $V_{u,mv}$, $V_{u,sv}$, $V_{u,ev}$, venous unstressed volume in skeletal muscle, splanchnic and extrasplanchnic vascular bed, respectively; $E_{max,lv}$ and $E_{max,rv}$, end-systolic elastance of the left and right ventricle, respectively; *HP*, heart period.

Briefly, the model includes the action of carotid sinus baroreceptors, peripheral chemoreceptors, lung stretch receptors, autoregulation mechanisms and a CNS directly mediated ischemic response. Particularly, the model distinguishes between an afferent pathway, represented by the barorecptors, chemoreceptors and lung stretch receptors, and an efferent pathway, represented by the autonomic nervous system (ANS) and its sympathetic and parasympathetic neural fibers. Carotid baroreceptors respond to variation in systemic arterial blood pressure (P_{sa}), peripheral chemoreceptors respond to variations in arterial O_2 and CO_2 partial pressures (P_{aO2} and P_{aCO2}, respectively), whereas lung stretch receptors respond to variations in tidal volume (V_T). The afferent information from baroreceptors (f_{ab}), peripheral chemoreceptors (f_{apc}) and lung stretch receptors (f_{asr}) is first processed at the level of the ANS, thus modulating sympathetic and parasympathetic activities in the neural efferent pathways. Sympathetic and parasympathetic neural fibers, in turn, control the cardiovascular system via modifications of both the cardiac and the circulatory functions. Particularly, four different classes of effectors are assumed under the control of the ANS: heart period (HP), maximum ventricular contractilities ($E_{max,lv}$ and $E_{max,rv}$), resistances of the systemic peripheral beds (R_{jp}) and systemic venous unstressed volumes ($V_{u,jp}$). Heart period is assumed to be dependent on a balance between sympathetic and parasympathetic activities, whereas all other effectors are assumed under control of sympathetic fibers only. A distinction between sympathetic fibers directed to the heart (f_{sh}), sympathetic fibers directed to the arteries (f_{sp}) and sympathetic fibers directed to the veins (f_{sv}) is also made based on the assumption that sympathetic activities in these different neural pathways do not change in parallel in response to afferent information from baroreceptors, chemoreceptors and lung stretch receptors. Circulation in the most vital vascular beds, i.e, the coronary and the brain compartments, is assumed to be independent from the ANS modulation, being only affected by local autoregulation mechanisms. These mechanisms respond to acute variations in blood gas composition (hypoxia or hypercapnia) of the specific vascular bed and are responsible for rapid redistribution of blood flow in order to resume normal gas level in compartments that have typically high metabolic needs. Hence, in the model, autoregulation is assumed to be triggered by variations in venous gas concentrations of the specific vascular bed ($C_{jv,O2}$ and $C_{jv,CO2}$) and to alter blood flow toward that compartment via modifications of its peripheral resistance. As a result, as shown in Figure 2.21, in the case of the brain and coronary compartments, peripheral resistances (R_{hp} and R_{bp}, respectively) are under the influence of autoregulation only, whereas the unstressed volumes ($V_{u,hv}$ and $V_{u,bv}$, respectively) are assumed to be constant. Autoregulation mechanisms are also assumed to act on the skeletal muscle circulation, hence the peripheral resistance of this compartment (R_{mp}) is subject to a double control action exerted by both the ANS and the autoregulation mechanisms. Finally, a CNS ischemic response is also taken into account in the model by assuming that arterial blood gas partial pressures (P_{aO2} and P_{aCO2}) can alter the sensitivity of the efferent sympathetic fibers to the stimuli coming from the afferent receptors (barorecptors, chemoreceptors and lung stretch receptors).

The mathematical equations governing the model have been taken from [5, 6], but some modifications have been introduced. Particularly, the relationship relating peripheral chemoreceptor activity f_{apc} to P_{aO2} and P_{aCO2} (see Figure 2.21) presented in [5, 6] has been replaced with a more detailed model of the afferent peripheral chemoreceptors pathway [61]. This was necessary since the equations proposed in [5, 6] were not able to reproduce the overshoot and undershoot characterizing the typical peripheral chemoreceptors activity patterns, shown in Figure 2.22, observed in humans in response to a CO_2 step input [62].

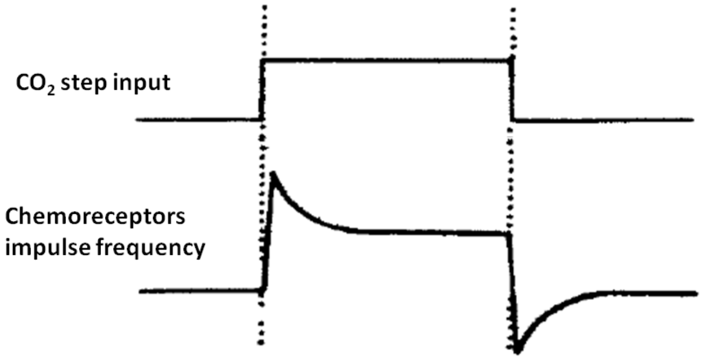

Figure 2.22 - Diagrams of time-dependent single-fiber responses of perfused carotid chemoreceptors to up and down steps of CO_2. Adapted from [62].

Additional details about the peripheral chemoreceptor model are provided in the next section, since this model is also used in the respiratory control module.

2.3.5 The Respiratory Control Model

Before moving to the description of the respiratory control model, it is worth providing some physiological background about the respiratory control system. Breathing is spontaneously initiated in the central nervous system. A cycle of inspiration and expiration is automatically generated by neurons located in a specific region of the brainstem, called *medulla*, that serves as a *central pattern generator*. This spontaneously generated cycle can be modified by reflexes of different nature (chemical, mechanical, etc.) or even temporarily suppressed by influences from higher brain centers (such as the hypothalamus or the cortex) in the case of voluntary control. The respiratory centre in the medulla effect the automatic rhythmic control of breathing via a final common pathway consisting of the spinal cord, the innervation of the muscles of respiration such as the phrenic nerves and the respiratory muscles themselves. Among the various reflexes that can modulate the automatic activity of the central pattern generator, the *chemoreflex* is definitely the most important. This reflex is activated by two classes of receptors, namely the *central chemoreceptors* and the *peripheral chemoreceptors*.

Central chemoreceptors are mainly located in a specific area of the brain, called *chemosensitive area*, anatomically separated from the medullary respiratory center and situated slightly below the ventral surface of the medulla. The central chemoreceptors are surrounded by brain extracellular fluid (ECF) and are especially excited by hydrogen ions H^+. In fact, it is believed that hydrogen ions concentration $[H^+]$ may be the only important direct stimulus for these neurons. However, hydrogen ions do not easily cross the blood-brain barrier and changes in the blood $[H^+]$ have considerably less effect in stimulating the chemosensitive area than do changes in blood CO_2 concentration, even though CO_2 is believed to stimulate these neurons only indirectly by changing $[H^+]$. The reason for this is that being the blood-brain barrier highly permeable to CO_2, whenever the blood P_{CO2} increases, CO_2 diffuses across it into the brain extracellular fluid and the cerebrospinal fluid (CSF). There, CO_2 immediately reacts with water liberating H^+ ions which stimulate the chemoreceptors. Thus, the CO_2 level in blood regulates ventilation chiefly by its effect on the pH of the cerebrospinal fluid. Peripheral chemoreceptors are located in the carotid bodies, at the bifurcation of the common carotid arteries, and in the aortic bodies, above and below the aortic arch. The chemoreceptors of the carotid bodies are however the most important in humans and they account for about 90% of the ventilatory response to hypoxaemia [63]. These receptors are especially important in detecting changes in arterial P_{O2}, although they also respond to a lesser extent to changes in arterial pH and P_{CO2}. When the oxygen concentration in the arterial blood falls below normal, the peripheral chemoreceptors become strongly stimulated. Their maximum sensitivity is reached for P_{O2} values between 30 - 60 mmHg. The peripheral chemoreceptors are thus responsible for all the increase of ventilation that occurs in humans in response to arterial hypoxemia. An increase in arterial carbon dioxide concentration also excites the chemoreceptors. Thus, increases in peripheral chemoreceptor activity in response to decreases in arterial P_{O2} are potentiated by increases in arterial P_{CO2} [64, 65]. The opposite is also true, i.e. hypoxia reinforces the peripheral chemoreceptors response to hypercapnia [66]. This suggests a multiplicative stimulus interaction at the peripheral chemoreceptors site.

In agreement with the physiological description provided above, the chemoreflex is the only control mechanism included in our respiratory control model. Hence, reflexes arising from mechanoreceptors, such as the Hering-Breuer reflexes, are not included in the model. A schematic block diagram of the model is shown in Figure 2.23.

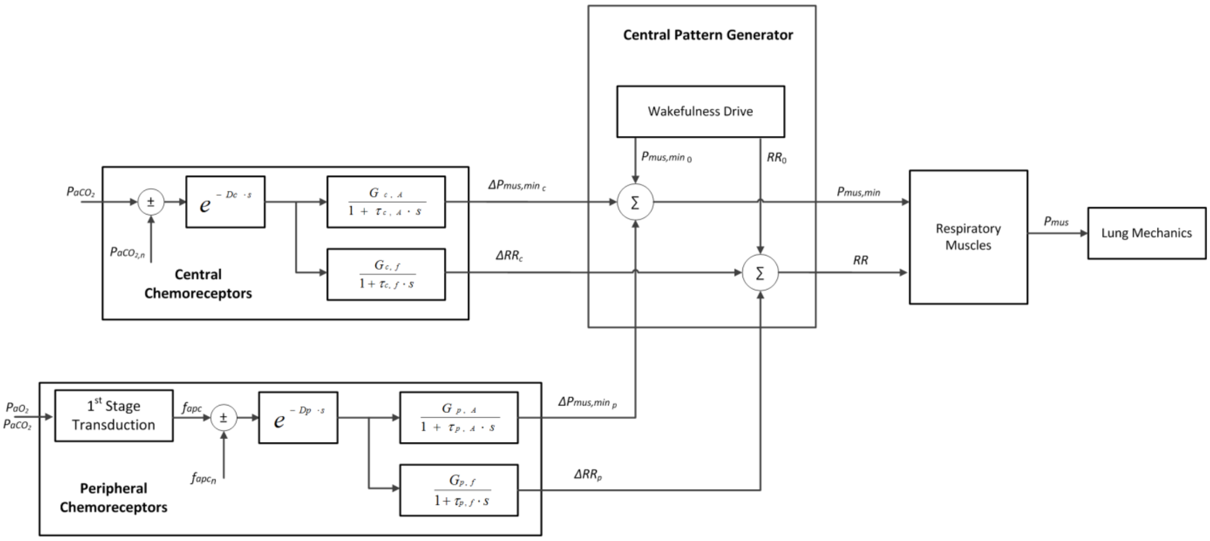

Figure 2.23 - Schematic block diagram of the respiratory control model. P_{aO2}, arterial O_2 partial pressure; P_{aCO2}, arterial CO_2 partial pressure; P_{mus}, respiratory muscle pressure driving the lung mechanics model; $P_{mus,min0}$ and RR_0, basal values of respiratory muscle pressure amplitude and respiratory rate, respectively; $\Delta P_{mus,min}c$ and ΔRR_c, variations in respiratory rate and respiratory muscle pressure amplitude induced by the central chemoreceptors; $\Delta P_{mus,min}p$ and ΔRR_p, variations in respiratory rate and respiratory muscle pressure amplitude induced by the peripheral chemoreceptors; f_{apc}, firing frequency of the afferent peripheral chemoreceptor fibers; $P_{aCO2,n}$ and $f_{apc,n}$, nominal value of P_{aCO2} and f_{apc}, respectively; D_c and D_p, time delay of the central and peripheral chemoreflex mechanisms, respectively; $G_{c,A}$ and $G_{c,f}$, gain factors for the central regulatory mechanism of P_{mus} amplitude and frequency, respectively; $G_{p,A}$ and $G_{p,f}$, gain factors for the peripheral regulatory mechanism of P_{mus} amplitude and frequency, respectively; $\tau_{c,A}$ and $\tau_{c,f}$, time constant of the central regulatory mechanism of P_{mus} amplitude and frequency, respectively; $\tau_{p,A}$ and $\tau_{p,f}$, time constant of the peripheral regulatory mechanism of P_{mus} amplitude and frequency, respectively.

The central chemoreceptors are assumed to be sensitive to arterial P_{CO2}, whereas the peripheral chemoreceptors are assumed to be sensitive to both arterial P_{O2} and P_{CO2}. The central and peripheral chemoreceptors directly affect the respiratory frequency, RR, and the amplitude of the inspiratory muscle pressure generator, $P_{mus,min}$ (see *The Respiratory System Model* section). This inclusion is an essential feature that differentiates our integrated cardiopulmonary model from others large scale models presented in literature. The majority of these models, in fact, assumes that chemoreceptors act on the respiratory system either by directly changing minute ventilation V_E [6, 13, 39, 67, 12] or by modifying tidal volume V_T and respiratory rate RR [68] hence ultimately affecting minute ventilation. In these models, a set of static or dynamic equations coupling P_{aO2} and P_{aCO2} (or some surrogates of these variables) to V_E (or V_T and RR) is used to describe the entire respiratory control system, bypassing the physiological link between chemoreceptors and respiratory muscles. Very few models account for the relationship between blood gas contents and respiratory efforts [32, 31, 53] expressed in terms of either intrapleural pressure P_{pl} or respiratory muscle pressure P_{mus}, and even fewer make a distinction between mechanisms affecting respiratory efforts amplitude and mechanisms affecting respiratory rate [32, 31].

As supported by experimental studies performed on humans [69], there is no active interaction between the two distinct central and peripheral chemoreceptor mechanisms. Hence, the central and the peripheral contributions to the ventilation response, in terms of variations in RR and $P_{mus,min}$, are assumed to be additive. Contributions from the chemoreceptors are then added to the basal values of RR and $P_{mus,min}$ generated by the intrinsic respiratory rhythm generator that produces a wakefulness drive when chemoreceptors are not stimulated.

$$P_{mus,min} = P_{mus,min0} + \Delta P_{mus,min}c + \Delta P_{mus,min}p \tag{2-18}$$

$$RR = RR_0 + \Delta RR_c + \Delta RR_p \tag{2-19}$$

where $P_{mus,min0}$ is the basal value of the respiratory muscle pressure amplitude, RR_0 is the basal value of the respiratory muscle pressure frequency, ΔRR_c and $\Delta P_{mus,min}c$ are the variations in respiratory rate and respiratory muscle pressure amplitude induced by the central chemoreceptors, and ΔRR_p and $\Delta P_{mus,min}p$ are the variations in respiratory rate and respiratory muscle pressure amplitude induced by the peripheral chemoreceptors.

As shown in Figure 2.23, the central chemoreceptor mechanism is described as a first-order dynamic system with a pure delay, having as input the variation of artrail blood P_{CO2} with respect to a set-point value $P_{aCO2,n}$ (assuming that variations of P_{CO2} in arterial blood and in the medulla are proportional) :

$$\frac{d\Delta P_{mus,min}c}{dt} = \frac{-\Delta P_{mus,min}c + G_{c,A} \cdot u_c}{\tau_{c,A}} \tag{2-20}$$

$$\frac{d\Delta RR_c}{dt} = \frac{-\Delta RR_c + G_{c,f} \cdot u_c}{\tau_{c,f}} \tag{2-21}$$

$$\text{with } u_c(t) = P_{aCO2}(t - D_c) - P_{aCO2,n}$$

where D_c is a delay that accounts for the time it takes to blood to travel from the systemic arteries to the central chemosensitive area in the brain, $G_{c,f}$ and $G_{c,A}$ are the gains of the P_{mus} amplitude and frequency control mechanisms, respectively, $\tau_{c,f}$ and $\tau_{c,A}$ are the corresponding time constants and $P_{aCO2,n}$ is the arterial O_2 partial pressure set-point value.

The peripheral chemoreceptors mechanism has been described as a two-stage transduction mechanism: in the 1st transduction stage, P_{aO2} and P_{aCO2} signals are converted into electrical activity of the afferent peripheral chemoreceptors f_{apc}; in the 2nd stage, the continuous value of f_{apc} is compared with a reference nominal value and the distance from the nominal value is then converted into variations of $P_{mus,min}$ and RR. The input-output relationship characterizing the 1st stage transduction mechanism has been taken from Ursino and Magosso [61]. This relationship is also used in the cardiovascular control module. It takes into account the above mentioned multiplicative interaction between O_2 and CO_2 at the peripheral chemoreceptor level and it has been validated using experimental data from animals under a variety of combined O_2 and CO_2 stimuli. For sake of brevity, we do not report the equations describing this 1st stage transduction mechanism and he interested reader can refer to the original publication for further details. As for the 2nd transduction mechanism, this has been described via relationships analogous to those used for the central chemoreceptors, that is as a first-order dynamic system with a pure delay, the input being the variations in f_{apc} with respect to a set-point value $f_{apc,n}$:

$$\frac{d\Delta P_{mus,min}p}{dt} = \frac{-\Delta P_{mus,min}p + G_{p,A} \cdot u_p}{\tau_{p,A}} \tag{2-22}$$

$$\frac{d\Delta RR_p}{dt} = \frac{-\Delta RR_p + G_{p,f} \cdot u_p}{\tau_{p,f}} \tag{2-23}$$

$$\text{with } u_p(t) = f_{acp}(t - D_p) - f_{apc,n}$$

where D_p is a delay that accounts for the time it takes to blood to travel from the systemic arteries to the peripheral chemosensitive area, $G_{p,f}$ and $G_{p,A}$ are the gains of the P_{mus} amplitude and frequency control mechanisms, respectively, $\tau_{p,f}$ and $\tau_{p,A}$ are the corresponding time constants and $f_{acp,n}$ is the afferent peripheral chemoreceptor activity set-point value.

2.4 Parameter Assignment

All the parameters of the $CP\ Model$ have been assigned with reference to a 70-Kg healthy subject. Most of them are based on previous studies, but some have been modified or newly introduced. They are summarized in Tables 2-2 – 2.9, along with the corresponding literature references when applicable. In the following sections, the choice of the parameter values for each subsystem will be discussed with particular emphasis on the new parameters and the modifications with respect to previous studies.

2.4.1 Vascular System

The parameters of the uncontrolled vascular system model have been taken from [5, 6], where detailed justifications about their values can be found. However, some parameters needed to be adjusted or defined to reflect the aforementioned modifications (see *Model Development* section) introduced to the original model presented in these previous work. Particularly: *1)* The values of resistance and compliance of the pulmonary peripheral and pulmonary shunt compartments have been given starting from the assumption that 1.7% of the total blood flow coming out of the pulmonary arteries (Q_{pa} in Figure 2.12) enters the pulmonary shunts, whereas the remaining 98.3% enters the pulmonary capillaries [70]. Particularly, by imposing this condition on the blood flows to be valid at steady state, when the compliances C_{ps} and C_{pp} do not contribute to the flow entering the two compartments, the ratio R_{ps}/R_{pp} is found to be $98.3/1.7$; to obtain a value for R_{ps} and R_{pp}, it has been assumed that the parallel arrangement of pulmonary shunt and pulmonary peripheral compartments provides the same resistance value used in [5, 6] for the overall pulmonary peripheral compartment. Analogous reasoning was applied to determine the values of the compliances. Particularly, by imposing the same $1.7/98.3$ ratio between blood flow entering the pulmonary shunt and blood flow entering the pulmonary peripheral compartment also during the transient phase and using the ratio R_{ps}/R_{pp} determined above, it was possible to determine a value for the C_{ps}/C_{pp} ratio; finally, assuming that the parallel arrangements of pulmonary shunt and pulmonary peripheral compartments provides the same overall compliance value used in [5, 6] it was possible to determine the values of C_{ps} and C_{pp}. *2)* The values of the parameters pertaining to the thoracic veins compartment have been given based on [39, 51]. *3)* As a consequence of the introduction of the thoracic veins compartment, the venous compliance in all the parallel systemic district has been reduced by 30% relative to the value used in [5, 6] so that the total venous compliance is maintained as per the previous studies. *4)* To compensate for the added excess volume due to the introduction of the negative intrapleural pressure, the basal value of unstressed volume in every vascular compartment within the thoracic cavity has been reduced by 12% relative to the values used in the previous studies [5, 6]. *5)* The compliance of the overall systemic peripheral circulation has been redistributed among the five parallel districts in order to guarantee realistic and valid simulation results based on literature. All the parameters characterizing the uncontrolled vascular system in basal condition (without the action of the regulatory mechanisms) are reported in Table 2-2, along with their corresponding reference source.

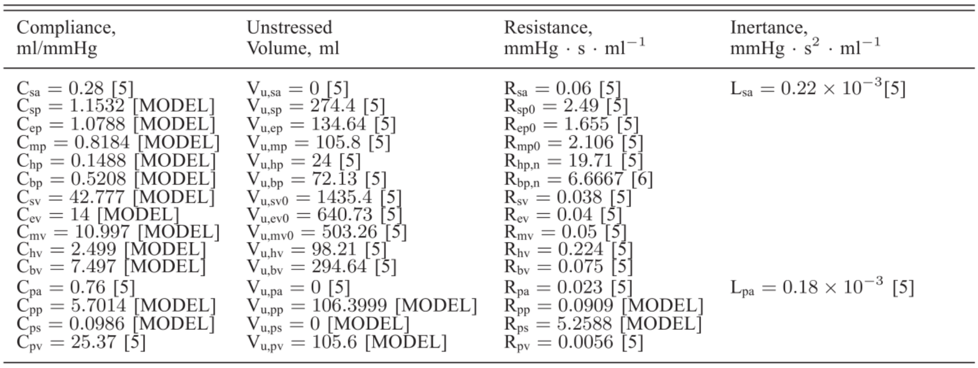

Compliance, ml/mmHg	Unstressed Volume, ml	Resistance, mmHg · s · ml^{-1}	Inertance, mmHg · s^2 · ml^{-1}
$C_{sa} = 0.28$ [5]	$V_{u,sa} = 0$ [5]	$R_{sa} = 0.06$ [5]	$L_{sa} = 0.22 \times 10^{-3}$[5]
$C_{sp} = 1.1532$ [MODEL]	$V_{u,sp} = 274.4$ [5]	$R_{sp0} = 2.49$ [5]	
$C_{ep} = 1.0788$ [MODEL]	$V_{u,ep} = 134.64$ [5]	$R_{ep0} = 1.655$ [5]	
$C_{mp} = 0.8184$ [MODEL]	$V_{u,mp} = 105.8$ [5]	$R_{mp0} = 2.106$ [5]	
$C_{hp} = 0.1488$ [MODEL]	$V_{u,hp} = 24$ [5]	$R_{hp,n} = 19.71$ [5]	
$C_{bp} = 0.5208$ [MODEL]	$V_{u,bp} = 72.13$ [5]	$R_{bp,n} = 6.6667$ [6]	
$C_{sv} = 42.777$ [MODEL]	$V_{u,sv0} = 1435.4$ [5]	$R_{sv} = 0.038$ [5]	
$C_{ev} = 14$ [MODEL]	$V_{u,ev0} = 640.73$ [5]	$R_{ev} = 0.04$ [5]	
$C_{mv} = 10.997$ [MODEL]	$V_{u,mv0} = 503.26$ [5]	$R_{mv} = 0.05$ [5]	
$C_{hv} = 2.499$ [MODEL]	$V_{u,hv} = 98.21$ [5]	$R_{hv} = 0.224$ [5]	
$C_{bv} = 7.497$ [MODEL]	$V_{u,bv} = 294.64$ [5]	$R_{bv} = 0.075$ [5]	
$C_{pa} = 0.76$ [5]	$V_{u,pa} = 0$ [5]	$R_{pa} = 0.023$ [5]	$L_{pa} = 0.18 \times 10^{-3}$ [5]
$C_{pp} = 5.7014$ [MODEL]	$V_{u,pp} = 106.3999$ [MODEL]	$R_{pp} = 0.0909$ [MODEL]	
$C_{ps} = 0.0986$ [MODEL]	$V_{u,ps} = 0$ [MODEL]	$R_{ps} = 5.2588$ [MODEL]	
$C_{pv} = 25.37$ [5]	$V_{u,pv} = 105.6$ [MODEL]	$R_{pv} = 0.0056$ [5]	

Table 2-2 – Parameters of the vascular system in basal condition. See Eqs. A.1-A.29 in *Appenidx*. Note the use of subscripts 0 and n in the unstressed volumes and resistances that are subject to control mechanisms. Total blood volume (V_{tot}) is 5,300 mL.

PV Relationship	Resistance
$D_1 = 0.3855$ mmHg [39]	$K_R = 0.001$ mmHg·s·ml^{-1} [39]
$K_1 = 0.15$ mmHg/ml [39]	$V_{tv,max} = 350$ ml [39]
$V_{u,tv} = 130$ mL [39]	$R_{tv,0} = 0.025$ mmHg·s·ml^{-1} [39]
$D_2 = -5$ mmHg [39]	
$K_2 = 0.4$ mmHg [39]	
$V_{tv,min} = 50$ ml [39]	
$K_{xp} = 2$ mmHg [51]	
$K_{xv} = 8$ ml [51]	

Table 2-3 – Parameters of the thoracic veins. See Eqs.2.4 -2.5 in the *Model Development* section. See text and references for explanation of symbols.

2.4.2 Heart

The parameters characterizing the heart model have been given the same values as in previous studies [5, 6], where motivation for these values is provided based on literature data. For the sake of completeness, the parameters of the heart model are listed in Table 2-4 below.

Left Heart	Right Heart
$C_{la} = 19.23$ ml/mmHg	$C_{ra} = 31.25$ ml/mmHg
$V_{u,la} = 22$ ml	$V_{u,ra} = 22$ ml
$R_{la} = 2.5 \cdot 10^{-3}$ mmHg·s·ml^{-1}	$R_{ra} = 2.5 \cdot 10^{-3}$ mmHg·s·ml^{-1}
$P_{0,lv} = 1.5$ mmHg	$P_{0,rv} = 1.5$ mmHg
$K_{E,lv} = 0.014$ ml^{-1}	$K_{E,lv} = 0.011$ ml^{-1}
$V_{u,lv} = 14.7576$ ml	$V_{u,rv} = 35.904$ ml
$E_{max,lv} = 2.392$ mmHg/ml	$E_{max,rv} = 1.412$ mmHg/ml
$K_{R,lv} = 3.75 \cdot 10^{-4}$ s/ml	$K_{R,rv} = 1.4 \cdot 10^{-3}$ s/ml
Additional parameters	
$T_{sys,0} = 0.5$ s	$K_{sys} = 0.075$ s^2

Table 2-4 – Parameters of the Heart model. See Eqs. A.30 – A.48 in the *Appendix*.

2.4.3 Lung Mechanics

The parameters of the lung mechanics model (resistances, compliances and unstressed volumes of the four respiratory mechanics compartments) have been assigned starting from values reported in [52, 53]. However, some adjustments have been made in order to account for the newly introduced pleural pressure and chest wall dynamics and to reproduce realistic simulated lung volumes typically observed in normal subjects under quite breathing conditions. Particularly: *1)* The chest wall compliance C_{cw}, not included in [52, 53], has been assigned a value based on [60];. *2)* The amplitude and frequency of the respiratory muscle pressure generator P_{mus} in basal condition (without the action of the respiratory control model) have been assigned in order to attain a tidal volume of about 500 mL and a respiratory rate of 12 breaths/min [70]. *3)* The initial conditions for the five different pressure nodes in Fig. 7 (state variables) have been assigned assuming that at time $t = 0$, corresponding to the end exhalation time, all the pressures in the lungs equilibrate to atmospheric pressure whereas intrapleural pressure has a subatmospheric value of -5 cmH_2O [70]. *5)* The unstressed volumes of larynx, trachea and bronchea have been given the same values reported in [52, 53]. *6)* The unstressed volume of the alveolar compartment has been modified in order to guarantee an end expiratory lung volume equal to normal functional residual capacity (FRC), based on the following equation:

$$V_{u,A} = FRC + C_A \cdot P_{pl,EE} - V_{l,EE} - V_{t,EE} - V_{b,EE} \tag{2-24}$$

where $P_{pl,EE}$ is the pleural pressure value at end exhalation, $V_{l,EE}$, $V_{t,EE}$ and $V_{b,EE}$ represent the end-expiratory volumes of the larynx, trachea and bronchea, respectively, and FRC is 2.4 L [70]. *7)* Finally, the value of the time constant τ governing the exponential expiratory profile has been assumed to be equal to 1/5 of the expiratory time to guarantee enough time for lung emptying, and a value of 0.6 has been used for the inspiratory-expiratory time ratio

IE_{ratio}. All the parameters of the lung mechanics model are reported in Table 2-5, along with their corresponding reference source when applicable.

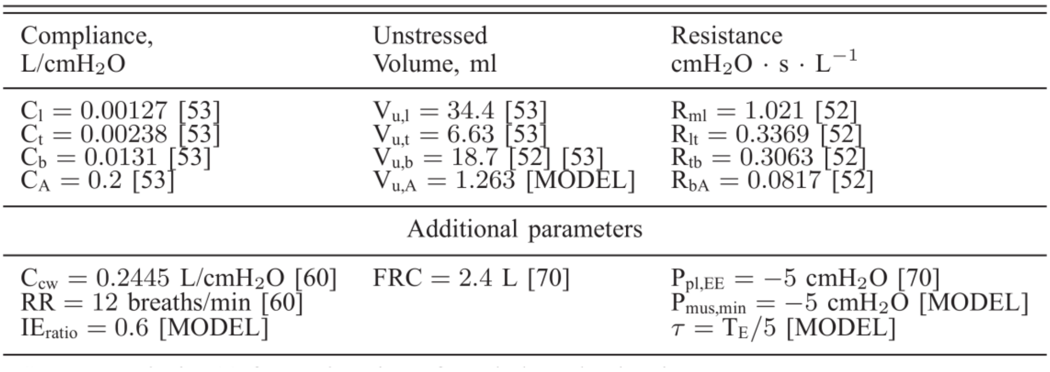

Compliance, L/cmH$_2$O	Unstressed Volume, ml	Resistance cmH$_2$O · s · L^{-1}
$C_l = 0.00127$ [53]	$V_{u,l} = 34.4$ [53]	$R_{ml} = 1.021$ [52]
$C_t = 0.00238$ [53]	$V_{u,t} = 6.63$ [53]	$R_{lt} = 0.3369$ [52]
$C_b = 0.0131$ [53]	$V_{u,b} = 18.7$ [52] [53]	$R_{tb} = 0.3063$ [52]
$C_A = 0.2$ [53]	$V_{u,A} = 1.263$ [MODEL]	$R_{bA} = 0.0817$ [52]
Additional parameters		
$C_{cw} = 0.2445$ L/cmH$_2$O [60]	FRC = 2.4 L [70]	$P_{pl,EE} = -5$ cmH$_2$O [70]
RR = 12 breaths/min [60]		$P_{mus,min} = -5$ cmH$_2$O [MODEL]
$IE_{ratio} = 0.6$ [MODEL]		$\tau = T_E/5$ [MODEL]

Table 2-5 – Parameters of the lung mechanics model in basal conditions. See Eqs. A.49 – A.60 in the *Appendix*. See text and Figure 2.17 for explanation of symbols and subscripts. Note the use of subscripts 0 for the parameters that are subjects to control mechanisms.

2.4.4 Gas Exchange and Transport

The parameters describing the gas exchange and transport model can be subdivided into parameters pertaining to the lung gas exchange model, parameters pertaining to the tissue gas exchange model, and parameters pertaining to blood trasnport, i.e. the two circulatory transport delays τ_{LT} and τ_{VL}(see Figure 2.18).

The parameters characterizing the lung gas exchange model can be further divided into 3 different groups: *1)* parameters pertaining to the environmental conditions, which have been assigned based on common knowledge; *2)* parameters pertaining to the O_2 and CO_2 dissociation curves, which have been taken from [71]; *3)* parameters pertaining to the physiological status of the subject (percentage of pulmonary shunts, sh, and hemoglobin content, Hgb), which have been chosen to simulate a 70 Kg healthy adult male. The values of the parameters are reported in Table 2-8 for each group.

As for the tissue gas exchange model, the only parameters involved are the tissue volumes ($V_{T,jp}$) and the O_2 and CO_2 metabolic rates ($M_{O2,jp}$ and $M_{CO2,jp}$), where j corresponds to the different combined blood-tissue compartments. The values of $V_{T,jp}$ have been assigned based on literature data [72, 73, 74, 75, 76, 77], whereas the values of the metabolic rates have been assigned as follows. First, the values of M_{O2} for the brain, coronary and skeletal muscle compartments have been taken from [5, 6]. Then, the values of M_{O2} for the splanchnic and extrasplanchnic compartments have been given based on the assumption that total O_2 consumption rate is 250 mL/min [78] and that the ratio $M_{O2,sp}/M_{O2,ep}$ is 7.384 [79]. Finally, the values of M_{CO2} for the different compartments have been computed by assuming that the total CO_2 production rate is 210 mL/min [78], corresponding to a respiratory quotient of 0.84, and that the M_{CO2} ratio between compartment i and compartment j is equal to the corresponding M_{O2} ratio between the same compartments.

The values of the two blood transport delays have been assigned from literature. Some adjustments were made in order to reflect the fact that part of the circulatory delay has been explicitly taken into account in the venous pool transport model. Particularly, the time delay from lungs to tissue, τ_{LT}, has been given the same value used in [31] and [80]. As for the veins to lungs time delay, τ_{VL}, a value of 10 sec has been chosen considering that a value of 25 sec has been used in the model by Lu *et al.* [31] for the overall tissue to lungs delay. This choice is then equivalent to the assumption that a time delay of around 15 sec can be attributed to the systemic and the thoracic veins compartments. All the parameters of the tissue gas exchange model are reported in Table 2-7, along with the corresponding reference source.

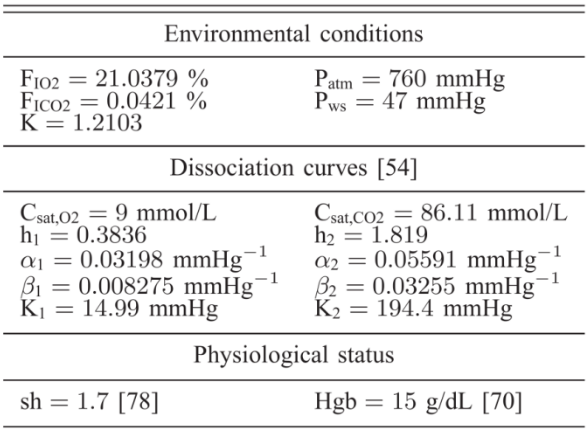

Environmental conditions	
$F_{IO2} = 21.0379$ %	$P_{atm} = 760$ mmHg
$F_{ICO2} = 0.0421$ %	$P_{ws} = 47$ mmHg
$K = 1.2103$	
Dissociation curves [54]	
$C_{sat,O2} = 9$ mmol/L	$C_{sat,CO2} = 86.11$ mmol/L
$h_1 = 0.3836$	$h_2 = 1.819$
$\alpha_1 = 0.03198$ mmHg^{-1}	$\alpha_2 = 0.05591$ mmHg^{-1}
$\beta_1 = 0.008275$ mmHg^{-1}	$\beta_2 = 0.03255$ mmHg^{-1}
$K_1 = 14.99$ mmHg	$K_2 = 194.4$ mmHg
Physiological status	
sh = 1.7 [78]	Hgb = 15 g/dL [70]

Table 2-6 – Parameters of the lung gas exchange model. See Eqs. A.61 – A.75 in the *Appendix*.

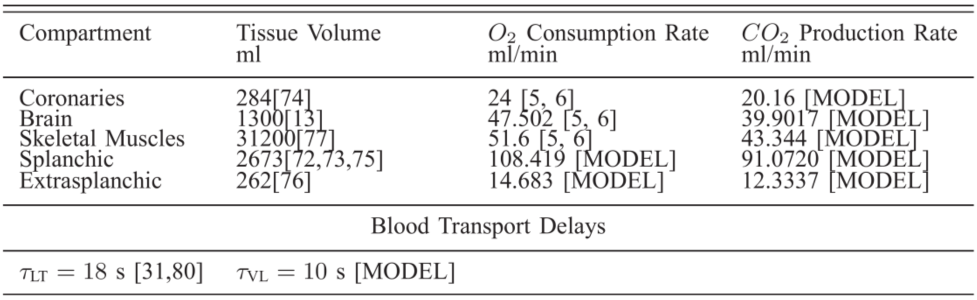

Compartment	Tissue Volume ml	O_2 Consumption Rate ml/min	CO_2 Production Rate ml/min
Coronaries	284[74]	24 [5, 6]	20.16 [MODEL]
Brain	1300[13]	47.502 [5, 6]	39.9017 [MODEL]
Skeletal Muscles	31200[77]	51.6 [5, 6]	43.344 [MODEL]
Splanchic	2673[72,73,75]	108.419 [MODEL]	91.0720 [MODEL]
Extrasplanchic	262[76]	14.683 [MODEL]	12.3337 [MODEL]
Blood Transport Delays			
$\tau_{LT} = 18$ s [31,80]	$\tau_{VL} = 10$ s [MODEL]		

Table 2-7 – Parameters of the tissue gas exchange model. See Eqs. A.76 – A.85 in the *Appendix*.

2.4.5 Cardiovascular Control

The parameters characterizing the cardiovascular control model have been taken from [5, 6] with exception to those related to the afferent peripheral chemoreceptor model that have been taken from [61]. Some of the parameters that describe the integration of the afferent information from the different receptors operated by the ANS have been modified with respect to their original values presented [5, 6]. This was necessary in order to reproduce the typical cardiovascular responses to respiratory challenges (hypercapnia and hypoxia) observed in healthy population and reported in literature [81, 82]. The modified parameters are reported in Table 2-8, but no attempt to motivate their values is made. The interested reader can refer to the previous publications [5, 6, 61] for a list of the additional unchanged parameters.

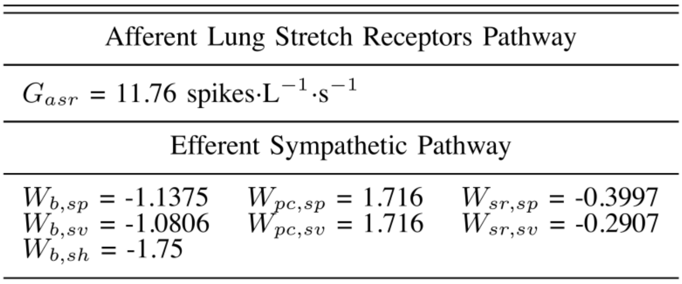

Afferent Lung Stretch Receptors Pathway		
G_{asr} = 11.76 spikes·L^{-1}·s^{-1}		
Efferent Sympathetic Pathway		
$W_{b,sp}$ = -1.1375	$W_{pc,sp}$ = 1.716	$W_{sr,sp}$ = -0.3997
$W_{b,sv}$ = -1.0806	$W_{pc,sv}$ = 1.716	$W_{sr,sv}$ = -0.2907
$W_{b,sh}$ = -1.75		

Table 2-8 – Parameters of the cardiovascular control model modified with respect to [5, 6, 61].

2.4.6 Respiratory Control

The choice of the parameters of the respiratory control model, other than the aforementioned parameters of the afferent peripheral chemoreceptor model, is now explained. As we mentioned in the *Model Development* section, the majority of the ventilation control models presented in literature assume a very simplified structure of the respiratory control system. Hence, assignment of the parameters pertaining to the respiratory control model based on previous models presented in literature was not possible. The parameters had to then be chosen so as to reproduce experimental data [83, 84] obtained from healthy volunteers under specific respiratory challenges, while adhering to physiological constraints. Particularly, the following parameter assignment process has been followed. *1)* The values of the time delays of the central and peripheral chemoreflex mechanisms (D_c and D_p, respectively) and the set point values of P_{aCO2} and f_{apc} have been taken from [6]. *2)* Based on the experimental data, [83, 84] the time constants for the respiratory rate response were given higher values than the corresponding time constants for the P_{mus} amplitude response. *3)* By using experimental data from human subjects under isocapnic hypoxic challenges [83], where the contribution of the central chemoreceptor to the respiratory response is essentially abolished due to the non hypercapnic condition, it was possible to isolate the peripheral chemoreflex response and hence tune its time constants and gains ($\tau_{p,A}$,$\tau_{p,f}$,$G_{p,A}$ and $G_{p,f}$). *4)* The time constant $\tau_{c,A}$ of the central regulatory mechanism of P_{mus} amplitude have been taken from [85]. *5)* Finally, the remaining parameters of the central chemoreceptor mechanism where chosen in order to fit the experimental data from hypercapnic experiments [84], and by recognizing that the time constants for the central mechanism should always be greater than the corresponding time constants of the peripheral mechanism [85]. The parameters of the respiratory control model are provided in Table 2-9, along with the corresponding reference source when applicable.

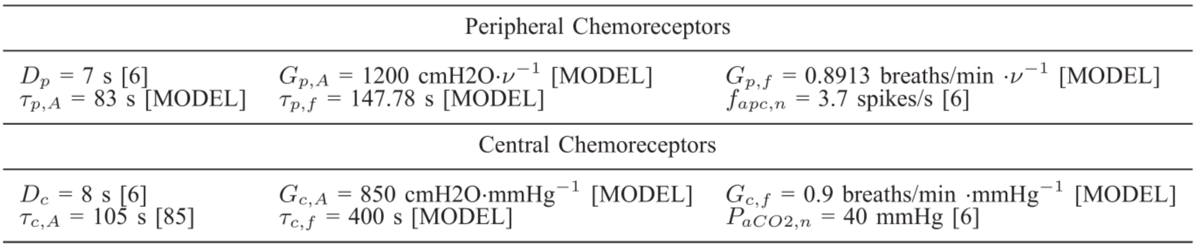

	Peripheral Chemoreceptors	
D_p = 7 s [6]	$G_{p,A}$ = 1200 cmH2O$\cdot\nu^{-1}$ [MODEL]	$G_{p,f}$ = 0.8913 breaths/min $\cdot\nu^{-1}$ [MODEL]
$\tau_{p,A}$ = 83 s [MODEL]	$\tau_{p,f}$ = 147.78 s [MODEL]	$f_{apc,n}$ = 3.7 spikes/s [6]
	Central Chemoreceptors	
D_c = 8 s [6]	$G_{c,A}$ = 850 cmH2O$\cdot$mmHg^{-1} [MODEL]	$G_{c,f}$ = 0.9 breaths/min $\cdot$mmHg^{-1} [MODEL]
$\tau_{c,A}$ = 105 s [85]	$\tau_{c,f}$ = 400 s [MODEL]	$P_{aCO2,n}$ = 40 mmHg [6]

Table 2-9 – Parameters of the respiratory control model. See Eqs. 2.18 – 2.23 in the *Model Development* section. ν is spikes/s.

2.5 Model Implementation

The combined model has 78 differential equations, more than 70 algebraic equations and 240 parameters associated with its components. Table 2-10 shows the distribution of the state variables, the model parameters and the the outputs in the combined cardiopulmonary model.

	State Variables	Parameters	Outputs
Cardiovascular System	17	74	43
Respiratory System	5	19	8
Gas Exchange and Transport	26	29	9
Cardiovascular Control	26	104	8
Respiratory Control	4	14	2

Table 2-10 – Number of state variables, parameters and outputs in the combined *CP Model*.

The model was programmed in Matlab-Simulink (The Mathworks Inc.) and the numerical integration of the differential equations was performed using the 4th order Runge-Kutta method with fixed-step size. The higher level Simulink implementation is shown in Figure 2.24. Each component of the *CP Model* has a corresponding Simulink block, and according to a hierarchical criterion all the equations pertaining to that component are implemented inside the block. The different blocks are then linked to each other through their inputs and outputs by using tags (to reduce clutter). To facilitate usability of the model and to allow the user to change parameter settings and to simulate different disease scenarios and interventions, a standalone Graphical User Interface (GUI) was created by members of our research group (see Figure 2.25).

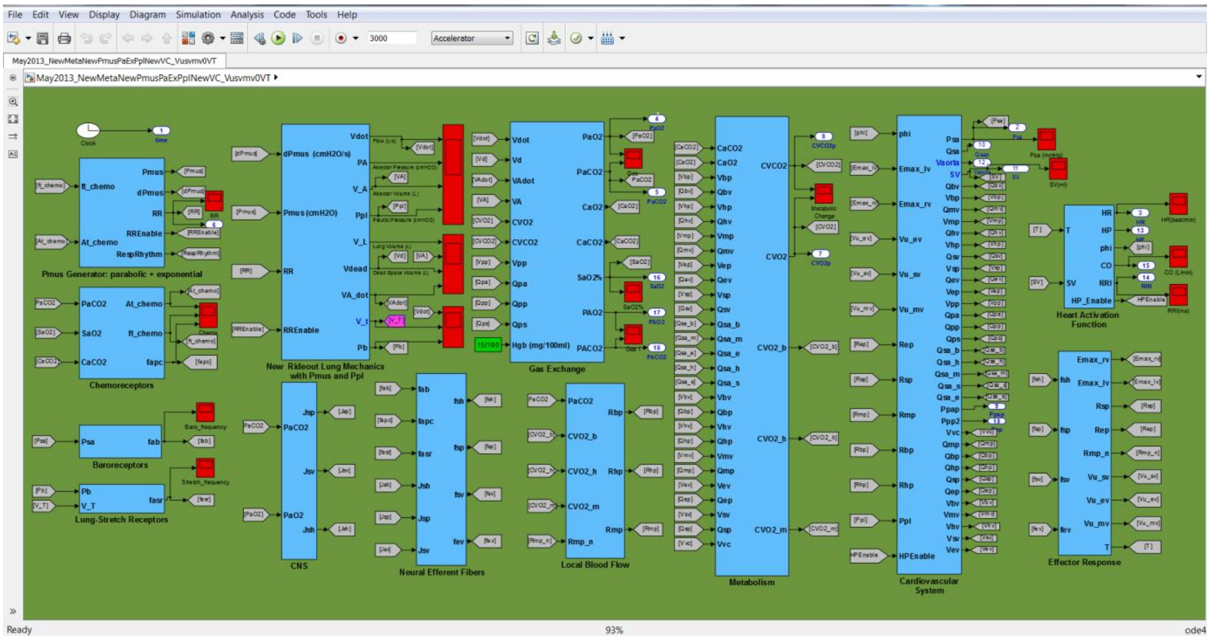

Figure 2.24 – High level Simulink implementation of the *CP Model*.

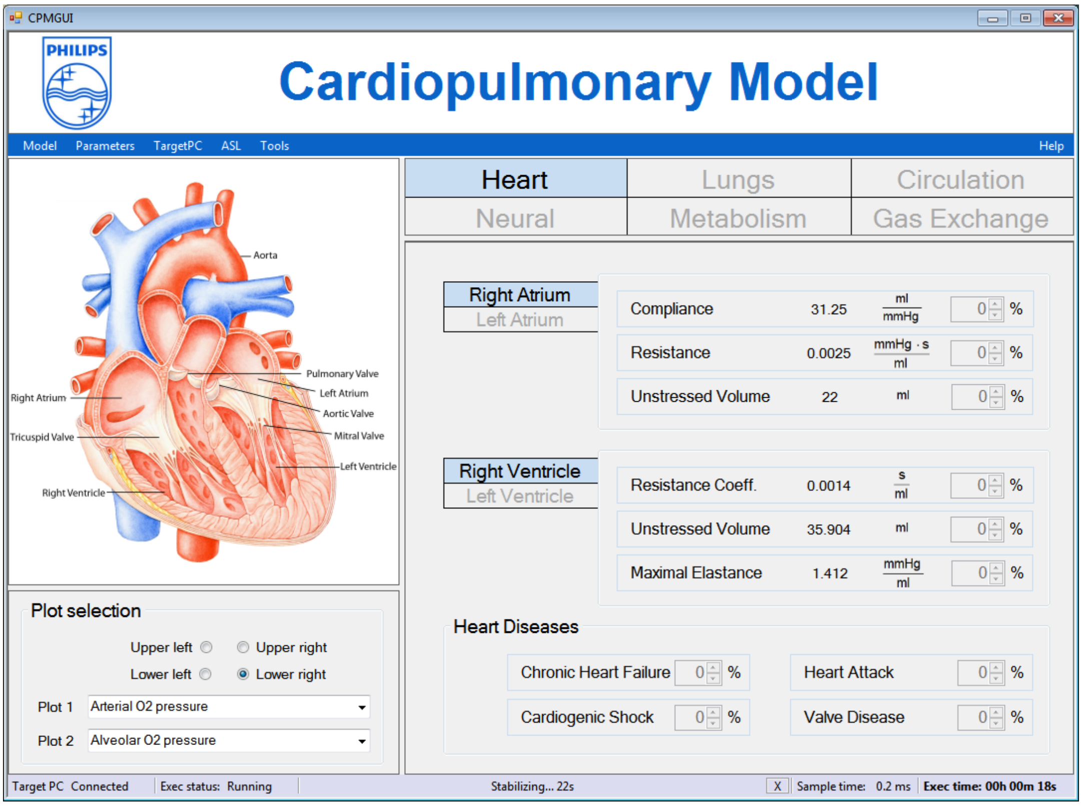

Right Atrium			
Compliance	31.25	ml/mmHg	0 %
Resistance	0.0025	mmHg · s/ml	0 %
Unstressed Volume	22	ml	0 %

Right Ventricle			
Resistance Coeff.	0.0014	s/ml	0 %
Unstressed Volume	35.904	ml	0 %
Maximal Elastance	1.412	mmHg/ml	0 %

Heart Diseases

Chronic Heart Failure	0 %	Heart Attack	0 %
Cardiogenic Shock	0 %	Valve Disease	0 %

Plot selection

Upper left ○ ○ Upper right
Lower left ○ ● Lower right

Plot 1 Arterial O2 pressure
Plot 2 Alveolar O2 pressure

Target PC Connected | Exec status: Running | Stabilizing... 22s | X | Sample time: 0.2 ms | Exec time: 0h 00m 18s

Figure 2.25 – GUI of the *CP Model*; courtesy of Roberto Buizza, Philips Research North America.

2.6 Model Validation

A critical aspect in physiological modeling is model validation, i.e. making sure that model's predictions match the behaviour of the physiological system that is object of the study. A typical approach in model validation is to compare the predictions of the model under specific conditions with those obtained in-vivo from a group of subjects representative of the class of patients that the model is trying to simulate. This process is very demanding and often unpractical because of the high variability of responses between different subjects and the need for specific experiments. Another possibility is to compare the model predictions with those previously obtained by similar mathematical models or with human or animl data available in the literature. In the following sections we will show how the *CP Model* has been validated under normal resting conditions, hypercapnia, hypoxia and isocapnic hypoxia, using data available in the literature. All the simulations shown in the subsequent sections have been obtained using the same set of parameter values reported in Table 2-2 – Table 2-9. The literature date used in the validation studies pertained to healthy 70 Kg subjects, hence further fine-tuning of the parameters was not needed. Notice that the choice to concentrate on these respiratory scenarios (hypoxia, hypercapnia and isocapnic hypoxia) is driven by the intended future applications of the model to mechanical ventilation.

2.6.1 Normal Resting Conditions

A reasonable reproduction of variables typically observed on a general healthy adult population is the basis for further applications of our integrated cardiopulmonary model. To verify the ability of the present model in these regards, we analyze the model's predicted outputs in normal resting conditions and we present a comparison with waveforms or average values typically observed in humans. Particularly, our analysis includes the model behavior both in terms of mean-values, i.e. averaged values over a respiratory or cardiac cycle, and intra-cycle (respiratory or cardiac cycle) values. In presenting the results, major emphasis is put on the new aspects of the model compared to previous work [5, 6].

Hemodynamics: Table 2-1 summarizes the static values of the relevant clinical hemodynamic variables that the *CP model* generates, and compares them with values typically measured on healthy humans in normal resting conditions [86, 49]. The table shows that the model predicted outputs are within normal physiological ranges of the general population.

Variable	Model Simulation	Normal Range
Arterial Pressure mmHg		
Mean	90.74	70-105 [86]
Systolic	122.79	90-140 [49]
Diastolic	78.86	60-90 [49]
Venae Cavae Pressure mmHg		
Systolic	3.79	2-14 [49]
Diastolic	2.72	0-8 [49]
Right Atrium Pressure mmHg		
Mean	0.7	2-6 [86]
Right Ventricle Pressure mmHg		
Systolic	24.45	15-28 [49]
Diastolic	-1.2	0-8 [49]
Pulmonary Artery Pressure mmHg		
Systolic	24.41	15-28 [49]
Diastolic	7.38	5-16 [49]
Left Atrium Pressure mmHg		
Mean	4	2-6 [86]
Left Ventricle Pressure mmHg		
Systolic	122.79	90-140 [49]
End-diastolic	0.2	4-12 [49]

Table 2-11- Static values of main hemodynamic variables

Figure 2.26 shows a representative simulated left ventricle P-V loop, along with the pressure and volume time profiles over an entire cardiac cycle. The model is thus able to capture the typical features of a realistic P-V loop, both in terms of shape and amplitude. For the specific cardiac cycle shown in the figure, the left ventricular volume ranged from 132 mL (end-diastolic volume) to 54 mL (end-systolic volume) providing a stroke volume of 78 mL and an ejection fraction of 78/132, or 59 %. Note that these values slightly change from one cardiac cycle to the next because of variations of intrapleural pressure and the effects of cardiovascular control mechanisms that induce cyclic changes in heart rate, ventricular contractility and afterload.

The simulated pressure profiles across the different compartments of the systemic and pulmonary circulation are shown in Figure 2.27. Again, model simulation have physiological correspondence in the sense that the model correctly predicts a progressive drop in the pressure levels and in the degree of pulsatility moving from the big arteries (systemic and pulmonary) towards the periphery.

Figure 2.28 compares model generated left and right ventricular output flows to experimental waveforms [30]. Both the amplitude and duration of the simulated flow waveforms match experimental data. The left ventricular flow has a higher peak value and shorter time duration compared with the right ventricular flow. For the specific cardiac cycle shown in the figure, the left ventricle peak flow is 688.5 mL/s and the right ventricle peak flow is 484.5 mL/s; the left ventricle ejection phase lasts for 0.192 s, whereas the right ventricle ejection phase lasts for 0.252 s. This is due to the greater contractility and higher afterload of the left ventricle, as compared to the right. Numerical integration of the flow waveforms over the entire cardiac cycle gives the values of left and right ventricular stroke volume as 78.6 mL and 82.9 mL, respectively. This proves that, despite the dissimilarities in amplitude and time duration, the area enclosed by the two waveforms are essentially the same, in agreement with physiology.

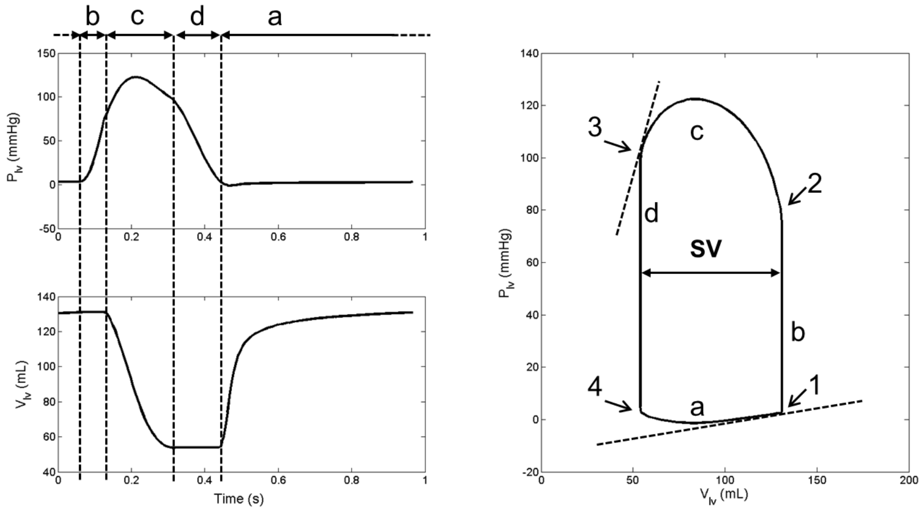

Figure 2.26- Left ventricle pressure and volume outputs. *Left*: time patterns of left ventricle pressure (top) and volume (bottom). Dotted lines mark the four cardiac phases: *a*, filling phase; *b*, isometric contraction phase; *c*, ejection phase; *d*, isometric relaxation phase. *Right*: pressure-volume loop of the left ventricle. The four cardiac phases (a, b, c and d) are shown along with the stroke volume SV and the opening and closing points of the heart valves: *1*, mitral valve closing point; *2*, aortic valve opening point; *3*, aortic valve closing point; *4*, mitral valve opening point. The two dotted lines tangent to the P-V loop at the point 1 and 3 represent the diastolic and the end-systolic pressure/volume functions, respectively.

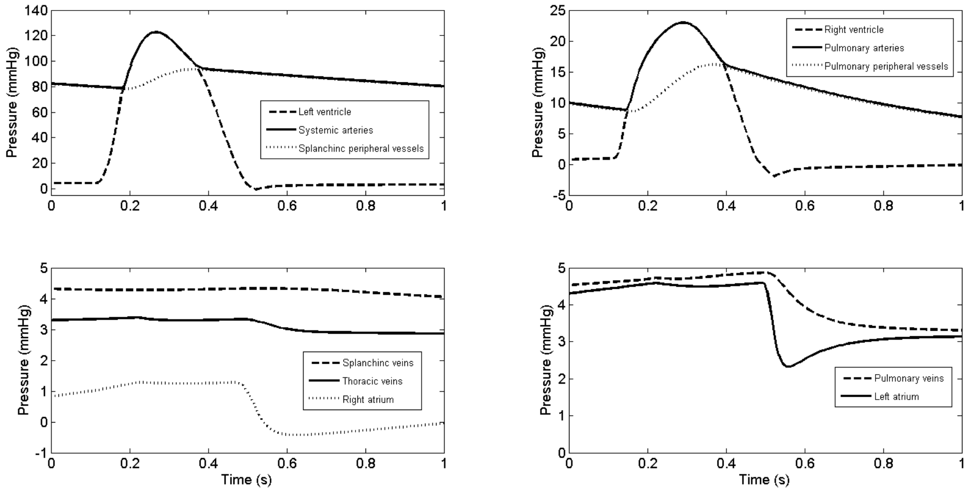

Figure 2.27 - Pressure waveforms at different levels of the circulatory system.*Top Left*: time patterns of left ventricle pressure, systemic arterial pressure and systemic splanchnic peripheral vessels pressure. *Bottom Left*: time patterns of systemic pressure in the splanchnic venous compartment, thoracic veins pressure and right atrium pressure. *Top Right*: time patterns of right ventricle pressure, pulmonary arterial pressure and pulmonary peripheral vessels pressure. *Bottom Right*: time patterns of pulmonary veins pressure and left atrium pressure.

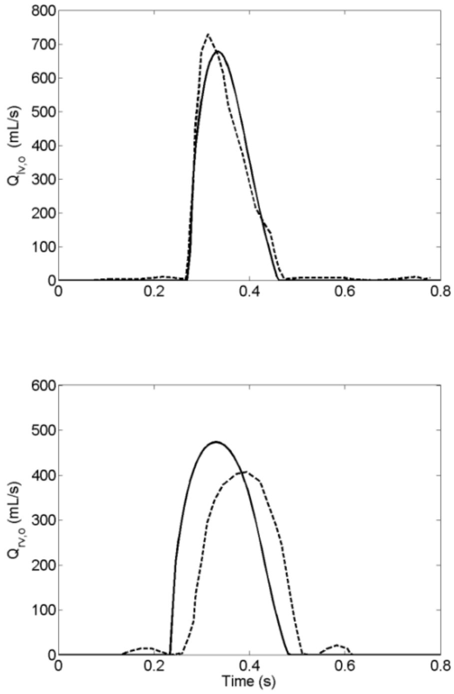

Figure 2.28 - Model-predicted flows (continuous line) compared with reported experimental data (dashed line). *Top*: left ventricle output flow ($Q_{lv,o}$). *Bottom*: right ventricle output flow ($Q_{rv,o}$). The experimental data have been redrawn from Fig. 7 of [30].

Respiratory Mechanics: Figure 2.29 shows the pressure and flow waveforms generated by the lung mechanics model in normal resting conditions, when the chemoreceptors are silent and RR and $P_{mus,\min}$ are equal to their basal values. At the beginning of inspiration, alveolar pressure equals atmospheric pressure, i.e. zero pressure. During inspiration, the negative P_{mus} drives pleural pressure to decrease from its resting value of -5 $\mathrm{cmH_2O}$ to about -8 $\mathrm{cmH_2O}$, which in turn decreases alveolar pressure below atmospheric value and allows air to flow into the mouth, trachea, bronchea and alveoli. At the end of inspiration, when the respiratory muscles start relaxing, pleural pressure returns to its baseline value and alveolar pressure becomes slightly positive allowing air to flow out of the lung. The tidal volume produced by the model is approximately 540 mL, 40 mL of which are spent in expanding the dead space and the remaining flowing into the alveoli to participate to gas exchange (see Figure 2.29).

This is in agreement with normal physiological behavior under quiet breathing conditions [70]. Furthermore, both the model generated air flow and pleural pressure waveforms resemble in-vivo measurements that are typically obtained from humans or animals, as shown in Figure 2.30 and Figure 2.31. Particularly, the inspiratory flow pattern has the typical dome shape that has been reported in literature [87], with the rise being slightly more abrupt than the fall and the peak flow being reached early in the inspiratory part of the cycle, whereas the expiratory flow is less symmetrical and tends to approach zero slowly (see Figure 2.30).

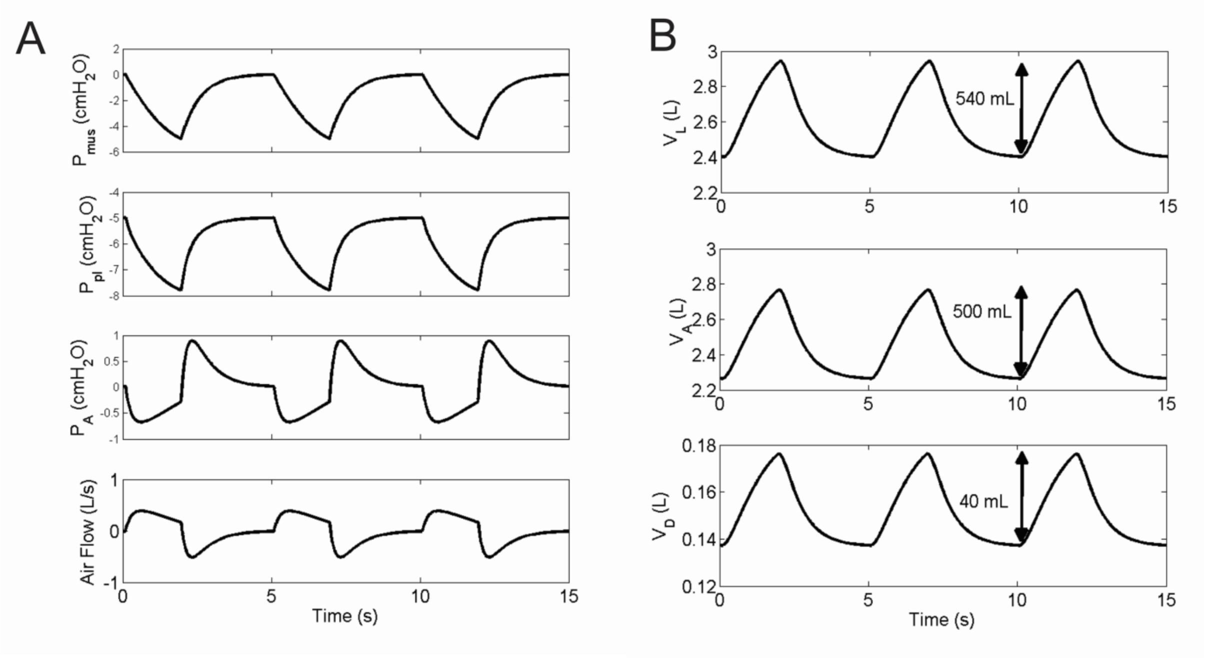

Figure 2.29 – Pressure, volume and flow waveforms generated by the lung mechanics model. (A) From top to bottom: Respiratory muscle pressure (P_{mus}), pleural pressure (P_{pl}), alveolar pressure (P_A), and air flow. (B) From top to bottom: Lung volume (V_L), alveolar volume (V_A) and dead space volume (V_D).

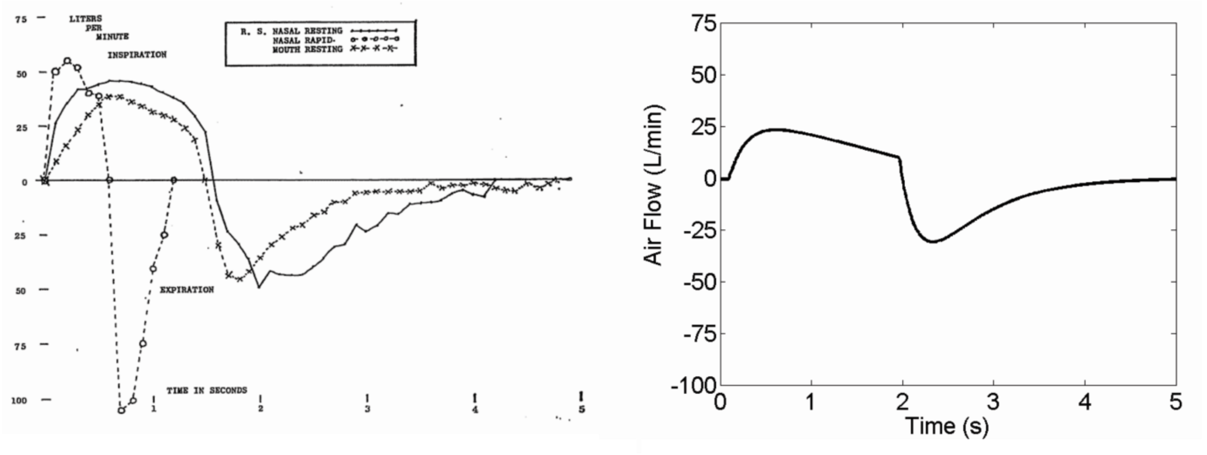

Figure 2.30 – Comparison between simulated and experimental airflow waveforms. Left figure: pneumotachogram from a normal subject showing patterns of flow in nasal (both quiet and rapid) and mouth breathing; reproduced from [87]. Right figure: model generated airflow. Note that the scales of the two figures have been adjusted to allow visual comparison.

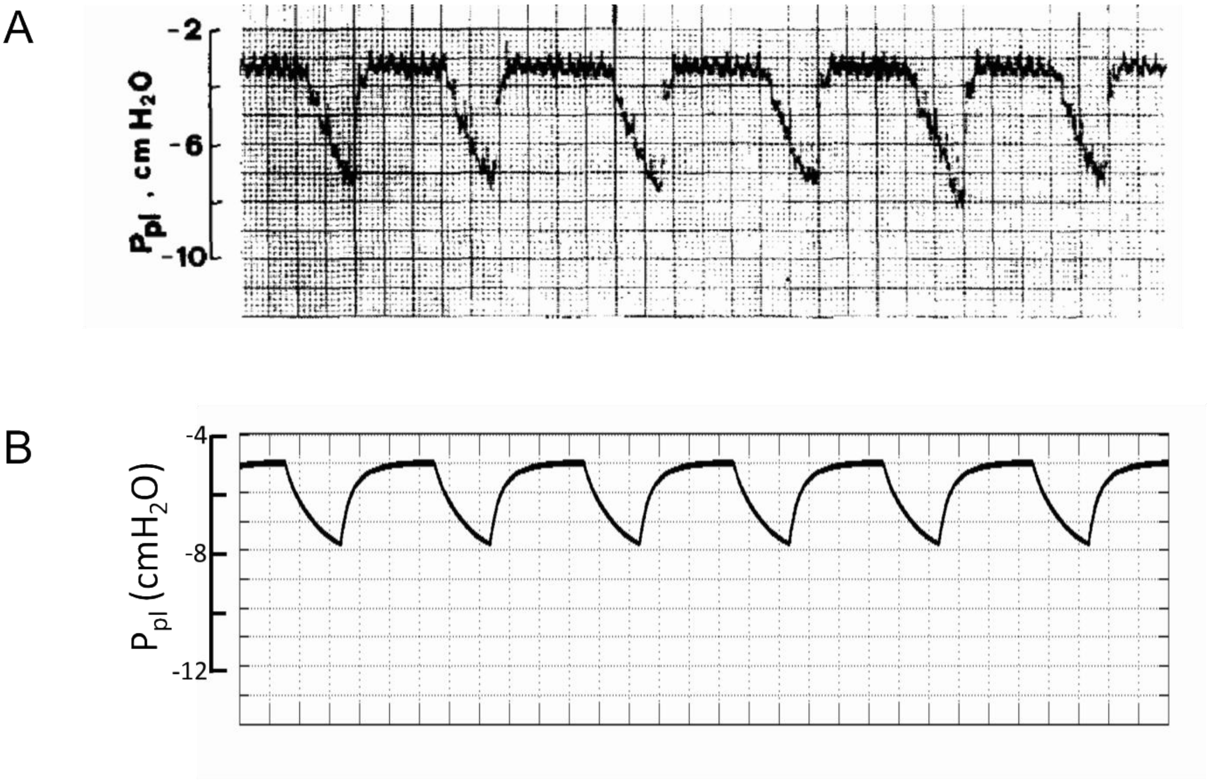

Figure 2.31 – Comparison between simulated and experimental pleural pressure waveforms. (A) Tracing of pleural pressure from a dog in supine position during spontaneous breathing; reproduced from [88]. (B) Model generated pleural pressure waveform. Note that the time division in both figures is 1 sec and the scales of the two figures have been adjusted to allow visual comparison.

__Gas Exchange and Transport__: The main outputs of the gas exchange and transport model are summarized in Table 2-12 in terms of their mean values over one respiratory cycle and compared with typical values in resting healthy humans [86, 89, 90]. Furthermore, in Figure 2.32 - Figure 2.36, the time profiles of partial pressures at different levels throughout the cardiopulmonary system are shown.

Figure 2.32 shows the variation of arterial O_2 and CO_2 partial pressures, along with the lung volume waveform. Arterial P_{O2} and P_{CO2} are relatively constant and oscillate around their mean values, 98.9 and 39.55 mmHg respectively (see Table 2-12), in synchrony with the respiratory cycle. Arterial P_{O2} varies from 96.93 to 100.8 mmHg, it increases during inhalation and decreases during exhalation. The opposite is valid for P_{aCO2}, which oscillates between 37.89 and 41.06 mmHg. The mean values of the simulated P_{aO2} and P_{aCO2} waveforms are in agreement with the values typically observed in healthy humans from arterial blood gas analysis (ABG test) during normal resting conditions (see Table 2-12). Comparison of model generated P_{aO2} and P_{aCO2} fluctuations with corresponding human data is more difficult to obtain due to the lack of continuous P_{aO2} and P_{aCO2} measurements available in the literature. However, P_{aO2} fluctuations of $\pm$ 1-4 mmHg in synchrony with the respiratory cycle and in the same direction as those generated by the model have been reported in animal studies performed on cats and lambs. Furthermore, the magnitudes of the model generated fluctuations agree with those reported in previous simulation studies [91, 92]. It is worth noticing that cardiogenic oscillations are present in the simulated P_{aO2} and P_{aCO2} profiles, a phenomenon that has been reported by previous investigators as well [91, 53]. This is essentially due to the coupling between the tidal respiratory model and the pulsatile cardiovascular model, which is an essential feature of our integrative modeling approach.

Figure 2.33 shows the variations of blood gas composition in the venous section in terms of partial pressure. Again, similarly to what observed in the arterial P_{O2} and P_{CO2} waveforms, the variations of P_{vO2} and P_{vCO2} are affected by the respiratory cycle events, but the effects of blood pulsatility are less evident due to the filtering introduced by the venous circulation. The mean values of P_{vO2} and P_{vCO2} are also in the typical ranges observed in normal resting subjects (see Table 2-12).

Figure 2.34 shows the variation in lung gas composition, distinguishing between alveolar and dead space region, and compare the model generated outputs with those generated by the model of Lu *et al*. [30] described in section. Notice that in this model, gas exchange was described using a 35-segment pulmonary capillaries compartment. The agreement between the present model and the model of Lu *et al*. is remarkable and proves that, despite the decreased level of complexity of the present model in terms of gas exchange, the two models are comparable at least for what concerns the respiratory gas variables in normal resting conditions. Furthermore, by comparing the alveolar and dead space P_{O2} and P_{CO2} profiles, we can observe how the cardiogenic oscillations are so pronounced in the alveolar partial pressure curves whereas are lost in the comparatively large variations characterizing the dead space partial pressure profiles.

Figure 2.35 proves that the intrabreath alveola P_{O2} and P_{CO2} dynamics predicted by the model agree quite well with the expected behaviour reported in the literature and shown in several textbook figures [90, 53]. During the very first beginning of the inspiratory phase, alveolar P_{CO2} rises to a maximum and P_{O2} drops to a minimum; this represents the period during which dead space air is entering the alveoli. This is followed by a period of rapidly increasing P_{O2} and falling P_{CO2}, which reflects the effects of the introduction of fresh inspired air into the alveoli. The maximum P_{O2} and minimum P_{CO2} are reached toward the end of the inspiratory phase, when maximum dilution with fresh air has been achieved. During the expiratory phase, the partial pressures variations change direction, with P_{O2} progressively falling and P_{CO2} progressively rising. This reflects the effects of continued gas exchange during a period when no fresh air is supplied to the alveoli.

Finally, Figure 2.36 shows a comparison between the model generated dead space P_{CO2} and a typical time-based capnographic waveform [93] obtained in normal adult patients over a single respiratory cycle. The simulated dead space P_{CO2} resembles the capnogram in terms of both shapes and amplitude, even though some minor differences can be observed. First, the baseline in the simulated dead space P_{CO2} tracing is slightly above zero (see Table 2-12), whereas the normal capnogram has a zero baseline value. Second, during the inhalation phase the capnographic waveform suddenly reaches the zero baseline value and remains flat until early exhalation; this is not the case for the simulated dead space P_{CO2} waveform. These differences, however, can be explained considering the fact that the capnographic waveform is obtained by sampling the air flow at the mouth, whereas the simulated P_{CO2} waveform is representative of a lumped dead space compartment which is anyway in between the atmospheric air and the internal alveolar compartment.

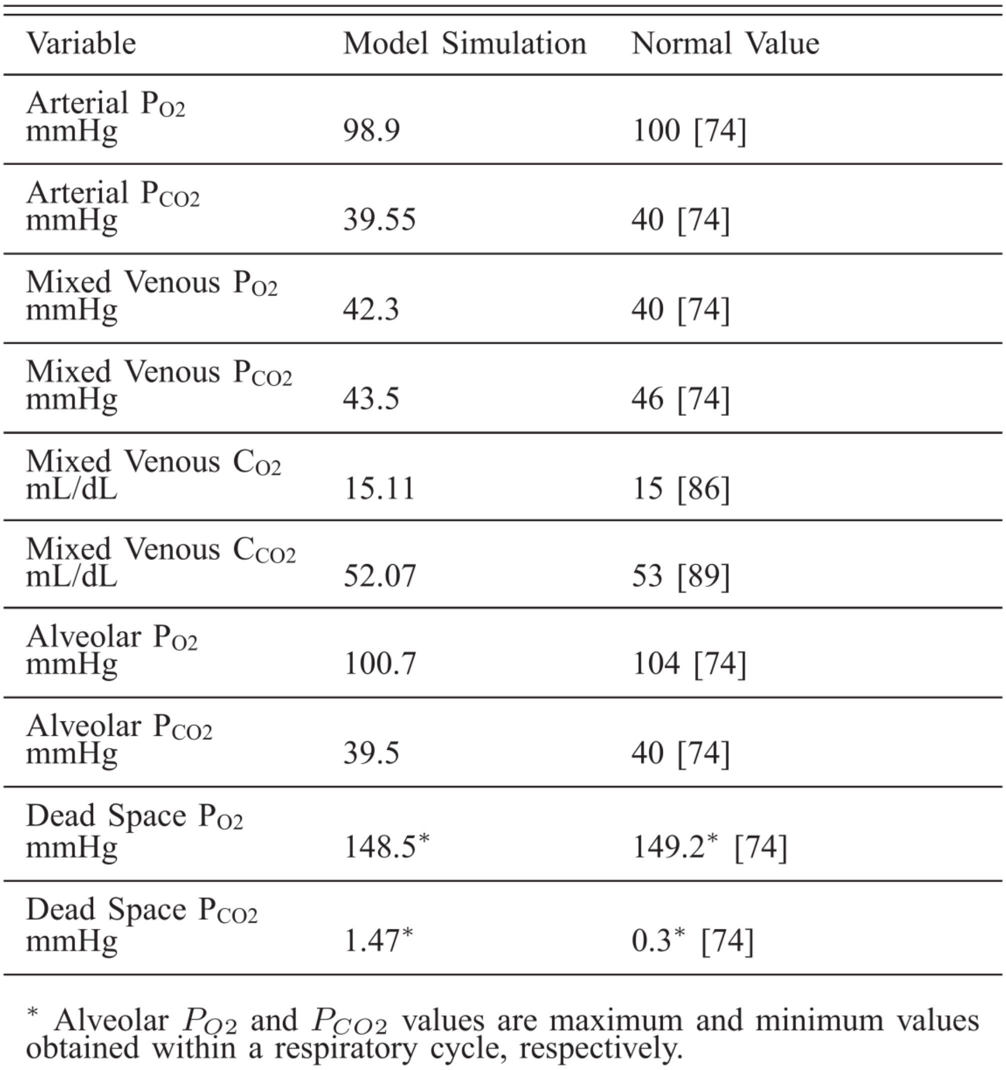

Variable	Model Simulation	Normal Value
Arterial P_{O2} mmHg	98.9	100 [74]
Arterial P_{CO2} mmHg	39.55	40 [74]
Mixed Venous P_{O2} mmHg	42.3	40 [74]
Mixed Venous P_{CO2} mmHg	43.5	46 [74]
Mixed Venous C_{O2} mL/dL	15.11	15 [86]
Mixed Venous C_{CO2} mL/dL	52.07	53 [89]
Alveolar P_{O2} mmHg	100.7	104 [74]
Alveolar P_{CO2} mmHg	39.5	40 [74]
Dead Space P_{O2} mmHg	148.5*	149.2* [74]
Dead Space P_{CO2} mmHg	1.47*	0.3* [74]

* Alveolar P_{O2} and P_{CO2} values are maximum and minimum values obtained within a respiratory cycle, respectively.

Table 2-12 – Mean values of the main gas composition variables.

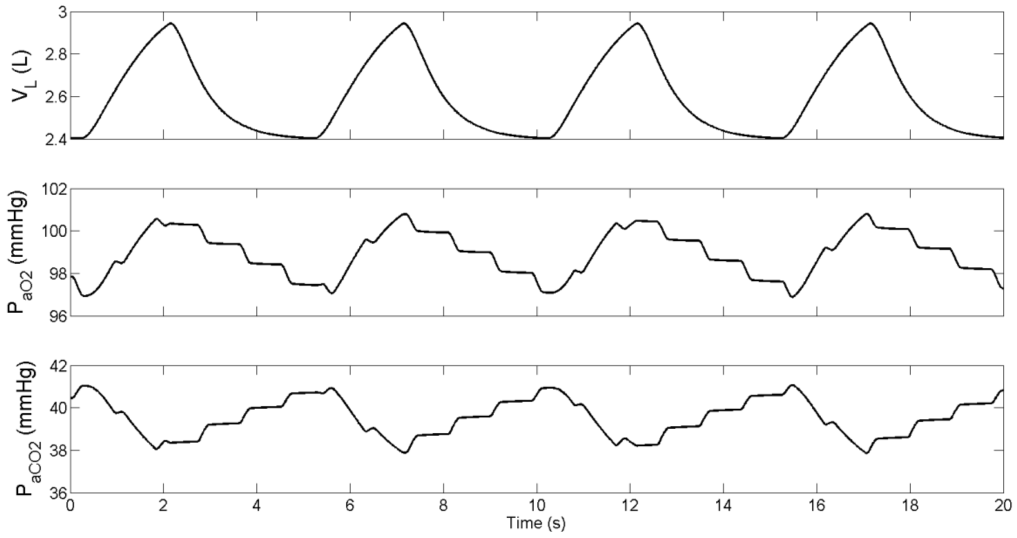

Figure 2.32 – Time profiles of model generated arterial O_2 and CO_2 partial pressures. From top to bottom: total lung volume (V_L), partial pressure of oxygen in the arterial blood (P_{aO2}) and partial pressure of carbon dioxide in the arterial blood (P_{aCO2}).

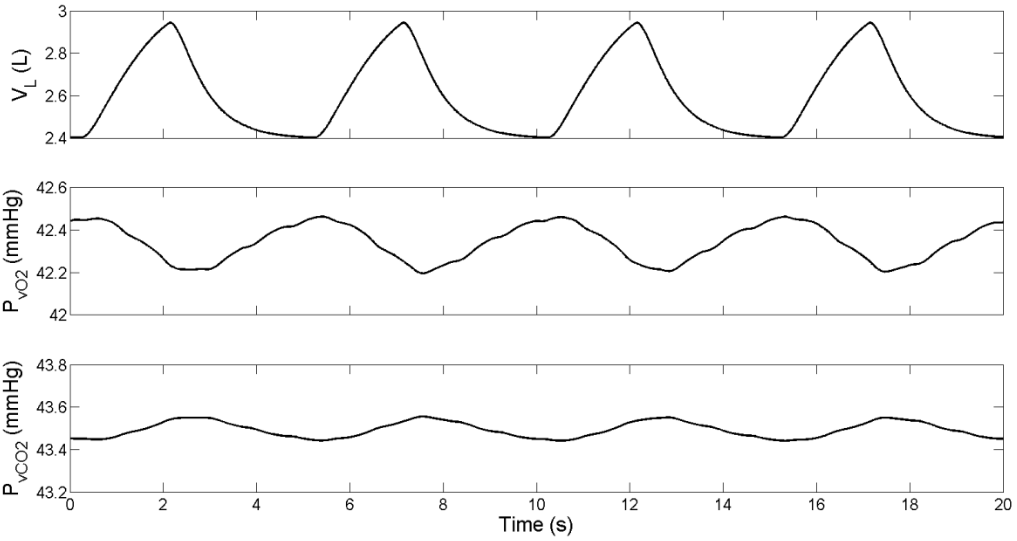

Figure 2.33 – Time profiles of model generated mixed venous O_2 and CO_2 partial pressures. From top to bottom: total lung volume (V_L), partial pressure of oxygen in the mixed venous blood (P_{vO2}) and partial pressure of carbon dioxide in the mixed venous blood (P_{vCO2}).

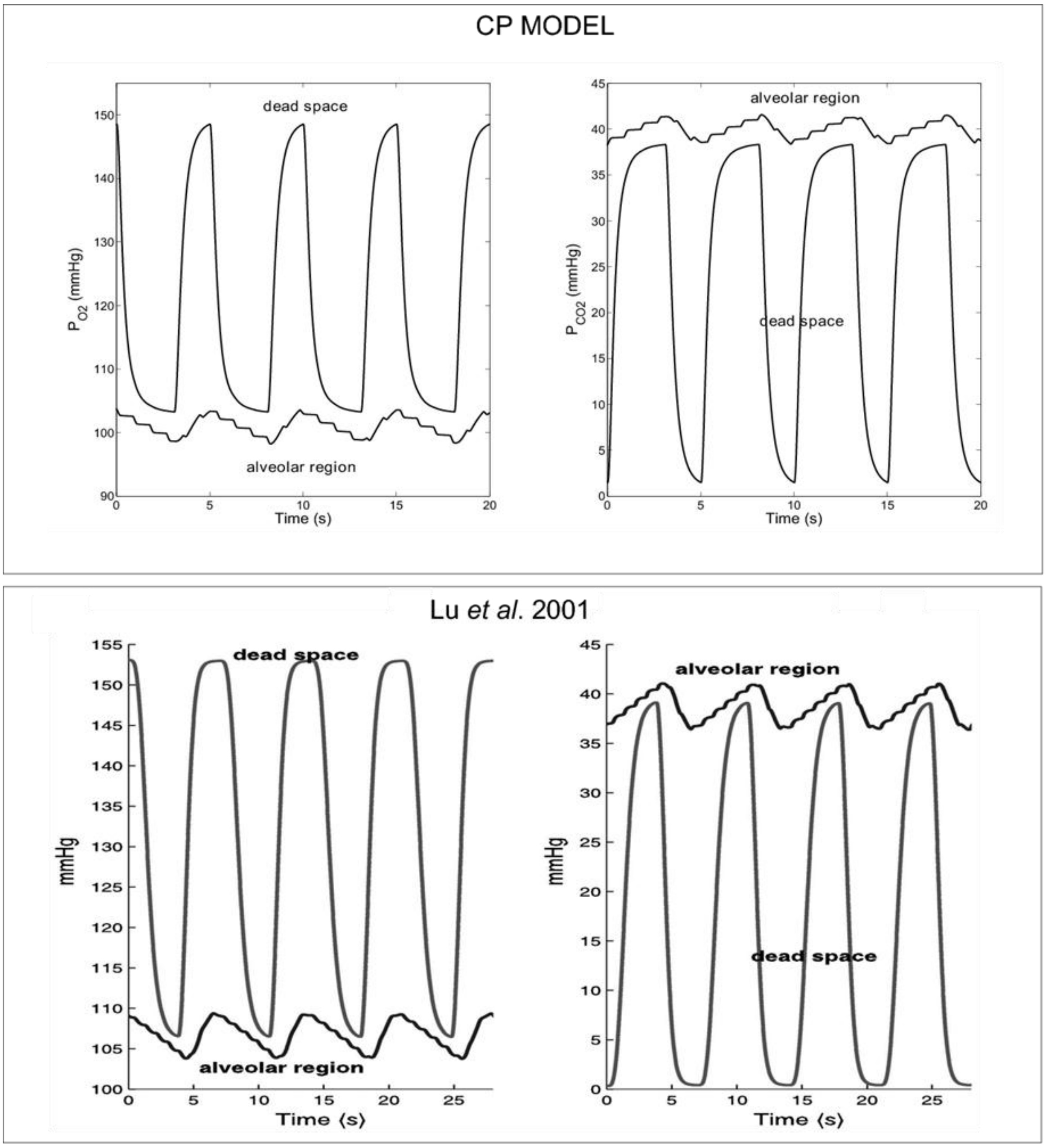

Figure 2.34 – Time profiles of O_2 and CO_2 partial pressures in the dead space and alveolar region. *Top figure*: CP Model outputs; *Bottom figure*: Lu *et al*. [30] model outputs.

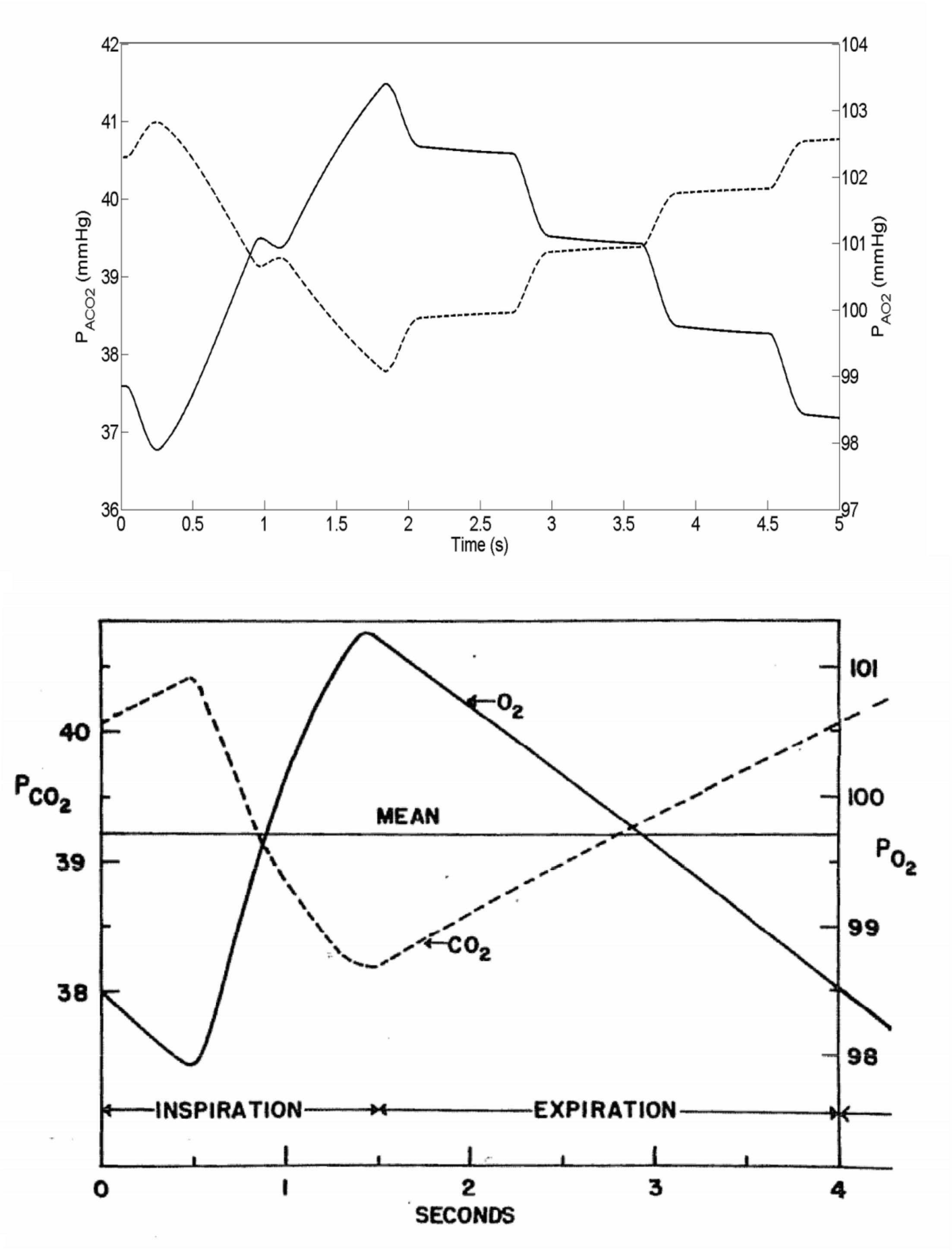

Figure 2.35 – Time profiles of O_2 and CO_2 partial pressures in the alveolar space during a respiratory cycle. *Top figure*: model simulations; *Bottom figure*: expected behaviour from literature [90, 53].

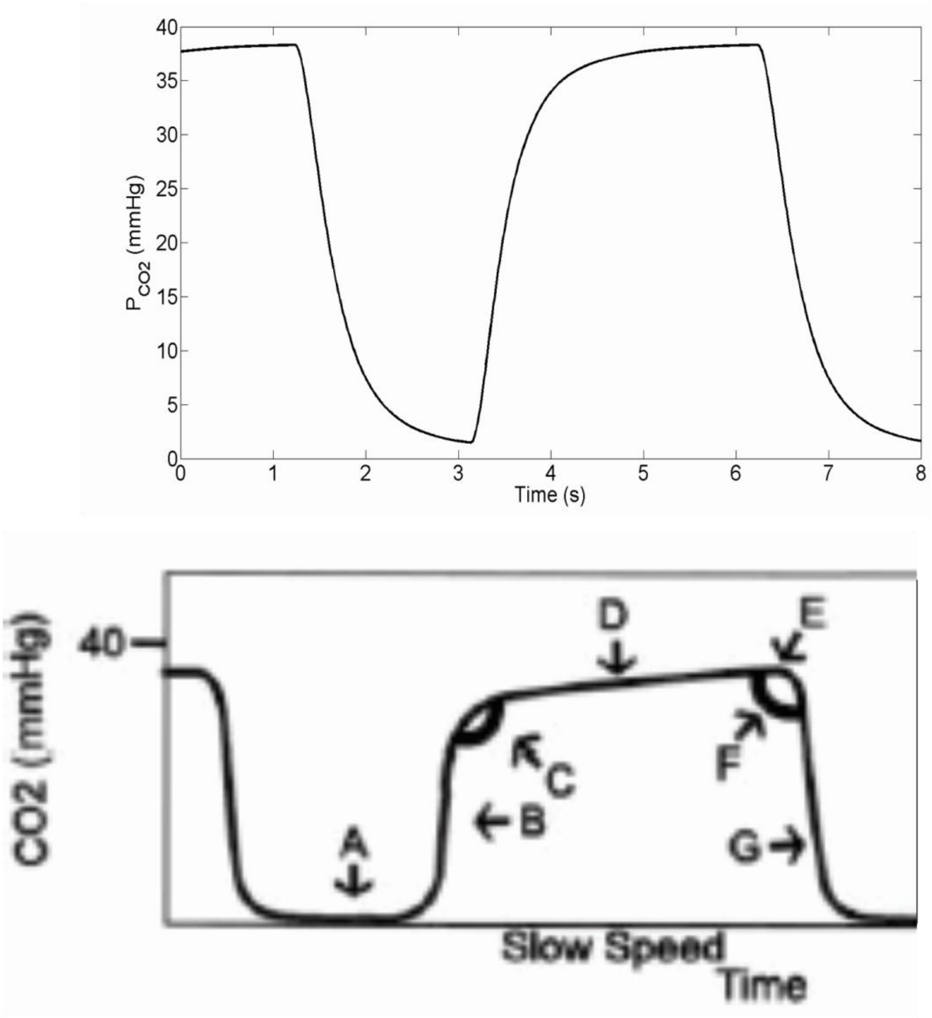

Figure 2.36 – Comparison between model generated CO_2 partial pressures in the dead space (*Top figure*) and a representative normal time-based capnogram (*Bottom figure*) [93].

Heart-lung interactions: As mentioned in the *Introduction* section, heart-lung interactions take a variety of forms. Mechanical interactions are one of these forms and are mainly due to the effects of intrathoracic pressure on venous return and cardiac function. During inhalation, venous return (VR) increases due to the decreasing intrapleural pressure that produces a shift in blood volume from the systemic to the pulmonary circulation. The variations in VR are associated with variations in cardiac performance: the increased VR during inhalation improves right ventricular filling and preload, thus generating an increase in right ventricular output flow and stroke volume according to the Frank-Starling mechanism. The effects of inspiration on the left ventricle are in the opposite direction: the decreasing intrapleural pressure affects the pulmonary vasculature, which acts as a capacitance reservoir that holds more blood so that left ventricular filling is reduced with the consequent drop in left ventricular output flow and stroke volume via the Frank-Starling mechanism. The situation is reversed during expiration, when intrapleural pressure gradually returns to baseline. In this case, VR and right ventricular output flow are reduced, whereas more blood is forced from the pulmonary vasculature into the left heart and hence left ventricular output flow is increased. The variations of intrathoracic pressure associated with the respiratory events have also effects on systemic arterial pressure. Systolic, diastolic and pulse arterial pressures are lowest during inspiration and highest at the peak of expiration. These variations result in part from transmission of intrathoracic pressure to the ascending and thoracic aorta, and in part from the respiratory-related changes in left ventricular output flow [94], discussed above. The inspiratory drop in systemic arterial pressure has also been ascribed to a delay in transmission through the pulmonary vascular bed due to the fall in right ventricular output flow which accompanies expiration. Reductions in systolic blood pressure during inhalation of about 4-5 mmHg have been reported in the literature [94] and variations of more than 5 mmHg are considered signs of pathological conditions and are commonly referred to as "pulsus paradoxus" [95].

The present model is able to account for such mechanical interactions between heart and lungs, thanks to the inclusion of the intrapleural pressure as the reference external pressure for the vascular compartments that lie within the thoracic cavity (see *The Uncontrolled Cardiovascular System Model* section). Figure 2.37 shows the simulated time profiles of venous return (computed in the model as the instantaneous flow entering the right atrium), left and right ventricular output flow and stroke volume, along with the pleural pressure waveform over few representative respiratory cycles. The model predicted hemodynamic changes driven by the respiratory events are indeed qualitatively in agreement with the physiological mechanisms above described: venous return and right ventricular stroke volume rise during inspiration and fall during exhalation, whereas left ventricular stroke volume variations have opposite direction. The model predicts an inspiratory rise in right ventricular stroke volume of about 7 mL, which agrees well with the expected variations in normal condition (5 mL according to [94]). On the other hand, the model predicted changes in left ventricular stroke volume are slightly underestimated: 1.16 mL inspiratory fall with respect to the end-exhalation value, only. This may be due to the fact that the present model does not account for ventricular interdependence via the septum, which may play an important role in explaining the reduced left ventricular stroke volume during inhalation. The left and right ventricles, in fact, share a common pericardial space and are separated by a mobile intraventricular septum. When the right ventricular diastolic volume increases during inhalation, the septum tends to shift to the left, reducing left ventricular compliance and causing a further reduction in stroke volume [96].

The effects of respiration are visible in the systemic arterial blood pressure waveform (P_{sa}) as well, as shown in Figure 2.38 where the systolic and diastolic P_{sa} values are plotted together with the pleural pressure waveform over a few consecutive respiratory cycles. The model predicted changes in systolic and diastolic blood pressure are qualitatevily in agreement with the expected behaviour: systolic and diastolic blood pressure drop during inhalation and rise during exhalation. However, even in this case, the magnitude of the model predicted variations is smaller than what is typically observed in normal subjects: 0.6 mmHg model predicted reduction in systolic blood pressure, corresponding to about 0.5% of the end-exhalation value, as compared to 4 mmHg and 3% variation in normal subjects [94]. The reason for this discrepancy can partially be attributed to the underestimated inspiratory fall in left ventricular output flow, and hence to the unmodeled ventricular septum dynamics, but also to the fact that the lumped systemic arterial compartment in the model is not subject to intrapleural pressure, whereas in reality the ascending and the thoracic aorta are within the thoracic cavity and hence are directly affected by intrapleural pressure variations. This aspect, together with the inclusion of the intraventricular septum, might be the object of further expansion of the model.

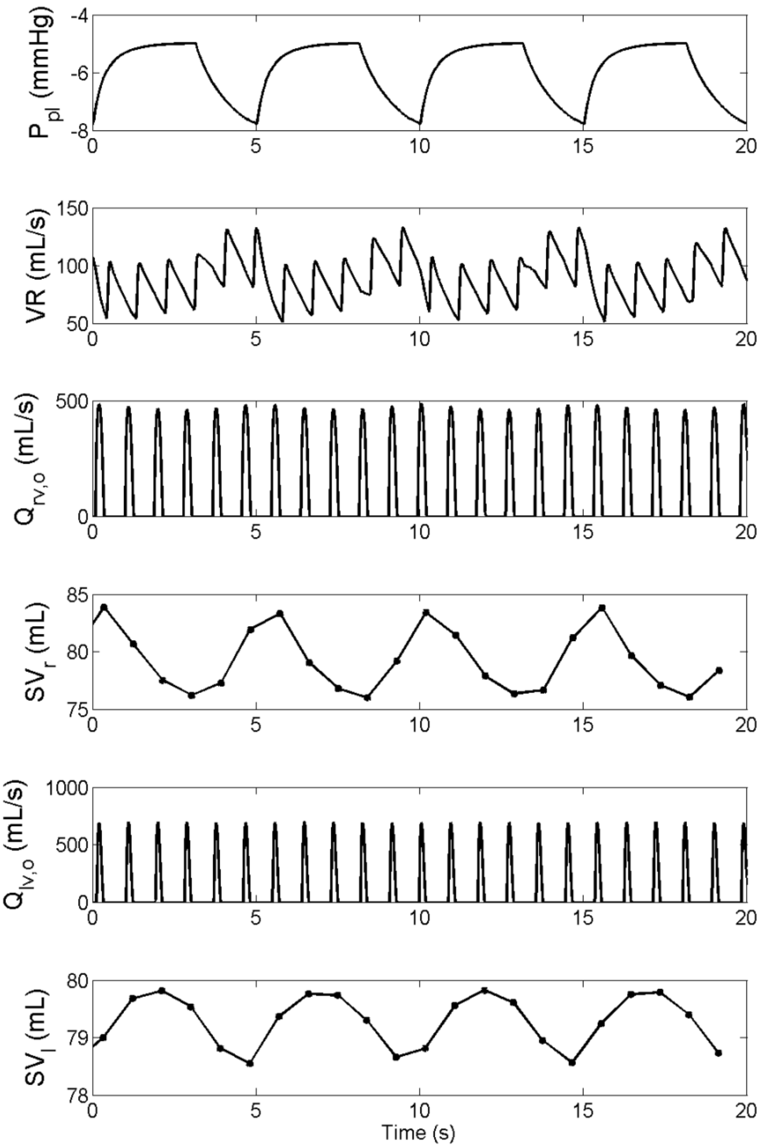

Figure 2.37 - Mechanical effects of respiration on cardiovascular function. From top to bottom: time profiles of intrapleural pressure (P_{pl}), venous return (VR), right ventricular output flow ($Q_{rv,o}$), right ventricular stroke volume (SV_r), left ventricular output flow ($Q_{lv,o}$) and left ventricular stroke volume (SV_l).

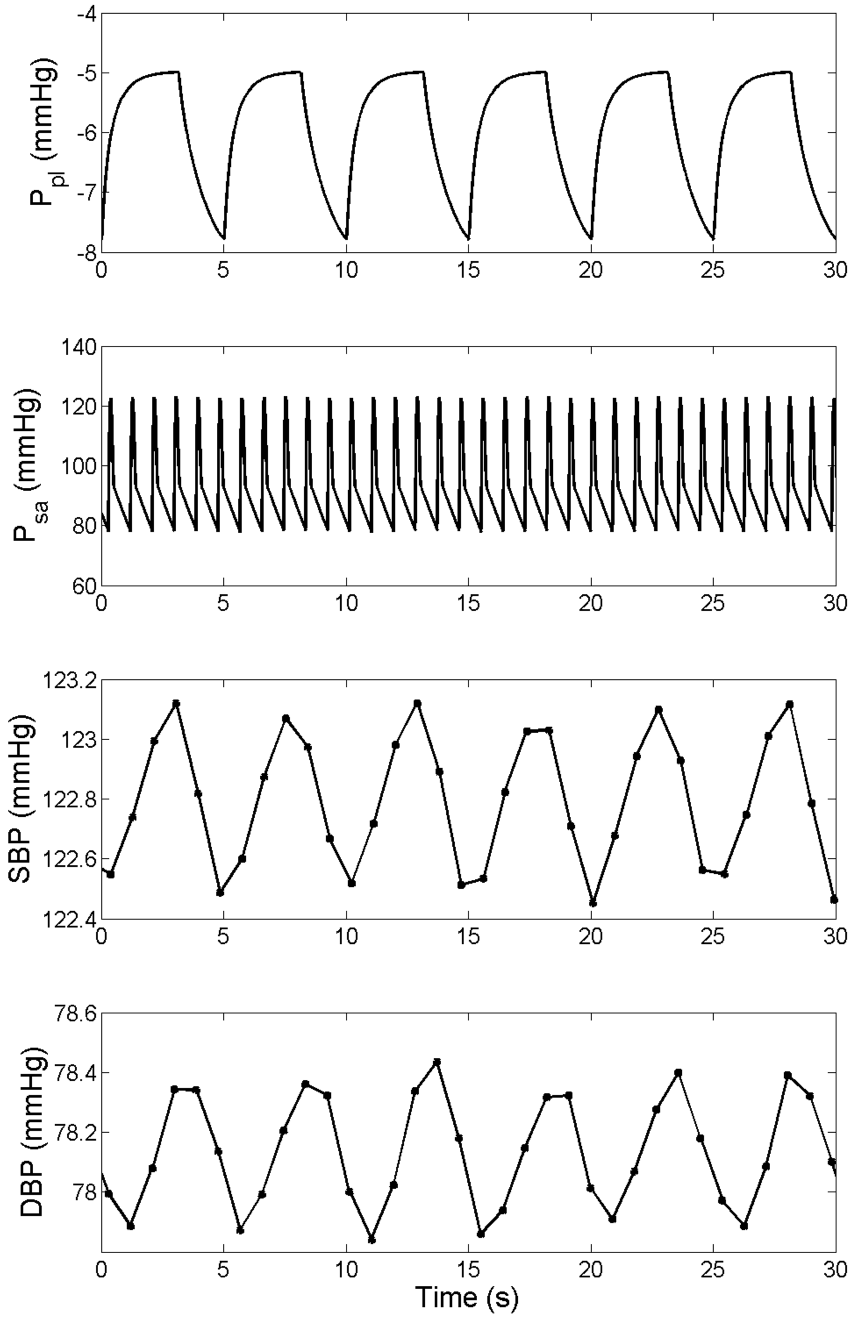

Figure 2.38 - Mechanical effects of respiration on systemic arterial pressure. From top to bottom: time profiles of intrapleural pressure (P_{pl}), systemic arterial pressure (P_{sa}), systolic blood pressure (SBP) and diastolic blood pressure (DBP).

2.6.2 Hypercapnia

To validate the *CP model* response to CO_2 blood content perturbations, hypercapnic conditions were simulated and model predictions, in terms of respiratory, gas exchange and cardiovascular variables, were compared against published human data. Simulations were performed with the cardiopulmonary model in closed-loop configuration and using the inspired gas concentrations $FiCO_2$ and FiO_2 as input. Step inputs of various amplitudes were applied to $FiCO_2$, whereas FiO_2 was kept fixed to its normal room ambient value of 21% (see Table 2-6).

Figure 2.39 shows both the model predicted and experimental responses to a 25 minutes 7% CO_2 step input in terms of alveolar gas partial pressures (P_AO_2 and P_ACO_2), tidal volume (V_T), minute ventilation (V_e) and respiratory frequency (RR). The experimental data have been obtained from a group of 15 healthy subjects [84] and represent average values across subjects. Model predictions agree quite well with the experimental results both in the steady-state and transient phases for all the variables under study. The most significant level of discrepancy is represented by the pronounced undershoot in the simulated P_ACO_2 waveform. This discrepancy, however, could be justified by taking into account the averaging of the experimental data. The authors actually reported that the averaging of data over a number of subjects tended to smear the undershoot in P_ACO_2 and that natural oscillations in partial pressures were observed in individual subjects. The results prove that the model is able to explain the ventilatory increase triggered by the hypercapnic stimulus: at the onset of the stimulus, P_ACO_2 increases due to $FiCO_2$ increase; hence, tidal volume and respiratory rate increase due to activation of the central chemoreceptors, thus, in turn, increasing minute ventilation; the increase in minute ventilation generate a concomitant increase in P_AO_2; at the removal of the stimulus, all the variables return to baseline values after a short transient phase. Note that in hypercapnic conditions, since PaO_2 is above its target value, ventilation is driven by the isolated action of the central chemoreceptors (see 2.3.5 *The Respiratory Control Model* section). Hence, by validating the model under hypercapnic conditions we are implicitely validating the central chemoreceptors model.

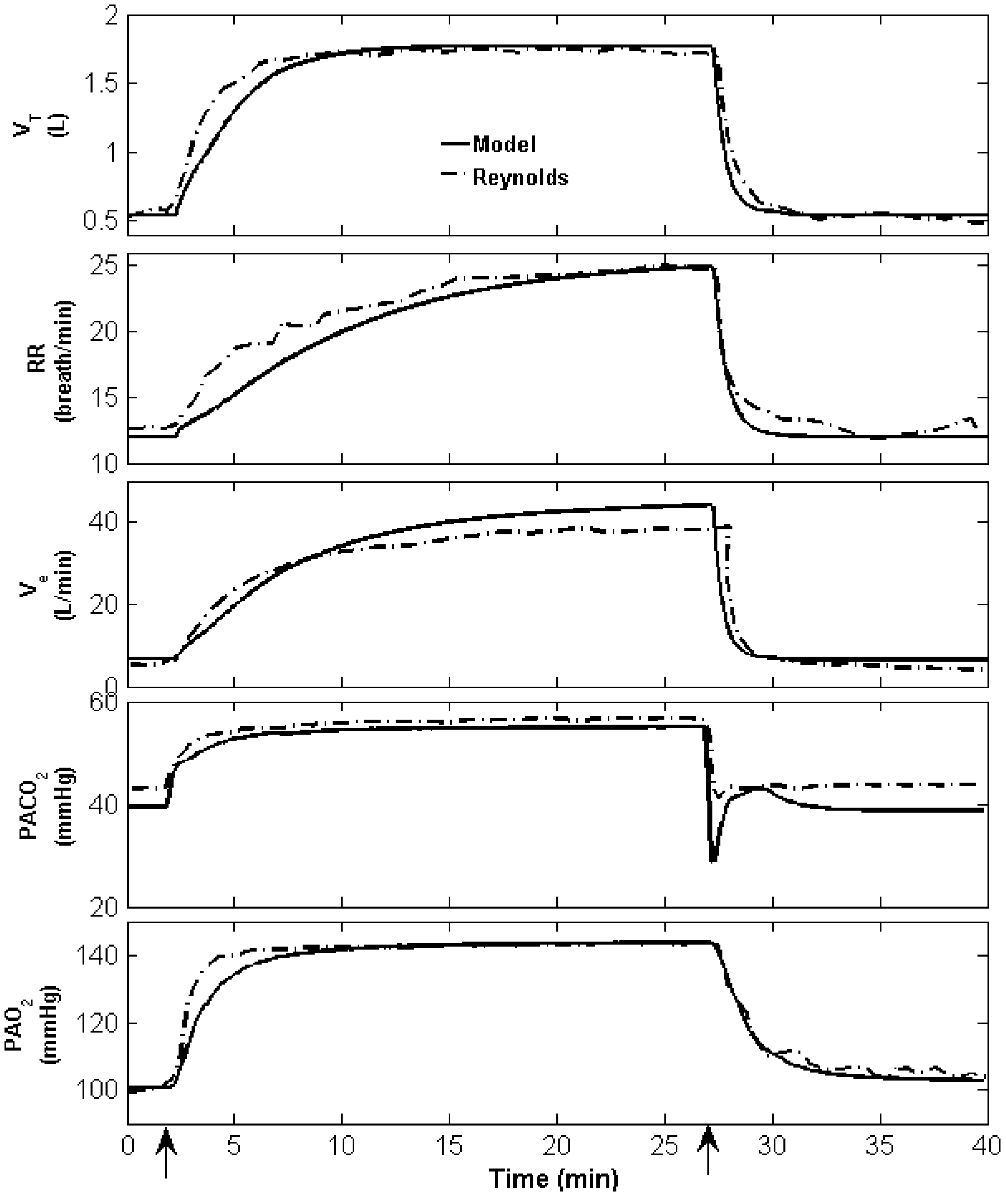

Figure 2.39 - Respiratory response to a 7% CO_2 step input performed at 2 min and lasting 25 min. Continuous lines are model results; dashed lines are experimental data redrawn from [84]. Experimental data are means over 15 subjects. Figure courtesy of Limei Cheng, Philips Research North America

Figure 2.40 shows that the model responses to different CO_2 stimulus intenisty levels, ranging from 3% to 7%, were also compared with the experimental results from the same study in terms of respirate rate, tidal volume and minute ventilation. For the 3%, 5%, and 6% hypercapnic cases, experimental data are means over 10 subjects. Again, the agreement between model predictions and experimental data is quite remarkable. This proves that the model is able to correctly reproduce the physiological response to a wide range of $FiCO_2$ values, in terms of respiratory and gas variables, with a single set of unchanged parameters.

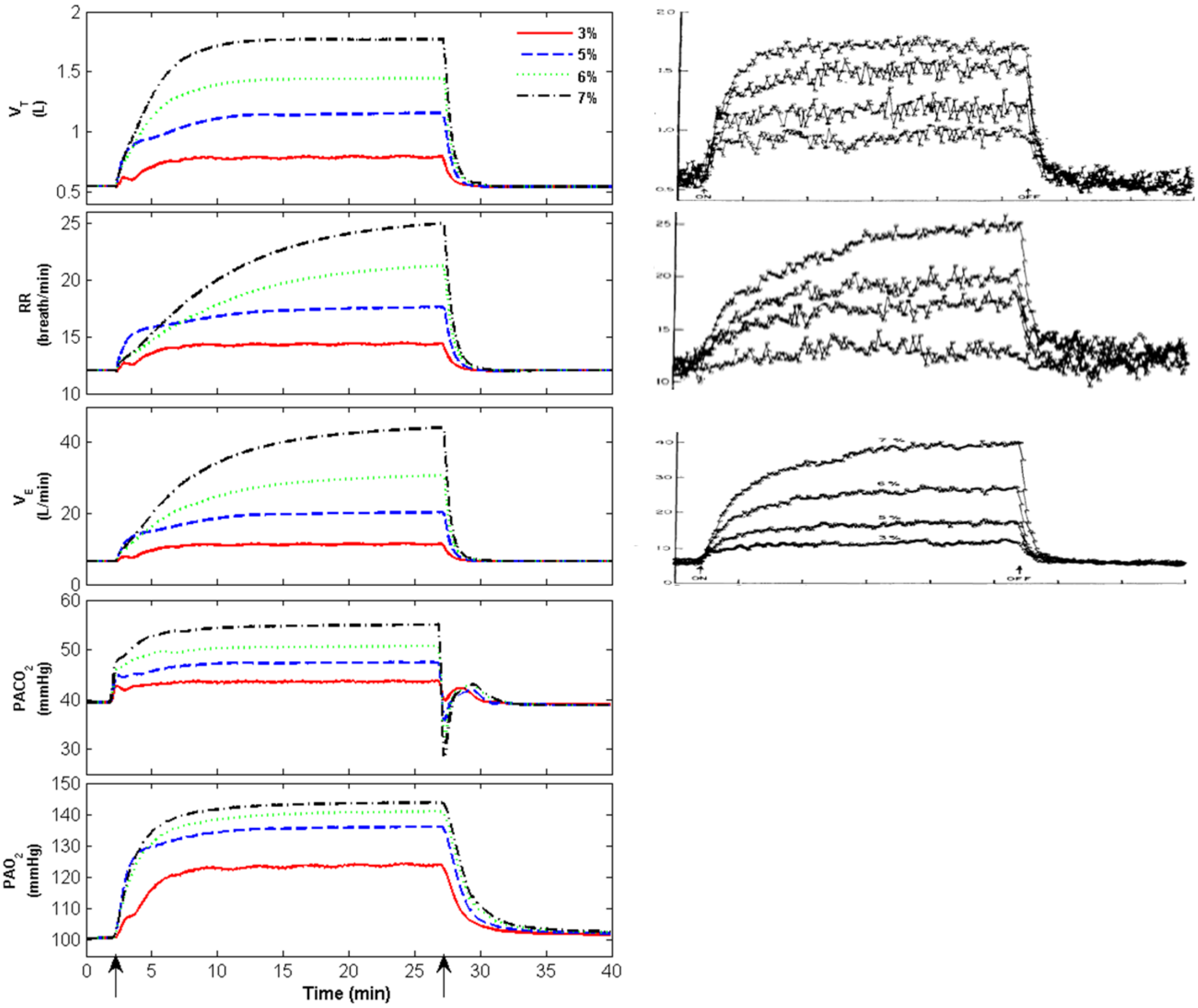

Figure 2.40- Respiratory response to 3, 5, 6 and 7% CO_2 step input performed at 2 min and lasting 25 min. Left: model simulations; Right: experimental data from [84]. Experimental data represent means over 10 subjects except for 7% which are means of 14 subjects. Figure courtesy of Limei Cheng, Philips Research North America

Finally, Figure 2.41 shows the model response to 7% and 8% hypercapnic step inputs in terms of the main cardiovascular variables: heart rate (HR), cardiac output (CO), total peripheral resistance (TPR), mean arterial pressure (MAP), systolic blood pressure (SBP) and diastolic blood pressure (DBP). Comparison against experimental data during the transient phase was not performed due to a lack of available literature data. Nevertheless, the model predicts a steady-state increase in all the variables except for TPR, which shows almost no steady state variations. This behavior is in agreement with experimental observations, as summarized in Table 2-13 where the model predicted steady-state variations in HR, CO, TPR, MAP, SBP and DBP are compared against human data from two different studies [81, 82] on 10 and 8 healthy subjects, respectively.

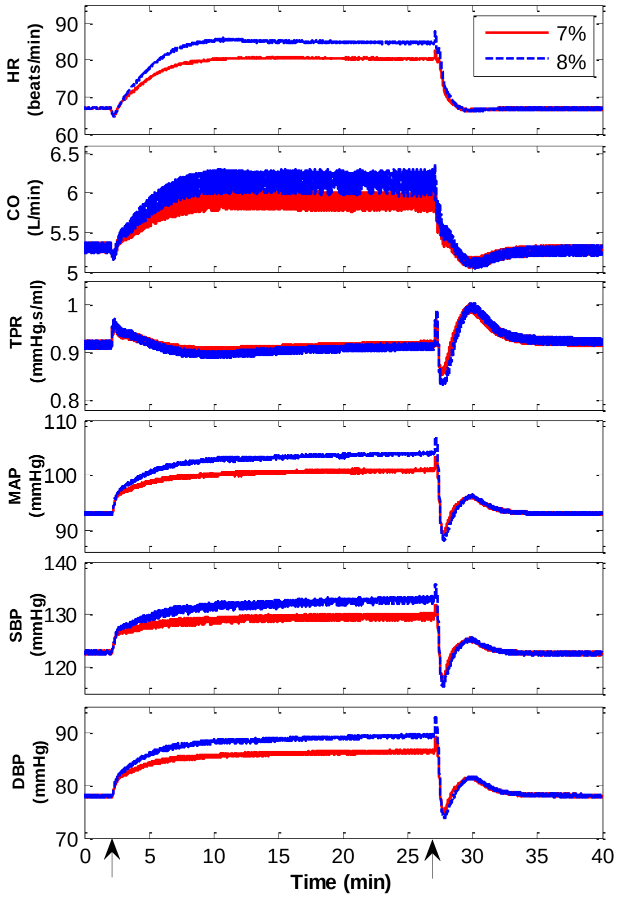

Figure 2.41- Model predicted cardiovascular response to a 7% (red lines) and 8% (blue lines) CO_2 step input performed at 2 min and lasting 25 min. Figure courtesy of Limei Cheng, Philips Research North America

	Model (7% CO2)	Kiely et al (Chest, 1996)	Model (8% CO2)	Mengesha (2000)
Mean ΔHR (beat/min)	13.5 (+20%)	9.8 (+13.1%)	17.7 (+26.5%)	9.7
Mean ΔCO (L/min)	.6 (+11.4%)	0.8 (+14.3%)	.86 (+16.2%)	
Mean ΔMAP(mmHg)	7.9 (+8.5%)	8.5 (+10.6%)	11.0 (+11.8%)	12.5
Mean ΔSBP(mmHg)	6.9 (+5.6%)	11 (+9.6%)	10.1 (+8.2%)	
Mean ΔDBP	8.4 (+10.8%)	6.4 (+10.1%)	11.4 (+14.6%)	
Mean ΔTPR	0 (0%)	~0	-0.004 (-.44%)	

Table 2-13 – Steady-state changes in heart rate (HR), cardiac output (CO), total peripheral resistance (TPR), mean arterial pressure (MAP), systolic blood pressure (SBP) and diastolic blood pressure (DBP), in response to 7% and 8 % CO_2 step input. Experimental data are mean values from 8 subjects for the 7% case and from 10 subjets for the 8% case . Data courtesy of Limei Cheng, Philips Research North America

2.6.3 Isocapnic Hypoxia

To validate the *CP model* response to O_2 blood content perturbations, isocapnic hypoxia conditions (i.e., hypoxia with constant P_{aCO2}) were simulated. Model predictions, in terms of respiratory and gas exchange variables, were compared against published human data. Similar to the hypoxia case, simulations were performed with the cardiopulmonary model in closed-loop configuration and using the inspired gas concentrations $FiCO_2$ and FiO_2 as input. Particularly, FiO_2 was decreased to different % values starting from a resting nominal values of 21% (room ambient), whereas $FiCO_2$ was dynamically adjusted during the simulations by means of an external proportional controller in order to maintain P_ACO_2 constant to its resting nominal value. Note that in isocapnic hypoxia conditions, since $PaCO_2$ is essentially constant and PaO_2 drops, ventilation is driven by the isolated action of the peripheral chemoreceptors and the O_2-CO_2 multiplicative intercation at the peripheral chemoreceptor site (see 2.3.5 *The Respiratory Control Model* section) is abolished. Hence, by validating the model under isocapnic hypoxia we are implicitely validating the response of the peripheral chemoreceptors model to O_2 perturbations.

Figure 2.42 shows both the model predicted and experimental responses to 8% O_2 in air with controlled P_ACO_2. The responses are shown in terms of alveolar gas partial pressures (P_AO_2 and P_ACO_2), tidal volume (V_T), minute ventilation (V_e) and respiratory frequency (RR). The stimulus is applied for 10 minutes. The experimental data have been obtained from a group of 10 healthy subjects [83] and represent average values across subjects.

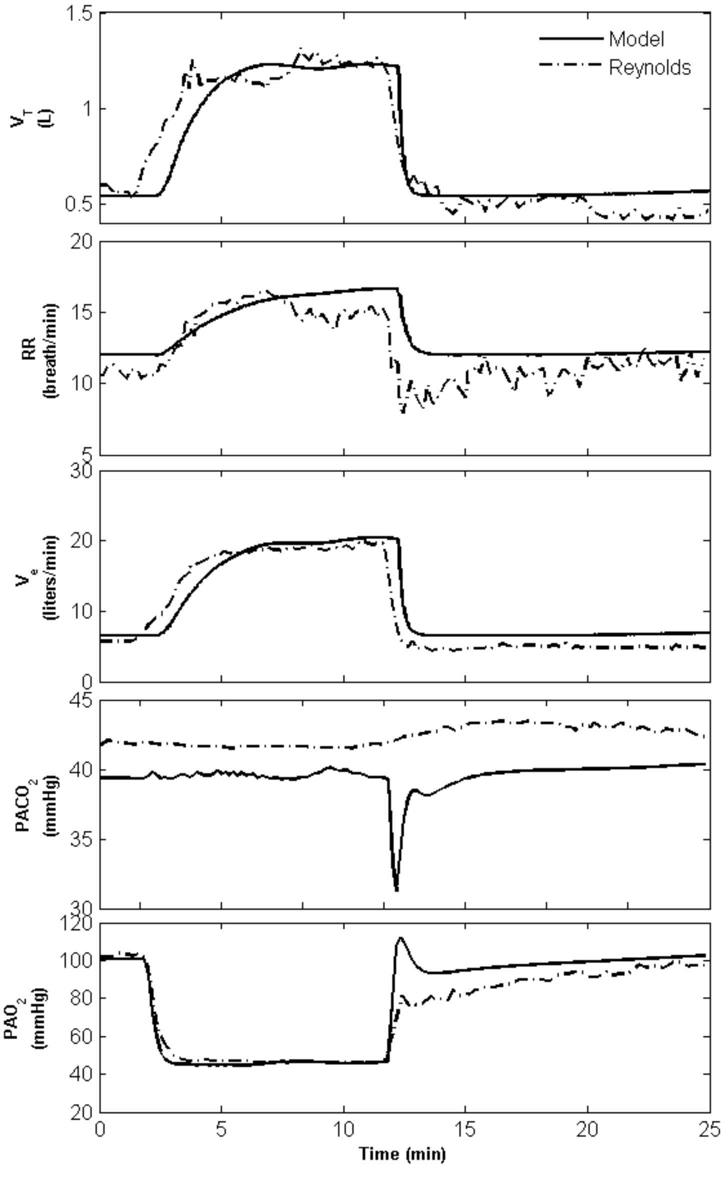

Figure 2.42 - Respiratory response to a 8% O_2 in air with controlled P_{ACO2}. The stimulus is applied at 2 min and lasts 10 min. Continuous lines are model results; dashed lines are experimental data redrawn from [83]. Experimental data are means over 10 subjects. Figure courtesy of Limei Cheng, Philips Research North America

Once again, model predictions agree quite well with the experimental results both in the steady-state and transient phases for all the variables under study. The most evident discrepancy is represented by a downward spike in the simulated P_ACO_2 waveform upon removal of the stimulus. This, however, is due to the controller implementation used to mainatin constant P_ACO_2 during the simulation. The results prove that the model is able to explain the ventilatory increase triggered by isocapnic hypoxia: at the onset of the stimulus, P_AO_2 dramatically decreases due to the FiO_2 decrease, whereas P_ACO_2 remains constant; hence, tidal volume and respiratory rate increase due to the activation of the peripheral chemoreceptors, thus, in turn, increasing minute ventilation; at the removal of the stimulus all the variables return to baseline values after a short transient phase.

2.6.4 Hypoxia

Finally, to further validate the *CP model* response to O_2 blood content perturbations, hypoxia conditions with uncontrolled P_ACO_2 were simulated. Model predictions, in terms of respiratory and gas exchange variables, were compared against published human data. Simulations were performed with the cardiopulmonary model in closed-loop configuration and using the inspired gas concentrations $FiCO_2$ and FiO_2 as input. FiO_2 was decreased to different % values starting from a resting nominal values of 21% (room ambient), whereas F_{ICO2} was kept fixed to its normal room ambient value of 0.04% (see Table 2-6).

Figure 2.43 shows both the model predicted and the experimental responses to 8% O_2 in air, in terms of alveolar gas partial pressures (P_AO_2 and P_ACO_2), tidal volume (V_T), minute ventilation (V_e) and respiratory frequency (RR). The stimulus is applied for 10 minutes. The experimental data have been obtained from a group of 10 healthy subjects [83] and represent average values across subjects. Still, model predictions agree quite well with the experimental results both in the steady-state and transient phases for all the variables under study. The results prove that the model is able to explain the ventilatory increase triggered by severe hypoxia: at the onset of the stimulus, P_AO_2 dramatically decreases due to FiO_2 decrease, whereas P_ACO_2 remains constant; hence, tidal volume and respiratory rate increase due to activation of the peripheral chemoreceptors, thus, in turn, increasing minute ventilation; the increase in minute ventilation generate a concomitant decrease in P_ACO_2 that inhibits peripheral chemoreceptors and limits the ventilatory increases in RR, V_t and V_e to lower values compared to the isocapnic hypoxia case; finally, at the removal of the stimulus all the variables return to baseline values after a short transient phase.

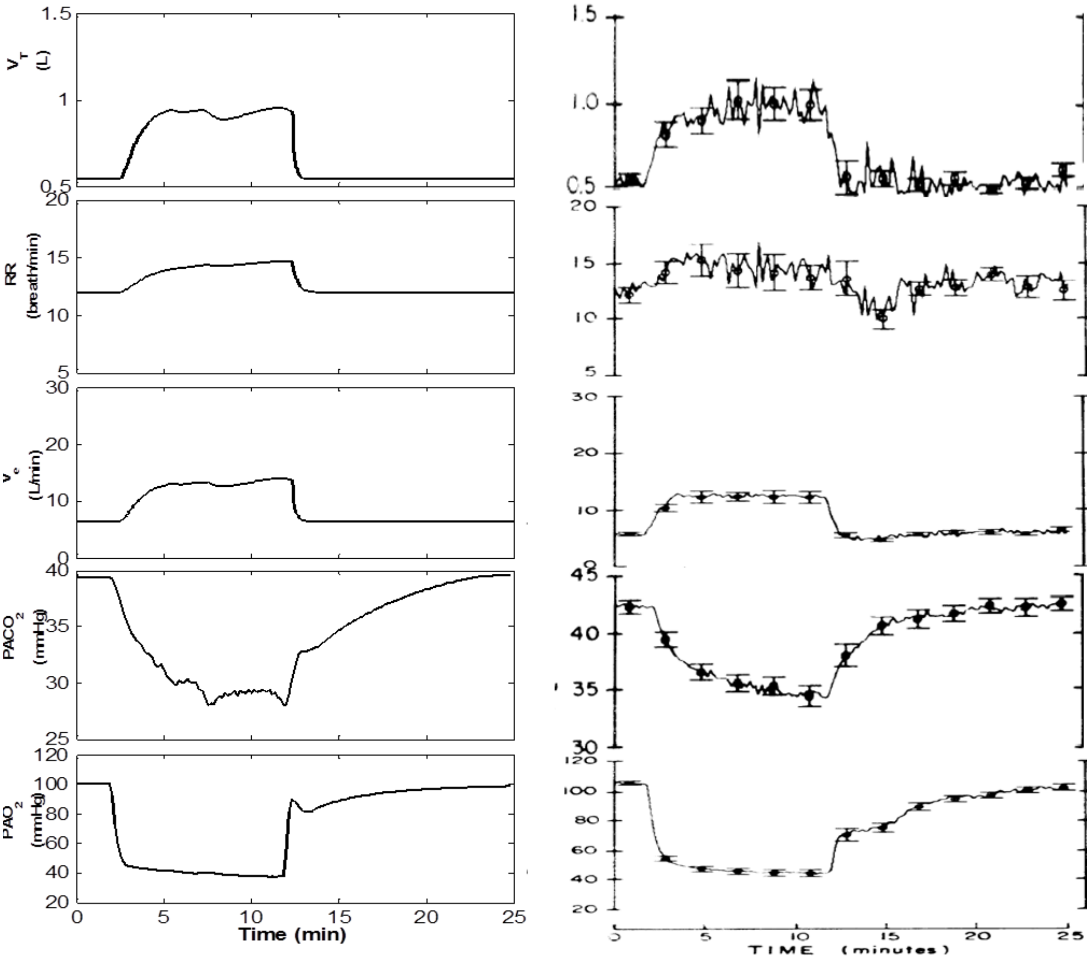

Figure 2.43 - Respiratory response to 8% inspired O_2 in air with uncontrolled P_{ACO2}; step input performed at 2 min and lasting 10 min. Left: model simulations; Right:experimental data from [83]. Experimental data are means over 10 subjects. Figure courtesy of Limei Cheng, Philips Research North America

Chapter 3: Work of Breathing and Respiratory Mechanics Estimation

3.1 Introduction

Knowledge of the mechanical properties of the respiratory system is of paramount importance to the clinicians for the management of mechanically ventilated patients. Quantitative determination of respiratory mechanics can aid the clinician to: *1)* diagnose the disease underlying respiratory failure; *2)* assess the status and progress of the disease; *3)* measure the effects of treatments; *4)* tune the ventilator setting to the patient's specific needs, and thus minimize the risk of ventilator-induced complications, such as ventilator-induced lung injury (VILI). Methods for the assessment of respiratory mechanics are currently available at the bedside but they all present some limitations. Particularly, the majority require the patient to be fully passive. Spontaneously breathing patients are much harder to "estimate" due to the presence of the additional respiratory muscle pressure source. However, in mechanically ventilated patients, spontaneous respiratory activity by the patient is often present. One of the main goals of mechanical ventilation is indeed to restore normal spontaneous respiratory activity as early as possible in order to discontinue mechanical therapy. Hence, there is a need for reliable techniques to characterize the mechanical properties of patients' respiratory system even in the presence of spontaneous respiratory efforts. In active patients, quantification of these efforts is also very important in order to optimally adjust the respiratory load via the ventilator and maintain the patient in a comfort zone, thus avoiding patient's respiratory muscles atrophy and fatigue. In this chapter we will first review the state-of-art of respiratory mechanics assessment and quantification of patient's efforts, then highlight the limitations of the current methods. Then, we will present a novel model-based noninvasive technique that overcomes these limitations and allows for simultaneous assessment of patient’s respiratory mechanics and efforts in spontaneously breathing subjects. Validation of the proposed technique via simulated and real experimental data obtained from animal tests will be shown. The use of a (simplistic) physiological model of the patient’s respiratory system coupled with a parameter estimation method, form the core of our technique. Hence, this represents a concrete application of the patient-specific (personalized) physiological modeling concept that has been introduced in *1.1 Motivation* section and that constitutes the driving principle behind this research.

3.2 Respiratory Mechanics

The lungs are completely passive. Forces need to be applied to the respiratory system in order to move it from its resting equilibrium position at end exhalation. In spontaneous breathing, the respiratory muscles generate the required forces, whereas in mechanical ventilation (MV) the forces are externally supplied by the ventilator. In both cases, for a given applied driving force, the resulting movement of the lungs depends on the impedance of the lung and chest wall, the two components of the respiratory system. The impedance is essentially due to the elastic and resistive mechanical properties of the system. The inertial component of gas and lung tissue is usually negligible [54].

Elastic Properties: Both the lungs and the chest wall can be considered as elastic structures, where the transmural pressure gradients correspond to stress, and lung volume corresponds to strain. Elasticity of the lungs is essentially due to the elastic properties of the pulmonary tissue and to surface tension. Over a certain range of volumes and pressures, lung and chest-wall structures obey Hooke’s law and the change in the volumes divided by the transmural pressures required to produce them defines their *compliance* (C):

$$C = \frac{\Delta V}{\Delta P}$$

Elastance (*E*), or stiffness, is the reciprocal of the compliance and is usually expressed in $\frac{cmH_2O}{L}$. Stiff structures present a high elastance and a reduced compliance. A schematic representation of the respiratory system and its structures, highlighting the transmural pressure gradients involved, is shown in Figure 3.1.

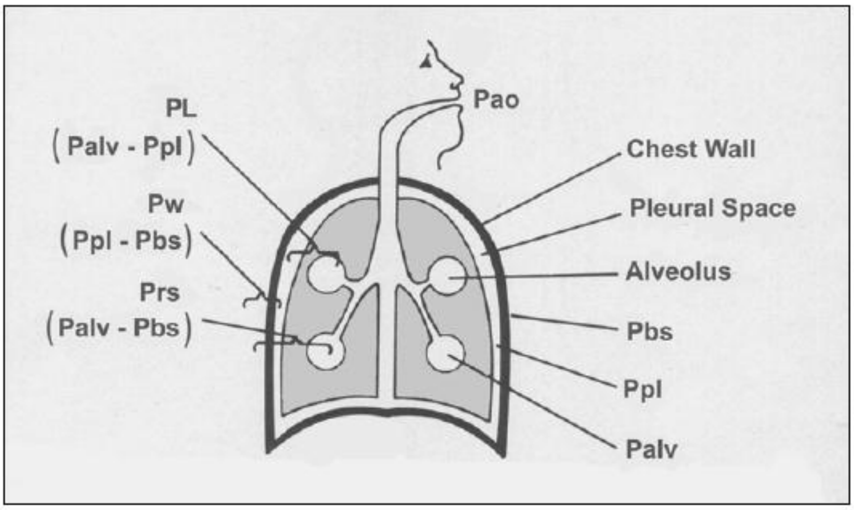

Figure 3.1 – Schematic respresentation of the structures and pressures involved in breathing. P_{ao}, pressure at the airway opening; P_{bs}, body surface pressure (typically equal to atmospheric pressure); P_{pl}, intrapleural pressure; P_{alv}, alveolar pressure; P_L, transpulmonary lung pressure; P_w, chest-wall pressure; P_{rs}, pleural difference across the respiratory system.

Under static conditions (i.e., in the absence of flow and air movement) the distending pressure of the respiratory system (P_{rs}), lung (P_L) and chest wall (P_{cw}) are given by:

$$P_L = P_{alv} - P_{pl}$$

$$P_w = P_{pl} - P_{bs}$$

$$P_{rs} = P_L + P_w = P_{alv} - P_{bs}$$

where P_{alv} represents the alveolar pressure, P_{pl} represents the intrapleural pressure and P_{bs} is the body surface pressure (usually barometric pressure). As can be easily observed from the equations above, knowledge of the variations in intrapleural pressure during breathing is necessary in order to divide respiratory system mechanics into their lung and chest-wall components.

The elastic properties of lungs and chest generate elastic recoil pressures that must be overcome in order to breath. These pressures depend on the volume and elastance of the particular structures (lung, chest wall, etc.) that generate them and they are purely static in the sense that they are independent of the existence of airflow.

Resistive Properties: When airflow is present, an additional mechanical element must be considered: *resistance* (R). This generates a corresponding resistive pressure that must be overcome by the driving force of the system. The resistance can be computed by dividing the resistive pressure (P_{res}) by the airflow ($\dot{V}$):

$$R = \frac{P_{res}}{\dot{V}}$$

Respiratory system resistance can be attributed to the airways, viscosity of the pulmonary tissues and partially to the shear forces that develop during movement of the chest-wall tissues.

3.2.1 State-of-art of Respiratory Mechanics Assessment

A well-established technique for assessing respiratory mechanics in ventilated patients is the Inspiratory Hold Maneuver, also called Flow Interrupter Technique (FIT) [54] or End Inspiratory Pause (EIP) [97]. This technique consists of rapidly occluding the circuit through which the patient is breathing (see

Figure 3.2) under conditions of constant inspiratory flow, while measuring the pressure in the circuit behind the occluding valve. As illustrated in Figure 3.3, under conditions of constant inspiratory flow ($\dot{V}$), airway opening pressure increases from the positive end-expiratory value (PEEP) to peak inspiratory pressure (PIP). When the circuit is occluded, flow is stopped temporarily thus eliminating the resistive pressure component and causing airway opening pressure to drop from PIP to a plateau pressure value (P_{plat}). Then the patient is allowed to exhale to set PEEP. The gradient between PIP and P_{plat} allows for calculation of airway resistance according to:

$$R_{rs} = \frac{PIP - P_{plat}}{\dot{V}}$$

whereas the value of P_{plat} reflects the total elastic recoil pressure and hence allows for calculation of the respiratory system compliance according to:

$$C_{rs} = \frac{V_t}{P_{plat} - PEEP}$$

where V_t is the inhaled tidal volume.

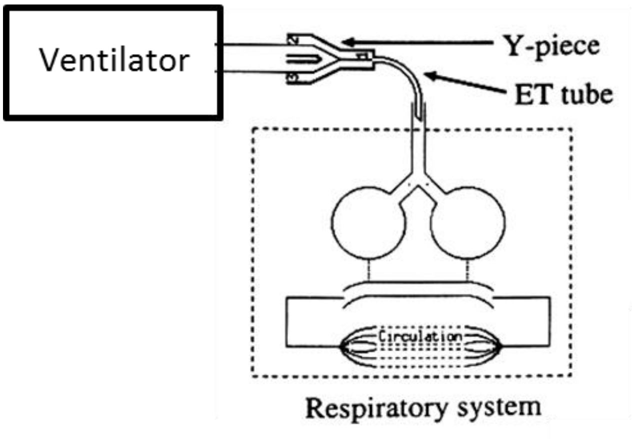

Figure 3.2–Schematic representation of mechanical ventilation showing the connection between the patient and the ventilator. ET stands for endotracheal tube.

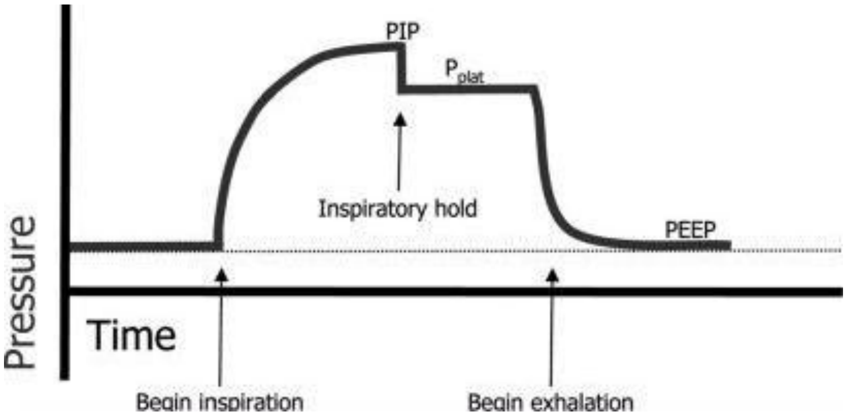

Figure 3.3 – Airway opening pressure profile during an Inspiratory Hold Maneuver. PEEP, positive end-expiratory pressure; PIP, peak inspiratory pressure; P_{plat}, plateau pressure.

The technique is noninvasive and easy to be performed. Furthermore, the majority of the modern commercial ventilators have software that automate the procedure and compute resistance and compliance values. However, the maneuver interferes with normal operation of the ventilator as it requires constant inspiratory flow and hence can only be applied in volume-controlled ventilation (VCV) mode. As a result, it is not suitable for continuous monitoring of respiratory mechanics and patient status. This is a severe limitation, as in critically ill patients mechanical properties of the respiratory systems can rapidly change, thus a continuous monitoring of resistance and compliance would be highly desirable. Moreover, the measurements provided by this technique are valid only if the patient is completely passive throughout the duration of the inspiratory hold. As shown in Figure 3.4, in fact, if spontaneous respiratory activity is present artefacts get generated in the airway pressure profile causing erroneous measurements of P_{plat}. However, the majority of patients receiving MV are not completely passive. For instance, spontaneously breathing patients may receive pressure support ventilation (PSV) and/or volume-controlled synchronized mandatory ventilation (VC-SIMV). Intermittent applications of the maneuver in these patients will interfere with the patient' breathing, predisposing to patient-ventilator dissynchrony, and likely cause the patient to attempt inhaling and exhaling spontaneously during the hold. Recently, Al-Rawas and colleagues [97] have reported such phenomenon to happen approximately 75% of the time according to their experience. Hence, it appears evident that despite its simplicity, the assessment of respiratory mechanics via the inspiratory hold maneuver is far from being optimal.

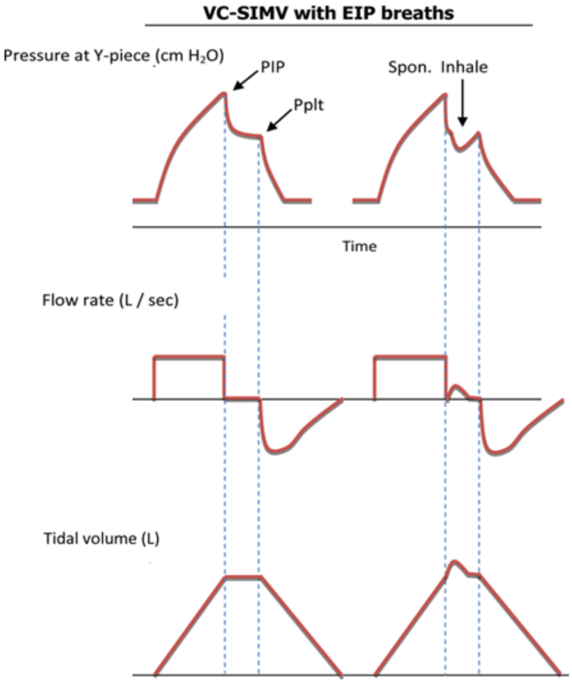

Figure 3.4 – Examples of a correct EIP (left), when no patient's respiratory muscles activity is present, and an incorrect EIP (right), when patient's respiratory muscles activity generates artefacts in the airway pressure profile. Adapted from [97].

An alternative to the inspiratory hold maneuver consists in using the Least Squares (LS) method to fit a mathematical model of the respiratory system to pressure and flow measurements obtained noninvasively at the Y-piece of the breathing circuit (see Figure 3.2). The model most frequently used is the *1st order single-compartment model* [98] that describes the respiratory system as an elastic compartment served by a single resistive pathway. The electrical analog of the model is shown in Figure 3.5. Its governing equation, also known as the *equation of motion of the respiratory system*, can be written as:

$$P_{ao}(t) = R_{rs} \cdot \dot{V}(t) + E_{rs} \cdot V(t) + P_{mus}(t) + P_0 \tag{3-1}$$

where P_{ao} is the airway opening pressure, $\dot{V}$ is the air flow, V is the lung volume above functional residual capacity (FRC), P_{mus} is the pressure generated by the patient respiratory muscles (driving source), R_{rs} is the respiratory system resistance, E_{rs} is the respiratory system elastance (inverse of the compliance) and P_0 is a constant term added to account for the pressure that remains in the lungs at the end of expiration.

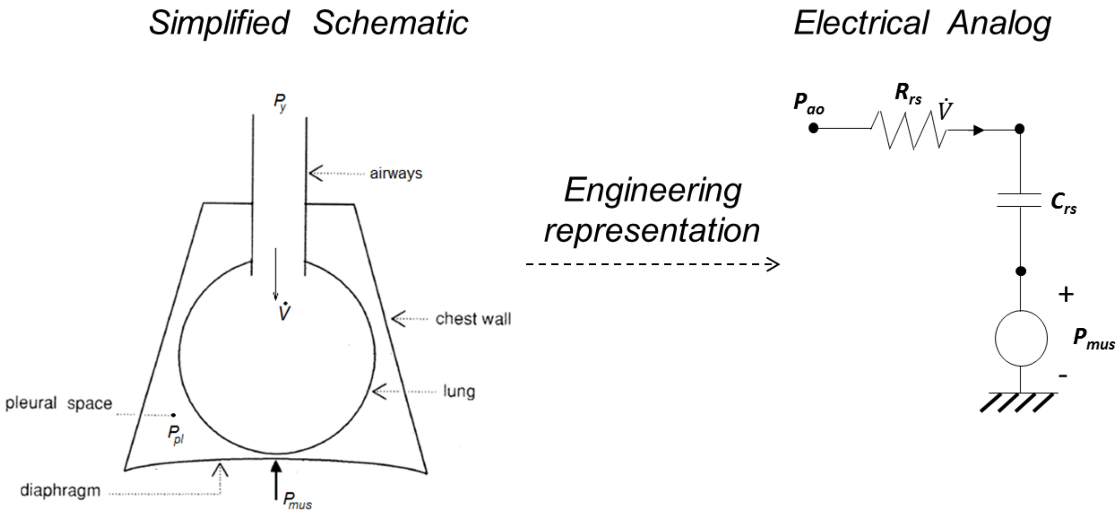

Figure 3.5 – Simplified conceptual model of the respiratory system (left) and corresponding electrical analog (right). P_{ao}, airway opening pressure; R_{rs}, respiratory system resistance; C_{rs}, respiratory system compliance; P_{mus}, respiratory muscle pressure.

In patients who are not breathing spontaneously, the term P_{mus} in Eq. 3-1 can be removed and the resulting equation

$$P_{ao}(t) = R_{rs} \cdot \dot{V}(t) + E_{rs} \cdot V(t) + P_0 + w(t) \tag{3-2}$$

can be imposed for N different time samples, obtaining:

$$Z = \begin{bmatrix} z_1 \\ z_2 \\ \cdot \\ \cdot \\ \cdot \\ \cdot \\ z_N \end{bmatrix} = \begin{bmatrix} P_{ao}(t_1) \\ P_{ao}(t_2) \\ \cdot \\ \cdot \\ \cdot \\ \cdot \\ P_{ao}(t_N) \end{bmatrix} = \begin{bmatrix} \dot{V}\,(t_1) & V(t_1) & 1 \\ \dot{V}\,(t_2) & V(t_2) & 1 \\ & \cdot & \\ & \cdot & \\ & \cdot & \\ & \cdot & \\ \dot{V}\,(t_N) & V(t_N) & 1 \end{bmatrix} \cdot \begin{bmatrix} R_{rs} \\ E_{rs} \\ P_0 \end{bmatrix} + \begin{bmatrix} w(t_1) \\ w(t_2) \\ \cdot \\ \cdot \\ \cdot \\ \cdot \\ w(t_N) \end{bmatrix} =$$

$$= \begin{bmatrix} \dot{V}_1 & V_1 & 1 \\ \dot{V}_2 & V_2 & 1 \\ & \cdot & \\ & \cdot & \\ & \cdot & \\ & \cdot & \\ \dot{V}_N & V_N & 1 \end{bmatrix} \cdot \begin{bmatrix} R_{rs} \\ E_{rs} \\ P_0 \end{bmatrix} + \begin{bmatrix} w_1 \\ w_2 \\ \cdot \\ \cdot \\ \cdot \\ \cdot \\ w_N \end{bmatrix} = H \cdot \theta + W \qquad (3\text{-}3)$$

Note that in Eq. 3-2 an extra term $w(t)$ has been included in order to account for the presence of measurements and model errors. Equation 3-3 above represents a standard mathematical tractable linear regression problem, where H is the matrix containing the input variables, Z is the output vector, θ is the parameter vector containing the unknown parameters (R_{rs}, E_{rs} and P_0), and N is the number of samples. Hence, in the case of fully passive patients, an estimate of the parameter vector $\hat{\theta}$ (containing the estimated resistance and compliance) can be obtained via the classical Least Squares (LS) method:

$$\hat{\theta} = (H^T H)^{-1} H^T Z \qquad (3\text{-}4)$$

provided that airway pressure and flow at the patient's mouth are measured (lung volume V is typically obtained via numerical integration of the flow signal). This is an ideal non-invasive alternative to the end-inspiratory hold maneuver, one that does not interfere with the normal operation of the ventilator and hence allows for continuous monitoring of respiratory mechanics. The technique has been applied in several respiratory mechanics studies [99, 100] and, thanks to the advancement in microprocessor technology, it is implemented in some of the modern mechanical ventilators (e.g., V200-Philips Respironics). Note that the LS formulation in Eq. 3-4 above assumes that a batch of data (typically covering the entire duration of a breath) is available in order to construct the matrix *H* and the output vector *Z*. An on-line version of the LS technique, based on the Recursive Least Squares (RLS) formulation [101], exists and can be used to avoid the need for data storage. Furthermore, in order to cope with time varying parameters, a forgetting factor can be introduced in the RLS formulation (RLS with exponential forgetting [101]). This has been proposed in the literature [102, 103, 104] in order to track time variations of respiratory mechanics that correlate with disease progression. However, the main drawback of this technique is that it can only be applied for passive patients. In fact, if the patient is actively contributing to the breath, i.e. spontaneously breathing, then the term P_{mus} in Eq. 3-1 cannot be neglected and the standard LS method will provide erroneous results unless P_{mus} is a known input quantity. To obviate for this limitation, a similar approach can be applied to study the lungs without including the dynamics of the chest wall. In other words, the 1st order single-compartment model described above (Figure 3.5) can be converted into the equivalent model shown in Figure 3.6 and, accordingly, the equation of motion of the respiratory system can be converted into the *equation of motion of the lungs*:

$$P_{ao}(t) = R_L \cdot \dot{V}(t) + E_L \cdot V(t) + P_{pl}(t) + P_0 \tag{3-5}$$

where R_L and E_L are lung resistance and elastance. Note the addition of the term P_{pl} that represents the intrapleural pressure.

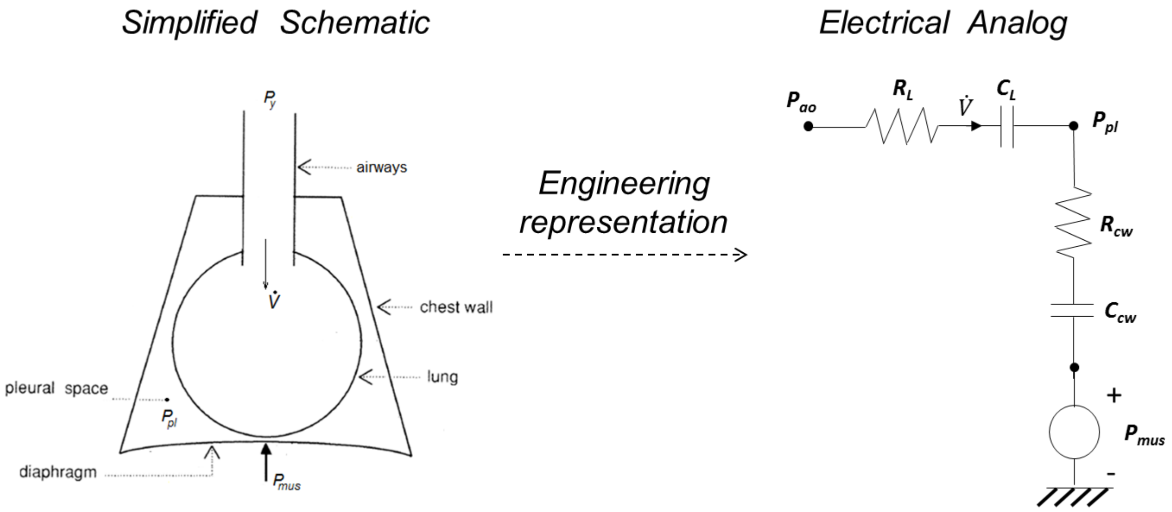

Figure 3.6 – Simplified conceptual model of the respiratory system (left) and corresponding electrical analog (right) highlighting both the lung and the chest wall components.

From Eq. 3-5, the following linear regression problem can be obtained:

$$Z = \begin{bmatrix} z_1 \\ z_2 \\ \cdot \\ \cdot \\ \cdot \\ \cdot \\ z_N \end{bmatrix} = \begin{bmatrix} P_{ao}(t_1) - P_{pl}(t_1) \\ P_{ao}(t_2) - P_{pl}(t_2) \\ \cdot \\ \cdot \\ \cdot \\ \cdot \\ P_{ao}(t_N) - P_{pl}(t_N) \end{bmatrix} = \begin{bmatrix} \dot{V}(t_1) & V(t_1) & 1 \\ \dot{V}(t_2) & V(t_2) & 1 \\ & \cdot & \\ & \cdot & \\ & \cdot & \\ & \cdot & \\ \dot{V}(t_N) & V(t_N) & 1 \end{bmatrix} \cdot \begin{bmatrix} R_L \\ E_L \\ P_0 \end{bmatrix} + \begin{bmatrix} w(t_1) \\ w(t_2) \\ \cdot \\ \cdot \\ \cdot \\ \cdot \\ w(t_N) \end{bmatrix} =$$

$$= \begin{bmatrix} \dot{V}_1 & V_1 & 1 \\ \dot{V}_2 & V_2 & 1 \\ & \cdot & \\ & \cdot & \\ & \cdot & \\ & \cdot & \\ \dot{V}_N & V_N & 1 \end{bmatrix} \cdot \begin{bmatrix} R_L \\ E_L \\ P_0 \end{bmatrix} + \begin{bmatrix} w_1 \\ w_2 \\ \cdot \\ \cdot \\ \cdot \\ \cdot \\ w_N \end{bmatrix} = H \cdot \theta + W \tag{3-6}$$

and the LS method can be applied to estimate the parameter vector θ, provided that intrapleural pressure P_{pl} is known. Note that in this case, the estimated resistance and elastance (or compliance) pertain to the lung component only, rather than to the entire respiratory system. The clear drawback of this approach is that knowledge of intrapleural pressure is required. Direct measurement of P_{pl} (pleural manometry) requires an invasive procedure to place needles, catheters, or transducers. The risk of infection and other complications makes this approach unattractive in the clinical setting. For this reason, the pressure into the esophagus (P_{es}) is typically used as a surrogate to P_{pl}. The esophageal balloon technique is the most popular method for P_{es} measurement. This technique, however, not only requires the patient to swallow a balloon-tipped catheter (see Figure 3.7), but it also requires an expert operator for correct placement and inflation of the balloon, special equipment and particular attention to avoid errors and artifacts [105]. These drawbacks have limited somewhat the use of esophageal manometry as a way of monitoring P_{pl} and have diminished its adoption into standard clinical practice.

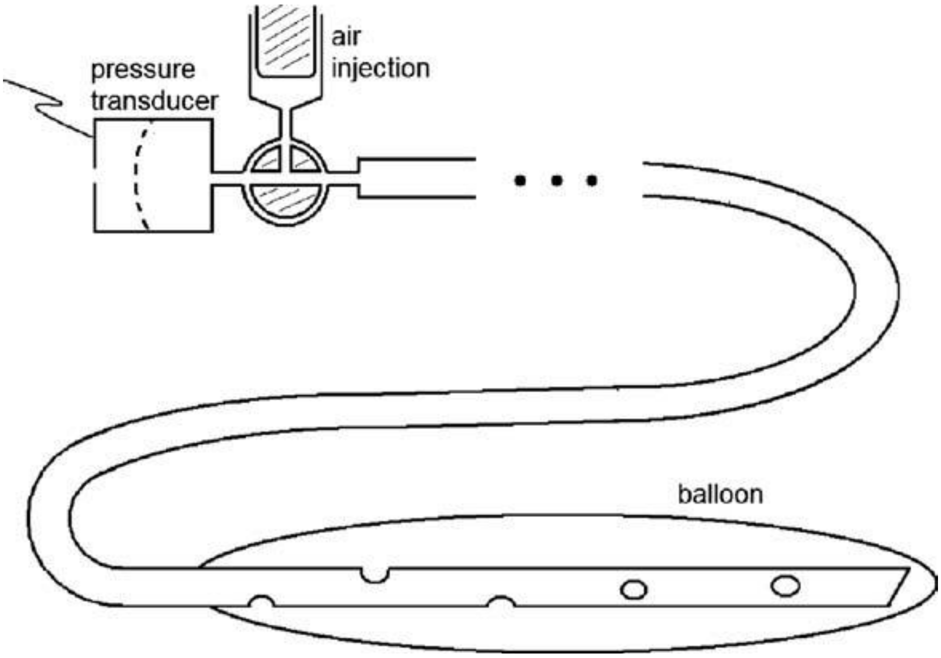

Figure 3.7 – The esophageal balloon catheter. The pressure inside a latex balloon on the end of a thin catheter is sensed by a pressure transducer connected to the proximal end. A three-way stopcock permits injection of a small volume of air into the balloon so that its sides clear the multiple holes in the end of the catheter.

As a result of this review, the need for a robust method to monitor respiratory mechanics in spontaneously breathing ventilated patients appears evident.

3.3 Work of Breathing (WOB)

Another very important parameter in MV, in addition to resistance and compliance, is Work of Breathing (WOB). WOB is defined as the effort done by the respiratory muscles to breath. When the patient is connected to a mechanical ventilator, the work of breathing can be divided into 2 major components: the physiologic work of breathing, which is dissipated against the resistive and elastic pressures of the respiratory system, and the imposed work of breathing due to the breathing apparatus (endotracheal tube and ventilator). The total WOB is usually computed at each breath and normalized with respect to tidal volume to give Joule/L. Sometimes, in order to account for the respiratory frequency, WOB is also expressed in Joule/min to yield Power of Breathing (POB). Real-time measurements of WOB in mechanically ventilated patients can be used to assess patient readiness for weaning [106], to appropriately select pressure support ventilation (PSV) levels [107], to diagnose and treat excessive respiratory muscle loading [108], and to monitor and prevent respiratory muscle fatigue or atrophy [109].

3.3.1 State-of-art of WOB Estimation

The gold standard of WOB computation is the Campbell diagram [110, 111], which is constructed by plotting lung volume (V) against intrapleural pressure (P_{pl}), thus forming the so called PV loop, at each breath. The Campbell diagram is an effective tool to evaluate the effects of lung mechanics abnormalities on WOB [108] and it allows partitioning of WOB into its flow-resistive component (both physiologic and imposed) and elastic component [107]. However, as mentioned in the previous section, direct measurement of intrapleural pressure is invasive and hence, to construct the Campbell diagram, esophageal pressure (P_{es}) is usually used as a surrogate of P_{pl}. An example of a typical Campbell diagram is shown in

Figure 3.8. In the diagram, lung volume is usually referred to functional residual capacity (FRC) whereas esophageal pressure is usually referred to its baseline value, so that the breaths start at the origin of the diagram (zero pressure and volume point). During spontaneous breathing, the *PV* loop moves in a clockwise direction and its slope represents the dynamic lung compliance (C_L). During inhalation (*I*), esophageal pressure decreases due to the movements of the diaphragm (and other additional inspiratory muscles) and lung volume increases. Exhalation (*E*) is normally passive, with both volume and pressure returning to zero at the end of the breath (if intrinsic positive end-expiratory pressure, PEEP_i, is not developed). A line, whose slope is equal to the chest wall compliance (C_{CW}), is also drawn on the diagram, usually starting at the zero flow point. WOB is computed as the area enclosed within the inspiratory portion of pressure-volume loop and the chest wall compliance line. It can be partitioned into an inspiratory flow-resistive component (vertical lines area in Figure 3.8) and an elastic component (triangular shaped area with diagonal lines in Figure 3.8).

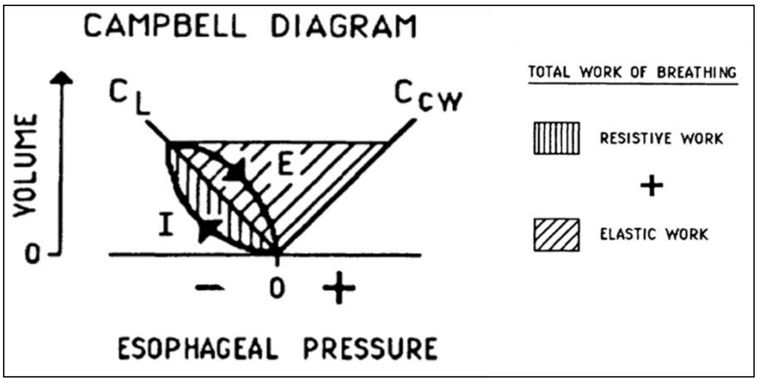

Figure 3.8 – Campbell diagram for a spontaneously breathing patient; reproduced from [107].

The value of C_{CW} is usually computed by mechanically inflating the patient, provided that the patient is completely relaxed. Under this condition, the esophageal pressure increases as the lung is inflated and the pressure-volume loop moves in a counterclockwise direction. The slope of this loop is taken as the chest wall compliance. If complete relaxation of the inspiratory muscles cannot be achieved, normal values of 0.1 – 0.2 L/cmH_2O are used for C_{CW}. Commercial devices, such as the Bicore CP100 (Bicore Monitoring Systems, Irvine, CA) and the Ventrak 1500 (Novametrix Medical Systems, Wallingford, CT), were designed in the 1990s to assess WOB via the Campbell diagram using esophageal pressure measurements [112, 113, 114]. However, due to the aforementioned drawbacks associated with the esophageal balloon technique, this has not been accepted as a routine clinical practice. For these reasons, the popularity of the above mentioned commercial devices have progressively declined [11]. At present, WOB computation via esophageal manometry is offered only in the AVEA ventilator system (VIASYS Healthcare, CareFusion) using the BiCore technology originally implemented in the CP100 monitor.

Alternative noninvasive methods for WOB computation, that are not based on the Campbell diagram and do not require esophageal pressure measurements, have been considered in recent years and have contributed to renewed interest in WOB as a meaningful clinical parameter. An Artificial Neural Network (ANN) algorithm has been recently proposed [8] to estimate POB non-invasively and is currently implemented in the NM_3 monitor as part of the VentAssist clinical decision support tool (Philips - Respironics). Statistical equivalence between non-invasive POB and invasive POB, derived using esophageal pressure measurements, has been proved in a group of 45 adult mechanical ventilated patients receiving pressure support ventilation (PSV) [8]. The main limitation of this method is the inability to explain the underlying physiological mechanisms behind WOB computation. ANN, are indeed data-driven (or black-box) approaches and hence do not provide quantitative understanding of the underlying input-output relations. As a result, the algorithm proposed in [8] receives input data and generates an estimate of POB, but it is not possible to correlate this number with the underlying physiological scenario. Furthermore, the performance of ANN-based approaches is typically highly dependent on the training datasets and this may represent an additional limitation.

Others [9, 7, 115] have proposed a model-based approach, where an estimate of P_{mus} is first computed and then WOB is found as:

$$WOB = \int_{0}^{T_i} P_{mus}(t) \cdot \dot{V}(t)\, dt \tag{3-7}$$

where T_i is the inspiratory time. These methods are all based on the 1st order single-compartment model of the respiratory system (see Figure 3.5 and Eq. 3-1) and they rely on a two-step approach: *1)* R_{rs} and C_{rs} are first estimated; *2)* the equation of motion is then applied to compute P_{mus} (t) using the estimated values of R_{rs} and C_{rs} and the available measurements. Estimation of R_{rs} and C_{rs} is performed either by applying the inspiratory hold maneuver [9], or via Least-Squares fitting of Eq. 3-1 under specific conditions where the term $P_{mus}(t)$ is arguably assumed to be zero [7, 115]. Clear limitations can be found in all these approaches. Particularly, the limitations related to the use of the inspiratory hold maneuver [9] have been already discussed in the previous section. The method described in [7] requires intermittent periods of high level pressure support ventilation (PSV) in order to unload the respiratory muscles and legitimately neglect P_{mus} in the LS fitting procedure. Hence, this method still interferes with the normal operation of the ventilator and does not allow for continuous monitoring of WOB. Finally, the method described in [115] uses only small selected portions of PSV breaths, where the flow signal satisfies specific conditions that are compatible with the assumption of negligible P_{mus}. Hence, it does not exploit all the data available and it is prone to errors due to measurement noise.

3.4 Proposed Method

In order to overcome the above limitations we propose a method for the assessment of respiratory mechanics (R_{rs} and C_{rs}) and quantification of patient's efforts (P_{mus} and WOB) with the following characteristics:

- Completely noninvasive (i.e., no esophageal catheter needed);
- Maneuver-free (i.e., not interfering with normal ventilator operation);
- Real-time;
- Model-based (so as to allow physiological interpretation);
- Not dependent on training datasets;
- Continually updated (so as to allow for continuous monitoring of WOB and respiratory mechanics);
- Using readily available data from ventilator or monitoring devices;
- Applicable in spontaneous as well as passive patients;
- Independent from ventilator modes;
- Robust to noise and disturbances in the data (possibly using all measured data points).

The method is based on the same 1st order single-compartment model of the respiratory system shown above (see Figure 3.5). This model has been chosen, despite its simplicity, as it is widely accepted in the clinical community and can be easily interpreted. Our method uses pressure and flow data measured non-invasively at the patient airways and estimates the resistance R_{rs}, the compliance C_{rs} as well as the respiratory muscle pressure signal $P_{mus}(t)$. Once an estimate of P_{mus} over a respiratory cycle is available, then WOB is computed by simply integrating P_{mus} over volume as shown in Eq. 3-7.

To highlight the degree of complexity of the problem at hand, Figure 3.9 shows a block diagram representation where the input and output of the system under exam are specified.

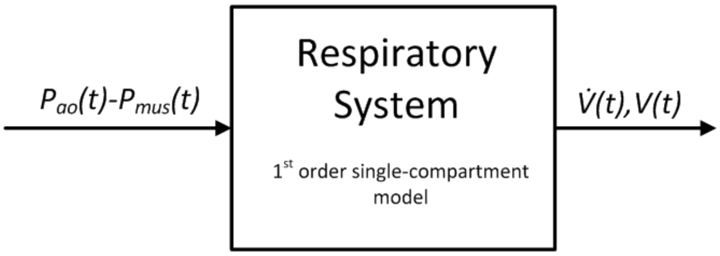

Figure 3.9 – Input-output block diagram of the 1st oder single-compartment model of the respiratory system. P_{ao}, airway opening pressure; P_{mus}, respiratory muscle pressure; $\dot{V}$, air flow; V, lung volume; t, time.

It is evident that P_{mus}, which in this case is one of the unknown quantities to be estimated, is actually one of the inputs to the system. Hence, the problem we are facing is a combined input estimation - system identification problem: using complete knowledge of the output signals ($\dot{V}(t)$ and $V(t)$) and only partial knowledge of the input ($P_{ao}(t)$), we would like to identify the system (i.e. estimate the parameters R_{rs} and C_{rs}) and at the same time recover (estimate) the input information that is missing, i.e. $P_{mus}(t)$. This is clearly a very challenging problem since it poses major technical obstacles. In fact, typical system identification techniques require complete knowledge of the input-output signals of the system to be identified, and hence cannot be directly applied. Two different algorithms, with complementary features, have been developed by our group. In the next section, detailed description of both algorithms is provided.

3.4.1 Constraint Least-Squares (CLS) Algorithm

The first algorithm works on breath-by-breath batches of data (made of, say, N recorded time samples) and provides simultaneous estimation of average respiratory system resistance R_{rs} and elastance E_{rs} (or compliance C_{rs}), as well as a time-continuous estimated $P_{mus}(t)$ signal pertaining to that particular batch of data (and hence to that particular breath). The starting point of the algorithm is the standard LS problem applied to a batch of data corresponding to a respiratory cycle. Given measurements of $P_{ao}(t)$, $\dot{V}(t)$ and $V(t)$ at N different time samples, we want to find the values of R_{rs}, E_{rs} an $P_{mus}(t)$ that minimize the residual sum of squares between measured and model predicted output:

Standard Least Squares	Find R_{rs} , E_{rs} , P_{mus} *(t)* such that $J = \sum_{t=1}^{N}\left(P_{ao}(t) - R_{rs}\cdot\dot{V}(t) - E_{rs}\cdot V(t) - P_{mus}(t)\right)^2$ is minimized

Note that to simplify notation, in writing the cost function J the term P_0 in Eq. 3-1 has been absorbed into P_{mus}. Hence, practically, when solving the LS problem above we would be estimating a shifted version of the P_{mus} waveform:

$$P_{mus}^{*}(t) = P_{mus}(t) + P_0$$

This however, does not affect the resulting WOB computation since when integrating the estimated P_{mus} waveform over volume (see Eq. 3-7) we can account for the offset P_0 by referring P_{mus} to its end exhalation value.

Then, it is realized that simultaneous estimation of R_{rs}, C_{rs} and $P_{mus}(t)$ is an underdetermined problem, since it requires the computation of N+2 unknowns (N values of $P_{mus}(t)$, 1 value for R_{rs}, and 1 value for C_{rs}) from N available equations (1 for each time sample):

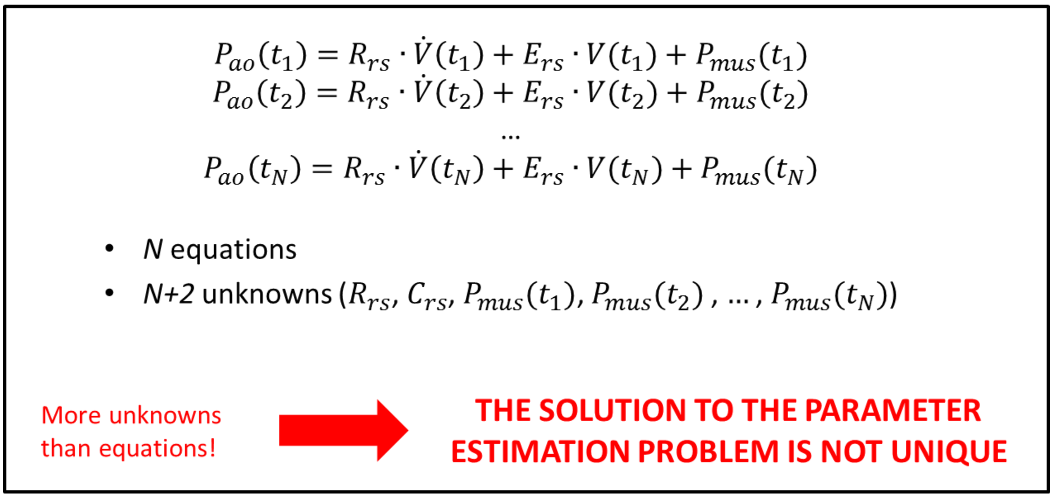

$$P_{ao}(t_1) = R_{rs} \cdot \dot{V}(t_1) + E_{rs} \cdot V(t_1) + P_{mus}(t_1)$$
$$P_{ao}(t_2) = R_{rs} \cdot \dot{V}(t_2) + E_{rs} \cdot V(t_2) + P_{mus}(t_2)$$
$$\ldots$$
$$P_{ao}(t_N) = R_{rs} \cdot \dot{V}(t_N) + E_{rs} \cdot V(t_N) + P_{mus}(t_N)$$

- *N* equations
- *N+2* unknowns (R_{rs}, C_{rs}, $P_{mus}(t_1)$, $P_{mus}(t_2)$, … , $P_{mus}(t_N)$)

More unknowns than equations! → **THE SOLUTION TO THE PARAMETER ESTIMATION PROBLEM IS NOT UNIQUE**

Hence, to address the issue of underdeterminacy, we introduced inequality and equality constraints on the possible values that $P_{mus}(t)$, R_{rs} and C_{rs} can take, thus reducing the space of feasible solutions. Particularly, we assumed that over a respiratory cycle, $P_{mus}(t)$ is a piece-wise monotonic function (*monotonicity constraints*) made of three different regions: *1)* a region in which P_{mus} is monotonically decreasing up to a minimum point; *2)* a region in which P_{mus} is monotonically increasing; *3)* a region in which P_{mus} is flat. Then we also assumed that the values of $P_{mus}(t)$, R_{rs} and C_{rs} are limited within specific physiological ranges (*domain constraints*). These assumptions are mathematically formulated as:

$$\left.\begin{array}{c} P_{mus}(t_2) \leq P_{mus}(t_1) \\ P_{mus}(t_3) \leq P_{mus}(t_2) \\ \ldots \\ P_{mus}(t_{m-1}) \leq P_{mus}(t_{m-2}) \\ P_{mus}(t_m) \leq P_{mus}(t_{m-1}) \\ P_{mus}(t_m) \leq P_{mus}(t_{m+1}) \\ P_{mus}(t_{m+1}) \leq P_{mus}(t_{m+2}) \\ . \\ . \\ P_{mus}(t_{q-1}) \leq P_{mus}(t_q) \\ P_{mus}(t_q) = P_{mus}(t_{q+1}) \\ . \\ . \\ P_{mus}(t_{N-1}) = P_{mus}(t_N) \end{array}\right\} \textit{monotonicity constraints}$$

$$\left.\begin{array}{l} P_{min} \leq P_{mus}(t_k) \leq P_{max} \\ R_{min} \leq R_{rs} \leq R_{max} \\ E_{min} \leq E_{rs} \leq E_{max} \\ k = 1,2,\ldots,N \end{array}\right\} \textit{domain constraints}$$

where t_m represents the time of transition between regions 1 and 2, and t_q represents the time of transition between regions 2 and 3.

Note that the monotonicity constraints were obtained from the observation that during a spontaneous breath, the respiratory muscles (mainly the diaphragm) first gradually contract (P_{mus} monotonically decreasing), then gradually relax (P_{mus} monotonically increasing) and then finally they become completely silent (P_{mus} flat). A representative “gold standard” P_{mus} profile was obtained experimentally from a pig by measuring airway pressure (P_{ao}) and esophageal pressure (P_{es}) during an occlusion maneuver (see Figure 3.10). In this condition, since the breathing circuit was occluded and no airflow was present, all the pressures in the electrical analog of Figure 3.6 are equal and hence the measured variations in P_{ao} and P_{es} correspond to variations in P_{mus}.

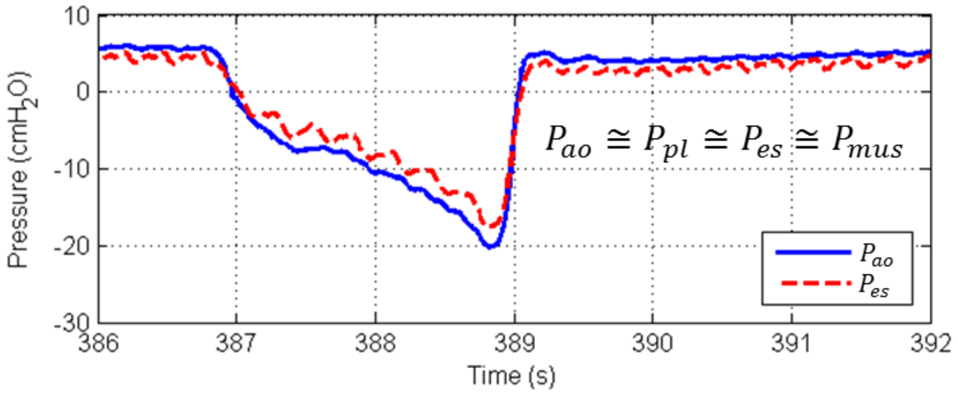

Figure 3.10 – Experimental profile of aiway pressure (P_{ao}) and esophageal pressure (P_{es}) obtained from a pig during an occlusion maneuver. The profile can be assumed as a “gold standard” profile of P_{mus}. Figure courtesy of Francesco Vicario, Philips Research North America

Hence, by combining the aforementioned constraints with the LS type objective function J (to be minimized) we obtain a Constraint Least Squares (CLS) problem:

Constrained Least Squares	Find R_{rs} , E_{rs} , P_{mus} *(t)* such that $J = \sum_{t=1}^{N}\left(P_{ao}(t) - R_{rs}\cdot\dot{V}(t) - E_{rs}\cdot V(t) - P_{mus}(t)\right)^2$ is minimized subject to piecewise monotonicity constraints on $P_{mus}(t)$

The mathematical formulation of the CLS problem to be solved is a quadratic programming optimization problem, where the objective function is a quadratic function of the decision variables and the constraints are linear:

Objective Function

$$J = \sum_{t=1}^{N} \left(P_y(t) - R_{rs} \cdot \dot{V}(t) - E_{rs} \cdot V(t) - P_{mus}(t)\right)^2$$

Decision Variables

$$R_{rs} \qquad E_{rs} \qquad P_{mus}\,(t_1) \qquad P_{mus}\,(t_2) \quad \ldots\ldots\ldots P_{mus}\,(t_N)$$

Constraints

$$\left.\begin{array}{c} P_{mus}(t_2) \le P_{mus}(t_1) \\ P_{mus}(t_3) \le P_{mus}(t_2) \\ \ldots \\ P_{mus}(t_{m-1}) \le P_{mus}(t_{m-2}) \\ P_{mus}(t_m) \le P_{mus}(t_{m-1}) \\ P_{mus}(t_m) \le P_{mus}(t_{m+1}) \\ P_{mus}(t_{m+1}) \le P_{mus}(t_{m+2}) \\ . \\ . \\ P_{mus}(t_{q-1}) \le P_{mus}(t_q) \\ P_{mus}(t_q) = P_{mus}(t_{q+1}) \\ . \\ . \\ P_{mus}(t_{N-1}) = P_{mus}(t_N) \end{array}\right\} \textit{monotonicity constraints}$$

$$\left.\begin{array}{l} P_{min} \le P_{mus}(t_k) \le P_{max} \\ R_{min} \le R_{rs} \le R_{max} \\ E_{min} \le E_{rs} \le E_{max} \\ k = 1,2,\ldots,N \end{array}\right\} \textit{domain constraints}$$

Note that the monotonicity constraints written above assume knowledge of the transition time , t_m and t_q, between regions with different P_{mus} monotonicity. However, this is not the case in real applications. Therefore, the algorithm should also search for the optimal monotonicity transition times. However, since the transition time t_m has a more critical effect as it determines the time of maximum P_{mus}, a search is performed only for t_m whereas t_q is fixed:

$$t_q = t_m + K$$

where K is a constant that can be optimized off-line.

The full algorithm is summarized below and it has been implemented in Matlab using the *quadprog* subroutine (Optimization Toolbox) that solves a standard quadratic programming optimization method using the interior point method:

① $for\ i = 1\ to\ M$

solve the minimization problem

$$\min J_i = \sum_{t=1}^{N}\left(P_y(t) - R_{rs}\dot{V}(t) - E_{rs}V(t) - P_{mus}(t)\right)^2$$

$$\left.\begin{array}{c}
P_{mus}(t_2) \leq P_{mus}(t_1) \\
P_{mus}(t_3) \leq P_{mus}(t_2) \\
\dots \\
P_{mus}(t_{m-1}) \leq P_{mus}(t_{m-2}) \\
P_{mus}(t_m) \leq P_{mus}(t_{m-1}) \\
P_{mus}(t_m) \leq P_{mus}(t_{m+1}) \\
P_{mus}(t_{m+1}) \leq P_{mus}(t_{m+2}) \\
. \\
. \\
P_{mus}(t_{q-1}) \leq P_{mus}(t_q) \\
P_{mus}(t_q) = P_{mus}(t_{q+1}) \\
. \\
. \\
P_{mus}(t_{N-1}) = P_{mus}(t_N)
\end{array}\right\} \textit{monotonicity constraints}$$

$$\left.\begin{array}{c}
P_{min} \leq P_{mus}(t_k) \leq P_{max} \\
R_{min} \leq R_{rs} \leq R_{max} \\
E_{min} \leq E_{rs} \leq E_{max} \\
k = 1,2,\dots,N
\end{array}\right\} \textit{domain constraints}$$

② choose $R_{rs}, E_{rs}, P_{mus}(t_1), \dots, P_{mus}(t_N)$ from $\min \{J_1, J_2, \dots, J_M\}$

where M is the number of possible candidates monotonicity switching time t_m. In order to reduce computational complexity, since knowledge of the exhalation and inhalation time is typically available from the ventilator, the search can be limited to a time window between the inhalation and the exhalation time. In fact, it is reasonable to assume that the peak of P_{mus} is always reached before the exhalation starts.

In conclusion, the algorithm is based on physiological assumptions on the actual P_{mus} profile that are translated into mathematical constraint to reduce the space of possible solutions of the LS problem. It accepts as inputs flow ($\dot{V}$), pressure (P_{ao}) and volume (V) data pertaining to a respiratory cycle and provides as output an estimated single value of R_{rs} and E_{rs} (or C_{rs}), and an estimated $P_{mus}(t)$ signal for that particular respiratory cycle. From the estimated $P_{mus}(t)$, then WOB can be computed at each breath. The algorithm requires a batch of data and hence it is an off-line algorithm. However, provided that the optimization routine is fast enough, it can theoretically provide a value of R_{rs} and E_{rs} (or C_{rs}) and WOB at every breath (with a certain delay) and hence it allows for continuous monitoring of respiratory mechanics and WOB. The drawback of the algorithm is its computational complexity. It currently takes about 7 sec to process a 5 sec batch of data on a regular i7 CORE processor laptop.

3.4.2 Modified Kalman Filter (MKF) Algorithm

This second algorithm works on-line, without requiring a batch of data and provides estimation of respiratory system resistance R_{rs} and elastance E_{rs} (or compliance C_{rs}), as well as a time-continuous estimated $P_{mus}(t)$ signal in real time. It is based a multi-stage process, where the elastance E_{rs} is first estimated, then the current estimate of E_{rs} is used as input to a second estimator for R_{rs}, and then finally an estimate of $P_{mus}(t)$ is computed from the equation of motion (Eq. 3-1) using the estimated values of R_{rs} and E_{rs}. A schematic diagram explaining the principles of operation of the algorithm is shown in Figure 3.11. A description of the three different estimation stages is provided next.

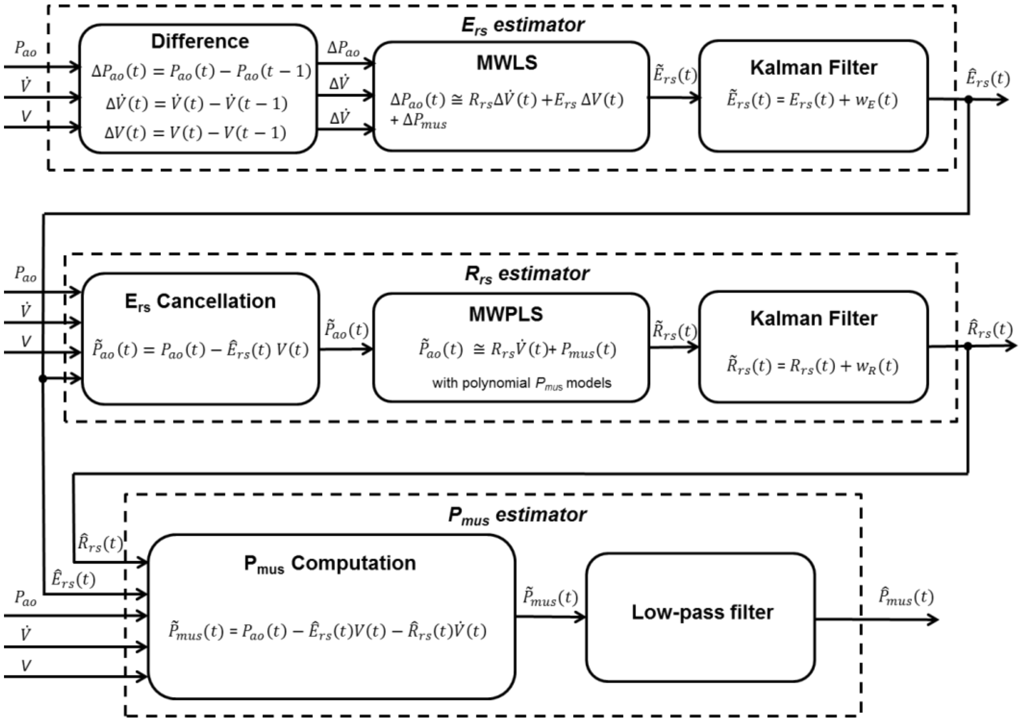

Figure 3.11- Schematic diagram of the MKF algorithm. Figure courtesy of Dong Wang, Philips Research North America.

E_{rs} *Estimator* **:** The first stage of the proposed algorithm consists in estimating the elastance E_{rs} using the available measurements ($\dot{V}$, P_{ao} and V). A difference operation is performed on the input data and then a Moving Window Least Squares (MWLS) algorithm is applied on the differential version of the 1st order single-compartment equation of motion:

$$\Delta P_{ao}(t) = R_{rs}\Delta\dot{V}(t) + E_{rs}\Delta V(t) + \Delta P_{mus}(t)$$

The difference operation improves the dynamics of the input signals and hence improves the performance of the LS estimator. The MWLS estimator works as described hereafter. A sliding window of size L is considered. Within that window, the P_{mus} difference signal, $\Delta P_{mus}(t)$, is assumed to be a constant, ΔP_{mus}. This means that P_{mus} is locally approximated by a linear function of time within the window. Also, it is assumed that R_{rs} and E_{rs} are constant in a sliding window. Therefore, the above difference equation becomes:

$$\Delta P_{ao}(t) \cong R_{rs}\Delta\dot{V}(t) + E_{rs}\Delta V(t) + \Delta P_{mus}$$

At time t, the MWLS algorithm uses the input signals within the sliding window $[t-L+1, t]$ to estimate R_{rs}, E_{rs}, and ΔP_{mus} jointly based on the classical LS formulation. The output of this operation is a vector of parameter estimates for that specific window $[\tilde{E}_{rs}(t), \tilde{R}_{rs}(t), \Delta\tilde{P}_{mus}(t)]$. Then, the window is shifted one sample ahead and the LS computation is repeated obtaining estimates of the parameters for the shifted window $[\tilde{E}_{rs}(t+1), \tilde{R}_{rs}(t+1), \Delta\tilde{P}_{mus}(t+1)]$. The process is repeated sequentially, as data are collected. The concept of MWLS is illustrated in Figure 3.12.

$$\Delta P_{ao}(t) \cong R_{rs}\Delta\dot{V}(t) + E_{rs}\,\Delta V(t) + \Delta P_{mus}$$
$$[\tilde{E}_{rs}, \tilde{R}_{rs}, \Delta\tilde{P}_{mus}]^T = (H^T H)^{-1} H^T Z$$
$$Z = [\Delta P_{ao}(t), \Delta P_{ao}(t-1), \dots, \Delta P_{ao}(t-L+1)]^T$$
$$H = [h(t), h(t-1), \dots, h(t-L+1)]^T$$
$$h(t) = [\Delta V(t), \Delta\dot{V}(t), 1]^T$$
$$\delta_{\tilde{E}_{rs}} = (H^T H)^{-1}_{1,1} * \delta_{\Delta P_{ao}}$$

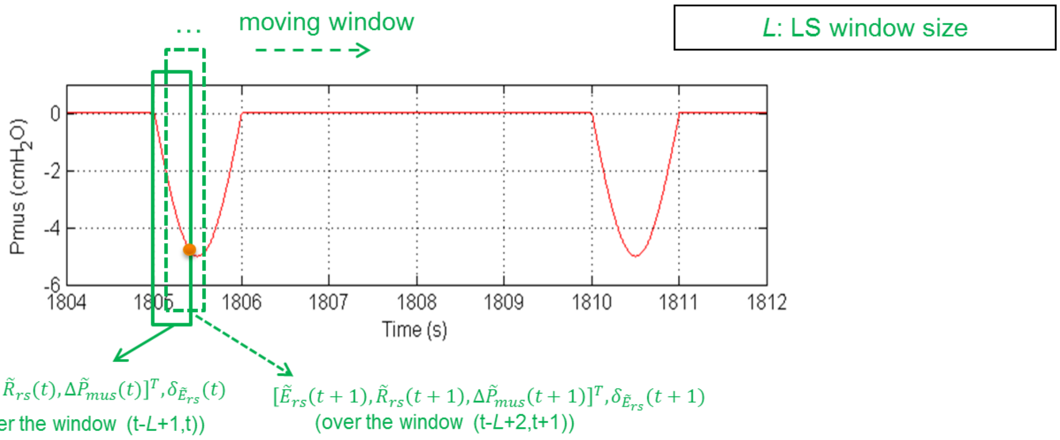

Figure 3.12- Schematic illustration of the MWLS algorithm. Figure courtesy of Dong Wang and Francesco Vicario, Philips Research North America.

From the MWLS outputs, only the E_{rs} estimate ($\tilde{E}_{rs}$) is used in the subsequent steps. In fact, it has been verified via simulation studies that estimation of E_{rs} is robust and the errors in the estimates are absorbed by the resistive and the ΔP_{mus} terms. Furthermore, the variance $\delta_{\tilde{E}_{rs}}(t)$ of the estimated elastance $\tilde{E}_{rs}$ is computed for every window as shown in Figure 3.12, where $\delta_{\Delta P_{ao}}$is the variance of the noise estimated as the variance of the sum of square residuals:

$$\delta_{\Delta P_{ao}} = \left(Z - H[\tilde{E}_{rs}, \tilde{R}_{rs}, \Delta\tilde{P}_{mus}]^T \right)^T \left(Z - H[\tilde{E}_{rs}, \tilde{R}_{rs}, \Delta\tilde{P}_{mus}]^T \right) / L$$

Since the estimated elastance $\tilde{E}_{rs}$ has a high variance, a Kalman filter operator is applied in order to filter out artefacts due to noise. The implementation of the Kalman filter is based on the following state-space model:

- ✓ **State process equation:** $E_{rs}(t) = E_{rs}(t-1) + \omega_E(t), \quad \omega_E(t) \sim N(0, \delta_E)$
- ✓ **Observation equation:** $\tilde{E}_{rs}(t) = E_{rs}(t) + \omega_{LE}(t), \quad \omega_{LE}(t) \sim N(0, \delta_{\tilde{E}_{rs}}(t))$

Where E_{rs} is modelled as a random walk process, based on the assumption that it can only vary slowly in time. The standard formulation of the Kalman filter is shown in Figure 3.13.

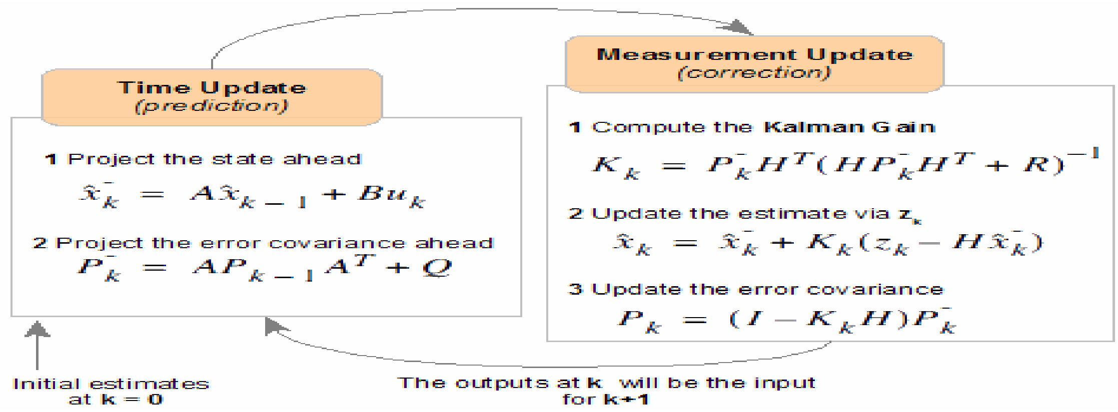

Figure 3.13- Standrad formulation of the Kalman filter. X_k, true state varaible at time k; X_{k-1}, true state variable at time k-1; u_k, input to the system; z_k, observed state at time k; Q, covariance matrix of the process noise; R, covariance matrix of the observation noise; P_k, error covariance matrix.

Hence, we can simply apply it to the above state space model assuming that:

$$A = 1 \qquad B = 0 \qquad Q = \delta_E \qquad R = \delta_{\tilde{E}_{rs}}(t) \qquad H = 1$$

where $\delta_E$is the design parameter and $\delta_{\tilde{E}_{rs}}(t)$ is the variance of the MWLS outputs computed for every window as described above.

***R_{rs}* Estimator** : The second stage of the proposed algorithm consists in estimating the resistance R_{rs} using the available measurements ($\dot{V}$, P_{ao} and V) and the estimated elastance $\hat{E}_{rs}(t)$ from the previous stage. First, the elastic term from the equation of motion is cancelled (E_{rs} cancellation) since the elastance is now assumed to be known:

$$\tilde{P}_{ao}(t) = P_{ao}(t) - \hat{E}_{rs}(t) \cdot V(t)$$

Then, a second MWLS algorithm is used in order to estimate R_{rs} and P_{mus} from the resulting simplified equation of motion:

$$\tilde{P}_{ao}(t) \cong R_{rs}\dot{V}(t) + P_{mus}(t)$$

In this case, since we have seen from simulation studies that estimation of R_{rs} is very sensitive to noise and model errors, a more accurate local approximation of P_{mus} is used in the moving window, as compared to the previous MWLS algorithm (where P_{mus} was assumed a linear function of time within the window). Particularly, based on the same “gold standard” P_{mus} profile shown in the previous section (Figure 3.10), here we assumed that P_{mus} can be locally approximated by a polynomial function of time, from which the name Polynomial Mowing Window Least Squares (PMWLS):

$$P_{mus}(t) \cong a_0 + a_1 t + a_2 t^2 + \cdots a_M t^M$$

The PMWLS will estimate R_{rs} and the coefficients $a_0, a_1, \ldots\ldots, a_M$ of the polynomial above. The degree M of the polynomial used to approximate P_{mus} will have huge impact on the estimator performance. Furthermore, as illustrated in Figure 3.14 it is reasonable to assume that the optimal degree of the polynomial will depend on the location of the moving window.

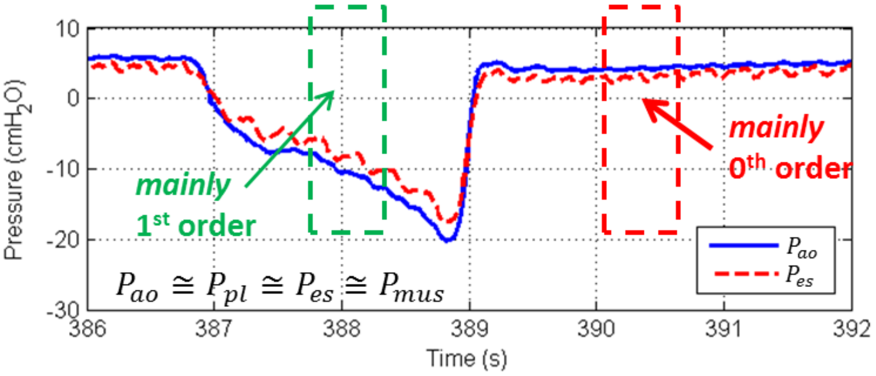

Figure 3.14 – Experimental profile of aiway pressure (P_{ao}) and esophageal pressure (P_{es}) obtained from a pig during an occlusion maneuver. The profile can be assumed as a “gold standard” profile of P_{mus}. Note the different regions where different polynomial orders can be used to locally approximate the actual P_{mus} profile. Figure courtesy of Dong Wang, Philips Research North America.

For instance, in the central region a 1st order polynomial seems appropriate, whereas in the relaxation region a 0th order polynomial seems more appropriate. Hence, a "dynamic" polynomial order optimization scheme is proposed: three MWLS estimations are performed in each moving window with the polynomial order of 0, 1, and 2, respectively; the resulting R_{rs} estimates from all the three MWLS estimators are then combined together in such a way that the one with the least estimate variance will dominate. Specifically, the three MWLS estimations are implemented as below:

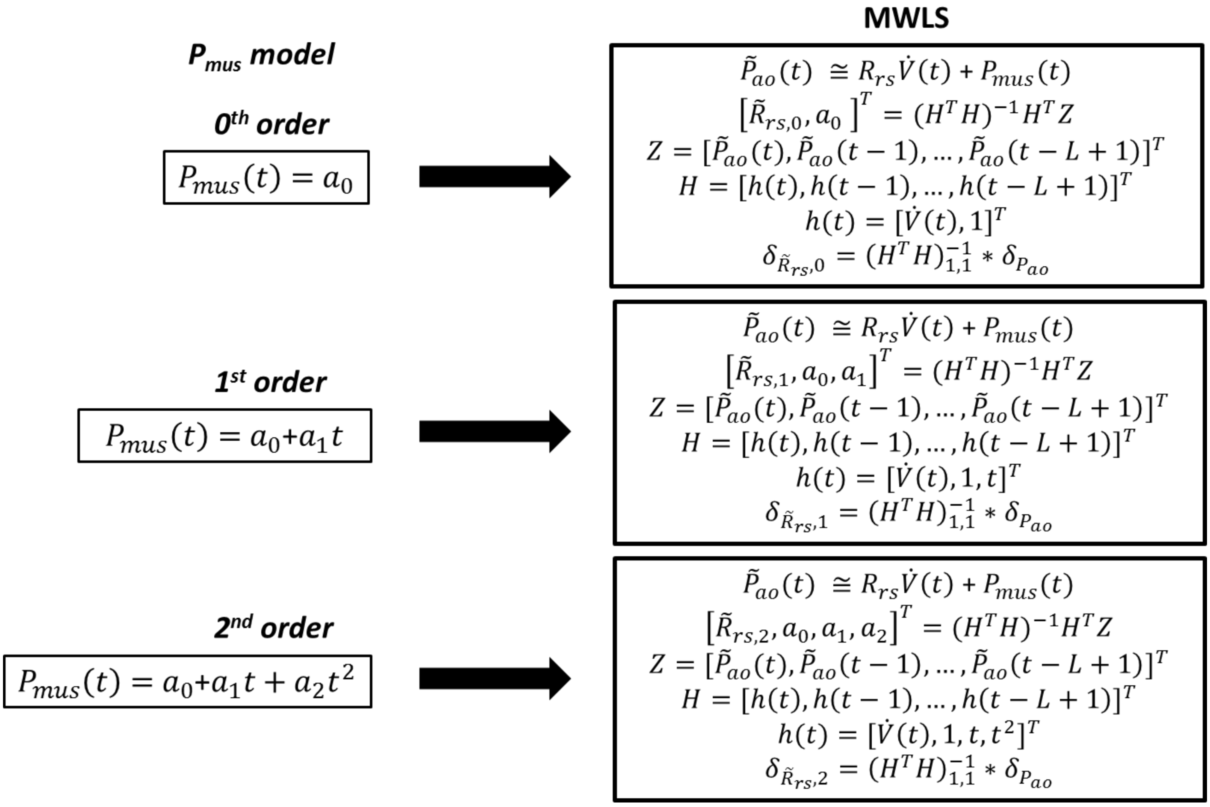

P_{mus} model

MWLS

0th order

$$P_{mus}(t) = a_0$$

$$\tilde{P}_{ao}(t) \cong R_{rs}\dot{V}(t) + P_{mus}(t)$$
$$\left[\tilde{R}_{rs,0}, a_0\right]^T = (H^TH)^{-1}H^TZ$$
$$Z = [\tilde{P}_{ao}(t), \tilde{P}_{ao}(t-1), \dots, \tilde{P}_{ao}(t-L+1)]^T$$
$$H = [h(t), h(t-1), \dots, h(t-L+1)]^T$$
$$h(t) = [\dot{V}(t), 1]^T$$
$$\delta_{\tilde{R}_{rs},0} = (H^TH)^{-1}_{1,1} * \delta_{P_{ao}}$$

1st order

$$P_{mus}(t) = a_0 + a_1 t$$

$$\tilde{P}_{ao}(t) \cong R_{rs}\dot{V}(t) + P_{mus}(t)$$
$$\left[\tilde{R}_{rs,1}, a_0, a_1\right]^T = (H^TH)^{-1}H^TZ$$
$$Z = [\tilde{P}_{ao}(t), \tilde{P}_{ao}(t-1), \dots, \tilde{P}_{ao}(t-L+1)]^T$$
$$H = [h(t), h(t-1), \dots, h(t-L+1)]^T$$
$$h(t) = [\dot{V}(t), 1, t]^T$$
$$\delta_{\tilde{R}_{rs},1} = (H^TH)^{-1}_{1,1} * \delta_{P_{ao}}$$

2nd order

$$P_{mus}(t) = a_0 + a_1 t + a_2 t^2$$

$$\tilde{P}_{ao}(t) \cong R_{rs}\dot{V}(t) + P_{mus}(t)$$
$$\left[\tilde{R}_{rs,2}, a_0, a_1, a_2\right]^T = (H^TH)^{-1}H^TZ$$
$$Z = [\tilde{P}_{ao}(t), \tilde{P}_{ao}(t-1), \dots, \tilde{P}_{ao}(t-L+1)]^T$$
$$H = [h(t), h(t-1), \dots, h(t-L+1)]^T$$
$$h(t) = [\dot{V}(t), 1, t, t^2]^T$$
$$\delta_{\tilde{R}_{rs},2} = (H^TH)^{-1}_{1,1} * \delta_{P_{ao}}$$

The three estimates $\tilde{R}_{rs,0}$, $\tilde{R}_{rs,1}$ and $\tilde{R}_{rs,2}$ are combined using a maximal ratio combining criteria, where the resulting resistance estimates $\tilde{R}_{rs}$ is a combination of the three estimates weighted by their corresponding variances ratio:

$$\tilde{R}_{rs} = \tilde{R}_{rs,0} * w_0 + \tilde{R}_{rs,1} * w_1 + \tilde{R}_{rs,2} * w_2$$

$$w_0 = \frac{\frac{1}{\delta_{\tilde{R}_{rs},0}}}{\frac{1}{\delta_{\tilde{R}_{rs},0}} + \frac{1}{\delta_{\tilde{R}_{rs},1}} + \frac{1}{\delta_{R_{rs},2}}}$$

$$w_1 = \frac{\frac{1}{\delta_{\tilde{R}_{rs},1}}}{\frac{1}{\delta_{\tilde{R}_{rs},0}} + \frac{1}{\delta_{\tilde{R}_{rs},1}} + \frac{1}{\delta_{\tilde{R}_{rs},2}}}$$

$$w_2 = \frac{\frac{1}{\delta_{\tilde{R}_{rs},2}}}{\frac{1}{\delta_{\tilde{R}_{rs},0}} + \frac{1}{\delta_{\tilde{R}_{rs},1}} + \frac{1}{\delta_{\tilde{R}_{rs},2}}}$$

$$\delta_{\tilde{R}_{rs}} = \frac{1}{\frac{1}{\delta_{\tilde{R}_{rs},0}} + \frac{1}{\delta_{\tilde{R}_{rs},1}} + \frac{1}{\delta_{\tilde{R}_{rs},2}}}$$

Finally, in order to further filter the noise effects, a Kalman filter is applied similar to what described for the previous stage (E_{rs} estimator).

***P_{mus} Estimator* :** In the last stage of the proposed algorithm, an estimate of $P_{mus}(t)$ is first computed via the equation of motion, using the available data and the resistance and elastance values from the 2 previous stages:

$$\tilde{P}_{mus}(t) = P_{ao}(t) - \hat{E}_{rs}(t) \cdot V(t) - \hat{R}_{rs}(t) \cdot \dot{V}(t)$$

Then, finally, a low pass filter is used in order to remove artefacts coming from the airway pressure signal (e.g., cardiogenic oscillations), resulting in the final estimate $\tilde{P}_{mus}(t)$. From the estimated $P_{mus}(t)$, then WOB can be computed at each breath.

3.5 Algorithm Validation

The first step in the successful development of any system identification, or parameter estimation, algorithm is its validation on synthetic data generated via simulations. Algorithm validation on synthetic data offers the advantage of a controlled environment and allows reproducibility. Only after validation on synthetic data, will the proposed algorithm be tested on real data under desired conditions. Hence, for each of the above mentioned methods, extensive validation has been performed using a simulation approach. When using data for validation or testing, it is preferable to use data that reflects the actual dynamics of the system we are identifying. For this reason, in the 1st verification process, data have been obtained using a commercial lung simulator (ASL5000, Ingmar Medical) connected to a real mechanical ventilator. After verifying algorithm correctness on these simulated data, both algorithms have been validated on real data obtained via a pig test. A detailed description of the verification on simulated data, the animal test and the data collection, and the final algorithms' validation on the real data follows.

3.5.1 Verification on Simulated Data

In the 1st verification stage, data (airway opening pressure, flow and volume) were obtained using a commercial breathing simulator (ASL5000, Ingmar Medical) connected to a real ventilator (Esprit, Philips-Respironics). The ASL5000 is essentially a physical model of the respiratory system that can be connected to a real ventilator as a virtual patient. The simulator consists of a mechanically controlled piston-cylinder that behaves as the 1st order single-compartment model shown above (see Figure 3.5). The simulator can be programmed with given profiles of R_{rs}, E_{rs} and P_{mus} and hence it can be used to simulate spontaneously breathing patients. In order to verify the 2 proposed algorithms, simulations were performed using the ASL5000 connected to the ventilator under pressure support ventilation (PSV) mode. The ASL5000 was programmed with a nominal realistic P_{mus} profile that was obtained by concatenating the P_{mus} profile shown in Figure 3.10 over several respiratory cycles. The resistance and compliance of the underlying 1st order single-compartment model were set to constant, but a step transition in both R_{rs} and E_{rs} was induced during the simulations. Data were collected using a flow and pressure sensor (NM_3 monitor, Philips-Respironics) at the Y-piece of the breathing circuit between the ventilator and the ASL5000 simulator. Both the CLS and the MKF algorithms were run on the collected data and the results were compared with the nominal values of R_{rs}, E_{rs} and P_{mus}. The agreement between the estimated parameters and their corresponding nominal values was excellent for both algorithms, even during the step transitions in the nominal parameters. Figure 3.15 – 3.18 show examples of such validations for both the CLS and the MKF algorithm. From these figures we can see how the two algorithms are able to correctly estimate the values of R_{rs} and E_{rs} and to track their variations almost immediately. This is very important in the contest of continuous monitoring of respiratory mechanics, where the mechanical properties of the patients' respiratory system can drastically change over time and we want our algorithm to be able to detect those changes. Furthermore, as clearly shown in Figure 3.16 and Figure 3.18, which are zoomed versions of Figure 3.15 and Figure 3.17, respectively, the estimation of P_{mus} is also very accurate with both algorithms. The proven correctness of the theoretical approach via this simulation study gave us confidence about the proposed algorithms, which were then further tested on real animal data.

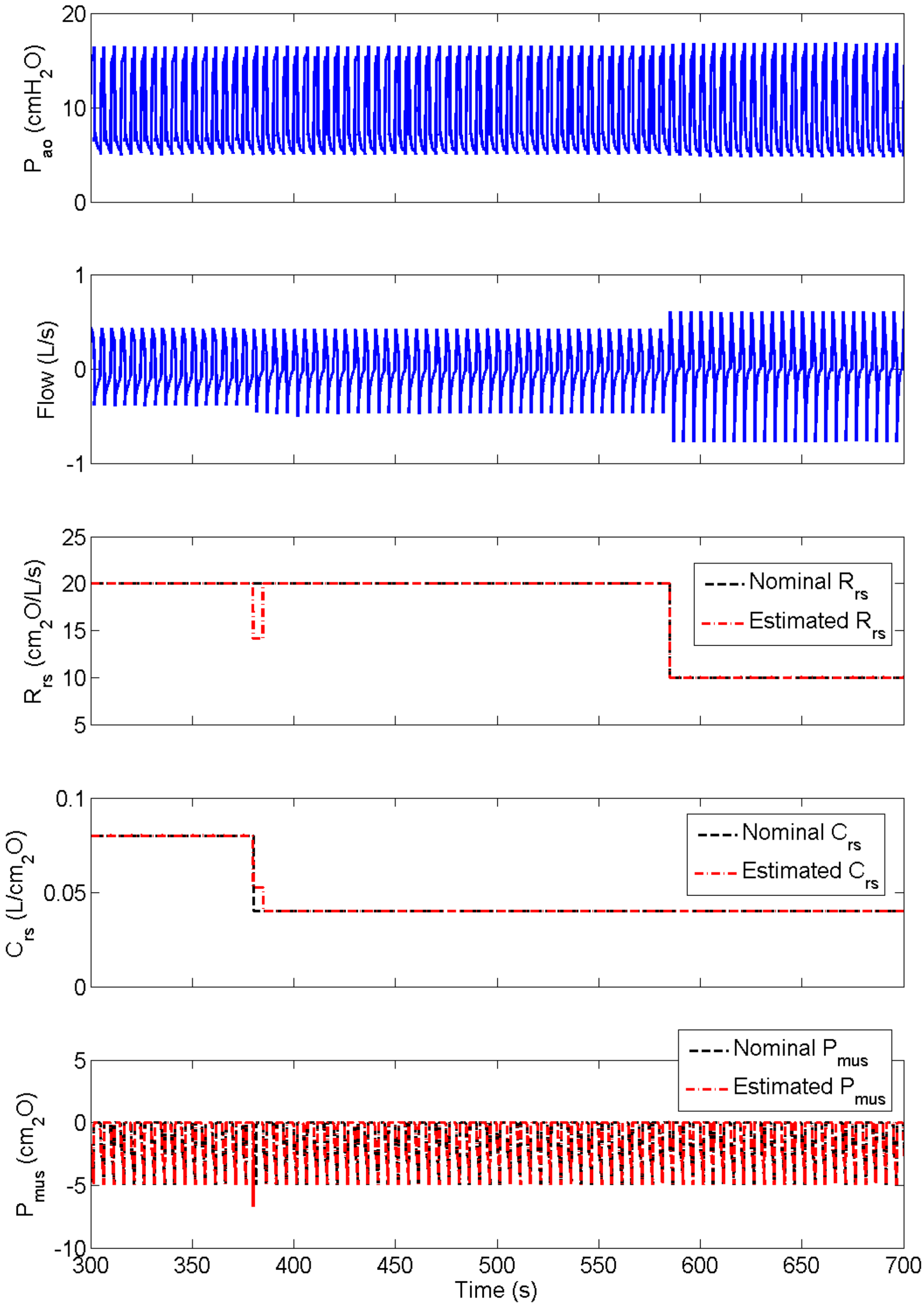

Figure 3.15-Results of CLS estimation using the ASL5000 generated data. Figure courtesy of Nikolaos Karamolegkos, Philips Research North America.

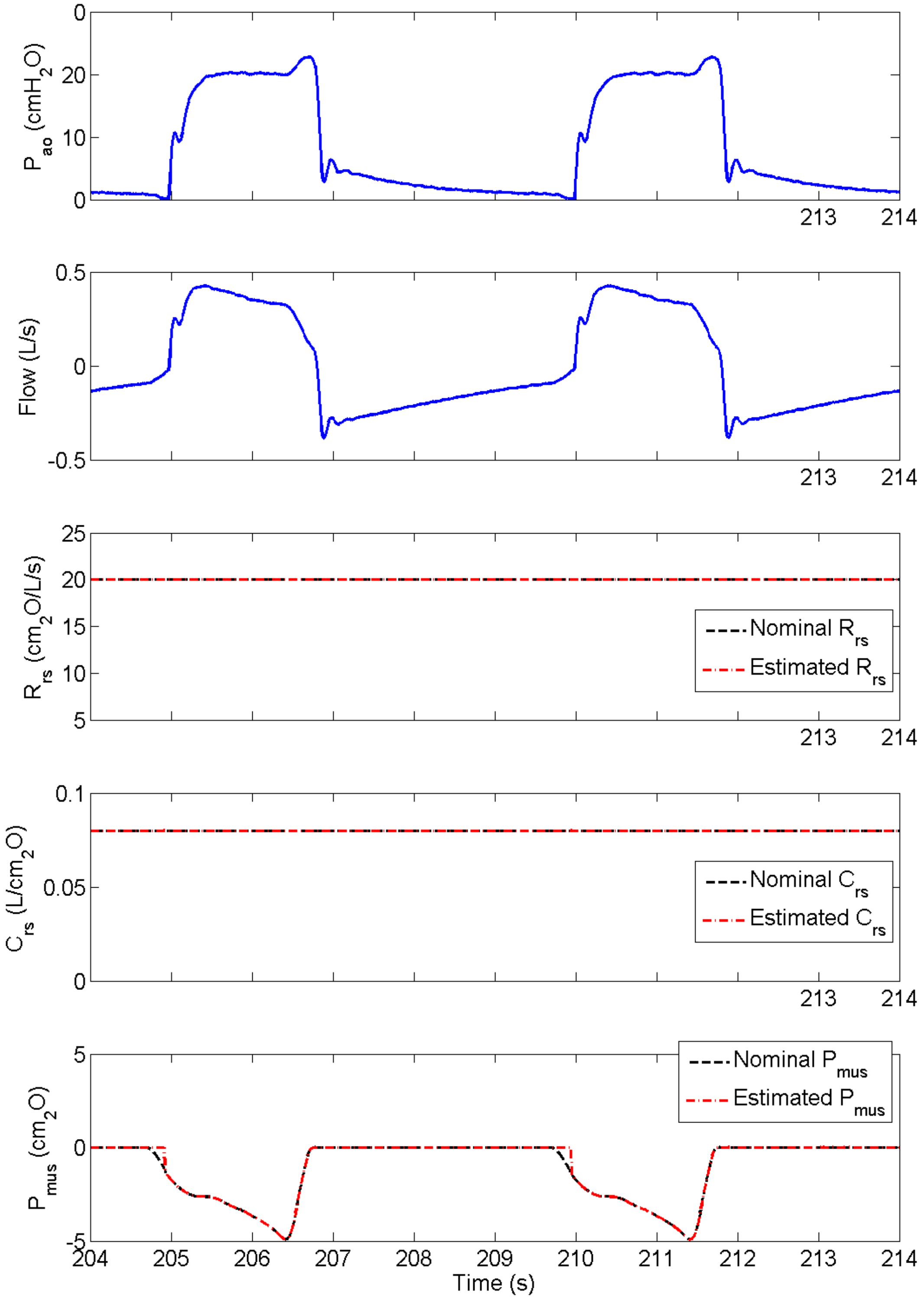

Figure 3.16 - Zoomed version of Figure 3.15 highlighting the accuracy of the P_{mus}, R_{rs} and C_{rs} estimation obtained using the CLS apporach. Figure courtesy of Nikolaos Karamolegkos, Philips Research North America.

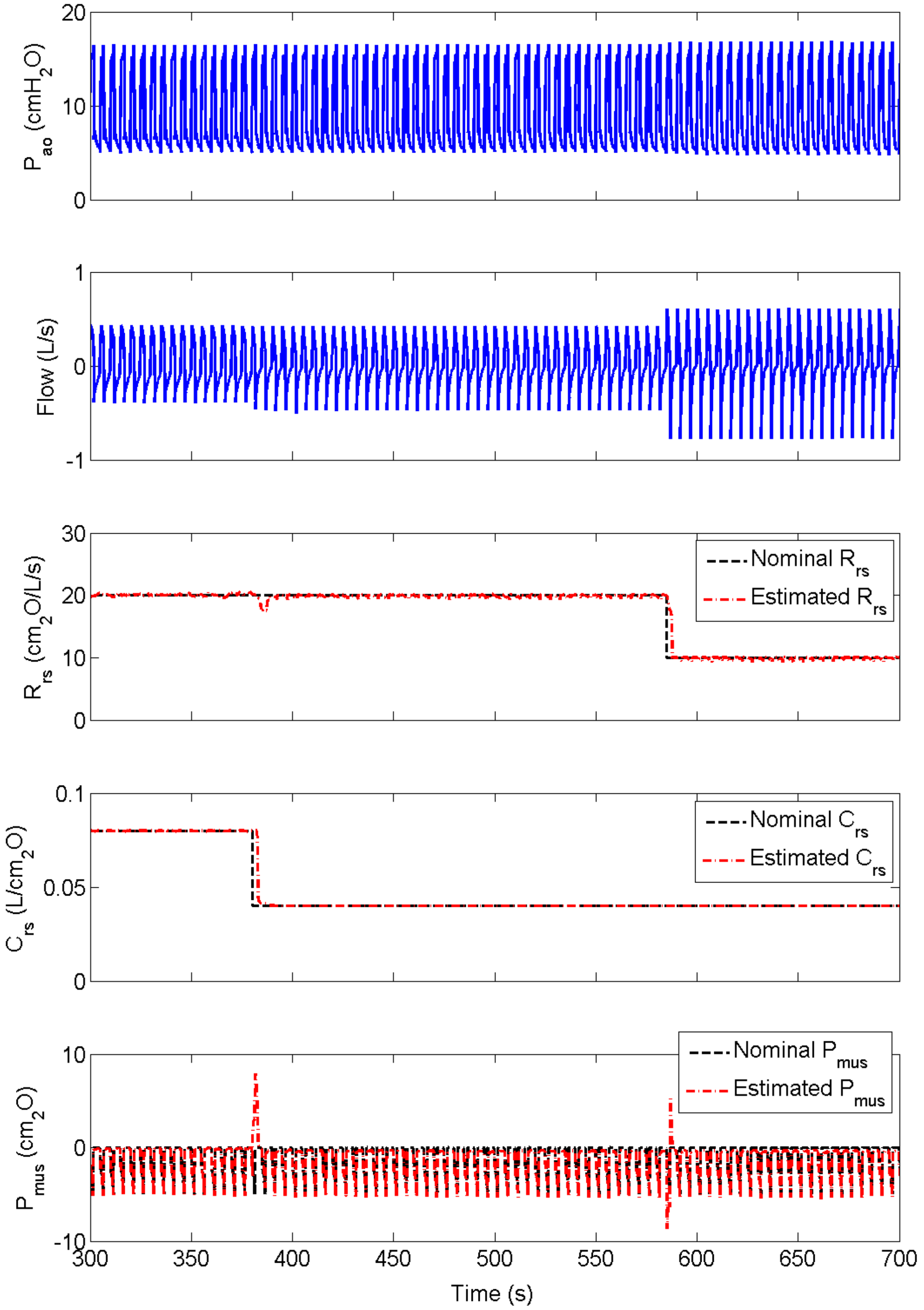

Figure 3.17 - Results of MKF estimation using the ASL5000 generated data. Figure courtesy of Nikolaos Karamolegkos, Philips Research North America.

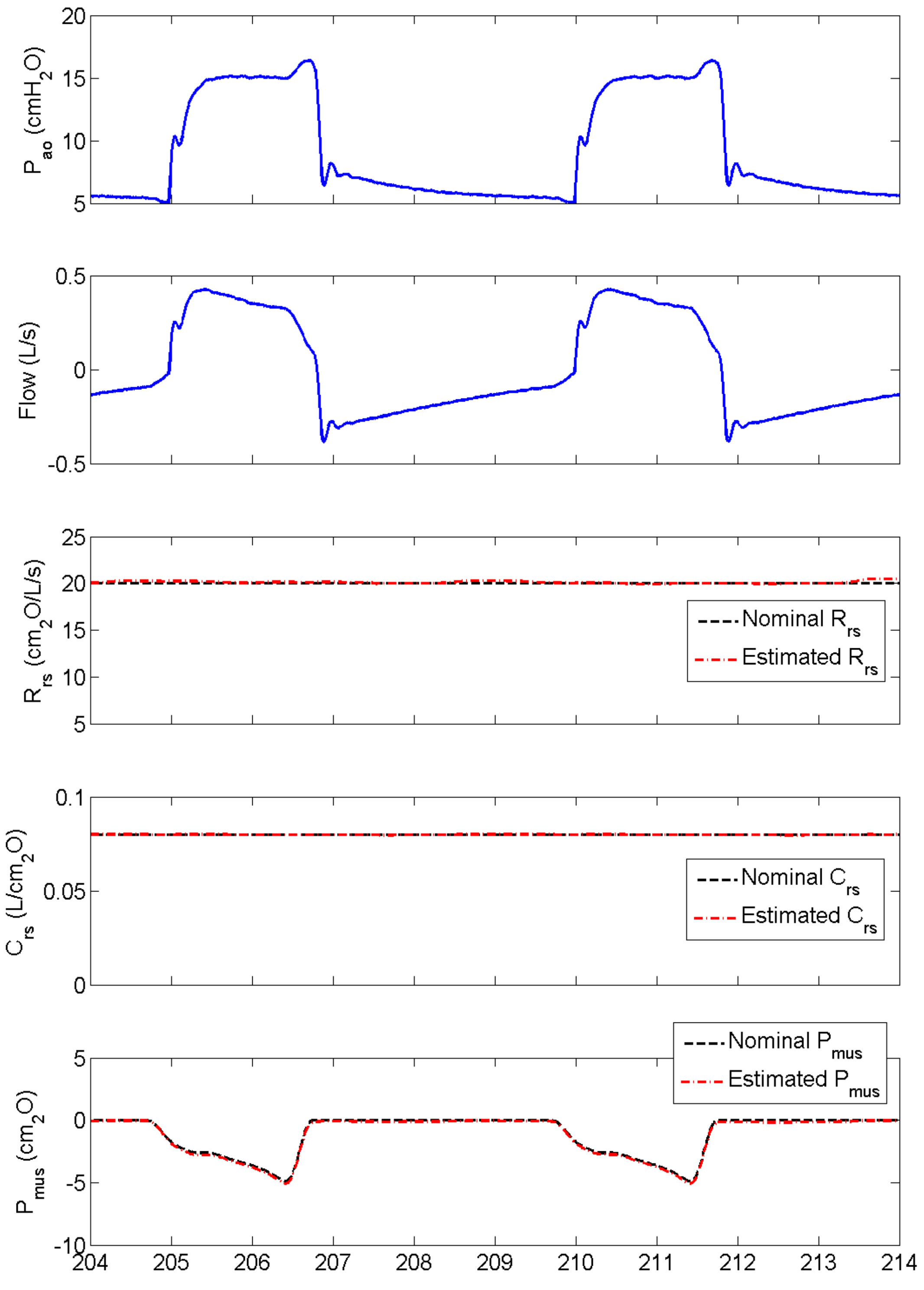

Figure 3.18 - Zoomed version of Figure 3.17 highlighting the accuracy of the P_{mus}, R_{rs} and C_{rs} estimation. Figure courtesy of Nikolaos Karamolegkos, Philips Research North America.

3.5.2 Pig Test and Data Collection

Because of the similarities between the human and the pig respiratory system, experiments for data collection and algorithm testing have been performed on a mechanically ventilated adult pig model. The experiments took place at the Pulmonary Research and Animal Laboratory of Duke University Medical Center. The experimental protocol was reviewed and approved by the local institutional committee, prior to execution of the experiment. The pig was anaesthetized, intubated and connected to a commercial mechanical ventilator (AVEA, Carefusion). The choice to use this particular ventilator was dictated by the need to compare the estimated WOB against a gold standard WOB (the AVEA is the only commercial ventilator that computes WOB via esophageal manometry). Airway pressure ($P_{ao}(t)$) and flow ($\dot{V}(t)$) were measured at the Y-piece, between the breathing circuit and the endotracheal tube, via sensors connected to the ventilator. The volume signal ($V(t)$) was obtained by numerical integration of the flow waveform. The esophageal pressure (P_{es}) was measured using an esophageal balloon connected to a pressure transducer embedded in the AVEA ventilator. This allows having gold standard P_{mus} and WOB measurements. All the data were acquired and collected at a sampling frequency of at least 100 Hz, using a dedicated system for real-time data acquisition. The two algorithms (CLS and MKF) previously described were implemented on a real-time platform and run during the experiment to allow for usability testing. The test was performed for several hours, during which the pig was subject to different ventilator modes and maneuvers, including periods of pressure support ventilation (PSV) at variable levels and hipercapnic challenges with variable $FiCO_2$ to induce changes in the respiratory muscle drive P_{mus}.

3.5.3 Validation on Real Data

Validation of the two proposed algorithms (CLS and MKF) was performed retrospectively using the real data from the pig test, by comparing the estimated R_{rs}, C_{rs} , P_{mus} and WOB against their corresponding gold standards. The gold standard WOB was computed by the ventilator, using the Campbell diagram and the invasive esophageal pressure measurements. The gold standard R_{rs} and C_{rs} were computed as follows:

1) The 1st order single compartment model of the lung (see Figure 3.6 and Eqs. 3-5 and 3-6) was fitted via the LS technique to the $P_{ao}(t) - P_{es}(t)$ signals, providing estimates of R_L and E_L.
2) The values of R_{cw} and E_{cw} (or C_{cw}) were estimated by applying the LS technique to the equation of motion of the chest wall (see Figure 3.6) under the assumptions of zero respiratory muscle pressure P_{mus}:

$$P_{pl}(t) = R_{cw} \cdot \dot{V}(t) + E_{cw} \cdot V(t) + P_0$$

   and using P_{es} as a surrogate for P_{pl}. Note that estimation of R_{cw} and E_{cw} was limited to specific datasets pertaining to conditions of Volume Controlled Ventilation (VCV), during which the absence of P_{mus} was confirmed by no negative deflections in the esophageal pressure tracing. Since there is no evidence in the literature that chest-wall mechanics is flow or volume-dependent, the values of R_{cw} and E_{cw} computed for the VCV conditions were assumed to be valid for the remaining datasets.

3) The lung and chest wall parameters were then combined to yield the parameters pertaining to the whole respiratory system (lungs+chest wall):

$$R_{rs} = R_L + R_{cw}$$

$$E_{rs} = E_L + E_{cw} \quad \text{or} \quad 1/C_{rs} = 1/C_L + 1/C_{cw}$$

Finally, the gold standard for P_{mus} was computed from the invasive esophageal pressure measurements (P_{es}) and using the chest wall parameters computed as described above, according to (see Figure 3.6):

$$P_{mus}(t) = P_{es}(t) - R_{cw} \cdot \dot{V}(t) - E_{cw} \cdot V(t)$$

In the following sections, the results of this validation process are summarized for each of the two algorithm proposed. In presenting the results, we denoted the gold standards as “invasive” measurements, whereas we denoted the results of the proposed algorithms as “noninvasive” estimates.

3.5.3.1 CLS Algorithm Validation

The validation results of the CLS algorithm are summarized in Figure 3.19 - Figure 3.24.

Figure 3.19 shows the comparison between estimated (noninvasive) and gold standard (invasive) R_{rs}, C_{rs} and WOB under different PSV levels ranging from 20 cmH_2O to 0 cmH_2O (no support from the ventilator). By looking at the invasive gold standard measurements (data in red), two interesting phenomenon can be observed as the PSV levels is gradually reduced (as indicated in the top P_{ao} waveform plot): *1)* The resistance R_{rs} is gradually reduced following the PSV level transitions; this is essentially due to the flow-dependent nature of R_{rs} [116] and to the fact that as PSV is reduced, the flow (not shown in the figure) drops as well. *2)* The WOB gradually increases in synchrony with the PSV reductions; this is in agreement with physiological knowledge [107] and can be explained by the fact that reductions in PSV induce increases in the respiratory muscle drive (P_{mus}) and hence in WOB. The mechanisms by which PSV changes alter the respiratory muscle drive are not clearly understood: the chemoreflex might certainly be involved if reductions in PSV (and hence in minute ventilation) cause an increase in the CO_2 and/or a decrease in the O_2 arterial blood contents that are sufficient to trigger peripheral and central chemoreceptors, thus increasing respiratory muscles drive; additional feedbacks mediated by mechanoreceptors in the lungs might also contribute to this phenomenon. By looking at the noninvasive estimated data (in green), we can observe that the CLS algorithm is able to estimate fairly accurately R_{rs}, C_{rs} and WOB up to PSV values of 10 cmH_2O. Particularly, the algorithm is capable of tracking variations in both R_{rs} and WOB and provide estimates of C_{rs} that matches the gold standard invasive measurements. However, as the PSV is further reduced to zero, the estimated R_{rs} and C_{rs} deviate from their corresponding gold standards and the estimated WOB, in turn, becomes inaccurate. Figure 3.20 shows how the estimated P_{mus} compare with the invasive gold standard measurements in the three different PSV regions (20, 10 and 0 cmH_2O). It confirms that the algorithm is able to estimate the P_{mus} profile with an acceptable level of accuarcy for PSV values of 20 and 10 (cmH_2O), whereas at 0 PSV the performance of the algorithm are compromised.

Figure 3.21 shows the comparison between estimated (noninvasive) and gold standard (invasive) R_{rs}, C_{rs} and WOB under conditions of constant PSV (5 cmH_2O) and variable FiCO_2 levels (0, 2.5 and 5%). By looking at the invasive gold standard measurements (data in red), we can clearly see how the resistance and compliance are not affected by the variations in FiCO_2, whereas the WOB directly follows the FiCO_2 variations. Particularly, as FiCO_2 increases, the WOB rises due to the respiratory drive increase induced by the hypercapnic stimulus. The opposite happens when FiCO_2 is decreased. This mechanism is in agreement with physiological knowledge and can be ascribed to the action of the central chemoreceptors (see section 2.6.2). By looking at the noninvasive estimated data (in green), we can observe that the CLS algorithm is able to estimate fairly accurately the resistance R_{rs}, whereas C_{rs} and WOB estimates present substantial deviations from their corresponding gold standards. Particularly, the C_{rs} is overestimated and the WOB is underestimated. Furthermore, the transition from 2.5 to 5% $FiCO_2$, seems to be the most critical: the algorithm essentially confounds the variations in P_{mus}, driven by the hypercapnic stimuli, with increase in the compliance C_{rs}. This interpretation is confirmed by the analysis on the P_{mus} waveforms shown in Figure 3.22, from which we can see how the algorithm is not capable to track the variations in P_{mus} amplitude when transitioning from 2.5 to 5% $FiCO_2$.

As outcome of the above analysis, and as confirmed by additional results that are not shown here for the sake of brevity, the CLS algorithm seems to perform quite well when the PSV levels are sufficiently high (10-20 cmH_2O) and suffereing at lower PSV levels (5-0 cmH_2O). The regression analysis between estimated (noninvasive) and gold standard (invasive) WOB measurements for the high PSV cases is shown in Figure 3.23. The corresponding Bland-Altman plot in shown in Figure 3.24. This diagram shows the WOB error values as a function of the gold standard WOB values. The mean of the error and the ± 1 standard deviation limits are also shown in the diagram. Figure 3.24 proves that at high PSV the proposed CLS algorithm provides a slightly biased WOB estimate with samll standard deviations: mean error of -0.1311 J/L with standard deviation of 0.1277 J/L.

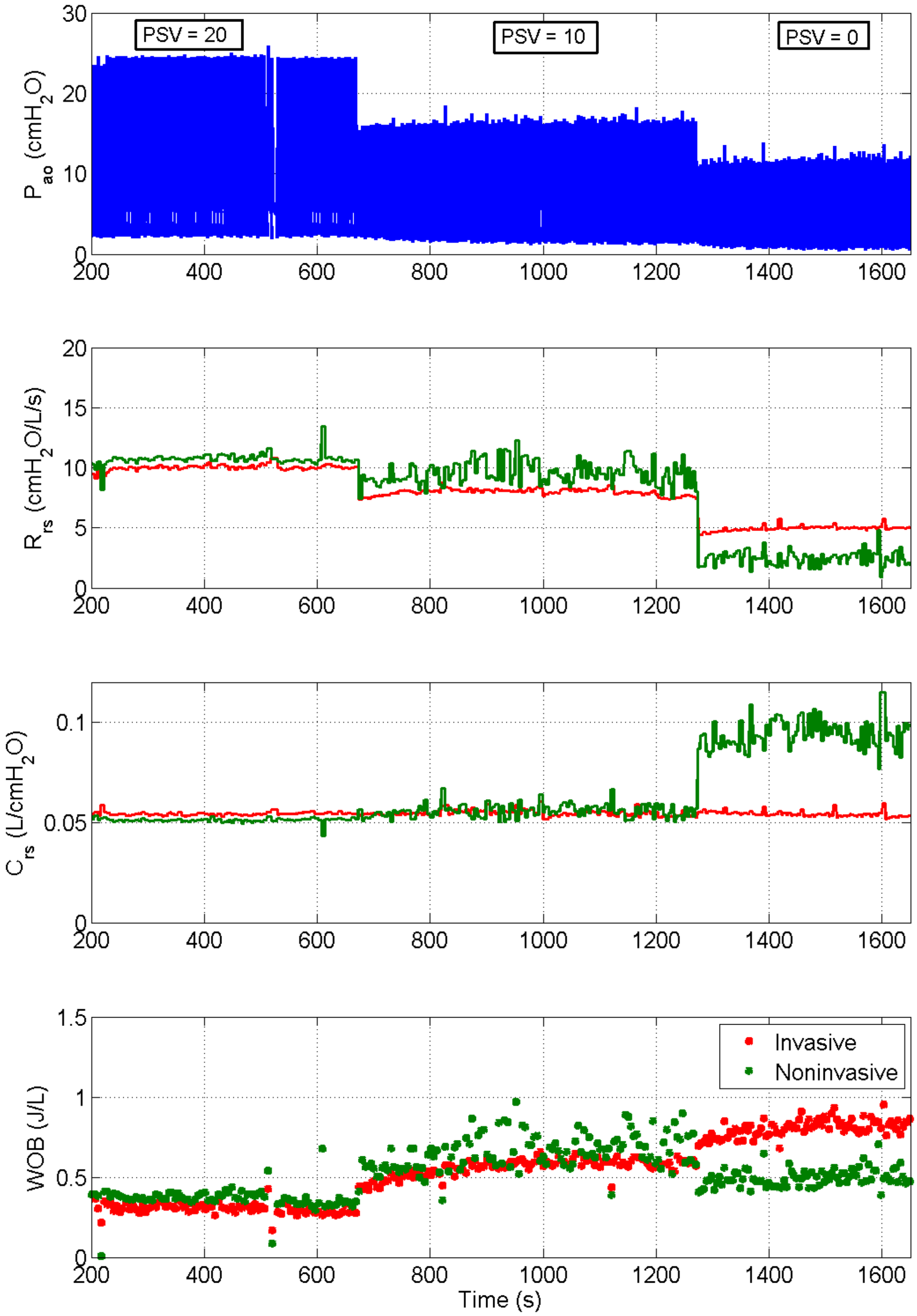

Figure 3.19 – Validation results of the CLS algorithm under different PSV levels (20, 10 and 0 cmH$_2$O). P_{ao}, airway opening pressure; R_{rs}, respiratory system resistance; C_{rs}, respiratory system compliance; WOB, work of breathing. Data in green are noninvasive estimates provided by the CLS algorithm; data in red are invasive gold standard measurements obtained as described above (see 3.5.3 section).

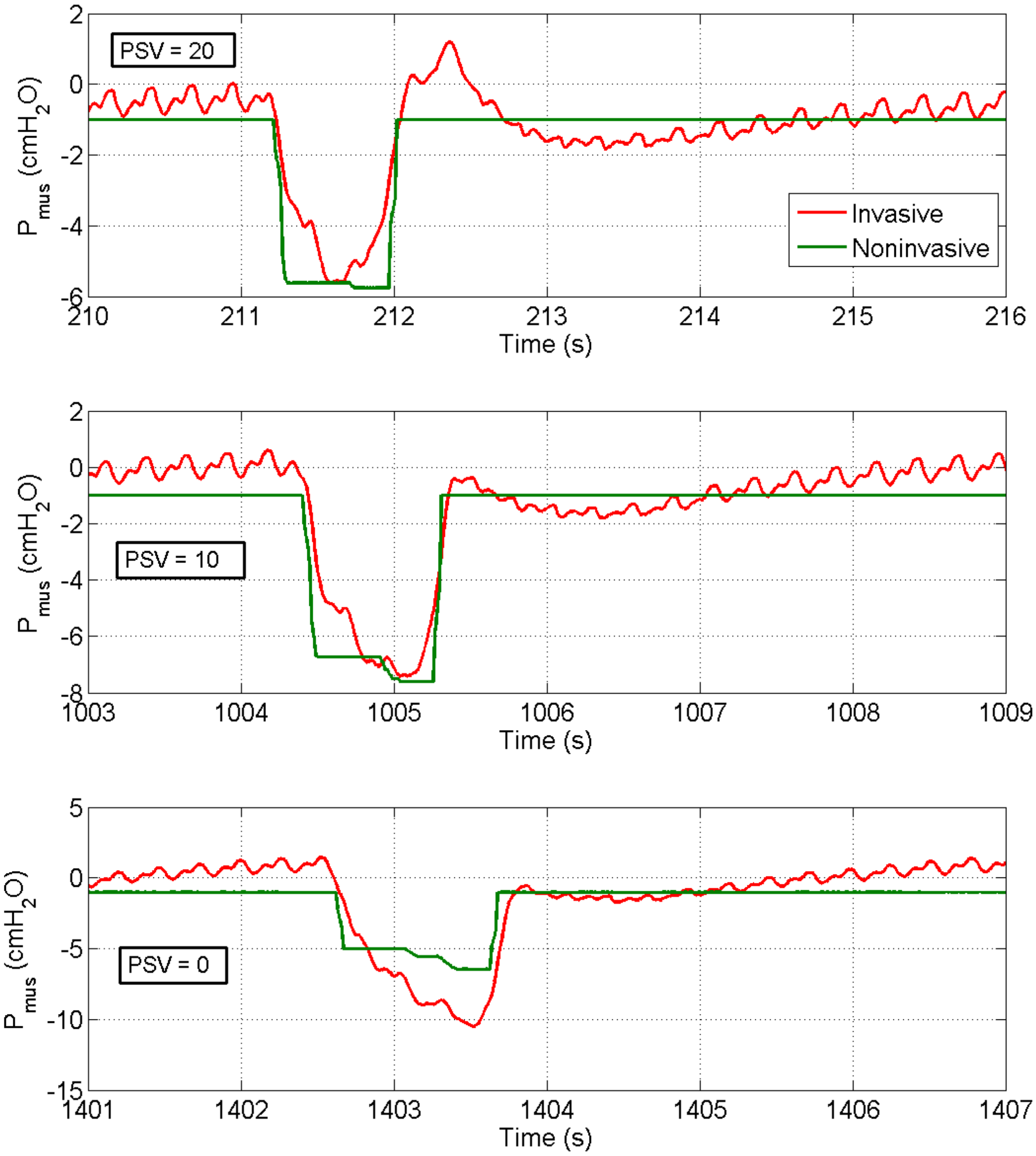

Figure 3.20 – Validation results of the CLS algorithm under different PSV levels (20, 10 and 0 cmH$_2$O). P_{mus}, respiratory muscle pressure. Data in green are noninvasive estimates provided by the CLS algorithm; data in red are invasive gold standard measurements obtained as described above (see 3.5.3 section).

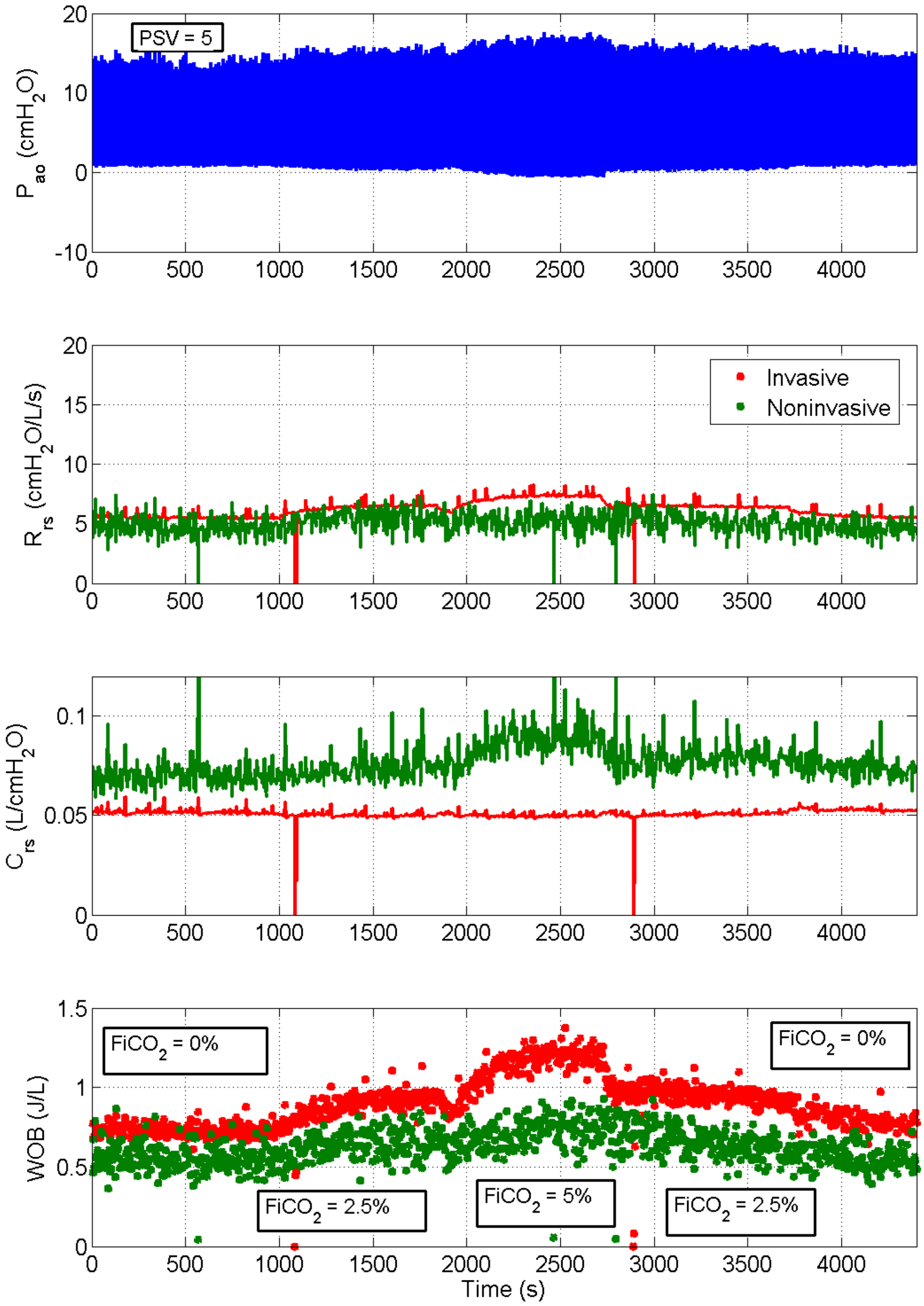

Figure 3.21 – Validation results of the CLS algorithm under 5 PSV level and different FiCO$_2$ levels (0, 2.5 and 5%). *P_{ao}*, airway opening pressure; *R_{rs}*, respiratory system resistance; *C_{rs}*, respiratory system compliance; WOB, work of breathing. Data in green are noninvasive estimates provided by the CLS algorithm; data in red are invasive gold standard measurements obtained as described above (see 3.5.3 section).

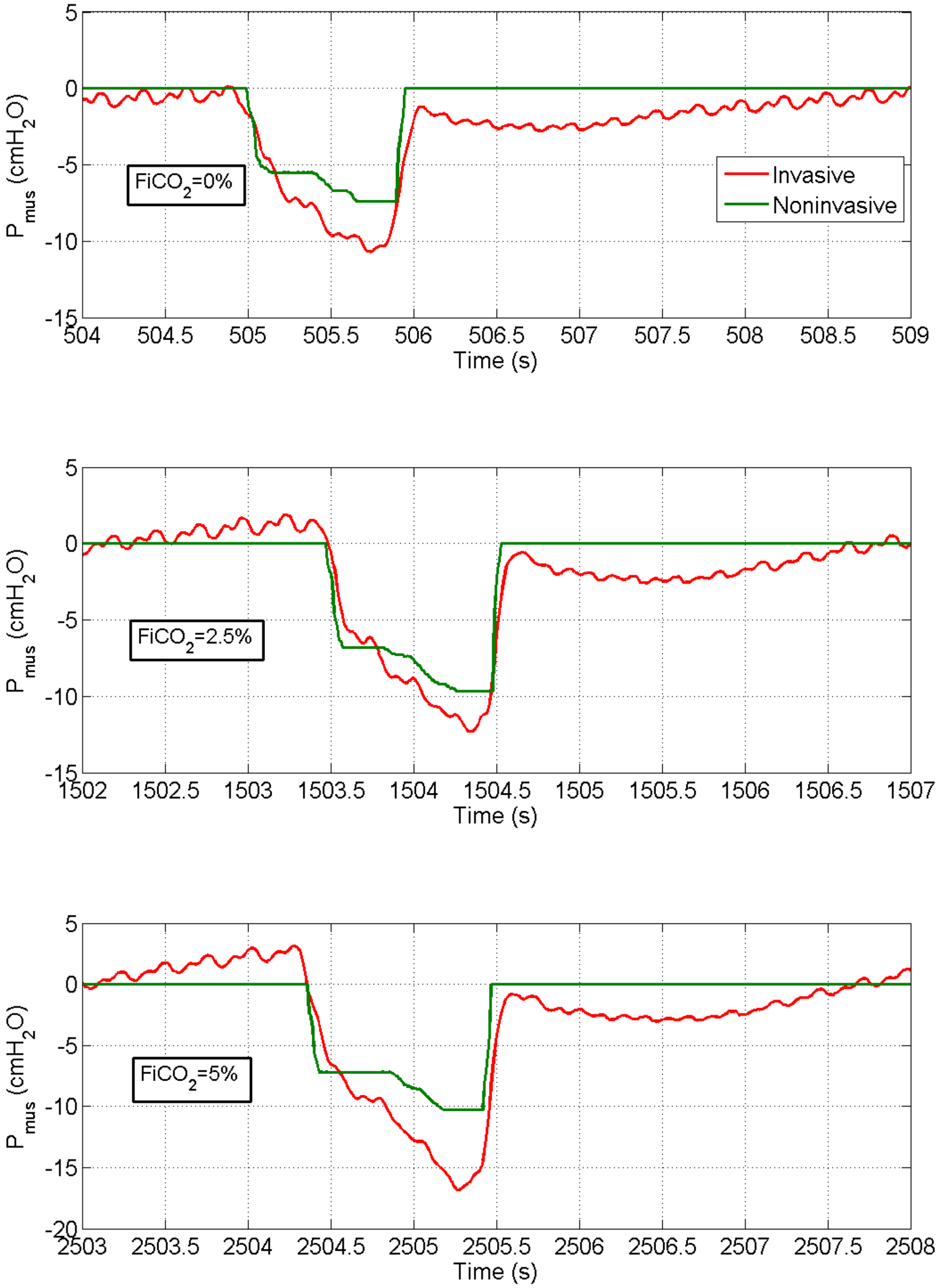

Figure 3.22 – Validation results of the CLS algorithm under 5 PSV level and different $FiCO_2$ levels (0, 2.5 and 5%). P_{mus}, respiratory muscle pressure. Data in green are noninvasive estimates provided by the CLS algorithm; data in red are invasive gold standard measurements obtained as described above (see 3.5.3 section).

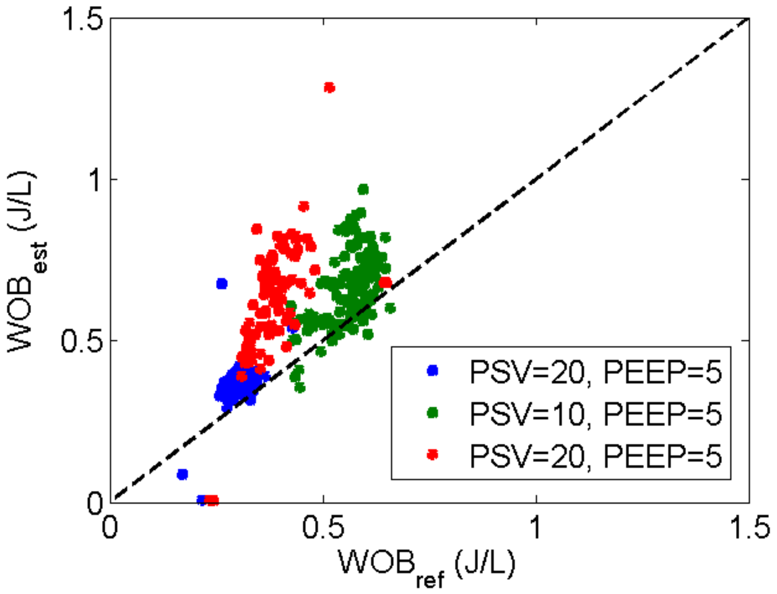

Figure 3.23 – Regression analysis between estimated WOB by the CLS algorithm (y axis) and gold standard WOB (x axis) under high PSV level (20-10 cmH$_2$O) conditions. The value of positive end expiratory pressure (PEEP) used in the corresponding experimental condition is also reported in the legend.

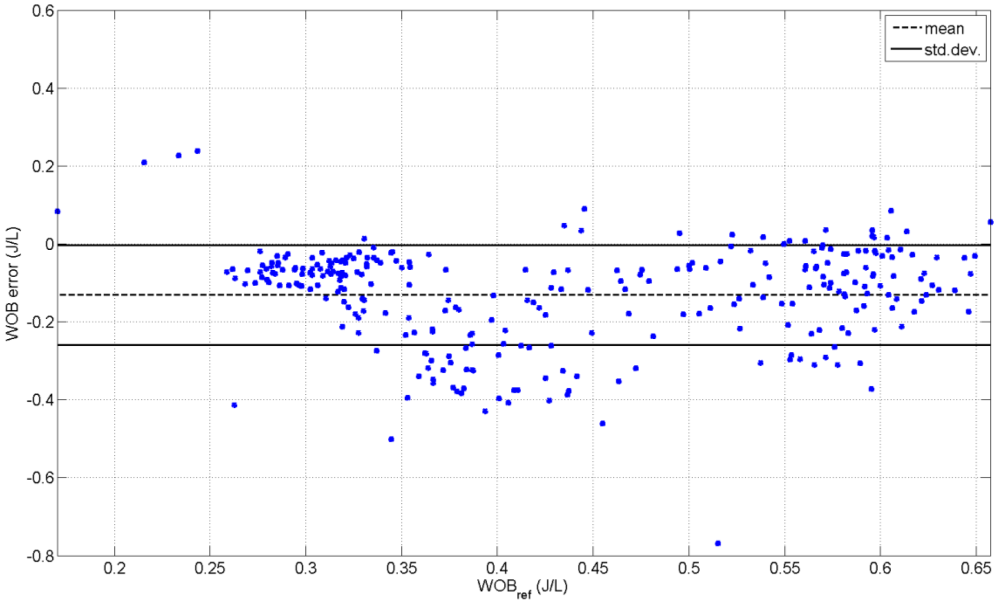

Figure 3.24 – Bland-Altman plot corresponding to the results in Figure 3.23. The WOB error (y axis) is plotted against the gold standard WOB (x axis). Mean (dashed horizontal lines) and ±1 std limits (solid horizontal lines) are also shown.

3.5.3.2 MKF Algorithm Validation

The validation results of the MKF algorithm are summarized in Figure 3.25 - Figure 3.30.

Figure 3.25 shows the results pertaining to the same dataset in Figure 3.19, characterized by the varying PSV levels (20, 10 and 0 cmH_2O). By looking at the noninvasive estimated data (in green), we can observe that the MKF algorithm is able to estimate fairly accurately R_{rs}, C_{rs} and WOB across the entire PSV range. However, greater accuracy is observed for the lower PSV levels (10 and 0 cmH_2O). Figure 3.26 shows how the estimated P_{mus} compare with the invasive gold standard measurements in the three different PSV regions (20, 10 and 0 cmH_2O). It confirms that the algorithm is able to estimate the P_{mus} profile with very high accuarcy at 0 PSV, whereas at higher PSV (10 and 20 cmH_2O) the performance of the algorithm degrade. Particularly, the presence of artefacts at the beginning of the discending phase and at the end of the relaxation phase can be observed in the estimated P_{mus} waveforms, especially at 20 PSV. These artefacts correspond to the triggering and cycling-off of the ventilator and may be due to non-linear intrabreath phenomenon (flow-dependent resistance, inhertance, valves dynamics, etc.) that the current 1st order single-compartment model does not take into account. Nevertheless, the algorithm is sill able to track the average changes of the resistance R_{rs}, due to the flow-dependency phenomenon, and the trend of the estimated WOB is always in agreement with the inavasive measurements even if the abosolute values are different.

Figure 3.27 shows the results pertaining to the same dataset in Figure 3.21, characterized by a constant PSV (5 cmH_2O) and variable $FiCO_2$ levels (0, 2.5 and 5%). By looking at the noninvasive estimated data (in green), we can observe the excellent performance of the MKF algorithm in this case: R_{rs} and C_{rs} are estimated fairly accurately; the agreemnt between invasive and noninvasive WOB is quite impressive for the whole range of $FiCO_2$. The level of accuracy in the WOB estimation is confirmed by the analysis on the

P_{mus} waveforms shown in Figure 3.28, from which we can see how well the algorithm tracks he variations in P_{mus} amplitude due to the $FiCO_2$ transitions. Furthermore, as opposed to the resulst of Figure 3.26, in this case since the PSV level is low (5 cmH_2O) the above mentioned artefacts at the ventilator triggering and cycling-off are no longer present.

As outcome of the above analysis, and as confirmed by additional results that are not shown here for the sake of brevity, the MKF algorithm seems to perform very well when the PSV levels are low (0-5 cmH_2O) and suffereing at higher PSV levels (10-20 cmH_2O). The regression analysis between estimated (noninvasive) and gold standard (invasive) WOB measurements for the low PSV cases is shown in Figure 3.29. The corresponding Bland-Altman plot (see Figure 3.30) shows that at low PSV the proposed MKF algorithm provides almost no bias and very samll standard deviations in the noninvasive estimated WOB: mean error of -0.0083 J/L with standard deviation of 0.0793 J/L.

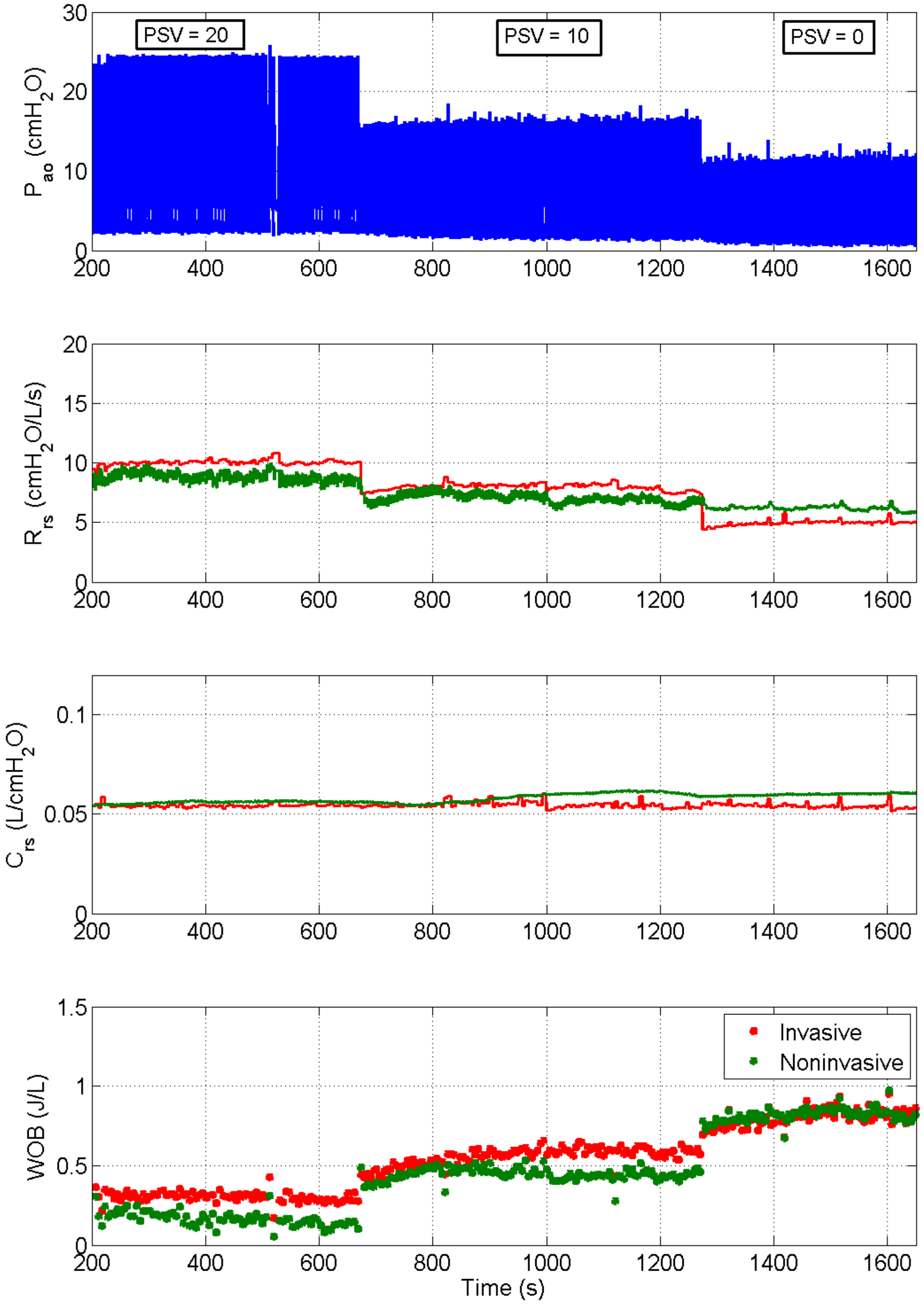

Figure 3.25 – Validation results of the MKF algorithm under different PSV levels (20, 10 and 0 cmH$_2$O). P_{ao}, airway opening pressure; R_{rs}, respiratory system resistance; C_{rs}, respiratory system compliance; WOB, work of breathing. Data in green are noninvasive estimates provided by the MKF algorithm; data in red are invasive gold standard measurements obtained as described above (see 3.5.3 section).

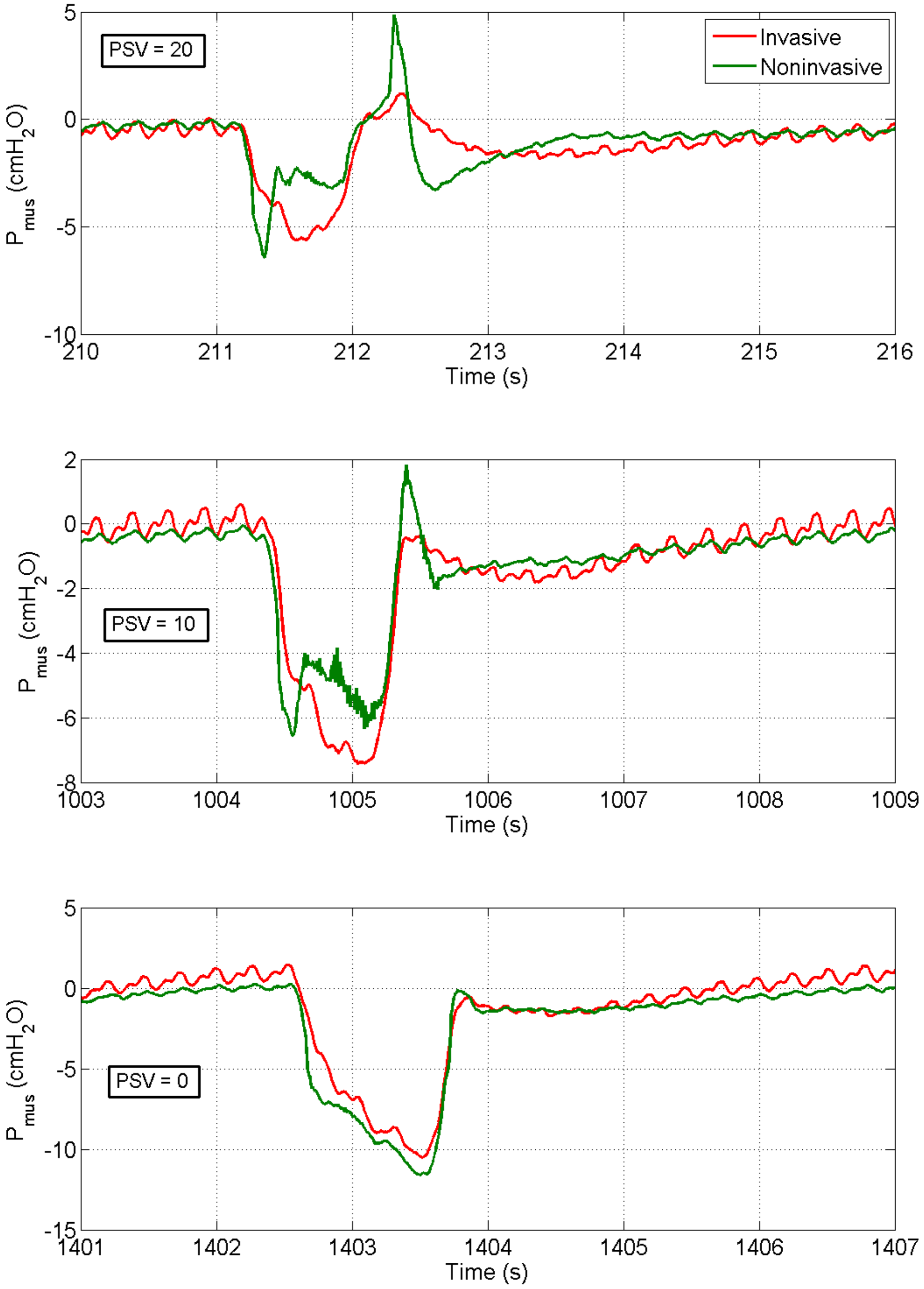

Figure 3.26 – Validation results of the MKF algorithm under different PSV levels (20, 10 and 0 cmH$_2$O). P_{mus}, respiratory muscle pressure. Data in green are noninvasive estimates provided by the MKF algorithm; data in red are invasive gold standard measurements obtained as described above (see 3.5.3 section).

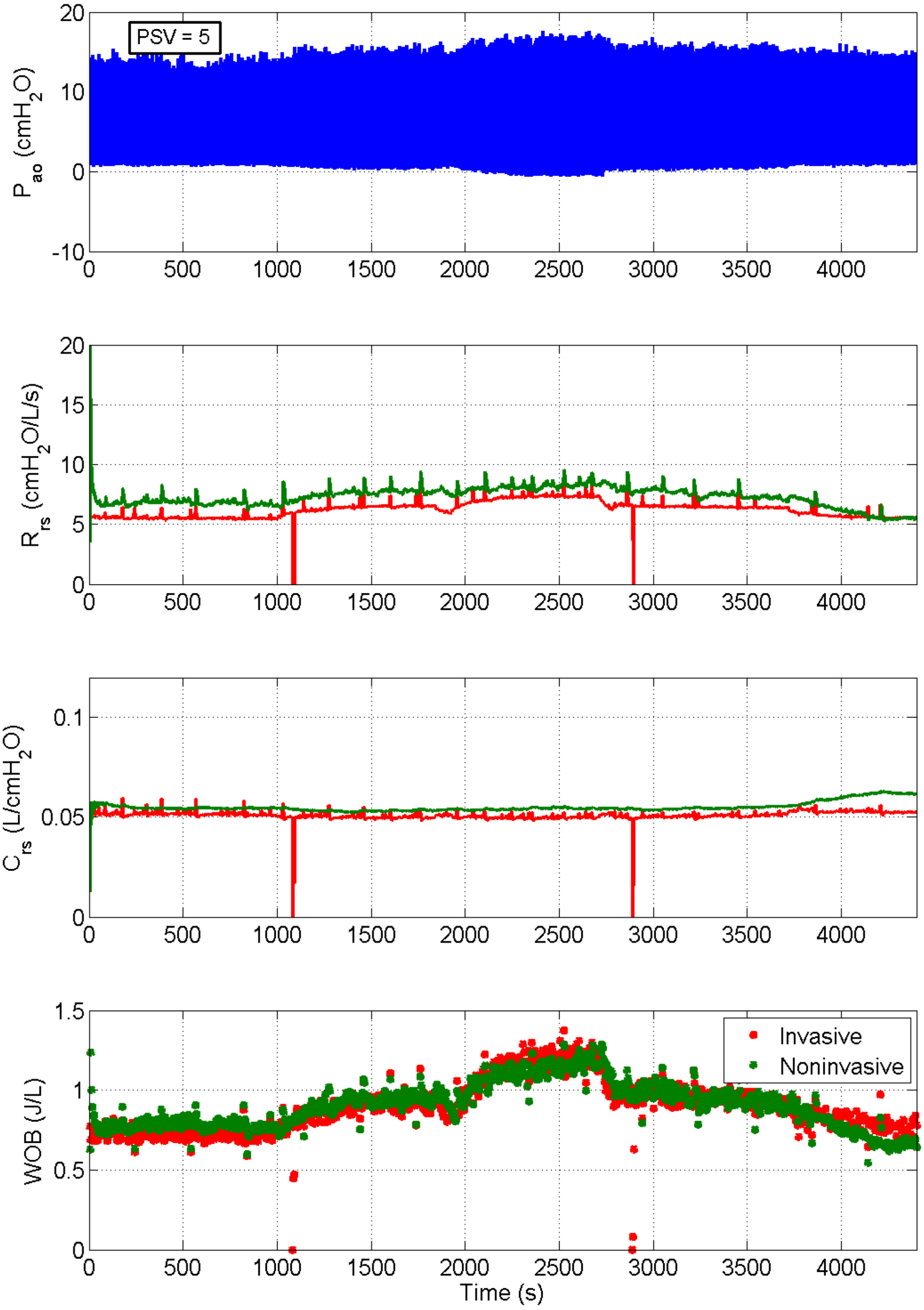

Figure 3.27 – Validation results of the MKF algorithm under 5 PSV level and different $FiCO_2$ levels (0, 2.5 and 5%). P_{ao}, airway opening pressure; R_{rs}, respiratory system resistance; C_{rs}, respiratory system compliance; WOB, work of breathing. Data in green are noninvasive estimates provided by the MKF algorithm; data in red are invasive gold standard measurements obtained as described above (see 3.5.3 section).

\

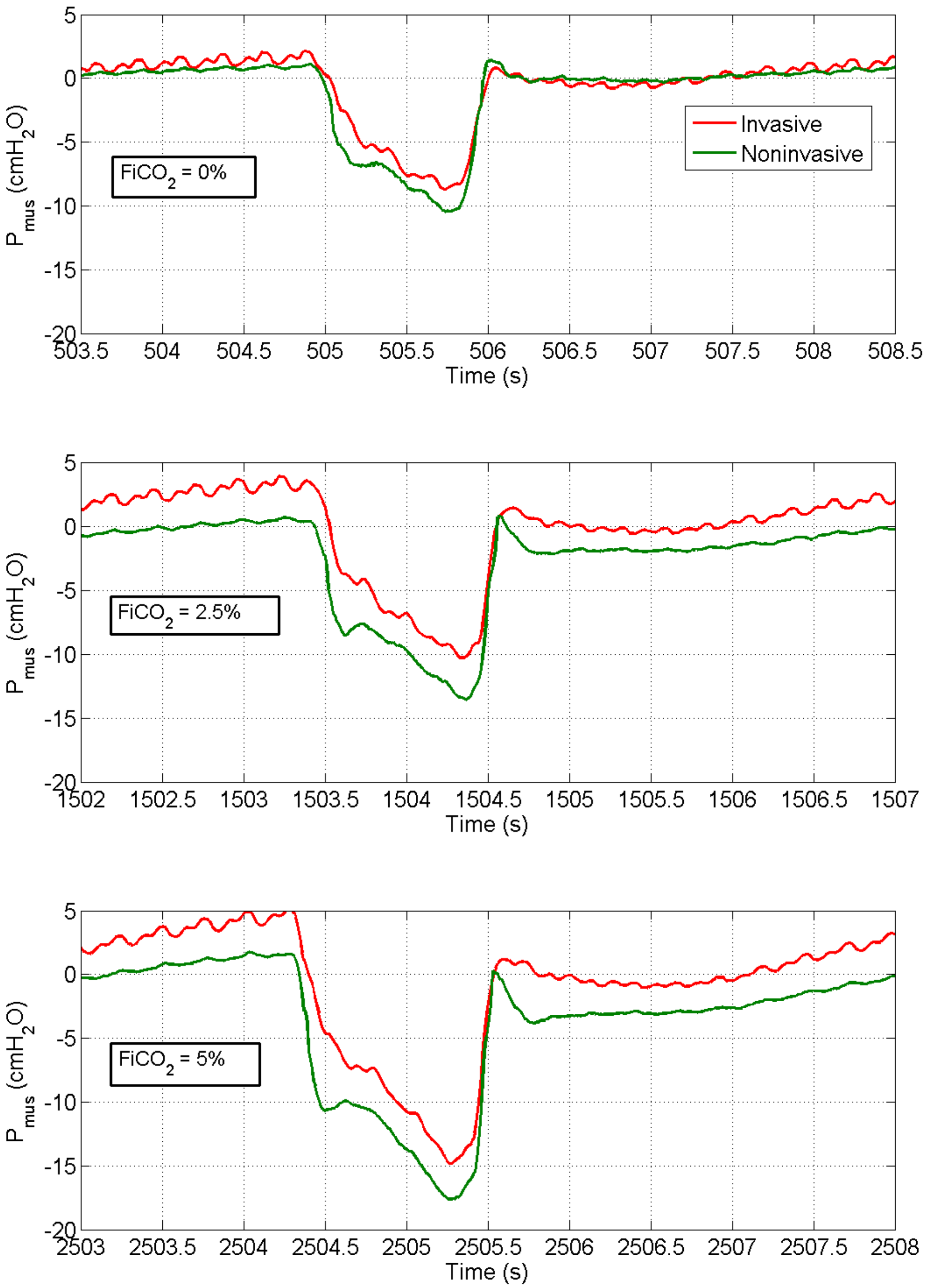

Figure 3.28 – Validation results of the MKF algorithm under 5 PSV level and different FiCO$_2$ levels (0, 2.5 and 5%). P_{mus}, respiratory muscle pressure. Data in green are noninvasive estimates provided by the MKF algorithm; data in red are invasive gold standard measurements obtained as described above (see 3.5.3 section).

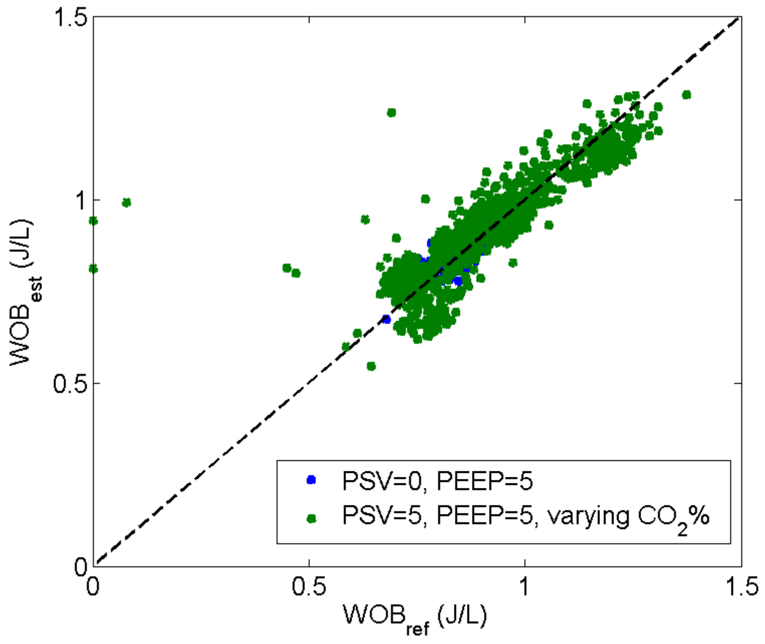

Figure 3.29 – Regression analysis between estimated WOB by the MKF algorithm (y axis) and gold standard WOB (x axis) under low PSV level (0-5 cmH$_2$O) conditions. The value of positive end expiratory pressure (PEEP) used in the corresponding experimental condition is also reported in the legend.

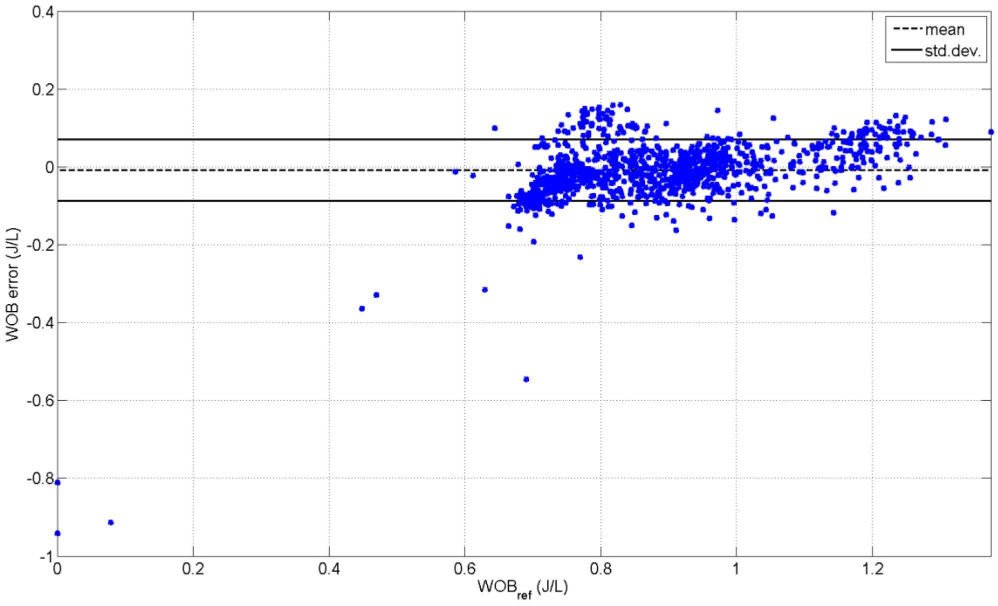

Figure 3.30 – Bland-Altman plot corresponding to the results in Figure 3.23. The WOB error (y axis) is plotted against the gold standard WOB (x axis). Mean (dashed horizontal lines) and ±1 std limits (solid horizontal lines) are also shown.

3.6 Conclusion and Future Work

In this chapter we have first discussed the resistive and elastic properties of the respiratory system and showed how determination of such mechanical properties is crucial for clinicians in order to optimize mechanical ventilation. We have reviewed the current methods for the assessment of resistance (R_{rs}) and compliance (C_{rs}) in mechanically ventilated patients, and we have emphasized their limitations and the need of a novel non-invasive approach for continuous monitoring of R_{rs} and C_{rs} in spontaneously breathing patients. Then, we have introduced the concept of work of breathing (WOB), discussed its importance in the clinical settings, and reviewed the current available methods for WOB computation. We then stated the need for a novel non-invasive method to quantify WOB at the bedside. Hence, we have proposed and developed a model-based technique to simultaneously assess patient's respiratory mechanics and WOB noninvasively and continually. The technique is based on the 1st order single-compartment model of the respiratory system, whose parameters are estimated using pressure and flow signals that are typically readily available at the bedside. Particularly, two different algorithms have been proposed: a Constraint Least Squares (CLS) method that exploits physiology-based constraint on the parameters to reduce the solution space of the otherwise underdetermined LS problem; and a Modified Kalman Filter algorithm that uses physiology-based assumptions to locally approximate the respiratory muscle pressure profile in order to cope with the issue of underdeterminacy. Via simulation studies using a breathing simulator, the feasibility of both algorithms was proven in an ideal noise-free environment. Then, both algorithms have been implemented in a real-time platform and usability has been verified during a pig test. Finally, the two algorithms have been retrospectively tested using the data from the pig test and compared against invasive gold standard measurements of R_{rs}, C_{rs}, P_{mus} and WOB. The validation showed the potential of the two algorithms and their limitations. Particularly, the CLS algorithm was proven to have satisfactory performance under high pressure support ventilation (PSV) conditions, whereas the MKF was proven to be superior at low PSV settings. As a result, we plan to combine the two algorithms based on a PSV threshold criterion, and develop a unified method where the two algorithms would complement each other. These aspects will be the object of subsequent investigation. In terms of applicability and clinical impact, the proposed technique will allow for continuous non-invasive monitoring of WOB and respiratory mechanics in both spontaneous and passive patients. The technique will not interfere with normal ventilator operation and it will not require any operator intervention. We conjecture that the technique can also be used as part of a closed-loop system were the patient WOB is automatically maintained within certain ranges based on clinician's inputs.

Chapter 4: Bayesian Parameter Estimation for Physiological Models

4.1 Introduction

As mentioned in *Chapter 1 – Introduction*, parameter estimation is a fundamental step toward the development of patient-specific physiological models that can eventually be applied in the ICU environment to help clinicians in the decision making process (e.g., to suggest optimal ventilator settings). In the previous chapter, we have seen how a subcomponent of the *CP Model* presented in Chapter 2 can be personalized to a specific patient via parameter estimation techniques using real-time measurements that are readily available at the bedside. The techniques described in the previous chapter rely on the available data to provide estimates of the parameters of the underlying mathematical model. In some cases (Constraint Least Square method), we have seen that the inclusion of mathematical constraints that are based on physiological knowledge is necessary in order to reduce the parameter space and render the estimation problem well-posed. Another additional source of information that can potentially be exploited in the parameter estimation process is represented by *population* studies. For instance, given a particular class of patients, it could be possible to consider that certain *values* of a parameter are more likely than others, based on previous studies or knowledge. In other words, it is reasonable to assume that certain *a-priori* knowledge about the parameters may be available. Given the uncertainty that characterizes this type of knowledge, it is also reasonable to assume that this knowledge is encoded in terms of probabilistic concepts, for instance in terms of probability density functions over the parameter space. The *a-priori* knowledge, if available, can (or should) then be used in the parameter estimation process with the hope of obtaining more accurate results. The estimation methods described in the previous chapter finds it difficult to make use of any prior knowledge in the form of probabilistic concepts. For this reason, in estimation theory a distinction is made between *Classic* (or *Fisherian*) approaches, which do not use any a-priori information and they only rely on the data, and *Bayesian* approaches, which make use of a-priori knowledge in addition to the information contained in the data. The mechanism by which the a-priori knowledge is incorporated into this class of estimators is a direct application of the Bayes' theorem, from which the name Bayesian estimation originates. Given the conceptual appealing simplicity and the computational advances brought by Monte-Carlo simulation methods, Bayesian approaches have been recently receiving more and more attention, especially in connections with physiological models. For instance, Zenker et *al*. [117] have applied Bayesian inference to a physiological model of the cardiovascular system and shown how this probabilistic framework can be used for differential diagnosis of hypotensive events. Murley and his colleagues [118] have proposed Bayesian learning to estimate two parameters of a physiological model of gas exchange. Yet, Bayesian approaches are widely used to estimate parameters of pharmacokinetic-pharmacodynamic (PKPD) models and their superiority with respect to classical approaches have been demonstrated in data poor conditions by Sparacino and colleagues [119].

In this chapter, we want to lay down the basis for the application of Bayesian estimation to the development of cardiopulmonary patient-specific physiological models. To introduce the concept of Bayesian estimation, we will first describe the general parameter estimation problem and distinguish between Classical and Bayesian approaches. We will then describe one of the most popular Bayesian estimators, the Maximum a Posteriori Probability (MAP) estimator, and show some of its properties under Gaussianity assumptions. Finally, as a proof-of-concept, we will implement a Bayesian MAP estimator and apply it to identify the parameters of the 1st order single-compartment model of the respiratory system described in the previous chapter, under the assumption of a passive patient. The performance of the MAP

Bayesian estimator will be compared to those of the classic Least Square (LS) method and conclusions will be drawn. Finally, some ideas for further extension and possible applications of this Bayesian estimation framework in the contest of patient-specific cardiopulmonary models will be discussed.

4.2 The General Parameter Estimation Problem

Consider a generic physiological system (e.g. the respiratory system or the cardiovascular system) and let us assume that the system can be described by a model that is characterized by P unknown parameters $\{\theta_1, \theta_2, \ldots., \theta_p\}$. These parameters can either have a physiological interpretation, as in the case of physiology-based, or first-principle type of models, such as those described in the previous chapters, or no physical meaning as in the case of black-box or I/O models. Let us assume that some signal $y(t)$ related to the system under exam can be measured (for the sake of simplicity, we will assume that only one signal is measured but our discussion can be extended to multiple signals $y_1(t)$, $y_2(t), \ldots, y_k(t)$). Obviously, the measured signal will contain information about the underlying physiological system and hence about the unknown model parameters $\{\theta_1, \theta_2, \ldots., \theta_p\}$. In general, by assuming an error-free model structure, the measured signal can be expressed as:

$$y(t) = g(t, \theta)$$

where the function g represents the model structure and $\theta = [\theta_1, \theta_2, \ldots, \theta_p]^T$ is the vector of model parameters. Say, N samples of the measured signal are collected at each discrete time step $\{t_1, t_2, \ldots., t_N\}$, and these sample values are inevitably corrupted by noise. Furthermore, the model used is a mathematical representation of a physical process and does not describe physics perfectly. Hence, the following equation can relate the *i-th* measurement z_i to the model parameters:

$$z_i = y(t_i) + w_i = g(t_i, \theta) + w_i \quad , \qquad i = 1, 2, \ldots\ldots, N$$

or equivalently:

$$Z = G(\theta) + W \tag{4-1}$$

where $W = [w_1\,, w_2, \ldots., w_N\,]^T$ is a noise vector term which accounts for both the measurement and the model errors, $Z = [z_1\,, z_2, \ldots., z_N\,]^T$ is the measurement vector, and $G(\theta) = [g(t_1, \theta),\ g(t_2, \theta), \ldots\ldots, g(t_N, \theta)]^T$ is our model. The parameter estimation problem consists in determining an estimate $\hat{\theta} = \left[\hat{\theta}_1, \hat{\theta}_2, \ldots., \hat{\theta}_p\right]^T$ of the true model parameters $\theta = \left[\theta_1, \theta_2, \ldots, \theta_p\right]^T$ from the available measurements $Z = [z_1\,, z_2, \ldots., z_N\,]^T$ that are corrupted with noise.

4.3 Bayesian vs Classical Parameter Estimation

The parameter estimation problem described above can be tackled by either a *Classical* (or *Fisherian*) approach or a *Bayesian* approach.

Classical Approach: In the classical approach, the parameters θ to be estimated are assumed deterministic and unknown, and the only information used in the parameter estimation process are the available measurements along with their noise characteristics (see Figure 4.1). Two of the most popular classical parameter estimation methods are the Least Squares (LS) and the Maximum Likelihood (ML) estimators.

Bayesian Approach: In the Bayesian approach, the parameter vector θ is assumed to be a random vector whose particular realization we must estimate. Bayesian estimation methods assume that a priori information about the unknown parameters is available in the form of a probability density function (p.d.f.) $p(\theta)$. The prior p.d.f. $p(\theta)$ summarizes the available knowledge about θ before any data is even observed. This information is provided to the estimator in addition to the measurements. In Figure 4.1, the a priori probability distribution $p(\theta)$ is then refined using the measurements in order to compute the so-called posterior probability distribution $p(\theta|Z)$. This is the probability distribution of the parameters conditional on knowing the measurements and it can be used to express the likelihood that our parameters have certain values after we have collected the measurements. Computation of the posterior distribution $p(\theta|Z)$ is performed by directly applying Bayes' theorem:

$$p(\theta|Z) = \frac{p(Z|\theta) \cdot p(\theta)}{p(Z)} \tag{4-2}$$

where $p(Z|\theta)$ is the conditional p.d.f. of the measurements Z given the parameters θ, also called "likelihood" function, and $p(Z)$ is the p.d.f. of the measurements Z. Note that in the Bayesian framework, since the parameters are assumed random variables, the data are described by the joint p.d.f. $p(Z, \theta)$ and the Bayes theorem above can also be rewritten in the equivalent form:

$$p(Z, \theta) = p(\theta|Z) \cdot p(Z) = p(Z|\theta) \cdot p(\theta)$$

Once $p(\theta|Z)$ has been computed, an estimate of the parameter vector $\hat{\theta}$ can be obtained according to a specific criterion that is related to the distribution $p(\theta|Z)$. For instance, the Maximum a Posteriori Probability (MAP) and the Minimum Mean Squares Error (MMSE) estimators, two of the most widely used Bayesian estimators, select the estimated parameter $\hat{\theta}$ as the mode and the mean of the posterior p.d.f. $p(\theta|Z)$, respectively.

Bayesian approaches have the clear advantage of using additional information compared to the classical approaches. Hence, when the prior knowledge is available, Bayesian estimation methods should provide more accurate results and hence may also allow the adoption of more complex models than those determinable by classical approaches. In the case of physiological models, prior knowledge on the parameters is often available from previous population studies. For this reason, Bayesian methods represent an attractive solution to the often challenging problem of parameter estimation and they have received great attention in the last decade, as mentioned in the *Introduction* section.

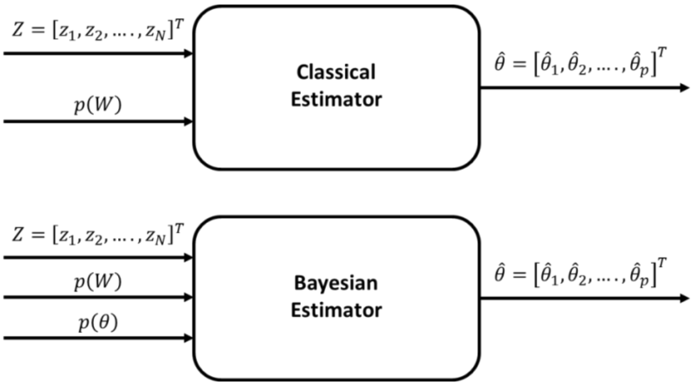

Figure 4.1 Classical vs Bayesian estimation

4.4 Maximum a Posteriori Probability (MAP) Estimator

Before moving to the mathematical derivation of one of the most popular Bayesian estimation methods, the Maximum a Posteriori Probability (MAP) estimator, it is first necessary to introduce the concept of *risk* and *cost* associated with an estimator. In Bayesian estimation, the starting point is to define a *cost* function *C* associated with the estimated and the true parameters:

$$C = C(\theta, \hat{\theta}) : \ \mathrm{R}^p \times \mathrm{R}^p \rightarrow \mathrm{R}$$

and then introduce the *risk* function *R*, defined as the expectation of the cost:

$$R = E[C(\theta, \hat{\theta})] = \iint C(\theta, \hat{\theta})\, p(Z, \theta)\, d\theta\, dZ$$

The Bayesian estimator is the one that minimizes the risk:

$$\hat{\theta}_B = \underset{\hat{\theta}}{\operatorname{argmin}} \{R\}$$

Now, using the Bayes theorem, the expression of the risk can be rewritten as:

$$R = \iint C(\theta, \hat{\theta})\ p(Z, \theta)\ d\theta\ dZ = \iint C(\theta, \hat{\theta})\, p(Z) p(\theta|Z)\ d\theta\ dZ =$$

$$= \int p(Z)\ \left[\int C(\theta, \hat{\theta})\, p(\theta|Z)\ d\theta\right] dZ$$

And $p(Z)$ being always positive, we can compute the Bayesian estimator as:

$$\hat{\theta}_B = \underset{\hat{\theta}}{\operatorname{argmin}} \left\{ \int C(\theta, \hat{\theta})\, p(\theta|Z)\ d\theta \right\} \tag{4-3}$$

Depending on the particular type of cost function, we will obtain different Bayesian estimators. The MAP estimator is derived by considering the so-called “hit-or-miss” cost function, defined as:

$$C(\theta, \hat{\theta}) = \begin{cases} 1 & if\ \|\hat{\theta} - \theta\| > \Delta \\ 0 & if\ \|\hat{\theta} - \theta\| \leq \Delta \end{cases}$$

where the term $\|\hat{\theta} - \theta\|$ represents the L^1 norm of the estimation error $\varepsilon = \hat{\theta} - \theta$ and in the case of a p-dimensional parameter vector it is given by $\|\hat{\theta} - \theta\| = \sum_{m=1}^{p} |\hat{\theta}_m - \theta_m|$. A graphical representation of the hit-or-miss cost function, sometimes also called uniform cost function, is shown in Figure 4.2. Basically, this function assigns a 0 cost if the estimation error is within a tolerance range [-Δ, +Δ] and it assigns a 1 cost if the estimation error is outside the tolerance range.

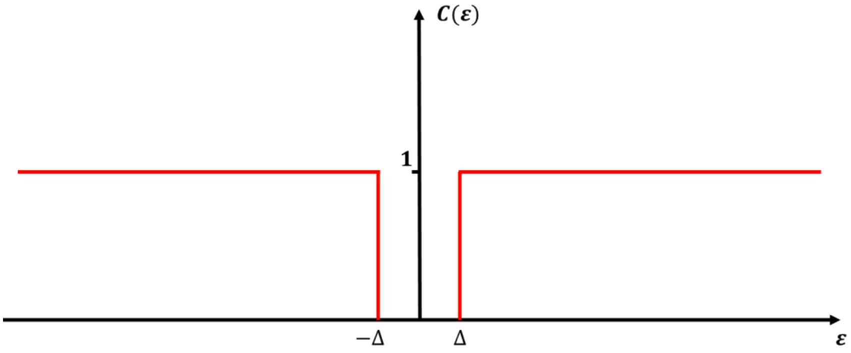

Figure 4.2 Hit-or-miss cost function

Substituting the above expression for the cost function $C(\theta, \hat{\theta})$ into Eq. 4-3 we obtain:

$$\hat{\theta}_{MAP} = \underset{\hat{\theta}}{\operatorname{argmin}} \left\{ \int_{-\infty}^{\hat{\theta}-\Delta} 1 \cdot p(\theta|Z)\, d\theta + \int_{\hat{\theta}+\Delta}^{+\infty} 1 \cdot p(\theta|Z)\, d\theta \right\} =$$

$$= \underset{\hat{\theta}}{\operatorname{argmin}} \left\{ 1 - \int_{\hat{\theta}-\Delta}^{\hat{\theta}+\Delta} 1 \cdot p(\theta|Z)\, d\theta \right\} =$$

$$= \underset{\hat{\theta}}{\operatorname{argmax}} \left\{ \int_{\hat{\theta}-\Delta}^{\hat{\theta}+\Delta} p(\theta|Z)\, d\theta \right\}$$

Hence, if Δ is arbitrarily small, the integral is maximized by centering it around the peak of the integrand, that is by choosing the estimate as the mode of the posterior p.d.f. $p(\theta|Z)$:

$$\hat{\theta}_{MAP} = \underset{\theta}{\operatorname{argmax}} \{ p(\theta|Z) \}$$

from which it appears evident that the MAP estimator is the one that maximizes the posterior probability density function $p(\theta|Z)$. Now, using the Bayes theorem, the MAP estimator can be rewritten as:

$$\hat{\theta}_{MAP} = \underset{\theta}{\operatorname{argmax}} \left\{ \frac{p(Z|\theta) \cdot p(\theta)}{p(Z)} \right\} \tag{4-4}$$

Observing that the denominator does not depend on θ, we obtain:

$$\hat{\theta}_{MAP} = \underset{\theta}{\operatorname{argmax}} \{\, p(Z|\theta) \cdot p(\theta) \,\} \tag{4-5}$$

Note the connection between the MAP estimator above and the Maximum Likelihood (ML) estimator, a Fisherian approach that does not use prior information and whose expression is given by:

$$\hat{\theta}_{ML} = \underset{\theta}{\operatorname{argmax}} \{\, p(Z|\theta) \,\}$$

The MAP estimator can thus be seen as a regularization of the ML estimator. Typically, because the logarithm is a monotonic function, it is mathematically convenient to maximize the logarithm and rewrite the MAP estimator in the form:

$$\hat{\theta}_{MAP} = \underset{\theta}{\operatorname{argmax}} \{\, \ln p(Z|\theta) + \ln p(\theta) \,\}$$

From the above expression we can observe that computation of the MAP estimator does not actually require the computation of the entire posterior p.d.f. $p(\theta|Z)$, but only the maximization of the term $p(Z|\theta)p(\theta)$. As such, even though the MAP estimator uses the Bayesian framework to exploit the available a priori information, it is considered a point estimator rather than a full Bayesian inference method. Also, by looking at the above expression we notice two terms that the MAP estimator is trying to maximize: the 1st term is related to the measurements and represents the likelihood that the data have been generated by our parameter θ; the 2nd term is related to the prior information about our parameters and it is independent on the data. Hence, the MAP estimator realizes a compromise between a priori information and information contained in the measurements. A general closed form of the MAP estimator does not exist because the posterior p.d.f. $p(\theta|Z)$ depends on the specific form of $p(\theta)$ and $p(Z|\theta)$. This, in turn, depends on the model structure and on the statistical properties of the noise. A tractable analytical expression for $p(\theta|Z)$ can only be obtained in few cases, one of them is described in the following section.

4.5 MAP Estimator in the Gaussian Case

Let us consider the model in Eq. 4-1 and let us assume that the noise $W$and the parameter vector θ are both normally distributed:

$$W \sim N(0, C_w) \qquad\qquad \theta \sim N(\mu_\theta, C_\theta)$$

where W has been assumed a zero-mean Gaussian noise with covariance matrix C_w, μ_θ is the mean of the parameter vector θ and C_θ is its covariance matrix. Then, it can be proven that the conditional p.d.f. $p(Z|\theta)$ is also Gaussian with the mean given by $G(\theta)$ and the covariance matrix equal to C_w [120]. Hence, we can write:

$$p(\theta) = \frac{1}{[(2\pi)^p det(C_\theta)]^{1/2}} \cdot e^{-\frac{1}{2}\cdot(\theta-\mu_\theta)^T \cdot C_\theta^{-1} \cdot (\theta-\mu_\theta)}$$

$$p(Z|\theta) = \frac{1}{[(2\pi)^N det(C_w)]^{1/2}} \cdot e^{-\frac{1}{2}\cdot\left(Z-G(\theta)\right)^T \cdot C_w^{-1} \cdot \left(Z-G(\theta)\right)}$$

and hence the MAP estimator will be:

$$\hat{\theta}_{MAP} = \underset{\theta}{\operatorname{argmax}} \{ \ln p(Z|\theta) + \ln p(\theta) \} =$$

$$\underset{\theta}{\operatorname{argmin}} \left\{ \left(Z - G(\theta)\right)^T \cdot C_w^{-1} \cdot \left(Z - G(\theta)\right) + (\theta - \mu_\theta)^T \cdot C_\theta^{-1} \cdot (\theta - \mu_\theta) \right\}$$

From the above expression we can again notice how the MAP estimator is trying to minimize the sum of two terms: the 1st term related to the distance of the model predictions $G(\theta)$ from the actual observed data, hence expressing the adherence to the measurements; the 2nd term related to the distance between the estimates and their a priori expected values, hence expressing the adherence to the prior knowledge. Particularly, we can also observe that if the measurements are very noisy and C_w grows larger, then the 1st term becomes negligible and the parameter estimates converge to their prior mean μ_θ. On the other hand, if the prior knowledge is weak, i.e. if the prior variances of the parameters are very large, then the 2nd term becomes negligible and the MAP estimator becomes equivalent to the Least Squares estimator (or the Maximum Likelihood estimator):

$$\hat{\theta}_{MAP} = \underset{\theta}{\operatorname{argmin}} \left\{ \left(Z - G(\theta)\right)^T \cdot C_w^{-1} \cdot \left(Z - G(\theta)\right) \right\} = \hat{\theta}_{ML} = \hat{\theta}_{LS}$$

This is true in general, not only in the case of Gaussian prior and noise. In fact, in the extreme case when our prior knowledge is very weak all the parameters tend to be equally probable and our prior $p(\theta)$ becomes equivalent to the uniform distribution. Then, if we consider the definition of the MAP estimator (see Eq. 4-5), the term $p(\theta)$ will not affect the maximization and the MAP estimator will be equivalent to the ML estimator.

4.5.1 The Gaussian Case with Linear Model

When, in addition to the above assumptions, the model is linear in the parameters:

$$Z = H\theta + W \tag{4-6}$$

where H is a known deterministic $p \times N$ matrix, and the noise vector W is independent of θ, the expression of the MAP estimator can further be simplified. In fact, it can be proven [121] that the posterior p.d.f. $p(\theta|Z)$ is Gaussian as well, with mean and covariance matrix given by:

$$\mu_{\theta|Z} = \mu_\theta + \left(C_\theta^{-1} + H^T C_w^{-1} H\right)^{-1} H^T C_w^{-1} (Z - H\mu_\theta) \tag{4-7}$$

$$C_{\theta|Z} = \left(C_\theta^{-1} + H^T C_w^{-1} H\right)^{-1} \tag{4-8}$$

Hence, being the mode of the Gaussian p.d.f. equivalent to the mean, the MAP estimator is exactly given by Eq. 4-7. It is worth noticing that in this case, not only does the expression of the MAP estimator have a closed form, but the entire posterior p.d.f. $p(\theta|Z)$ can be analytically computed as well.

4.6 Bayesian Estimation of Respiratory Mechanics

Let us now consider the case of the respiratory system and let us focus on the simple 1st order RC model described in Chapter 3:

$$P_{ao}(t) = R_{rs} \cdot \dot{V}(t) + E_{rs} \cdot V(t) + P_{mus}(t) + P_0 \tag{4-9}$$

where P_{ao} is the airway opening pressure, $\dot{V}$ is the airflow, V is the lung volume above functional residual capacity (FRC), P_{mus} is the pressure developed by the respiratory muscles, R_{rs} and E_{rs} are the resistance and the elastance of the respiratory system, and P_0 is a constant that account for the positive pressure that is present in the lungs at end expiration. To simplify the problem, let us assume that the patient is completely passive (sedated and paralyzed) and hence the term P_{mus} in Eq. 4-9 can be omitted. The problem we want to solve is the one of estimating the parameter $\theta = [R_{rs}\ E_{rs}\ P_0]^T$ from the available measurements $P_{ao}(t)$ and $\dot{V}(t)$ ($V(t)$ is obtained by numerical integration of the flow signal). Obviously, the measurements will be affected by noise, hence when trying to fit Eq. 4-9 above to the available measurements the presence of noise will have to be accounted for. By looking at Eq. 4-9 we can observe that noise can be present in the pressure measurement term $P_{ao}(t)$, in the flow measurement term $\dot{V}(t)$, or in both. As a first assumption, we will consider that the noise is present on the pressure measurements only. We will see later how the assumption of noise being present on the flow measurements as well will modify the nature of our problem and will impact the derivation of our parameter estimation approach. Hence, Eq. 4-9 can be rewritten as:

$$P_{ao}(t) = R_{rs} \cdot \dot{V}(t) + E_{rs} \cdot V(t) + P_0 + w(t)$$

where $w(t)$ is pressure sensor noise. The equation above can be rewritten in vector form as:

$$Z \equiv \begin{bmatrix} z_1 \\ z_2 \\ \cdot \\ \cdot \\ \cdot \\ \cdot \\ z_N \end{bmatrix} \equiv \begin{bmatrix} P_{ao}(t_1) \\ P_{ao}(t_2) \\ . \\ . \\ . \\ . \\ P_{ao}(t_N) \end{bmatrix} = \begin{bmatrix} \dot{V}\,(t_1) & V(t_1) & 1 \\ \dot{V}\,(t_2) & V(t_2) & 1 \\ & . & \\ & . & \\ & . & \\ & . & \\ \dot{V}\,(t_N) & V(t_N) & 1 \end{bmatrix} \cdot \begin{bmatrix} R_{rs} \\ E_{rs} \\ P_0 \end{bmatrix} + \begin{bmatrix} w(t_1) \\ w(t_2) \\ . \\ . \\ . \\ . \\ w(t_N) \end{bmatrix} =$$

$$= \begin{bmatrix} \dot{V}_1 & V_1 & 1 \\ \dot{V}_2 & V_2 & 1 \\ & . & \\ & . & \\ & . & \\ & . & \\ \dot{V}_N & V_N & 1 \end{bmatrix} \cdot \begin{bmatrix} R_{rs} \\ E_{rs} \\ P_0 \end{bmatrix} + \begin{bmatrix} w_1 \\ w_2 \\ . \\ . \\ . \\ . \\ w_N \end{bmatrix} = H \cdot \theta + W \tag{4-10}$$

Our objective is to estimate the parameter vector θ via Bayesian techniques. This is the same case as the one described above, where the model is linear in the parameters (see *The Gaussian Case with Linear Model* section). Hence, in the case of Gaussian priors and noise, an analytical expression for the posterior p.d.f. and for the MAP estimator exist (see Eq. 4-7 and 4-8). However, since we want our method to be independent from the particular choice of the a priori parameter distribution, we will not be using the analytical solutions but we will rather compute the posterior p.d.f. numerically in Matlab, by directly applying Bayes' theorem. Particularly, in the following sections we will apply Bayesian MAP estimation to both simulated data and experimental data obtained from the animal test described in Chapter 3 and we will compare the performance of the MAP estimator against the one of the Least Squares method. Our conjecture is that in data-poor conditions, i.e. when the noise is high and/or the number of data points used to construct the measurement vector Z is reduced, the MAP offers advantages with respect to the LS estimator thanks to the use of prior information. We consider three different cases corresponding to different choices of the a priori parameter distribution, and in the Gaussian case we will verify correctness of the numerical implementation by checking equivalence between the numerical and the analytical solutions.

4.6.1 Methods

We consider a series of respiratory cycles from the datasets collected during the animal test described in Chapter 3. The pressure, flow and volume signals corresponding to one of these cycles are shown in Figure 4.3. Since we assume that the term P_{mus} in Eq. 4-9 can be neglected, the selected respiratory cycles correspond to situations where the animal was not spontaneously breathing and the ventilator was set in Volume Control Ventilation (VCV), with a constant inspiratory flow. The absence of spontaneous respiratory activity is confirmed by the esophageal pressure tracing, that does not present any negative deflections from baseline. Hence, given the measurements needed to build the vector Z and the matrix H in Eq. 4-10, we are going to apply the Bayes theorem to compute the posterior probability density function of the parameter θ, according to:.

$$p(\theta|Z) = \frac{p(Z|\theta) \cdot p(\theta)}{p(Z)}$$

By looking at the above equation, we can identify three fundamental steps to solve the Bayesian estimation problem: 1. Computation of the prior probability density function $p(\theta)$; 2. Computation of the likelihood function $p(Z|\theta)$; 3. Computation of the posterior probability density function $p(\theta|Z)$. In the following, these three steps will be described in detail.

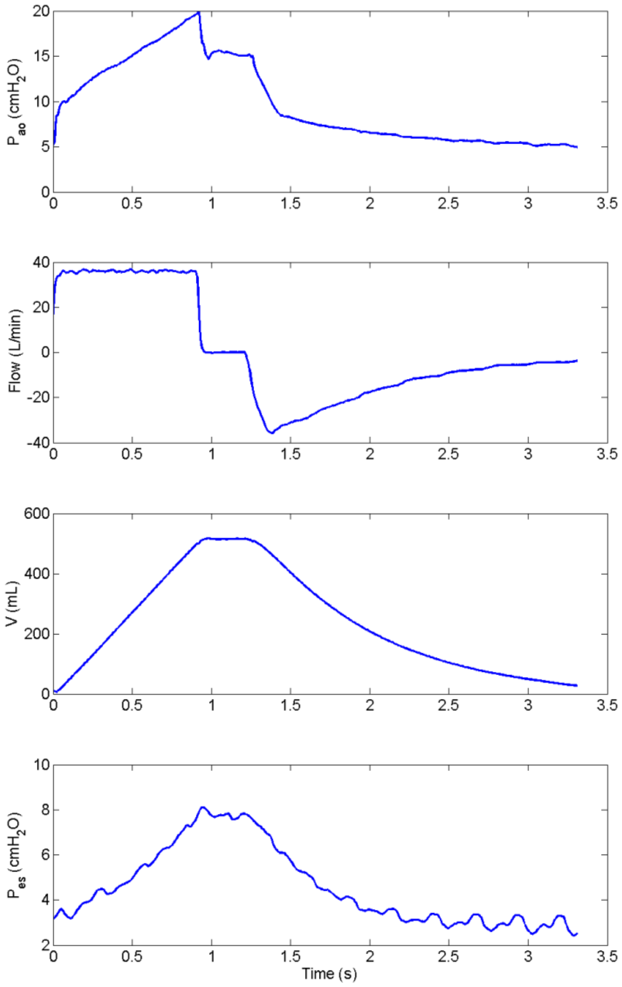

Figure 4.3 – Experimental dataset from the animal test described in Chapter 3 corresponding to a VCV breath with no spontaneous respiratory activity. From top to bottom: P_{ao} is the pressure measured at the airway opening; Flow is the air flow at the mouth; V is the volume above FRC obtained by numerical integration of the flow signal; P_{es} is the invasive esophageal pressure, surrogate for the intrapleural pressure.

Prior Probability Density Functions

The first step in Bayesian estimation is to define the prior p.d.f. of the parameters to be estimated. In order to create the prior distributions, the parameters R_{rs}, E_{rs} and P_0 have been given a range of possible values and this range has been discretized. Particularly:

- 81 values of the resistance R_{rs} have been given in a range of [0 - 20] $\frac{cmH_2O}{L} \cdot s^{-1}$ with a discretization step of 0.25;
- 201 values of the elastance E_{rs} have been given in a range of [0 - 50] $\frac{L}{cmH_2O}$ with a discretization step of 0.25;
- 41 values of the constant P_0 have been given a range of [0 - 20] cmH_2O with a discretization step of 0.5;

These ranges are all in agreement with physiological knowledge. Then, three different cases have been considered:

1. All the parameters (i.e., the a priori p.d.f.) are assumed to be Gaussian distributed. The mean of each parameter is selected as half of the corresponding range and the standard deviation is set at 10% of the range. This choice of priors corresponds to a generic healthy subject.
2. The resistance is assumed to be distributed according to an “extreme value” probability density function, shifted toward the right to indicate a condition of obstructive lung disease (e.g., COPD). The remaining parameters (E_{rs} and P_0) are assumed to be Gaussian distributed, with mean and standard deviation selected as described above.
3. The elastance is assumed to be distributed according to an “extreme value” probability density function, shifted toward the right to indicate a condition of restrictive lung disease, where the lungs are stiffened. The remaining parameters (R_{rs} and P_0) are assumed to be Gaussian distributed, with mean and standard deviation selected as described above.

The prior distributions corresponding to the three above cases are generated in Matlab using the *pdf* command. Figure 4.4 below shows the different parameter priors for each of these 3 cases. Note that in a real clinical application scenario, the prior distributions would have to be selected based on population studies or based on expert knowledge from the clinician.

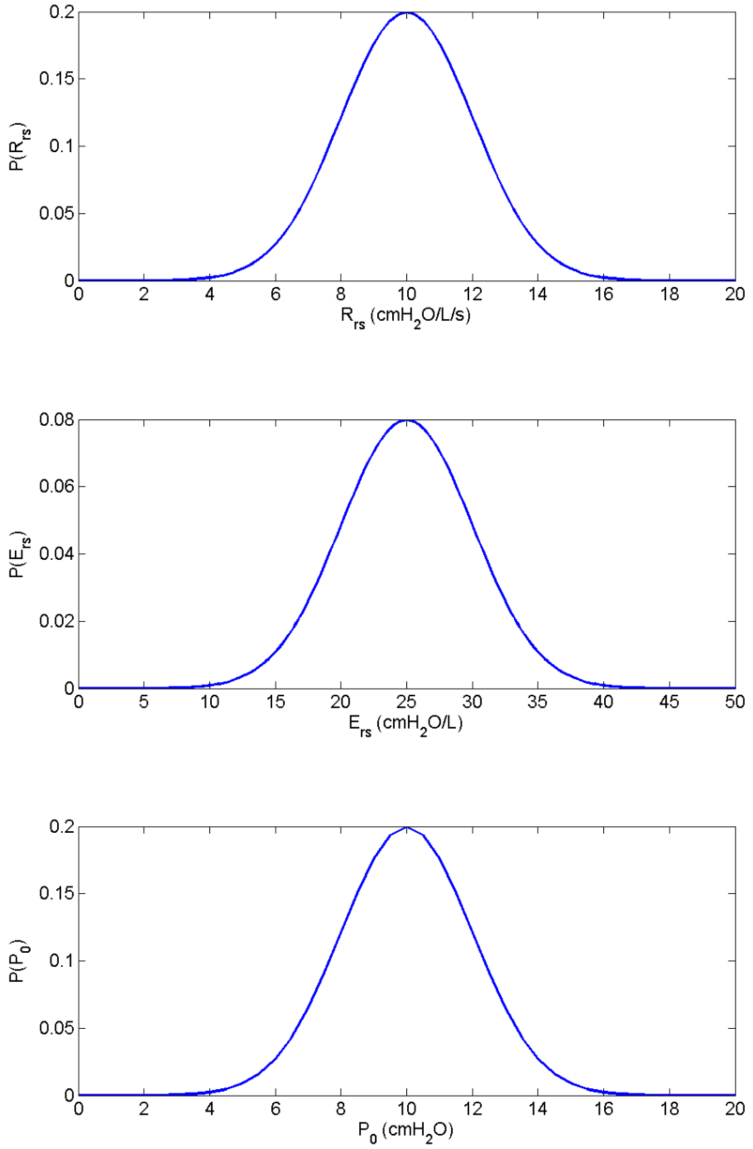

Figure 4.4 – A priori probability density functions of the parameters for a general healthy subject. From top to bottom: p.d.f. of R_{rs}; p.d.f. of E_{rs}; p.d.f. of P_0.

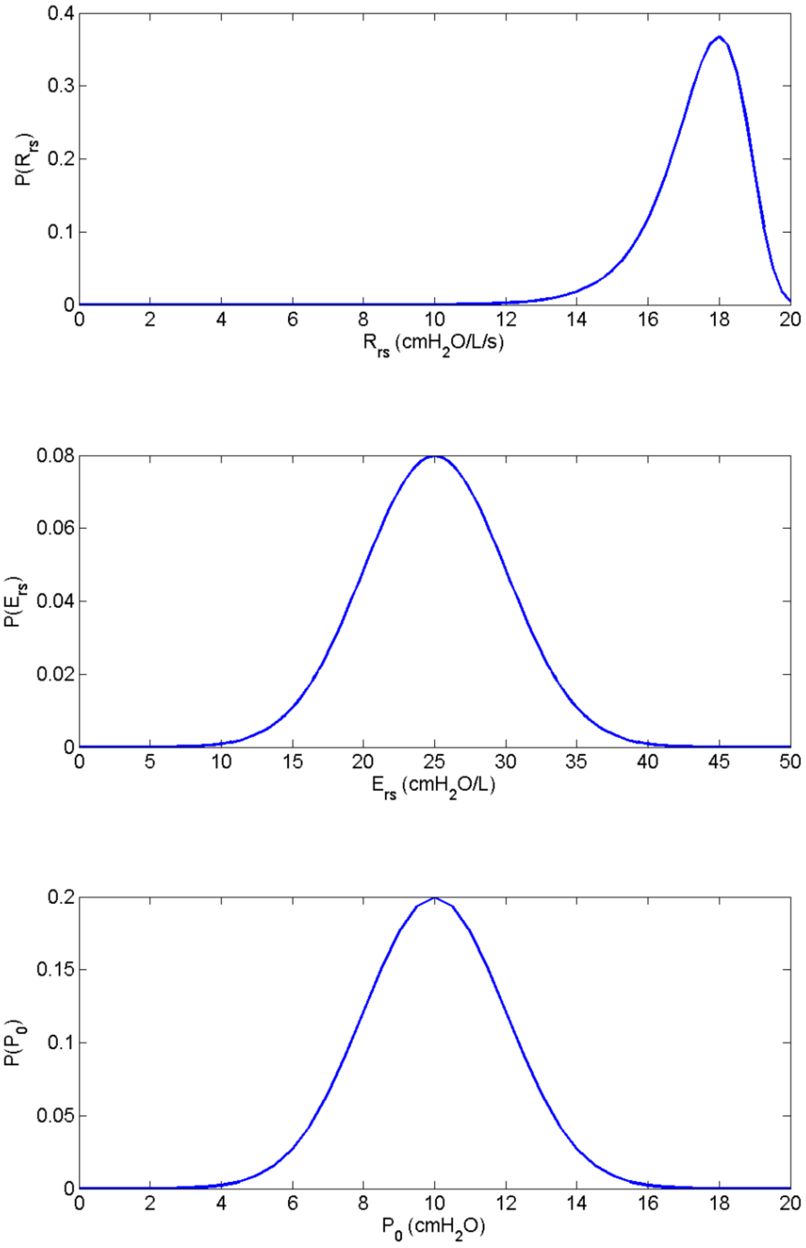

Figure 4.5 – A priori probability density functions of the parameters for an obstructive disease subject. From top to bottom: p.d.f. of R_{rs}; p.d.f. of E_{rs}; p.d.f. of P_0.

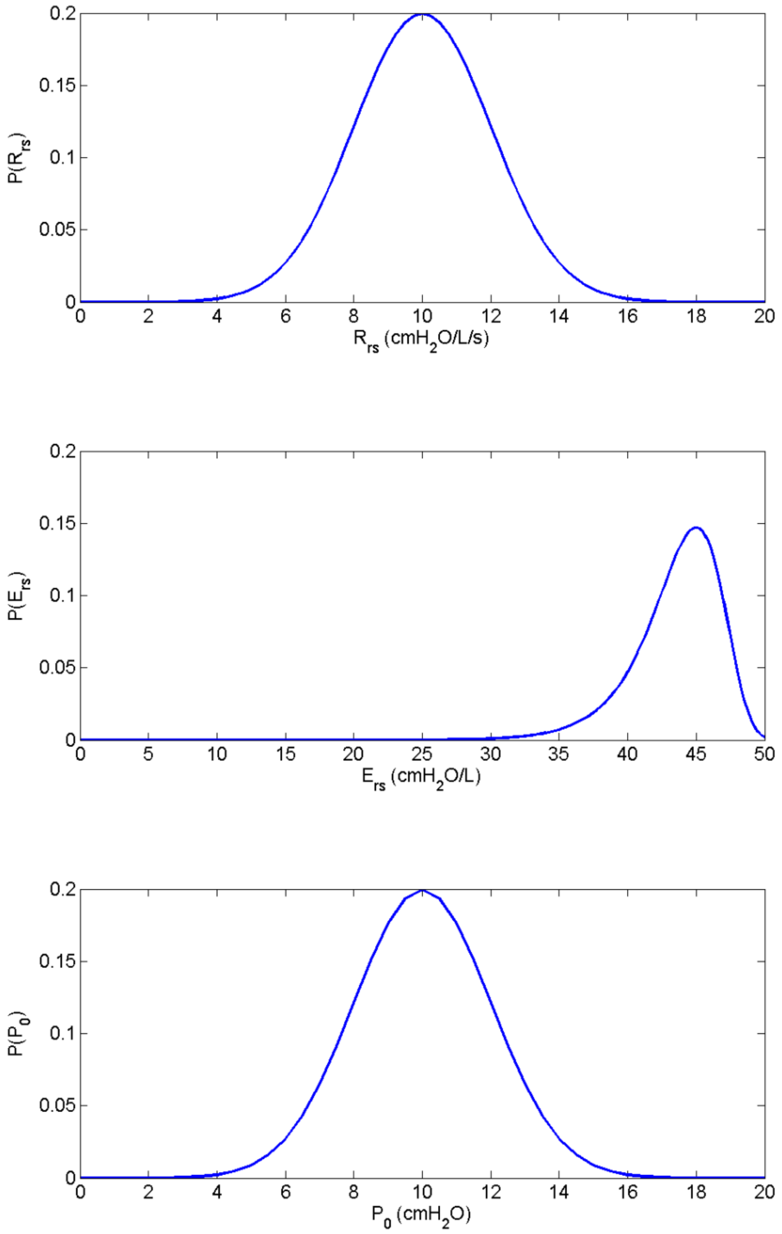

Figure 4.6 – A priori probability density functions of the parameters for a restrictive disease subject. From top to bottom: p.d.f. of R_{rs}; p.d.f. of E_{rs}; p.d.f. of P_0.

Computation of the Likelihood Function

In order to compute the likelihood function $p(Z|\theta)$ we have assumed that the noise terms $w_1, w_2, \ldots, w_N$ are independent and Gaussian distributed with zero mean and constant variance σ_w^2. In other words, the noise vector W is assumed white Gaussian noise with covariance matrix $C_w = \sigma_w^2 \cdot I_N$. Hence, using the model equations (see Eq. 4-10):

$$z_i = \left[\dot{V}_i \;\; V_i \;\; 1\right] \cdot \theta + w_i$$

we can conclude that the random variables $z_i|\theta$ are Gaussian as well, since they are just the sum of a deterministic quantity and a Gaussian variable, with mean and variance given by:

$$E\{z_i|\theta\} = E\{\left[\dot{V}_i \;\; V_i \;\; 1\right] \cdot \theta + w_i\} = \left[\dot{V}_i \;\; V_i \;\; 1\right] \cdot \theta + E\{w_i\} = \left[\dot{V}_i \;\; V_i \;\; 1\right] \cdot \theta$$

$$Var\{z_i|\theta\} = E\{(z_i|\theta - E\{z_i|\theta\})^2\} = E\left\{\left(\left[\dot{V}_i \;\; V_i \;\; 1\right] \cdot \theta + w_i - \left[\dot{V}_i \;\; V_i \;\; 1\right] \cdot \theta\right)^2\right\} =$$

$$= E\{(w_i - E\{w_i\})^2\} = \sigma_w^2$$

where $E\{\}$ represents mathematical expectation. Now, w_i being independent, it follows that z_i are independent as well and hence they are jointly Gaussian. So, we can conclude that the random vector $Z|\theta$ is a multivariate Gaussian variable with mean equal to $H \cdot \theta$ and covariance matrix equal to C_w:

$$Z|\theta \sim N(H \cdot \theta, C_w)$$

From what we have seen above, the likelihood function can then be easily computed as:

$$p(Z|\theta) = \frac{1}{[(2\pi)^N det(C_w)]^{1/2}} \cdot e^{-\frac{1}{2} \cdot (Z - H\theta)^T \cdot C_w^{-1} \cdot (Z - H\theta)} \tag{4-11}$$

Practically, the above function is numerically evaluated in Matlab for every possible parameter combination $\theta_{i,j,k} = \left[R_{rs}^i \;\; E_{rs}^j \;\; P_0^k\right]^T$ within the parameter space, using the available measurements Z. By doing so, we generate $I \times J \times K$ values of $p(Z|\theta)$, where I, J and K are the length of the parameter ranges defined earlier, i.e. $81 \times 201 \times 41$ (see *Prior Probability*

Density Functions section). Each term $p\big(Z|\theta = \theta_{i,j,k}\big)$ will then represent the likelihood that the measurements Z have been generated by the parameter vector $\theta_{i,j,k}$.

Computation of the Posterior Probability Density Functions

The $I \times J \times K$ values of the likelihood function $p(Z|\theta)$ computed as described above are then multiplied by the corresponding values of the prior probability density function $p(\theta)$. Particularly, under the assumption that the parameters are independent, the joint prior p.d.f. $p(\theta)$ is computed as the product of the individual priors:

$$p(\theta) = p(R_{rs}) \cdot p(E_{rs}) \cdot p(P_0)$$

In this way, we are able to map every possible triplet $\theta_{i,j,k} = \big[R_{rs}^{i}\ E_{rs}^{j}\ P_0^{k}\big]^T$ to its corresponding term $p\big(Z|\theta = \theta_{i,j,k}\big) \cdot p\big(\theta_{i,j,k}\big)$:

$$\theta_{i,j,k} \rightarrow p\big(Z|\theta = \theta_{i,j,k}\big) \cdot p\big(\theta_{i,j,k}\big)$$

The last step to compute the full posterior p.d.f. $p(\theta|Z)$ is to divide each product $p\big(Z|\theta = \theta_{i,j,k}\big) \cdot p\big(\theta_{i,j,k}\big)$ by the normalization factor $p(Z)$ (see Eq. 4-2). Note that the term $p(Z|\theta) \cdot p(\theta)$ represents the joint p.d.f. of the random vectors Z and θ:

$$p(Z,\theta) = p(Z|\theta) \cdot p(\theta)$$

Hence, in order to compute $p(Z)$, we can simply marginalize the joint p.d.f. $p(Z,\theta)$ that we have just computed according to:

$$p(Z) = \int_{\theta} p(Z,\theta)\, d\theta = \int_{\theta} p(Z|\theta) \cdot p(\theta)\, d\theta \tag{4-12}$$

Practically, a numerical approximation of the above integral is computed in Matlab using a summation over the ranges of the parameters:

$$p(Z) = \sum_{i=1}^{I}\left(\sum_{j=1}^{J}\left(\sum_{k=1}^{K} p\left(Z|\theta = \theta_{i,j,k}\right)\cdot p\left(\theta_{i,j,k}\right)\cdot \Delta P_0\right)\cdot \Delta E_{rs}\right)\cdot \Delta R_{rs}$$

where ΔR_{rs}, ΔE_{rs} and ΔP_0 are the discretization steps of the parameter ranges described earlier (see *Prior Probability Density Functions* section). In this way, we can link every possible triplet $\theta_{i,j,k} = \left[R_{rs}^{i}\ E_{rs}^{j}\ P_0^{k}\right]^T$ with its corresponding sample of the posterior probability density function $p(\theta|Z)$:

$$\theta_{i,j,k} \rightarrow p\left(\theta_{i,j,k}|Z\right)$$

In other words, we have computed a discretization of the posterior p.d.f. $p(\theta|Z)$. Finally, in order to compute the individual posterior p.d.f. $p(R_{rs}|Z)$, $p(E_{rs}|Z)$ and $p(P_0|Z)$, we can marginalize the joint p.d.f. $p(\theta|Z)$ according to:

$$p(R_{rs}|Z) = \int_{E_{rs}}\left(\int_{P_0} p(\theta|Z)\, dP_0\right) dE_{rs}$$

$$p(E_{rs}|Z) = \int_{R_{rs}}\left(\int_{P_0} p(\theta|Z)\ dP_0\right) dR_{rs}$$

$$p(P_0|Z) = \int_{E_{rs}}\left(\int_{R_{rs}} p(\theta|Z)\ dR_{rs}\right) dE_{rs}$$

where, again, a summation is used in order to numerically approximate the above integrals in Matlab:

$$p\left({R^{i}}_{rs}|Z\right) = \sum_{j=1}^{J}\left(\sum_{k=1}^{K} p\left(\theta_{i,j,k}|Z\right)\cdot \Delta P_0\right)\cdot \Delta E_{rs}$$

$$p\left({E^{j}}_{rs}|Z\right) = \sum_{i=1}^{I}\left(\sum_{k=1}^{K} p\left(\theta_{i,j,k}|Z\right)\cdot \Delta P_0\right)\cdot \Delta R_{rs}$$

$$p({P^{k}}_{0}|Z) = \sum_{j=1}^{J}\left(\sum_{i=1}^{I} p\left(\theta_{i,j,k}|Z\right)\cdot \Delta R_{rs}\right)\cdot \Delta E_{rs}$$

Once the posterior p.d.f. $p(R_{rs}|Z)$, $p(E_{rs}|Z)$ and $p(P_0|Z)$ have been computed, then an estimate of the parameters is found by simply looking for the maximum of the individual p.d.f. according to the MAP principle:

$$\hat{R}_{rs\,MAP} = \underset{R_{rs}}{\operatorname{argmax}}\,\{p(R_{rs}|Z)\}$$
$$\hat{E}_{rs\,MAP} = \underset{E_{rs}}{\operatorname{argmax}}\,\{p(E_{rs}|Z)\}$$
$$\hat{P}_{0\,MAP} = \underset{P_0}{\operatorname{argmax}}\,\{p(P_0|Z)\}$$

<u>Note</u>: We have mentioned earlier that when we included the noise term in Eq. 4-10 we have assumed that the noise was only present in the pressure measurements. This assumption led us to conclude that the random vector $Z|\theta$ was normally distributed with mean equal to $H \cdot \theta$ and covariance matrix equal to C_w (see *Computation of the Likelihood Function* section). Now we want to examine the case when the noise term is also present in the flow measurements and see how this would impact the computation of the conditional p.d.f. $p(Z|\theta)$. So, let's assume that noise is present in both pressure and flow measurements, hence the model equations can be rewritten as:

$$z_i = \begin{bmatrix}\dot{V}_i + w_{f,i} & V_i & 1\end{bmatrix} \cdot \theta + w_{p,i} = \begin{bmatrix}\dot{V}_i & V_i & 1\end{bmatrix} \cdot \theta + w_{p,i} + w_{f,i} \cdot R_{rs}$$

where the term $w_{f,i}$ represents the noise of the flow measurement and the term $w_{p,i}$ represents the noise of the pressure measurement. Hence, we can notice that, compared to the previous case, here there is an extra noise term that is modulated by the parameter R_{rs}. Let us assume that $w_{p,i}$ and $w_{f,i}$ are realizations of zero-mean white Gaussian processes with covariance matrices $C_{w_p} = \sigma_{w_p}^2 \cdot I_N$ and $C_{w_f} = \sigma_{w_f}^2 \cdot I_N$, respectively. Then, we can still say that the variables $z_i|\theta$ are the sum of two Gaussian variables and a deterministic quantity. Hence, under the assumption that the two noise terms $w_{p,i}$ and $w_{f,i}$ are independent (as it seems legitimate to assume), we can conclude that $z_i|\theta$ will still be Gaussian variables, with mean and variance given by:

$$E\{z_i|\theta\} = E\{\left[\dot{V}_i \;\; V_i \;\; 1\right] \cdot \theta + w_{p,i} + w_{f,i} \cdot R_{rs}\} =$$

$$= \left[\dot{V}_i \;\; V_i \;\; 1\right] \cdot \theta + E\{w_{p,i}\} + R_{rs} \cdot E\{w_{f,i}\} = \left[\dot{V}_i \;\; V_i \;\; 1\right] \cdot \theta$$

$$Var\{z_i|\theta\} = E\{(z_i|\theta - E\{z_i|\theta\})^2\} =$$

$$= E\left\{\left(\left[\dot{V}_i \;\; V_i \;\; 1\right] \cdot \theta + w_{p,i} + w_{f,i} \cdot R_{rs} - \left[\dot{V}_i \;\; V_i \;\; 1\right] \cdot \theta\right)^2\right\} =$$

$$= E\left\{\left(w_{p,i} + w_{f,i} \cdot R_{rs}\right)^2\right\} = \quad E\left\{w_{p,i}^2 + w_{f,i}^2 \cdot R_{rs}^2 + 2 \cdot w_{p,i} \cdot w_{f,i} \cdot R_{rs}\right\} =$$

$$= E\left\{w_{p,i}^2\right\} + R_{rs}^2\, E\left\{w_{p,i}^2\right\} + 2 \cdot R_{rs} \cdot E\left\{w_{p,i} \cdot w_{f,i}\right\} =$$

$$= E\left\{w_{p,i}^2\right\} + R_{rs}^2\, E\left\{w_{p,i}^2\right\} = \sigma_{w_p}^2 + R_{rs}^2 \cdot \sigma_{w_f}^2$$

where we have used the fact that $w_{f,i}$ and $w_{p,i}$ have zero means and are independent. So, we can then conclude that the random vector $Z|\theta$ is a multivariate Gaussian variable with mean equal to $H \cdot \theta$ and covariance matrix equal to C_{w_p}+$R_{rs}^2 \cdot C_{w_f}$:

$$Z|\theta \sim N\left(H \cdot \theta, C_{w_p} + R_{rs}^2 \cdot C_{w_f}\right)$$

Hence, the likelihood function would be computed as:

$$p(Z|\theta) = \frac{e^{-\frac{1}{2}\cdot(Z-H\theta)^T\cdot\left(C_{w_p}+R_{rs}^2\cdot C_{w_f}\right)^{-1}\cdot(Z-H\theta)}}{\left[(2\pi)^N det\left(C_{w_p} + R_{rs}^2 \cdot C_{w_f}\right)\right]^{\frac{1}{2}}} \tag{4-13}$$

In conclusion, by comparing Eq. 4-13 with Eq. 4-11, we can observe that the difference between the case with noise on the pressure measurement and the case with noise on both pressure and flow measurements would be in the covariance matrix of $Z|\theta$. Particularly, in the first case, $C_{Z|\theta}$would be given by the covariance matrix of the noise vector and hence it would be independent from the parameter θ, whereas in the second case $C_{Z|\theta}$would be given by the sum of the covariance matrix of the pressure noise vector and the covariance matrix of the flow noise scaled by the value of R_{rs} and it would be dependent on the parameter θ. Based on these observations, we can conclude that if we consider the noise on both pressure and flow measurements, the computational approach described above to derive the posterior p.d.f. $p(\theta|Z)$ would still be valid, provided that the covariance matrix C_w in Eq. 4-11 is replaced by $C_{w_p} + R_{rs}^2 \cdot C_{w_f}$.

4.6.2 Results

The feasibility of the proposed Bayesian estimation method was investigated via a two-stage process and its performance was compared against the classic LS method. In the first stage, the performance of both estimation methods were evaluated on simulated data, whereas in the second stage real animal data were used. In both cases, the noise was only considered on the pressure signal. However, considering the noise to be present on the flow signal as well would not change the results, for the reasons mentioned above.

Algorithm Evaluation on Simulated Data – Stage 1

A simulated airway pressure vector $\tilde{Z} = \begin{bmatrix} \tilde{P}_{ao}(t_1) \\ \tilde{P}_{ao}(t_2) \\ \cdot \\ \cdot \\ \cdot \\ \tilde{P}_{ao}(t_N) \end{bmatrix}$ was first generated by solving Eq. 4-10 and using the experimental flow and volume data collected during the animal test and shown in Figure 4.3. While solving Eq. 4-10 for $\tilde{Z}$, the values of the parameter vector were kept constant and fixed to a nominal value $\bar{\theta} = [\,\bar{R}_{rs}\ \ \bar{E}_{rs}\ \ \bar{P}_0]^T$. The nominal values of the parameters were selected as equal to the mean of the corresponding prior Gaussian distribution shown in Figure 4.4 plus an offset of $\pm 50\%$ of the parameter range. In other words, this choice is equivalent to assuming that when assigning the prior distribution the a priori mean will be off with respect to the nominal parameter value by 50% of the entire parameter range. The noise term W was generated in Matlab using the *randn* command as a sequence of random variables from a Gaussian distribution with 0 mean and standard deviation σ_w^2. The noise was then added to the simulated airway pressure vector $\tilde{Z}$ according to:

$$\bar{Z} = \tilde{Z} + W$$

The Bayesian MAP estimation method described above was applied to the simulated noisy airway pressure vector $\bar{Z}$, using the experimental flow $(\dot{V})$ and volume (V) signals to construct the input matrix H (see Eq. 4-10). The resulting posterior p.d.f. was then used to provide an estimate of the parameters according to the MAP principle and the estimated parameters were compared with the corresponding nominal values used to generate the data $\tilde{Z}$. To summarize the accuracy of the proposed approach, the residual sum of squares (RSS) between the model predicted airway pressure and the original noise-free pressure vectors was computed according to:

$$RSS = \sum_{i=1}^{N} \left(\tilde{P}_{ao}(t_i) - \hat{P}_{ao}(t_i) \right)^2$$

In order to assess the precision of the proposed approach, the variances of the estimated parameters were also computed from the corresponding posterior p.d.f. according to:

$$Var\{\hat{R}_{rs\,MAP}\} = \int_{R_{rs}} (R_{rs} - E\{R_{rs}|\bar{Z}\}) \cdot p(R_{rs}|\bar{Z})\ dR_{rs}$$

$$Var\{\hat{E}_{rs\,MAP}\} = \int_{E_{rs}} (E_{rs} - E\{E_{rs}|\bar{Z}\}) \cdot p(E_{rs}|\bar{Z})\ dE_{rs}$$

$$Var\{\hat{P}_{0\,MAP}\} = \int_{R_{rs}} (P_0 - E\{P_0|\bar{Z}\}) \cdot p(P_0|\bar{Z})\ dP_0$$

where, as usual, the integrals have been numerically approximated via summations. The estimated variances were then converted into standard deviations, by taking the square root, and scaled by the corresponding parameter estimates to yield the coefficients of variation (*CV*) defined as [122]:

$$CV_{R_{rs\,MAP}} = \frac{\sqrt{Var\{\hat{R}_{rs\,MAP}\}}}{\hat{R}_{rs\,MAP}} \cdot 100$$

$$CV_{E_{rs\,MAP}} = \frac{\sqrt{Var\{\hat{E}_{rs\,MAP}\}}}{\hat{E}_{rs\,MAP}} \cdot 100$$

$$CV_{P_{0\,MAP}} = \frac{\sqrt{Var\{\hat{P}_{0\,MAP}\}}}{\hat{R}_{rs\,MAP}} \cdot 100$$

The coefficient of variation *CV* (also known as fractional standard deviation *FSD*) is a standardized measure of the estimation accuracy, with values of $CV \gg 100\%$ indicating a poor accuracy and values $< 10\%$ indicating an excellent accuracy [123].

Analogous metrics for accuracy and precision were also computed for the LS derived estimates. In this case, the estimate variance was extracted from the diagonal of the estimate covariance matrix computed according to [124]:

$$C_{\hat{\theta}\,LS} = (H^T \cdot C_w^{-1} \cdot H)^{-1} \tag{4-14}$$

In order to evaluate the effects of noise and number of data points on the estimator performance, simulations were performed with different noise levels and different number of data points for the measurement vector $\tilde{Z}$. Particularly, we performed simulations with a standard deviation noise σ_w of 2% (low noise), 5% (medium noise) and 10% (high noise) of the dynamic range of the pressure signal and for each noise level we set the length of the data vector at N=10, N=50 and N=100 data points.

The results obtained when using Gaussian prior distributions (case 1 in *Prior Probability Density Functions* section) are summarized in Figure 4.7 - Figure 4.9. Comparison in terms of *RSS* and *CV* between the Bayesian MAP and the LS estimation methods is provided in Table 4-1 - Table 4-3. The results show how the prior Gaussian distributions are updated using the measurements, resulting in posterior distributions that are still Gaussian (a part from some numerical errors due to the discretization process) but more centred around the true parameter values. Furthermore, since the proposed Bayesian estimation framework provides an approximation of the full a-posteriori probability density function, it is possible to immediately have a visual assessment of the level of confidence that we can have on our estimates by simply looking at how much the posterior p.d.f. is spread around its mean value (i.e. by looking at its variance or standard deviation). This is a clear advantage of Bayesian estimation methods over classical approaches (LS or ML) that require computation of the parameter variances via numerical approximations that are valid only under white noise assumption (see Eq.4-14).

Particularly, Figure 4.7 shows how the proposed approach performs when the number of data points considered is sufficiently high (N=100). It proves that the method is effectively able to estimate the unknown parameters with good precision and accuracy at all noise levels, even though the a-priori parameter means are far from the true parameter values. We can observe that, at low noise level, the posterior distributions are practically delta functions centred around the true parameter values, indicating that the estimator is unbiased and with a very small variance. This is confirmed by the very low *CV* numbers (<1% for all parameters) shown in Table 4-1. As the level of noise increases from low to high, a very small bias is introduced and the a-posteriori p.d.f. become slightly wider indicating a reduced level of confidence on the estimated parameters. However, the coefficient of variations are still pretty low: $<$10% for all parameters, except for R_{rs} at high noise level for which *CV*=14%. This proves the capability of the proposed approach to cope with high noise levels. It is also interesting to notice that at all noise levels the *CV*s are higher for R_{rs} than for the other two parameters, indicating that when N=100 the estimation of this parameter is more critical. By comparing the Bayesian MAP estimator against the LS algorithm (see Table 4-1), we can observe no clear advantage in this specific case: the RSS numbers are in the same order of magnitude and both methods provide estimated parameters very close to their true nominal values at all noise levels. Only a slight reduction in the *CV* numbers is obtained when using the Bayesian approach, suggesting that the use of prior information can indeed improve precision of the estimates.

The behaviour of the proposed Bayesian estimation method when the number of data points is reduced to N=50 is summarized in Figure 4.8. It shows that by reducing the number of data points, the effect of the a-priori information becomes more evident. The mean of the a-posteriori parameter distributions are now slightly off from the corresponding nominal parameter values and the spread of the posterior p.d.f. around the mean value is increased at all noise levels compared to the N=100 case. Nevertheless, the algorithm is still able to provide satisfactory results at low and medium noise levels, in terms of both accuracy and precision. At high noise level, the estimates are significantly off from the corresponding nominal values but the improvements from the a-priori assumed distributions is still quite significant. The *CV*s for P_0 are below 6.5% and the *CV*s for E_{rs} are below 10.5% at all noise levels. As in the previous case (N=100), the *CV*s for R_{rs} are higher compared to those of the other two parameters at all noise levels, with a maximum of 18.8% at high noise. By comparing the performance of the MAP and the LS estimators (see Table 4-2) it emerges that the two algorithms provide comparable results at low and medium noise levels, in terms of parameter values and RSS. However, as observed for the previous case (N=100), the Bayesian MAP estimator results in significantly lower CVs for all parameters at all noise levels. This is in agreement with our previous intuition that the use of additional prior information improves accuracy of the estimator. Furthermore, by looking at the results for the high noise case, we can conclude that when the noise level is high and the number of data points is relatively low, the LS fails in estimating the most critical parameter R_{rs} (estimated value 1.3 vs nominal value of 5, with a CV of 202%), whereas the Bayesian MAP algorithm still provides acceptable results (estimated value of 7.75, with a CV of 18.8 %)

Figure 4.9 summarizes the results obtained when the number of data points is further reduced (N=10). In this extreme case, the performance of the proposed algorithm are significantly compromised, due to the very little information contained in the data especially at high noise levels. Nevertheless, the estimation of R_{rs} and P_0 is still quite acceptable, at least for the low and medium noise level cases. On the contrary, estimation of E_{rs} appears to be the critical. This is in contrast to what observed earlier for N=50 and N=100, where the critical parameter was R_{rs}. By comparing the Bayesian MAP and the LS algorithms (see Table 4-3) the superiority of the proposed Bayesian approach appears evident: at low noise level, the distance between estimated and true parameter values is much larger for the LS method than for the MAP method; at medium and high noise levels, the LS estimated E_{rs} even assume negative values with very high CV numbers (CV of 160% and 40%, respectively), whereas the MAP estimated E_{rs} remains bound by its prior p.d.f.. This is a clear example of how the incorporation of prior information into the estimation algorithm can be useful in data poor situations, where classical estimation approaches such as the LS or the ML may provide unreasonable solutions.

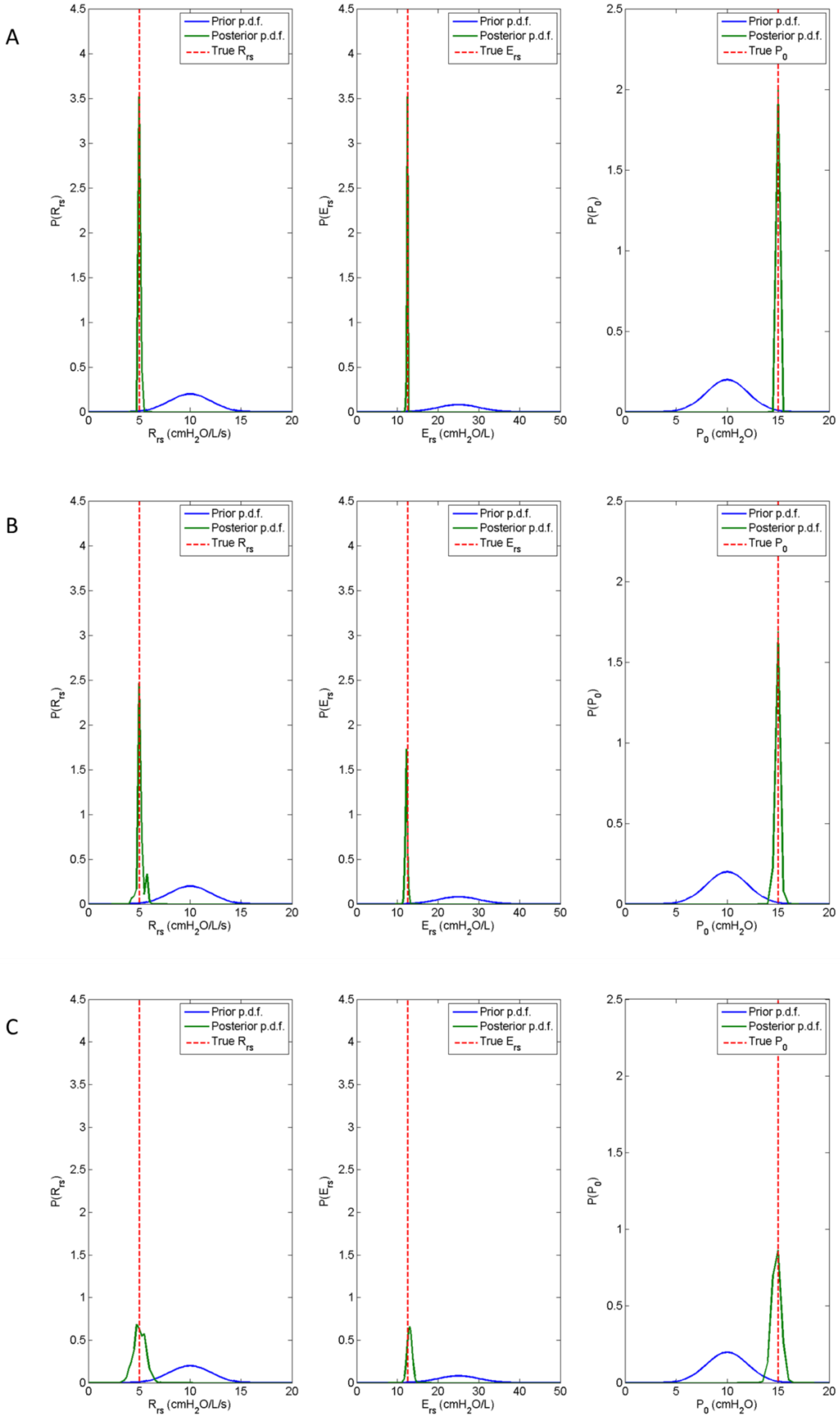

Figure 4.7 – Results obtained via Bayesian estimation when using N=100 data points and Gaussian prior distributions for different noise levels. A, low noise; B, medium noise; C, high noise. Left plots are the p.d.f. of R_{rs}, middle plots are the p.d.f. of E_{rs} and right plots are the p.d.f. of P_0. Blue curves indicate the a priori distributions, green curves indicate the computed posterior distributions and red lines represent the true nominal parameter values.

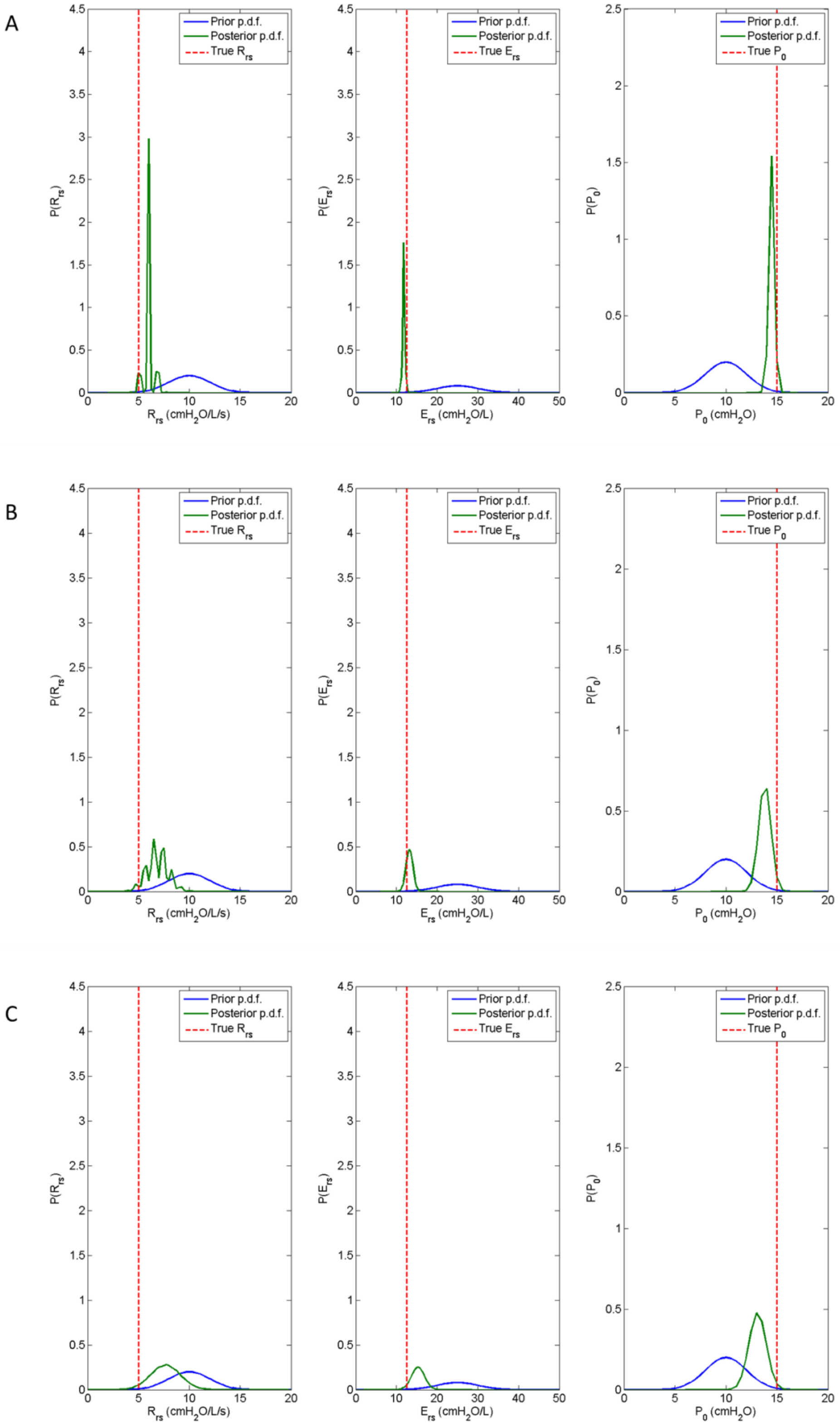

Figure 4.8 – Results obtained via Bayesian estimation when using N=50 data points and Gaussian prior distributions for different noise levels. A, low noise; B, medium noise; C, high noise. Left plots are the p.d.f. of R_{rs}, middle plots are the p.d.f. of E_{rs} and right plots are the p.d.f. of P_0. Blue curves indicate the a priori distributions, green curves indicate the computed posterior distributions and red lines represent the true nominal parameter values.

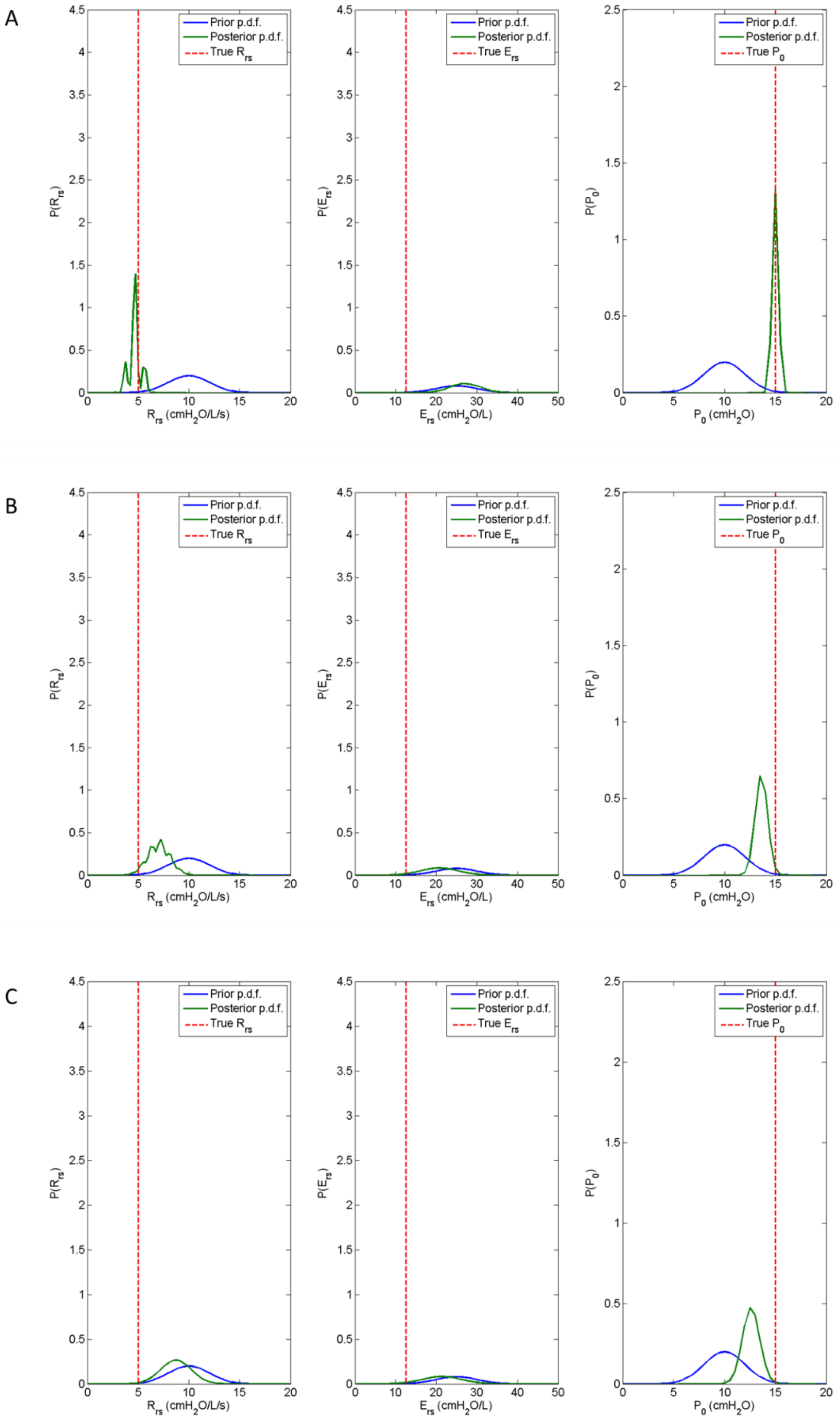

Figure 4.9 – Results obtained via Bayesian estimation when using N=10 data points and Gaussian prior distributions for different noise levels. A, low noise; B, medium noise; C, high noise. Left plots are the p.d.f. of R_{rs}, middle plots are the p.d.f. of E_{rs} and right plots are the p.d.f. of P_0. Blue curves indicate the a priori distributions, green curves indicate the computed posterior distributions and red lines represent the true nominal parameter values.

		N° Data Points = 100			
		R_{rs} (cmH2O/L·s^{-1}) $R_{rs\ true} = 5$	**E_{rs} (L/cmH2O)** $E_{rs\ true} = 12.5$	**P_0 (cmH2O)** $P_{0\ true} = 15$	**RSS**
2% Noise	**MAP**	5 (0.0634)	12.5 (0.0434)	15 (0.0098)	0
	LS	4.8268 (2.6732)	12.4810 (0.9934)	15.0985 (0.5996)	0.0658
5% Noise	**MAP**	5 (5.9588)	12.25 (2.3672)	15 (1.3112)	0.6049
	LS	4.8885 (6.5987)	12.0632 (2.5696)	15.1154 (1.4974)	0.8143
10% Noise	**MAP**	4.75 (14.1144)	13 (4.6659)	15 (3.0545)	1.0173
	LS	4.1338 (15.6068)	12.4049 (4.9976)	15.4925 (2.9219)	1.6445

Table 4-1 - Results obtained via Bayesian MAP and LS estimation when using N=100 data points and Gaussian prior distributions for different noise levels. The number in parenthesis represent the coefficient of variation CV of the corresponding estimated parameter.

		N° Data Points = 50			
		R_{rs} (cmH2O/L·s^{-1}) $R_{rs\ true}$ = 5	**E_{rs} (L/cmH2O)** $E_{rs\ true}$ = 12.5	**P_0 (cmH2O)** $P_{0\ true}$ = 15	**RSS**
2% Noise	**MAP**	6 (7.2559)	11.75 (2.6196)	14.5 (1.6851)	0.2088
	LS	5.6059 (9.4064)	11.8286 (2.9928)	14.7259 (2.0087)	0.1288
5% Noise	**MAP**	6.5 (17,1232)	13.25 (6.4358)	14 (4.4546)	0.7153
	LS	4.8031 (27.4466)	13.3368 (6.6359)	15.0018 (4.9294)	0.2023
10% Noise	**MAP**	7.75 (18.8096)	15.25 (10.4579)	13 (6.4453)	4.7925
	LS	1.3043(202.1418)	15.6493 (11.3107)	16.7897 (8.8089)	3.1912

Table 4-2 - Results obtained via Bayesian MAP and LS estimation when using N=50 data points and Gaussian prior distributions for different noise levels. The number in parenthesis represent the coefficient of variation CV of the corresponding estimated parameter.

		N° Data Points = 10			
		R_{rs} (cmH2O/L·s^{-1}) $R_{rs\ true} = 5$	**E_{rs} (L/cmH2O)** $E_{rs\ true} = 12.5$	**P_0 (cmH2O)** $P_{0\ true} = 15$	**RSS**
2% Noise	**MAP**	4.75 (12.208)	26.75 (14.0734)	15 (1.9446)	0.4662
	LS	3.6084 (18.879)	33.6768 (17.0557)	15.4473 (2.0711)	0.589
5% Noise	**MAP**	7.25 (15.7263)	20.75 (22.5364)	13.5 (4.5428)	1.0988
	LS	6.067 (28.1)	- 0.8978 (159.9)	14.5678 (5.5)	0.3346
10% Noise	**MAP**	8.75 (17.1473)	21.5 (22.8063)	12.5 (6.7385)	3.1371
	LS	9.6869 (35.1621)	-70.8396 (40.5409)	13.9457 (11.4705)	7.459

Table 4-3 - Results obtained via Bayesian MAP and LS estimation when using N=10 data points and Gaussian prior distributions for different noise levels. The number in parenthesis represent the coefficient of variation CV of the corresponding estimated parameter.

In order to verify the correctness of the numerical implementation of the Bayesian estimation method, we also compared the results obtained via the numerical method against those obtained using the analytical expression for the MAP estimator described earlier (see *The Gaussian Case with Linear Model* section). The comparison for the N=50 case is summarized in Table 4-4 from which we can notice that the two methods indeed provide the same estimated values except for numerical approximations due to the discretization process used in the numerical method.

	N° Data Points = 50		
	R_{rs} (cmH2O/L·s^{-1}) *$R_{rs\ true} = 5$*	**E_{rs} (L/cmH2O)** *$E_{rs\ true} = 12.5$*	**P_0 (cmH2O)** *$P_{0\ true} = 15$*
MAP	6	11.75	14.5
MAP analytical	6.0169	11.7923	14.4886
MAP	6.5	13.25	14
MAP analytical	6.865	13.1913	13.8067
MAP	7.75	15.25	13
MAP analytical	7.6535	15.2822	13.0988

Table 4-4 – Comparison between the numerical Bayesian MAP estimator and the analytical MAP estimator.

Finally, in order to show that the proposed approach is applicable to different patient classes, which would be characterized by different prior parameter distributions, simulations were also performed using the extreme value a-priori distributions simulating an obstructive and a restrictive disease (see *Prior Probability Density Functions* section). Results are shown in Figure 4.10 and Figure 4.11, respectively, for the N=100 and medium noise level case. They are not substantially different from the corresponding results obtained using Gaussian prior distribution and they confirm that the proposed approach can be virtually applied to different patient classes once the a-priori parameter distributions have been built.

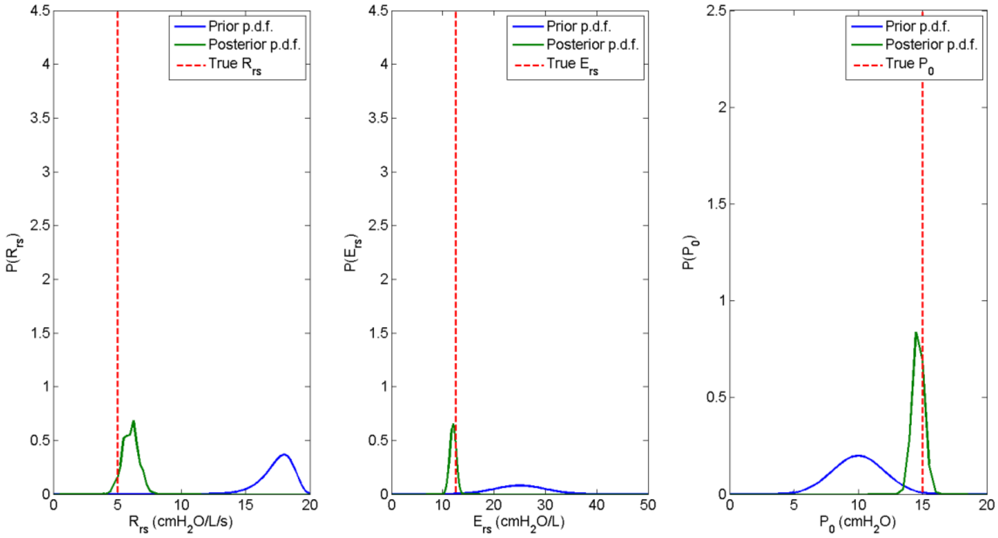

Figure 4.10 – Results obtained via Bayesian estimation at medium noise level when using N=100 data points and prior distributions simulating an obstructive disease patient. Left plots are the p.d.f. of R_{rs}, middle plots are the p.d.f. of E_{rs} and right plots are the p.d.f. of P_0. Blue curves indicate the a-priori distributions, green curves indicate the computed posterior distributions and red lines represent the true nominal parameter values.

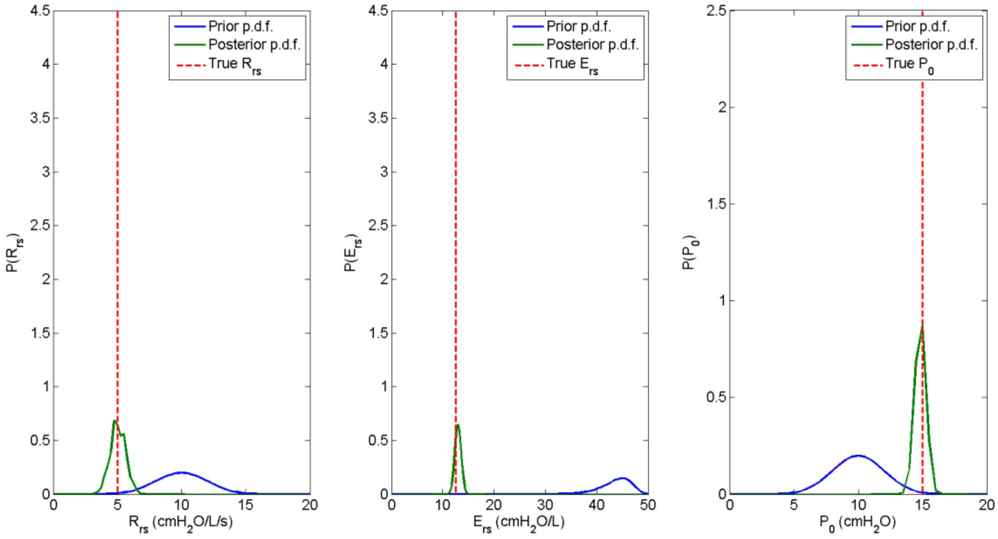

Figure 4.11– Results obtained via Bayesian estimation at medium noise level when using N=100 data points and prior distributions simulating a restrictive disease patient. Left plots are the p.d.f. of R_{rs}, middle plots are the p.d.f. of E_{rs} and right plots are the p.d.f. of P_0. Blue curves indicate the a-priori distributions, green curves indicate the computed posterior distributions and red lines represent the true nominal parameter values.

Algorithm Evaluation on Real Data – Stage 2

The performance of the proposed Bayesian estimation approach was finally evaluated on the real data without using the simulation approach described in the previous section. In this case, the experimental airway pressure signal $P_{ao}(t)$ was used to construct the data vector

$Z = \begin{bmatrix} P_{ao}(t_1) \\ P_{ao}(t_2) \\ \cdot \\ \cdot \\ \cdot \\ P_{ao}(t_N) \end{bmatrix}$ and the experimental flow $(\dot{V})$ and volume (V) signals were used to construct the input matrix H (see Eq.4-10). The a-priori parameter probability density functions were assumed to be Gaussian with the same mean and standard deviation used for the simulated data case. Since in this case the actual values of the parameters are not known, it was necessary to have some gold standards to assess the performance of the estimator. Hence, the gold standards for the R_{rs} and E_{rs} parameters were obtained from the ventilator via the inspiratory hold maneuver, whereas the gold standard P_0 was assumed to be equal to the external PEEP applied by the ventilator. The MAP Bayesian estimator method described above was applied to the dataset shown in Figure 4.12, corresponding to a VCV breath with no spontaneous respiratory activity as described in the *Methods* section. The LS method was applied to the same dataset as well, in order to allow for a direct comparison between the 2 approaches in terms of *RSS* and *CV* numbers. As shown in Eq. 4-11, when applying the MAP Bayesian method the covariance C_w of the noise term W needs to be selected. Under the assumption of white Gaussian noise, C_w has been assumed a diagonal matrix:

$$C_w = \sigma_w^2 \cdot I_N$$

where the variance σ_w^2 has been estimated from the residual errors obtained via the LS method according to [98]:

$$\sigma_w^2 = \frac{1}{N-p}\sum_{i=1}^{N}\left(P_{ao}(t_i) - \hat{P}_{ao\,LS}(t_i)\right)^2$$

where $\hat{P}_{ao\,LS}$ is the predicted airway pressure computed using the estimates parameters from the Least Squares algorithm.

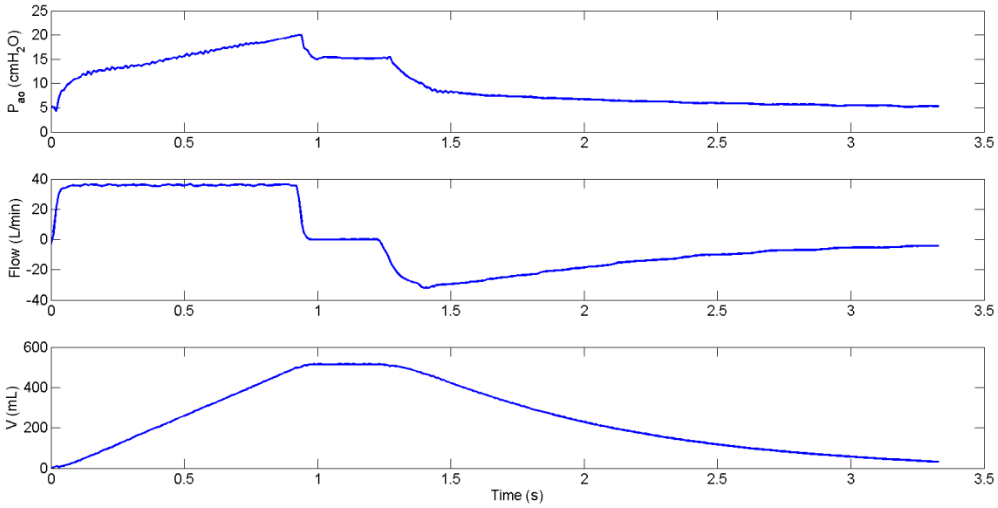

Figure 4.12 – Experimental dataset from the animal test described in chapter 3 used to in the 2nd stage validation step. From top to bottom: P_{ao}, is the pressure measured at the airway opening; Flow, is the air flow at the mouth; V, is the volume above FRC obtained by numerical integration of the flow signal; P_{es} is the invasive esophageal pressure, surrogate of the intrapleural pressure.

The results obtained by applying the proposed Bayesian approach to the dataset shown above with different data vector lengths (N=100, 50 and 10) are summarized in Figure 4.13. We can observe that when the number of data samples is sufficiently high (N=100), the method provides posterior parameters p.d.f. that are centered around the corresponding gold standard values and that are not very spread. This proves the accuracy of the proposed method also in a real case scenario. As observed in the simulation cases, as the number of data points used in the estimation is reduced (N=50 and N=10), small biases are introduced and the computed posterior p.d.f. becomes wider. Particularly, as it was also suggested from the simulation study, the elastance E_{rs} seems to be the most critical parameter, whereas estimation of P_0 seems to be sufficiently accurate even with few data samples (N=10). By comparing the Bayesian MAP estimator against the LS algorithm (see Table 4-5), we can observe that for N=100 and N=50 the two methods provide essentially similar results: the estimated parameter values are very close, the *RSS* numbers are in the same order of magnitudes and the *CV*s are very similar. However, for N=10 the Bayesian approach appears evidently better: the LS provides estimates of R_{rs} and E_{rs} that are way off from the corresponding gold standard values and *CV*s of 43% and 25%, respectively; on the contrary, the use of prior information in the Bayesian approach prevents the resulting estimates to deviate too much from the corresponding gold standard values, with *CV*s significantly lower than those obtained via the LS method.

		R_{rs} (cmH2O/L·s^{-1}) *$R_{rs\ true} = 7.9$*	**E_{rs} (L/cmH2O)** *$E_{rs\ true} = 20.543$*	**P_0 (cmH2O)** *$P_{0\ true} = 5$*	**RSS**
N=100	**MAP**	8 (5.9689)	20.5 (2.3421)	5.5 (5.9497)	57.9187
	LS	8.0827 (6.1369)	20.4637 (2.3447)	5.3709 (6.0876)	57.0283
N-50	**MAP**	9.25 (9.1875)	23.25 (6.0201)	4.5 (10.3178)	34.6851
	LS	9.8571 (9.7993)	23.0578 (6.4131)	4.1315 (12.4662)	34.3358
N=10	**MAP**	7.5(12.3133)	26.75 (18.4907)	4.5 (10.2373)	15.7466
	LS	3.6292 (43.1247)	151.8147 (25.0131)	4.4790 (11.5871)	9.3939

Table 4-5 - Results obtained via Bayesian MAP and LS estimation when using Gaussian prior distributions for different number of data points N.The number in parenthesis represent the coefficient of variation CV of the corresponding estimated parameter.

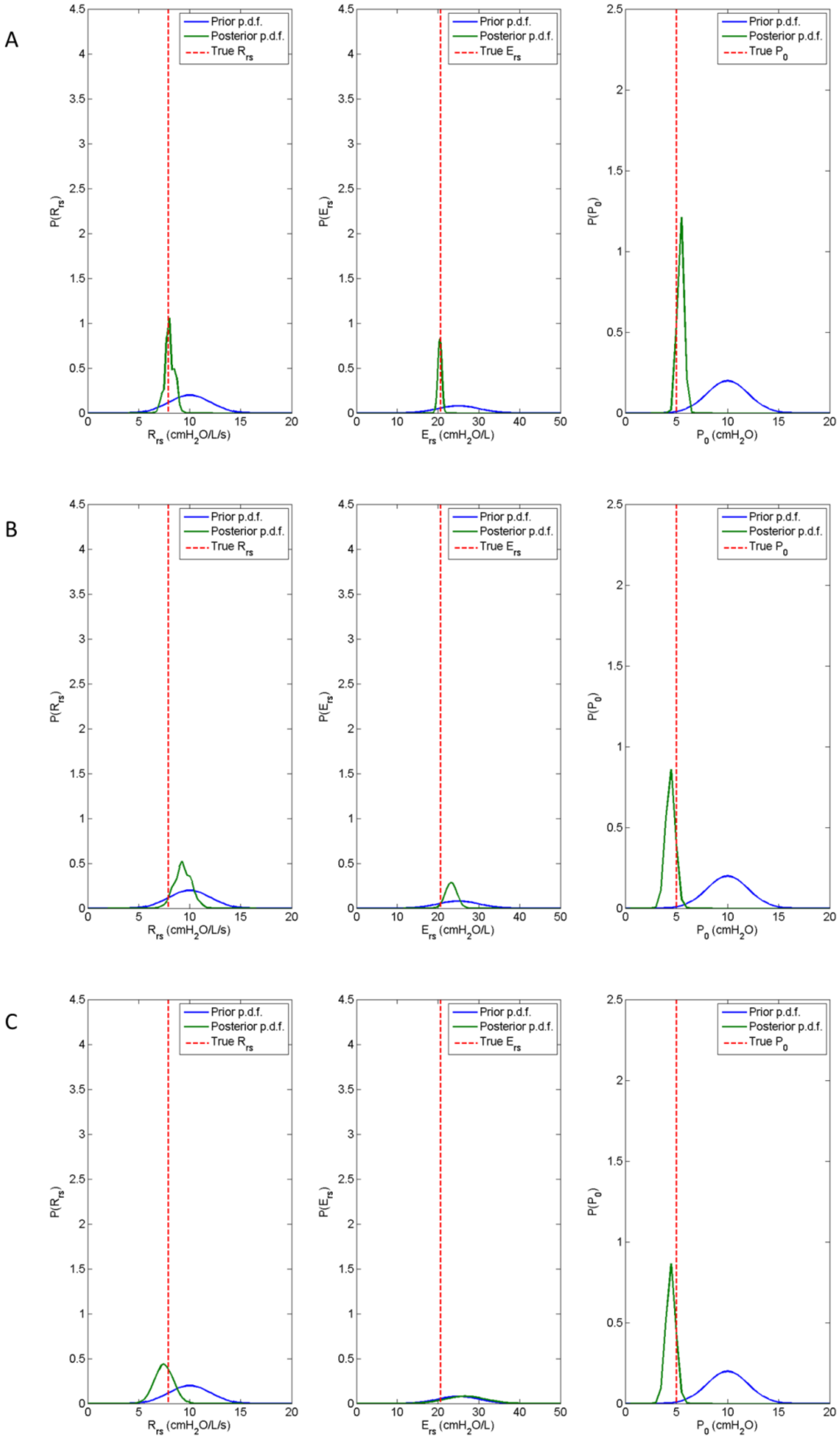

Figure 4.13 – Results obtained via Bayesian estimation when using Gaussian prior distributions for different number of data points N. A,N=100; B, N=50; C, N=10. Left plots are the p.d.f. of R_{rs}, middle plots are the p.d.f. of E_{rs} and right plots are the p.d.f. of P_0. Blue curves indicate the a priori distributions, green curves indicate the computed posterior distributions and red lines represent the nominal parameter values.

4.6.3 Discussion

In this work we have applied Bayesian inference and Maximum a Posteriori (MAP) estimator to a case study related to the estimation of the parameters of a 1st order single-compartment model of the respiratory system under passive conditions (no patient's spontaneous respiratory activity). The performance of the MAP Bayesian approach was compared with those of the Least Squares (LS) method, one of the most popular classic (or Fisherian) estimation methods. Our results show that: the parameter estimates do not significantly change between the two approaches when the noise present in the data is sufficiently low and the number of data points used in the estimation process is sufficiently high (i.e., when there is enough a-posteriori information available); the precision of the estimates always improve with the Bayesian approach; when the noise is high and/or the number of data samples used in the estimation process is reduced, the LS method can provide non-physiological parameter estimates (negative values) whereas the Bayesian approach remains bounded by the a-priori probability density function. Bayesian methods might be useful when the respiratory system parameters are assumed to be varying in time and the objective of the estimator is to track these variations. In such situations, a typical approach consists of fitting the model to very short window of data either by using the LS method on a moving window or by applying LS in his recursive formulation with forgetting factor (RLS with Exponential Forgetting). In these applications, the window size needs to be carefully selected in order to find the optimal trade-off between noise sensitivity and algorithm responsiveness. We conjecture that Bayesian methods, being more robust than classical methods when the available a-posteriori information is reduced, may represent a valuable alternative. Furthermore, Bayesian estimation allows to naturally include constraints in the parameter estimates in the form of possible range of values. This feature is definitely attractive in physiological parameter estimation problems since, in many cases, physiological ranges can be a-priori determined for the majority of the parameters involved.

Finally, the results obtained from this case-study can be generalized and allow us to conclude that when a-priori information on the unknown parameters of a physiological model is available, Bayesian estimation can be of relevant interest since it reduces the uncertainty of the parameter estimates and can also serve as a practical way to constraint the parameter estimates within specific ranges.

4.7 Conclusions and Future Work

In this chapter we have introduced the concept of Bayesian parameter estimation and explained the difference and the potential advantages of Bayesian techniques over classical approaches. We have shown how Bayesian methods naturally allow incorporating available a-priori knowledge about the parameters and we have provided examples of cases where the Bayesian formulation has an analytically tractable closed-form. Then, we have implemented Bayesian estimation and applied it to a case-study related to the same respiratory system model analysed in Chapter 3. Some conclusions about the potential advantages of Bayesian techniques have been drawn from this case-study and have been discussed in the previous section. Here, we want to conclude with the hypothesis that given the improvements in the estimate precision, Bayesian estimation methods may allow to adopt more complex models than those determinable by classical approaches. This hypothesis will be the object of further study. Moreover, we want to stress the point that the application of Bayesian estimation to the respiratory system case-study was only the first step toward the development of a Bayesian framework for the estimation of parameters of complex physiological models such as the one presented in Chapter 2. This aspect in particular will be the object of subsequent investigation. Finally, we want to mention the possibility to implement Bayesian estimation in a recursive fashion, rather than applying it on a batch of data as we have done in the respiratory system case-study. In fact, it is possible to update the posterior p.d.f. in Bayes' theorem every time a new data is collected and then use the computed posterior as prior distribution for the next updating step. This is a core concept in Bayesian learning that makes this approach particularly appealing for real-time implementation in an clinical environment. On the other hand, some computational challenges may be associated with this approach and will also be the subject of further investigation.

Chapter 5: Summary and Future Research

In this thesis we have taken a small step toward personalized medicine, which allows for optimized health assessment and therapy. We have postulated the use of physiology-based mathematical models combined with parameter estimation techniques for clinical diagnostic and therapeutic applications. This comprised several steps.

We have developed a novel comprehensive mathematical model (Chapter 2) of the cardiovascular and respiratory systems along with their main neural feedback, gas exchange, and tissue metabolism. The cardiopulmonary model results for both normo- and patho-physiology represented with good fidelity published human and animal studies. In normal conditions, the mean model predicted hemodynamics (arterial blood pressure, central venous pressure, pulmonary artery pressure, left atrium and ventricle pressure) as well as gas exchange variables (arterial, venous, alveolar and dead space gas partial pressures) were all within the normal ranges experimentally observed in healthy 70 Kg subjects. The model simulated cardiovascular and respiratory responses to hypercapnic (3% - 7% CO_2 in air) and hypoxic (8% O_2 in air) stimuli were analysed in terms of respiratory rate, tidal volume, minute ventilation, alveolar Po_2 and Pco_2, heart rate and arterial (mean, diastolic and systolic) blood pressure. Excellent agreement with human data from literature was found for all the variables in both transient phase and steady-state.

We then considered a very simple physiology-based lung mechanics model and we have developed two parameter estimation techniques (Chapter 3), the CLS and the MKF, in order to assess continually and non-invasively parameters that are indicative of lungs' health (respiratory system resistance and compliance) and patient's effort (work of breathing, WOB). The current ways of measuring these parameters are via interruptive manoeuvres to the mechanical ventilator and via invasive procedures. The validity of the two proposed estimation techniques was first proven on data obtained from a respiratory system simulator and subsequently tested on real pig data. Excellent agreement between the noninvasive estimates from the proposed techniques and the corresponding gold standard invasive measurements was found. The mean error in WOB estimates was -0.1311 J/L and -0.0083 J/L for the CLS and the MKF algorithm, respectively.

Physiology-based mathematical models can be deterministic or stochastic. The above work is based on a deterministic approach. We have also built (Chapter 4) a probability-based approach that uses a priori information about the parameters to be estimated, typically obtained from population studies. A Bayesian Maximum a Posteriori Probability (MAP) estimator was implemented and applied to a case-study of respiratory mechanics estimation. Superiority against the classical Least Squares method was proven in data-poor situations.

The tools developed in this thesis open several future research possibilities. This work can be further extended in terms of modeling, parameter estimation, and applications in diagnosis and therapy in order to make personalized medicine a companion to clinicians, hence complementing their clinical decision capacity. More specifically:

Chapter 2: The cardiopulmonary model can be expanded to include additional physiological mechanisms, such as long term regulation, kidney dynamics, acid-base balance, cerebrovascular regulation, etc.

Chapter 3: The parameter estimation techniques can be applied to more complex models of the respiratory system (non-linear and/or multi-compartment models). Other areas for their application can also be envisioned

a. Home ventilation
b. Anaesthesia

Furthermore, the estimated WOB can be used as a variable for closed-loop control of MV, where the clinician will enter a WOB trajectory (high-level therapy plan) and a controller will adjust ventilator settings in order to maintain patient WOB within the desired target.

Chapter 4: The Bayesian parameter estimation framework can be expanded to a larger number of model's parameters and applied to different physiological systems, such as the cardiovascular or gas exchange.

Finally, the model-based approach that is the driving principle of this research can be applied to other clinical and therapeutic areas:

- Anesthesia
- Fluid management
- Cardiovascular monitoring
- Drug infusion

as well as across the continuum of care (OR, ICU, general ward, home).

Bibliography

[1] N. Macintyre, “Evolution of the modern mechanical ventilator,” in *Ventilator Management Strategies for Critical Care*, Informa Healthcare, 2001.

[2] N. Halpern and S. Pastores, “Critical care medicine in the united states 2000-2005: an analysis of bed numbers, occupancy rates, payer mix, and costs,” *Crit Care Med,* vol. 38, pp. 65-71, 2010.

[3] J. Dasta, T. McLaughlin, S. Mody and C. Piech, “Daily cost of an intensive care unit day: the contribution of mechanical ventilation,” *Crit Care Med,* vol. 33, pp. 1266-71, 2005.

[4] F. Lellouche, P. Bouchard, S. Simard, E. L'Her and M. Wysocki, “Evaluation of fully automated ventilation: a randomized controlled study in post-cardiac surgery patients,” *Intensive Care Med,* vol. 39, pp. 463-471, 2013.

[5] M. Ursino and E. Magosso, “Acute cardiovascular response to isocapnic hypoxia. I. A mathematical model,” *Am J Physiol Heart Circ Physiol,* vol. 279, pp. H149-H165, 2000.

[6] M. Ursino and E. Magosso, “A mathematical model of CO2 effect on cardiovascular regulation,” *Am J Physiol Heart Circ Physiol,* vol. 281, pp. H2036-H2052, 2001.

[7] G. Iotti, A. Braschi, J. Brunner, A. Palo and M. Olivei, “Noninvasive evaluation of instantaneous total mechanical activity of the respiratory muscles during pressure support ventilation,” *Chest,* vol. 108, pp. 208-215, 1995.

[8] N. Euliano, V. Brenna, P. Blanch and M. Banner, “Power of breathing determined noninvasively with use of an artificial neural network in patients with respiratory failure,” *Crit Care Med,* vol. 34, pp. 1052-1059, 2006.

[9] Y. Yamada, M. Shigeta, K. Suwa and K. Hanaoka, “Respiratory muscle pressure analysis in pressure-support ventilation,” *J Appl Physiol,* vol. 77, pp. 2237-2243, 1994.

[10] F. Grodins, J. Gray, K. Schroeder, A. Norins and R. Jones, “Respiratory responses to CO2 inhalation; a theoretical study of nonlinear biological regulator,” *J Appl Physiol,* vol. 7, pp. 283-308, 1954.

[11] F. Grodins, J. Buell and A. Bart, “Mathematical analysis and digital simulation of the respiratory control system,” *J Appl Physiol,* vol. 22, pp. 260-276, 1967.

[12] L. Chiari, G. Avanzolini and M. Ursino, “A comprehensive simulator of the human respiratory system: validation with experimental and simulated data,” *Ann Biomed Eng,* vol. 25, pp. 985-999, 1997.

[13] M. Ursino, E. Magosso and G. Avanzolini, “An integrated model of the human ventilatory control system: the response to hypercapnia,” *Clin Physiol,* vol. 21, pp. 447-464, 2001.

[14] M. Ursino, E. Magosso and G. Avanzolini, “An integrated model of the ventilatory control system: the response to hypoxia,” *Clin Physiol,* vol. 21, pp. 465-477, 2001.

[15] A. Guyton, T. Coleman and H. Granger, “Circulation: overall regulation,” *Annu Rev Physiol,* vol. 34, pp. 13-46, 1972.

[16] S. Thomas, P. Baconnier, J. Fontecave, J. Francoise, F. Guillaud, P. Hannaert, A. Hernandez, V. Le Rolle, P. Maziere, F. Tahi and R. White, “SAPHIR: a physiome core model of body fluid homeostasis and blood pressure regulation,” *Philos Trans A Math Phys Eng Sci,* vol. 13, pp. 3175-3197, 2008.

[17] R. White, J. Leonard, R. Srinivasan and J. Charles, “Mathematical modelling of acute and chronic cardiovascular changes during extended duration orbiter (EDO) flights,” *Acta Astronaut,* vol. 23, pp. 41-51, 1991.

[18] T. Coleman, “A mathematical model of the human body in health, disease, and during treatment,” *ISA Trans,* vol. 18, pp. 65-73, 1979.

[19] T. Coleman and J. Randall, “HUMAN. A comprehensive physiological model,” *Physiologist,* vol. 25, pp. 15-21, 1983.

[20] S. Abram, B. Hodnett, R. Summers, T. Coleman and R. Hester, “Quantitative Circulatory Physiology: an integrative mathematical model of human physiology for medical education,” *Adv Physiol Educ,* vol. 31, pp. 202-210, 2007.

[21] “University of Mississipi Medical Center's Modeling Workshop,” [Online]. Available: http://physiology.umc.edu/themodelingworkshop.

[22] R. Hester, A. Brown, L. Husband, R. Iliescu, W. Pruett, R. Summers and T. Coleman, “HumMod: A modeling environment for the simulation of integrative human physiology,” *Front Physiol,* vol. 2, p. 12, 2011.

[23] “HumMod,” HC Simulations, LLC, [Online]. Available: http://hummod.org.

[24] S. Timischl-Teschl, *A global model of the cardiovascular and respiratory system,* PhD Thesis, Karl-Franzens-Uiversitat, Graz, Austria, 1998.

[25] S. Timischl-Teschl, J. Batzel and F. Kappel, “Modeling the human cardiovascular-respiratory control system: an optimal control application to the transition to non-REM sleep,” Technical Report 190, Karl-Franzens-Universitat, SFB Optimierung und Kontrolle, Graz, Austria, 2000.

[26] J. Batzel, F. Kappel and S. Timischl-Teschl, “A cardiovascular-respiratory control system model including state delay with application to congestive heart failure in humans,” *J Math Biol,* vol. 50, pp. 293-335, 2005.

[27] M. Fink, J. Batzel and F. Kappel, “An optimal control approach to modeling the cardiovascular-respiratory system: an application to orthostatic stress,” *Cardiovasc Eng,* vol. 4, pp. 27-38, 2004.

[28] F. Kappel, M. Fink and J. Batzel, “Aspects of control of the cardiovascular- respiratory system during orthostatic stress induced by lower body negative pressure,” *Math Biosci,* vol. 206, pp. 273-308, 2007.

[29] M. Ursino, “Interaction between carotid baroregulation and the pulsating heart: a mathematical model,” *Am J Physiol,* vol. 275, pp. 1733-1747, 1998.

[30] K. Lu, J. Clark, F. Ghorbel, D. Ware and A. Bidani, “A human cardiopulmonary

system model applied to the analysis of the Valsalva maneuver," *Am J Physiol Heart Circ Physiol,* vol. 281, pp. H2661-H2679, 2001.

[31] K. Lu, J. Clark, F. Ghorbel, D. Ware, J. Zwischenberger and A. Bidani, "Whole-body gas exchange in human predicted by a cardiopulmonary model," *Cardiovasc Eng,* vol. 3, pp. 1-19, 2003.

[32] K. Lu, J. Clark, F. Ghorbel, C. Robertson, D. Ware, J. Zwischenberger and A. Bidani, "Cerebral autoregulation and gas exchange studied using a human cardiopulmonary model," *Am J Physiol Heart Circ Physiol,* vol. 286, pp. H584-H601, 2004.

[33] J. Olansen, J. Clark, D. Khoury, F. Ghorbel, D. Ware and A. Bidani, "A closed-loop model of the canine cardiovascular system that includes ventricular interaction," *Comput Biomed Res,* vol. 33, pp. 260-295, 2000.

[34] A. Athanasiades, F. Ghorbel, J. Clark, S. Niranjan, J. Olansen, J. Zwichenberger and B. A, "Energy analysis of a nonlinear model of the normal human lung," *J Biol Sys,* vol. 8, pp. 115-139, 2000.

[35] C. Liu, S. Niranjan, J. Clark, K. San, J. Zwischenberger and A. Bidani, "Airway mechanics, gas exchange, and blood flow in a nonlinear model of the normal human lung," *J Appl Physiol,* vol. 84, pp. 1447-1469, 1998.

[36] "PNEUMA," BMSR Biomedical Simulations Resource, [Online]. Available: http://bmsr.usc.edu/software/pneuma/.

[37] H. Fan and M. Khoo, "PNEUMA: a comprehensive cardiorespiratory model," in *Joint EMBS-BMES Conf*, 2002.

[38] O. Ivanova and M. Khoo, "Simulation of spontaneous cardiovascular variability using PNEUMA," in *Conf Proc IEEE Eng Med Biol Soc*, 2004.

[39] L. Cheng, O. Ivanova, H. Fan and M. Khoo, "An integrative model of respiratory and cardiovascular control in sleep-disordered breathing," *Respir Physiol Neurobiol,* vol. 174, pp. 4-28, 2010.

[40] M. Khoo, "A model-based evaluation of the single-breath CO2 ventilatory response test," *J Appl Physiol,* vol. 68, pp. 393-399, 1990.

[41] W. Riddle and M. Younes, "A model of the relation between respiratory neural and mechanical outputs. II. Methods," *J Appl Physiol Respir Environ Exerc Physiol,* vol. 51, pp. 979-989, 1981.

[42] S. Rees, "The Intelligent Ventilator (INVENT) project: the role of mathematical models in translating physiological knowledge into clinical practice," *Comput Methods Programs Biomed,* vol. 104, pp. S1-29, 2011.

[43] J. Hardman, N. Bedforth, A. Ahmed, R. Mahajan and A. Aitkenhead, "A physiology simulator: validation of its respiratory components and its ability to predict the patient's response to changes in mechanical ventilation," *Br J Anaesth,* vol. 81, pp. 327-332, 1998.

[44] G. Rutledge, "VentSim: a simulation model of cardiopulmonary physiology," in *Proc Annu Symp Comput Appl Med Care,* 1994.

[45] E. Magosso and M. Ursino, “Cardiovascular response to dynamic aerobic exercise: a mathematical model,” *Med Biol Eng Comput,* vol. 40, pp. 660-674, 2002.

[46] G. Drzewiecki, S. Field, I. Moubarak and J. Li, “Vessel growth and collapsible pressure-area relationship,” *J Appl Physiol,* vol. 273, pp. H2030-H2043, 1997.

[47] M. Danielsen and J. Ottesen, “A cardiovascular model,” in *Applied Mathematical Models in Human Physiology,* Philadelphia, SIAM, Society for Industrial and Applied Mathematics, 2004.

[48] W. Timmons, “Cardiovascular models and control,” in *The Biomedical Engineering Handbook,* Boca Raton, CRC Press LLC, 2000.

[49] T. Heldt, E. Shim, R. Kamm and R. Mark, “Computational modeling of cardiovascular response to orthostatic stress,” *J Appl Physiol,* vol. 92, pp. 1239-1254, 2002.

[50] J. Olansen, J. Clark, D. Khoury, F. Ghorbel and A. Bidani, “A closed-loop model of the canine cardiovascular system that includes ventricular interaction,” *Comput Biomed Res,* vol. 33, pp. 260-295, 2000.

[51] M. Neal and J. Bassingthwaighte, “Subject-specific model estimation of cardiac output and blood volume during hemorrhage,” *Cardiovasc Eng,* vol. 7, pp. 97-120, 2007.

[52] V. Rideout, Mathematical and computer modeling of physiological systems, Prentice Hall, 1991.

[53] Y. Fukui, *A study of the human cardiovascular-respiratory system using hybrid computer modeling,* Madison: PhD Thesis, University of Winsconsin, 1972.

[54] G. Nucci and C. Cobelli, “Mathematical models of respiratory mechanics,” in *Modelling methodology for physiology and medicine,* San Diego, Academic Press, 2001.

[55] J. Mecklenburgh, T. al-Obaidi and W. Mapleson, “A model lung with direct representation of respiratory muscle activity,” *Br J Anaesth,* vol. 68, pp. 603-612, 1992.

[56] B. Ferris, J. Mead and L. Opie, “Partitioning of respiratory flow resistance in man,” *J Appl Physiol,* vol. 19, pp. 653-658, 1964.

[57] G. Grimby, T. Takishima, W. Graham, P. Macklem and J. Mead, “Frequency dependence of flow resistance in patients with obstructive lung disease,” *J Clin Invest,* vol. 47, pp. 1455-1465, 1968.

[58] J. Mecklenburgh and W. Mapleson, “Ventilatory assistance and respiratory muscle activity. 2: simulation with an adaptive active ("aa" or "a-squared") model lung,” *Br J Anaesth,* vol. 80, pp. 434-439, 1998.

[59] J. Comroe, “Mechanical factors in breathing,” in *Physiology of Respiration,* Chicago, Year Book Medical Publishers, 1977, pp. 94-141.

[60] W. Van Meurs, Modeling and simulation in biomedical engineering, Lippincott Williams and Wilkins, 2008.

[61] M. Ursino, “A theoretical analysis of the carotid body chemoreceptor response to O2 and CO2 pressure changes,” *Resp Physiol Neurobiol,* vol. 130, pp. 99-110, 2002.

[62] D. Cunningham, “Review lecture: studies on arterial chemoreceptors in man,” *J Physiol,* vol. 384, pp. 1-26, 1987.

[63] J. Santos, S. Nagato and W. Zin, “Control of breathing,” in *Respiratory System and Artificial Ventilation,* Springer, 2008.

[64] R. Fitzgerald and D. Parks, “Effect of hypoxia on carotid chemoreceptor response to carbon dioxide in cats,” *Respir Physiol,* vol. 12, pp. 218-229, 1971.

[65] S. Lahiri and R. DeLaney, “Relationship between carotid chemoreceptor activity and ventilation in the cat,” *Respir Physiol,* vol. 24, pp. 267-286, 1975.

[66] S. Lahiri and R. DeLaney, “Stimulus interaction in the responses of carotid body chemoreceptor single afferent fibers,” *Respir Physiol,* vol. 24, pp. 249-266, 1975.

[67] Z. Topor, M. Pawlicki and J. Remmers, “A computational model of the human respiratory control system: responses to hypoxia and hypercapnia,” *Ann Biomed Eng,* vol. 32, pp. 153-1545, 2004.

[68] J. Duffin, R. Mohan, P. Vasiliou, R. Stephenson and S. Mahamed, “A model of the chemoreflex control of breathing in humans: model parameters measurement,” *Respir Physiol,* vol. 120, pp. 13-26, 2000.

[69] C. StCroix, D. Cunningham and D. Paterson, “Nature of the interaction between central and peripheral chemoreceptor drives in human subjects,” *Can J Physiol Pharmacol ,* vol. 74, pp. 640-646, 1996.

[70] J. West, Respiratory Physiology: The Essentials, Lippincott Williams and Wilkins, 2008.

[71] J. Spencer, E. Firouztale and R. Mellins, “Computational expressions for blood oxygen and carbon dioxide concentrations,” *Ann Biomed Eng,* vol. 7, pp. 59-66, 1979.

[72] V. Andersen, J. Sonne, S. Sletting and A. Prip, “The volume of the liver in patients correlates to body weight and alcohol consumption,” *Alcohol Alcohol,* vol. 35, pp. 531-532, 2000.

[73] K. Goda, E. Sasaki, K. Nagata, M. Fukai, N. Ohsawa and T. Hahafusa, “Pancreatic volume in type 1 and type 2 diabetes mellitus,” *Acta Diabetol,* vol. 38, pp. 145-149, 2001.

[74] Y. Liu, R. Bahn and E. Ritman, “Myocardial volume perfused by coronary artery branches-a three dimensional x-ray CT evaluation in human cadaver hearts,” *Int J Card Imaging,* vol. 8, pp. 95-101, 1992.

[75] A. J. Rodrigues, C. Rodrigues, M. Germano, I. J. Rasera and G. Cerri, “Sonographic assessment of normal spleen volume,” *Clin Anat,* vol. 8, pp. 252-255, 1995.

[76] L. Lerman, A. Flickinger, P. Sheedy and S. Turner, “Reproducibility of human kidney perfusion and volume determinations with electron beam computed tomography,” *Invest Radiol,* Vols. 204-210, p. 31, 1996.

[77] W. Shen, M. Punyanitya, Z. Wang, D. Gallagher, M. StOnge, J. Albu, S. Heymsfield and S. Heshka, “Total body skeletal muscle and adipose tissue volumes: estimation from a single abdominal cross-sectional image,” *J Appl Physiol,* vol. 97, pp. 2333-

2338, 2004.

[78] A. Guyton and J. Hall, Textbook of Medical Physiology, Elsevier Saunders, 2006.

[79] T. Christensen and C. Draeby, “Models of the blood transport system,” in *Applied Mathematical Models in Human Physiology,* SIAM, Society for Industrial and Applied Mathematics, 2004.

[80] Z. Topor, K. Vasilakos, M. Younes and J. Remmers, “Model based analysis of sleep disordered breathing in congestive heart failure,” *Respir Physiol Neurobiol,* vol. 155, pp. 82-92, 2007.

[81] K. Kiely, R. Cargill and B. Lipworth, “Effects of hypercapnia on hemodynamic, inotropic, lusitropic, and electrophysiologic indices in human,” *Chest,* vol. 109, pp. 1215-1221, 1996.

[82] Y. Mengesha, “Variability of cardiovascular responses to hypercapnia in man,” *Ethiop J Health Dev,* vol. 14, pp. 135-141, 2000.

[83] W. Reynolds and H. Milhorn, “Transient ventilatory response to hypoxia with and without controlled alveolar PCO2,” *J Appl Physiol,* vol. 35, pp. 187-196, 1973.

[84] W. Reynolds, H. Milhorn and G. Holloman, “Transient ventilatory response to graded hypercapnia in man,” *J Appl Physiol,* vol. 33, pp. 47-54, 1972.

[85] J. Duffin, “Model validation and control issues in the respiratory system,” in *Mathematical modeling and validation in physiology: applications to the cardiovascular and respiratory systems,* Springer Verlag, 2013.

[86] “Normal hemodynamic parameters and laboratory values. Technical report.,” Edwards Lifescienses LLC, [Online]. Available: http://ht.edwards.com.

[87] D. Procter, “Physiology of the upper airway,” *Handbook of Physiology, Respiration,* pp. 309-343, 1964.

[88] E. D'Angelo and E. Agostoni, “Continuous recording of pleural surface pressure at various sites,” *Respir Physiol,* vol. 19, pp. 356-368, 1973.

[89] G. Arthurs and M. Sudhakar, “Carbon dioxide transport,” *Educ in Anaesth Crit Care Pain,* vol. 35, pp. 207-210, 2005.

[90] J. Comroe, “Alveolar ventilation,” in *Physiology of Respiration,* Chicago, IL, Year Book Medical Publishers, INC, 1977.

[91] R. Flumerfelt and E. Crandall, “An analysis of external respiration in man,” *Mathematical Biosciences* , vol. 3, pp. 205-230, 1968.

[92] K. Lin and G. Cumming, “A model of time-varying gas exchange in the human lung during a respiratory cycle at rest,” *Respir Physiol,* vol. 17, pp. 93-112, 1973.

[93] J. Thompson and M. Jaffe, “Capnographic waveforms in the mechanically ventilated patients,” *Respir Care* , vol. 50, pp. 100-108, 2005.

[94] J. Ruskin, R. Bache, J. Rembert and J. Greenfiel, “Pressure-flow studies in man: effect of respiration on the left ventricular stroke volume,” *Circulation,* vol. 48, pp. 79-85,

1973.

[95] F. Michard, “Changes in arterial pressure during mechanical ventilation,” *Anesthesiology,* vol. 103, pp. 419-428, 2005.

[96] B. Fuhrman, “Cardiopulmonary interactions,” in *Pediatric Critical Care,* 2011.

[97] N. Al-Rawas, M. Banner, N. Euliano, C. Tams, A. Martin and G. A, “Expiratory time constant for determinations of plateau pressure, respiratory system compliance, and total resistance.,” *Crit Care,* vol. 17, p. R23, 2013.

[98] J. H. Bates, “The Linear Single-Compartment Model,” in *Lung Mechanics - an Inverse Modeling Approach,* Cambridge, Cambridge University Press, 2009, pp. 47-49.

[99] R. Peslin, J. da Silva, F. Chabot and C. Duvivier, “Respiratory mechanics studied by multiple linear regression in unsedated ventilated patients,” *Eur Respir J,* vol. 5, pp. 871-878, 1992.

[100] J. Rousselot, R. Peslin and C. Duviver, “Evaluation of the multiple linear regression method to monitor respiratory mechanics in ventilated neonates and young children,” *Pediatr Pulmonol,* vol. 13, pp. 161-168, 1992.

[101] L. Ljung and T. Soderstrom, Theory and practice of recursive identification, Cambridge, MA: MIT Press, 1983.

[102] A. Louzon and J. Bates, “Estimation of time-varying respiratory mechanical parameters by recursive least squares,” *J Appl Physiol,* vol. 71, pp. 1159-1165, 1991.

[103] J. Bates and A. Louzon, “A nonstatiscal approach to estimating confidence intervals about model parameters: application to respiratory mechanics,” *IEEE Trans Biomed Eng,* vol. 39, pp. 94-100, 1992.

[104] G. Avanzolini, P. Barbini, A. Cappello, G. Cevenini and L. Chiari, “A new approach for tracking respiratory mechanical parameters in real-time,” *Ann Biomed Eng,* vol. 25, pp. 154-163, 1997.

[105] J. Benditt, “Esophageal and gastric pressure measurements,” *Respir Care,* vol. 50, no. 1, pp. 68-75, 2005.

[106] B. Cabello and J. Mancebo, “Work of breathing,” *Intensive Care Med,* vol. 32, pp. 1311-1314, 2006.

[107] M. Banner, R. Kirby, A. Gabrielli and A. Layon, “Partially and totally unloading respiratory muscles based on real-time measurements of work of breathing,” *Chest,* vol. 106, pp. 1835-1842, 1994.

[108] M. Banner, M. Jaeger and R. Kirby, “Componenets of the work of breathing and implications for monitoring ventilator-dependent patients,” *Crit Care Med,* vol. 22, pp. 512-523, 1994.

[109] M. Banner, “Respiratory muscle loading and the work of breathing,” *J Cardiothorac Vasc Anesth,* vol. 9, pp. 192-204, 1995.

[110] E. Campbell, The respiratory muscles and the mechanics of breathing, Chicago: Year Book Publishers, 1958.

[111] E. Agostoni, E. Campbell and S. Freedman, The respiratory muscles: mechanics and neural control, Philadelphia: WB Saunders, 1970.

[112] J. Petros, C. Lamond and D. Bennett, “The Bicore pulmonary monitor: A decvice to assess the work of breathing while weaning from mechanical ventilation,” *Anaesthesia,* vol. 48, pp. 985-988, 1993.

[113] B. Blanchy and M. Banner, “A new respiratory monitor that enables accurate measurement of work of breathingL a validation study,” *Respir Care,* vol. 39, pp. 897-905, 1994.

[114] S. Berman, M. Banner, P. Blanch and L. Widner, “A new pediatric respiratory monitor that accurately measures imposed work of breathing: a validation study,” *J Clin Monit,* vol. 11, pp. 14-17, 1995.

[115] E. Kondili, C. Alexopoulou, N. Xirouchaki, K. Vaporidi and D. Georgopoulus, “Estimation of inspiratory muscle pressure in critically ill patients,” *Intensive Care Med,* vol. 36, pp. 648-655, 2010.

[116] J. Bates, “Non-linear Single Compartment Models,” in *Lung Mechanics - and Inverse Modelling Approach,* Cambridge, Cambridge University Press, 2009, pp. 82-96.

[117] S. Zenker, J. Rubin and G. Clermont, “From Inverse Problems in Mathematical Physiology to Quantitaive Differential Diagnoses,” *PLoS Computat Biol,* vol. 3, no. 11, pp. 2072-2086, 2007.

[118] D. Murley, S. Rees, B. Rasmussen and S. Andreassen, “Decision support of inspired oxygen selection based on Bayesian learning of pulmonary gas exchange parameters,” *Artif Intell Med,* vol. 34, pp. 53-63, 2005.

[119] G. Sparacino, C. Tombolato and C. Cobelli, “Maximum-Likelihood Versus Maximum a Posteriori Parameter Estimation of Physiological System Models: The C-peptide Impulse Response Case Study,” *IEEE Trans Biomed Eng,* vol. 47, no. 6, pp. 801-811, 2000.

[120] C. Cobelli and E. Carson , “Parametric Models - The Estimation Probelm,” in *Introduction to Modeling in Physiology and Medicine,* New York, Academic Press, 2001, pp. 195-234.

[121] S. M. Kay, “The Bayesian Philosophy,” in *Fundamentals of Statiscal Signal Processing - Estimation Theory,* New Jersey, Prentice Hall, 1993, pp. 309-339.

[122] A. Bertoldo , G. Sparacino and C. Cobelli, “Population Approach Improves Parameter Estimation of Kinetic Models From Dynamic PET Data,” *IEEE Trans Med Imaging,* vol. 23, no. 3, pp. 297-306, 2004.

[123] R. Hovorka and P. Vicini, “Parameter Estimation,” in *Modelling Methodology for Physiology and Medicine,* 1st ed., San Diego, Academic Press, 2001, pp. 107-151.

[124] P. Magni and G. Sparacino, “Parameter Estimation,” in *Modelling Methodology for Physiology and Medicine,* 2nd ed., London, Elsevier, 2014, pp. 84-110.

Appendix: Cardiopulmonary Model's Equations

In the following section the complete equations describing the *CP Model* presented in *Chapter 2* are provided.

A1. The Circulatory System

The equations describing the circulatory system have been obtained by enforcing conservation of mass and balance of forces for each vascular compartments in Figure 2.12. The general form of these equations has been presented in the *Model Development* section (see Eq 2-1-2-3). Here, this general form is instantiated for each specific circulatory compartment included in the circulatory system model.

Systemic Circulation

$$C_{sa} \cdot \frac{dP_{sa}}{dt} = Q_{lv,o} - Q_{sa} \tag{A-1}$$

$$L_{sa} \cdot \frac{dQ_{sa}}{dt} = P_{sa} - P_{ep} - R_{sa} \cdot Q_{sa} \tag{A-2}$$

$$V_{sa} = C_{sa} \cdot P_{sa} + V_{u,sa} \tag{A-3}$$

$$C_{p,eq} \cdot \frac{dP_{ep}}{dt} = Q_{sa} - \sum_j Q_{jp} \tag{A-4}$$

$$P_{ep} = P_{sp} = P_{mp} = P_{bp} = P_{hp} \tag{A-5}$$

$$Q_{jp} = \begin{cases} \frac{P_{jp} - P_{jv}}{R_{jp}} & P_{jp} \geq P_{jv} \\ 0 & P_{jp} < P_{jv} \end{cases} \tag{A-6}$$

$$V_{jp} = C_{jp} \cdot P_{jp} + V_{u,jp} \tag{A-7}$$

$$C_{sv} \cdot \frac{dP_{sv}}{dt} + \frac{dVu,sv}{dt} = Q_{sp} - Q_{sv} \tag{A-8}$$

$$C_{mv} \cdot \frac{dP_{mv}}{dt} + \frac{dVu,mv}{dt} = Q_{mp} - Q_{mv} \tag{A-9}$$

$$C_{hv} \cdot \frac{dP_{hv}}{dt} = Q_{hp} - Q_{hv} \tag{A-10}$$

$$C_{bv} \cdot \frac{dP_{bv}}{dt} = Q_{bp} - Q_{bv} \tag{A-11}$$

$$P_{ev} = \frac{1}{C_{ev}} \cdot [V_{tot} - V_{sa} - V_{hp} - V_{bp} - V_{mp} - V_{sp} - V_{ep}$$

$$-V_{hv} - V_{bv} - V_{mv} - V_{sv} - V_{tv} - V_{ra} - V_{rv} \tag{A-12}$$

$$-V_{pa} - V_{pp} - V_{ps} - V_{pv} - V_{la} - V_{lv} - V_{u,ev}]$$

$$Q_{jv} = \begin{cases} \frac{P_{jv} - P_{tv}}{R_{jv}} & P_{jv} \geq P_{tv} \\ 0 & P_{jv} < P_{tv} \end{cases} \tag{A-13}$$

$$V_{jv} = C_{jv} \cdot P_{jv} + V_{u,jv} \tag{A-14}$$

$$\frac{dV_{tv}}{dt} = \sum_j Q_{jv} - Q_{tv} \tag{A-15}$$

$$Q_{tv} = \frac{P_{tv} - P_{ra}}{R_{tv}} \tag{A-16}$$

$$P_{tv} = P_{pl} + P_{tm,tv} \tag{A-17}$$

where $j = e, s, m, b, h$ indicates the specific systemic compartment, $C_{p,eq} = \sum_j C_{jp}$ is the equivalent peripheral compliance given by the parallel arrangement of the 5 different systemic peripheral compartments and $P_{tm,tv}$ is given by Eq. 2.4 (see *2.3 Model Development* section).

Pulmonary Circulation

$$C_{pa} \cdot \frac{d(P_{pa} - P_{pl})}{dt} = Q_{rv,o} - Q_{pa} \tag{A-18}$$

$$L_{pa} \cdot \frac{dQ_{pa}}{dt} = P_{pa} - P_{pp} - R_{pa} \cdot Q_{pa} \tag{A-19}$$

$$V_{pa} = C_{pa} \cdot (P_{pa} - P_{pl}) + V_{u,pa} \tag{A-20}$$

$$(C_{ps} + C_{pp}) \cdot \frac{d(P_{pp} - P_{pl})}{dt} = Q_{pa} - \mathrm{Q}_{ps} - \mathrm{Q}_{pp} \tag{A-21}$$

$$Q_{pp} = \frac{P_{pp} - P_{pv}}{R_{pp}} \tag{A-22}$$

$$Q_{ps} = \frac{P_{ps} - P_{pv}}{R_{ps}} \tag{A-23}$$

$$P_{ps} = P_{pp} \tag{A-24}$$

$$V_{pp} = C_{pp} \cdot (P_{pp} - P_{pl}) + V_{u,pp} \tag{A-25}$$

$$V_{ps} = C_{ps} \cdot (P_{ps} - P_{pl}) + V_{u,ps} \tag{A-26}$$

$$C_{pv} \cdot \frac{d(P_{pv} - P_{pl})}{dt} = Q_{pp} + Q_{ps} - Q_{pv} \tag{A-27}$$

$$Q_{pv} = \frac{P_{pv} - P_{la}}{R_{pv}} \tag{A-28}$$

$$V_{pv} = C_{pv} \cdot (P_{pv} - P_{pl}) + V_{u,pv} \tag{A-29}$$

A.2 The Heart

The equations describing the heart model are unchanged compared with previous studies [5, 6], except for the inclusion of the intrapleural pressure as the external reference pressure acting outside the heart.

Left Heart

$$C_{la} \cdot \frac{d(P_{la} - P_{pl})}{dt} = Q_{pv} - Q_{lv,i} \tag{A-30}$$

$$Q_{lv,i} = \begin{cases} \frac{P_{la} - P_{lv}}{R_{la}} & P_{la} \geq P_{lv} \\ 0 & P_{la} < P_{lv} \end{cases} \tag{A-31}$$

$$V_{la} = C_{la} \cdot (P_{la} - P_{pl}) + V_{u,la} \tag{A-32}$$

$$\frac{dV_{lv}}{dt} = Q_{lv,i} - Q_{lv,o} \tag{A-33}$$

$$Q_{lv,o} = \begin{cases} \frac{P_{lv,max} + P_{pl} - P_{sa}}{R_{lv}} & P_{lv,max} + P_{pl} \geq P_{sa} \\ 0 & P_{lv,max} + P_{pl} < P_{sa} \end{cases} \tag{A-34}$$

$$P_{lv} = P_{lv,max} + P_{pl} - R_{lv} \cdot Q_{lv,o} \tag{A-35}$$

$$R_{lv} = K_{R,lv} \cdot P_{lv,max} \tag{A-36}$$

$$P_{lv,max}(t) = \phi(t) \cdot E_{max,lv} \cdot (V_{lv} - V_{u,lv})$$

$$+[1 - \phi(t)] \cdot P_{0,lv} \cdot (e^{K_{E,lv} \cdot V_{lv}} - 1) \tag{A-37}$$

Right Heart

$$C_{ra} \cdot \frac{d(P_{ra} - P_{pl})}{dt} = Q_{tv} - Q_{rv,i} \tag{A-38}$$

$$Q_{rv,i} = \begin{cases} \frac{P_{ra} - P_{rv}}{R_{ra}} & P_{ra} \geq P_{rv} \\ 0 & P_{ra} < P_{rv} \end{cases} \tag{A-39}$$

$$V_{ra} = C_{ra} \cdot (P_{ra} - P_{pl}) + V_{u,ra} \tag{A-40}$$

$$\frac{dV_{rv}}{dt} = Q_{rv,i} - Q_{rv,o} \tag{A-41}$$

$$\dot{Q}_{rv,o} = \begin{cases} \frac{P_{rv,max} + P_{pl} - P_{pa}}{R_{rv}} & P_{rv,max} + P_{pl} \geq P_{pa} \\ 0 & P_{rv,max} + P_{pl} < P_{pa} \end{cases} \tag{A-42}$$

$$P_{rv} = P_{rv,max} + P_{pl} - R_{rv} \cdot Q_{rv,o} \tag{A-43}$$

$$R_{rv} = K_{R,rv} \cdot P_{rv,max} \tag{A-44}$$

$$P_{rv,max}(t) = \phi(t) \cdot E_{max,rv} \cdot (V_{rv} - V_{u,rv})$$

$$+[1 - \phi(t)] \cdot P_{0,rv} \cdot (e^{K_{E,rv} \cdot V_{rv}} - 1) \tag{A-45}$$

where $\phi(t)$ is the ventricle activation function (with $\phi(t) = 1$ at maximum contraction and $\phi(t) = 0$ at complete relaxation), assumed to be equal for both left and right ventricle and governed by the equation:

$$\phi(t) = \begin{cases} \sin^2\left[\frac{\pi \cdot T(t)}{T_{sys}(t)} \cdot u\right] & 0 \geq u \geq T_{sys}/HP \\ 0 & T_{sys}/HP \geq u \geq 1 \end{cases} \tag{A-46}$$

where HP is the heart period, T_{sys} is the duration of systole and u is a dimensionless variable ranging between 0 and 1 and indicating the fraction of cardiac cycle:

$$u = \mathrm{frac}\left[\int_{t_0}^{t} \frac{1}{HP(\tau)}\, \mathrm{d}\tau + u(t_0)\right] \tag{A-47}$$

where "frac" is the fractional part function (that resets the input to 0 as soon as it reaches 1). Finally, the duration of systole T_{sys} is assumed to decrease linearly with the heart rate according to:

$$T_{sys} = T_{sys,0} - K_{sys} \cdot \frac{1}{HP} \tag{A-48}$$

A.3 The Lung Mechanics

The equations describing the lung mechanics model have been obtained by applying conservation of mass to the electrical analog shown in Figure 2.17.

$$C_l \cdot \frac{dP_l}{dt} = \frac{P_{ao} - P_l}{R_{ml}} - \frac{P_l - P_{tr}}{R_{lt}} \tag{A-49}$$

$$C_{tr} \cdot \frac{d(P_{tr} - P_{pl})}{dt} = \frac{P_l - P_{tr}}{R_{lt}} - \frac{P_{tr} - P_b}{R_{tb}} \tag{A-50}$$

$$C_b \cdot \frac{d(P_b - P_{pl})}{dt} = \frac{P_{tr} - P_b}{R_{tb}} - \frac{P_b - P_A}{R_{bA}} \tag{A-51}$$

$$C_A \cdot \frac{d(P_b - P_{pl})}{dt} = \frac{P_b - P_A}{R_{bA}} \tag{A-52}$$

$$C_{cw} \cdot \frac{d(P_{pl} - P_{mus})}{dt} = \frac{P_l - P_{tr}}{R_{lt}} \tag{A-53}$$

$$\dot{V} = \frac{P_{ao} - P_l}{R_{ml}} \tag{A-54}$$

$$\dot{V}_A = \frac{P_l - P_{tr}}{R_{lt}} \tag{A-55}$$

$$V_l = C_l \cdot P_l + V_{u,l} \tag{A-56}$$

$$V_{tr} = C_{tr} \cdot (P_{tr} - P_{pl}) + V_{u,tr} \tag{A-57}$$

$$V_b = C_b \cdot (P_b - P_{pl}) + V_{u,b} \tag{A-58}$$

$$V_A = C_A \cdot (P_A - P_{pl}) + V_{u,A} \tag{A-59}$$

$$V_D = V_l + V_{tr} + V_b \tag{A-60}$$

The equations describing the profile of the respiratory muscle generator P_{mus} have been provided in the *Model Development* section (see Eq. 2-6).

A.4 The Lung Gas Exchange

The equations describing the lung gas exchange model have been already presented in the *Model Development* section (see Eqs. 2-8 – 2-16) but only in their general form. Here, the complete equations governing the model are specialized for the specific gas involved, i.e. for O_2 and CO_2.

$$\begin{aligned} V_D \cdot \frac{dF_{D,O2}}{dt} &= u(\dot{V}) \cdot \dot{V} \cdot (F_{I,O2} - F_{D,O2}) \\ &\quad + u(-\dot{V}) \cdot \dot{V}_A \cdot (F_{D,O2} - F_{A,O2}) \end{aligned} \tag{A-61}$$

$$\begin{aligned} V_D \cdot \frac{dF_{D,CO2}}{dt} &= u(\dot{V}) \cdot \dot{V} \cdot (F_{I,CO2} - F_{D,CO2}) \\ &\quad + u(-\dot{V}) \cdot \dot{V}_A \cdot (F_{D,CO2} - F_{A,CO2}) \end{aligned} \tag{A-62}$$

$$\begin{aligned} V_A \cdot \frac{dF_{A,O2}}{dt} &= u(\dot{V}) \cdot \dot{V}_A \cdot (F_{D,O2} - F_{A,O2}) \\ &\quad - K \cdot \left(Q_{pa} \cdot (1 - sh) \cdot (C_{pp,O2} - \tilde{C}_{v,O2}) + V_{pp} \frac{dC_{pp,O2}}{dt} \right) \end{aligned} \tag{A-63}$$

$$\begin{aligned} V_A \cdot \frac{dF_{A,CO2}}{dt} &= u(\dot{V}) \cdot \dot{V}_A \cdot (F_{D,CO2} - F_{A,CO2}) \\ &\quad - K \cdot \left(Q_{pa} \cdot (1 - sh) \cdot (C_{pp,CO2} - \tilde{C}_{v,CO2}) + V_{pp} \frac{dC_{pp,CO2}}{dt} \right) \end{aligned} \tag{A-64}$$

$$C_{pp,O2} = C_{sat,O2} \cdot \frac{(X_{pp,O2})^{\frac{1}{h_1}}}{1 + (X_{pp,O2})^{\frac{1}{h_1}}} \tag{A-65}$$

$$X_{pp,O2} = P_{pp,O2} \cdot \frac{1+\beta_1 \cdot P_{pp,CO2}}{K_1 \cdot (1+\alpha_1 \cdot P_{pp,CO2})} \qquad \text{(A-66)}$$

$$C_{pp,CO2} = C_{sat,CO2} \cdot \frac{(X_{pp,CO2})^{\frac{1}{h_2}}}{1+(X_{pp,CO2})^{\frac{1}{h_2}}} \qquad \text{(A-67)}$$

$$X_{pp,CO2} = P_{pp,CO2} \cdot \frac{1+\beta_2 \cdot P_{pp,O2}}{K_2 \cdot (1+\alpha_2 \cdot P_{pp,O2})} \qquad \text{(A-68)}$$

$$P_{pp,O2} = P_{A,O2} \qquad \text{(A-69)}$$

$$P_{pp,CO2} = P_{A,CO2} \qquad \text{(A-70)}$$

$$P_{A,O2} = F_{A,O2} \cdot (P_{atm} - P_{ws}) \qquad \text{(A-71)}$$

$$P_{A,CO2} = F_{A,CO2} \cdot (P_{atm} - P_{ws}) \qquad \text{(A-72)}$$

$$C_{a,O2} = \frac{Q_{pp} \cdot C_{pp,O2} + Q_{ps} \cdot \tilde{C}_{v,O2}}{Q_{pp}+Q_{ps}} \qquad \text{(A-73)}$$

$$C_{a,CO2} = \frac{Q_{pp} \cdot C_{pp,CO2} + Q_{ps} \cdot \tilde{C}_{v,CO2}}{Q_{pp}+Q_{ps}} \qquad \text{(A-74)}$$

$$S_{a,O_2}\% = \frac{C_{a,O_2} - P_{a,O_2} \cdot 0.003/100}{Hgb \cdot 1.34} \cdot 100 \qquad \text{(A-75)}$$

where Eqs. A-61, A-62, A-63, A-64 are derived based on conservation of mass principles, Eqs. A-65, A-66, A-67, A-68 are the dissociation functions as reported in [71], Eqs. A-69, A-70 represent the instantaneous equilibrium assumption between alveolar space and capillary blood, Eqs. A-71, A-72 relate gas fractions in the lungs to their corresponding partial pressures, Eqs. A-73, A-74 represent the mixing between capillary and shunted blood, and Eq. A-75 is used to compute O_2 saturation in the arterial blood.

A.5 The Tissue Gas Exchange

The equations describing the tissue gas exchange and the venous pool gas transport models have been already presented in the *Model Development* section (see Eqs. 2-15 - 2-17), but only in their general form and without mathematical derivation. Similar to what we have done for the lung gas exchange model, here we present the complete equations, specializing them for O_2 and CO_2 and for each compartment of the model (see Figure 2.20).

$$(V_{T,hp} + V_{hp}) \cdot \frac{dC_{hp,O2}}{dt} = Q_{hp,in} \cdot (\tilde{C}_{a,O2} - C_{hp,O2}) - M_{O2,hp} \tag{A-76}$$

$$(V_{T,hp} + V_{hp}) \cdot \frac{dC_{hp,CO2}}{dt} = Q_{hp,in} \cdot (\tilde{C}_{a,CO2} - C_{hp,CO2}) + M_{CO2,hp} \tag{A-77}$$

$$(V_{T,bp} + V_{bp}) \cdot \frac{dC_{bp,O2}}{dt} = Q_{bp,in} \cdot (\tilde{C}_{a,O2} - C_{bp,O2}) - M_{O2,bp} \tag{A-78}$$

$$(V_{T,bp} + V_{bp}) \cdot \frac{dC_{bp,CO2}}{dt} = Q_{bp,in} \cdot (\tilde{C}_{a,CO2} - C_{bp,CO2}) + M_{CO2,bp} \tag{A-79}$$

$$(V_{T,mp} + V_{mp}) \cdot \frac{dC_{mp,O2}}{dt} = Q_{mp,in} \cdot (\tilde{C}_{a,O2} - C_{mp,O2}) - M_{O2,mp} \tag{A-80}$$

$$(V_{T,mp} + V_{mp}) \cdot \frac{dC_{mp,CO2}}{dt} = Q_{mp,in} \cdot (\tilde{C}_{a,CO2} - C_{mp,CO2}) + M_{CO2,mp} \tag{A-81}$$

$$(V_{T,ep} + V_{ep}) \cdot \frac{dC_{ep,O2}}{dt} = Q_{ep,in} \cdot (\tilde{C}_{a,O2} - C_{ep,O2}) - M_{O2,ep} \tag{A-82}$$

$$(V_{T,ep} + V_{ep}) \cdot \frac{dC_{ep,CO2}}{dt} = Q_{ep,in} \cdot (\tilde{C}_{a,CO2} - C_{ep,CO2}) + M_{CO2,ep} \tag{A-83}$$

$$(V_{T,sp} + V_{sp}) \cdot \frac{dC_{sp,O2}}{dt} = Q_{sp,in} \cdot (\tilde{C}_{a,O2} - C_{sp,O2}) - M_{O2,sp} \tag{A-84}$$

$$(V_{T,sp} + V_{sp}) \cdot \frac{dC_{sp,CO2}}{dt} = Q_{sp,in} \cdot (\tilde{C}_{a,CO2} - C_{sp,CO2}) + M_{CO2,sp} \tag{A-85}$$

See Figure 2.20 for explanation of symbols.

A.6 The Venous Pool Gas Transport

The complete equations describing the venous pool gas transport model are the following:

$$V_{hv} \cdot \frac{dC_{hv,O2}}{dt} = Q_{hp} \cdot (C_{hp,O2} - C_{hv,O2}) \tag{A-86}$$

$$V_{hv} \cdot \frac{dC_{hv,CO2}}{dt} = Q_{hp} \cdot (C_{hp,CO2} - C_{hv,CO2}) \tag{A-87}$$

$$V_{bv} \cdot \frac{dC_{bv,O2}}{dt} = Q_{bp} \cdot (C_{bp,O2} - C_{bv,O2}) \tag{A-88}$$

$$V_{bv} \cdot \frac{dC_{bv,CO2}}{dt} = Q_{bp} \cdot (C_{bp,CO2} - C_{bv,CO2}) \tag{A-89}$$

$$V_{mv} \cdot \frac{dC_{mv,O2}}{dt} = \dot{Q}_{mp} \cdot (C_{mp,O2} - C_{mv,O2}) \tag{A-90}$$

$$V_{mv} \cdot \frac{dC_{mv,CO2}}{dt} = Q_{mp} \cdot (C_{mp,CO2} - C_{mv,CO2}) \tag{A-91}$$

$$V_{ev} \cdot \frac{dC_{ev,O2}}{dt} = Q_{ep} \cdot (C_{ep,O2} - C_{ev,O2}) \tag{A-92}$$

$$V_{ev} \cdot \frac{dC_{ev,CO2}}{dt} = Q_{ep} \cdot (C_{ep,CO2} - C_{ev,CO2}) \tag{A-93}$$

$$V_{sv} \cdot \frac{dC_{sv,O2}}{dt} = Q_{sp} \cdot (C_{sp,O2} - C_{sv,O2}) \tag{A-94}$$

$$V_{sv} \cdot \frac{dC_{sv,CO2}}{dt} = Q_{sp} \cdot (C_{sp,CO2} - C_{sv,CO2}) \tag{A-95}$$

$$\begin{gathered} V_{tv} \cdot \frac{dC_{v,O2}}{dt} = Q_{hv} \cdot (C_{hv,O2} - C_{v,O2}) + Q_{bv} \cdot (C_{bv,O2} - C_{v,O2}) \\ +Q_{mv} \cdot (C_{mv,O2} - C_{v,O2}) + Q_{ev} \cdot (C_{ev,O2} - C_{v,O2}) \\ +\mathrm{Q}_{sv} \cdot (C_{sv,O2} - C_{v,O2}) \end{gathered} \tag{A-96}$$

$$\begin{gathered} V_{tv} \cdot \frac{dC_{v,CO2}}{dt} = Q_{hv} \cdot (C_{hv,CO2} - C_{v,CO2}) + Q_{bv} \cdot (C_{bv,CO2} - C_{v,CO2}) \\ +Q_{mv} \cdot (C_{mv,CO2} - C_{v,CO2}) + Q_{ev} \cdot (C_{ev,CO2} - C_{v,CO2}) \\ +Q_{sv} \cdot (C_{sv,CO2} - C_{v,CO2}) \end{gathered} \tag{A-97}$$

where $Q_{jp,in}$ is the the blood flow entering the *j*-*t*h systemic peripheral compartment (see Figure 2.20).

A.7 The Respiratory Control

The respiratory control model has been described in the *Model Development* section and detailed equations have been already provided.

A.8 The Cardiovascular Control

The equations describing the cardiovascular control model are taken from [5, 6]. The only modification compared to these early work is in the description of the afferent peripheral chemoreceptor mechanism, which in the present model, as mentioned in the previous section, is based on the equations reported in [61]. For the sake of brevity, we prefer to omit the equations of the cardiovascular control model and we encourage the interested reader to refer to the original publications for additional details.